Implementation and Validation of a Cohesive Fracture Model through Contact Mechanics with Application to Cutting and Needle Insertion into Human Skin

Kevin Bronik

Department of Mechanical Engineering

University of Cardiff

This dissertation is submitted for the degree of

Doctor of Philosophy (PhD)

Cardiff   2017

Dedication

I would like to dedicate this thesis to my loving parents and family ... I also dedicate this thesis to all who believe in real science.

"Science is the belief in the ignorance of the experts" - Richard Feynman

Declaration of Authorship

DECLARATION

This work has not been submitted in substance for any other degree or award at this or any other university or place of learning, nor is being submitted concurrently in candidature for any degree or other award.

Signed..(candidate), Date...

STATEMENT 1

This thesis is being submitted in partial fulfillment of the requirements for the degree of PhD.

Signed..(candidate), Date...

STATEMENT 2

This thesis is the result of my own independent work/investigation, except where otherwise stated, and the thesis has not been edited by a third party beyond what is permitted by Cardiff University's Policy on the Use of Third Party Editors by Research Degree Students. Other sources are acknowledged by explicit references. The views expressed are my own.

Signed..(candidate), Date...

STATEMENT 3

I hereby give consent for my thesis, if accepted, to be available online in the University's Open Access repository and for inter-library loan, and for the title and summary to be made available to outside organisations.

Signed..(candidate), Date...

Acknowledgements

Publications

2016 ICTAM Congress [oral & poster presentation]

24th International Congress of Theoretical and Applied Mechanics ICTAM 2016, 21-26 August 2016, Montréal, Canada

Kevin Bronik, Prof Sam L Evans and Dr Pierre Kerfriden

Mechanical description and engineering analysis of cutting and needle insertion into Human skin

2016 ACME Conference [paper & oral presentation]

24th UK Conference of the Association for Computational Mechanics in Engineering, 31 March – 01 April 2016, Cardiff University, Cardiff

Kevin Bronik, Prof Sam L Evans and Dr Pierre Kerfriden

Mechanical description and engineering analysis of cutting and (sterile) needle insertion into Human skin

2016 PGR Conference [poster presentation]

Engineering PGR Conference 2016, Tuesday 9th February, Cardiff University, Cardiff

Kevin Bronik, Prof Sam L Evans and Dr Pierre Kerfriden

Mechanical description and engineering analysis of cutting and (sterile) needle insertion into Human skin

2015 Conference [oral presentation]

Biomechanics & Bioengineering Conference , Wednesday 15th April 2015, School of Optometry & Vision Sciences, Maindy Road, Cardiff University, Cardiff

[Cardiff Institute of Tissue Engineering and Repair (CITER)]

Kevin Bronik, Prof Sam L Evans and Dr Pierre Kerfriden

Smart Contact Mechanics

Abstract

Understanding the highly non-linear biomechanics of the complex structure of human skin would not only provide valuable information for the development of biological comparable products that could be used for the improvement, restoration or maintenance of the biological tissue or replacement of the whole organ, but would also support the development of an advanced computational model (e.g. finite element skin models) that do not differ (or do not differ very much!) from experimental data. This could be very useful for surgical training, planning and navigation. In particular, the major goal of this thesis was the development of robust and easy to use computational models of the cutting and tearing of soft materials, including large deformations, and the development of repeatable, reproducible and reliable physical skin models in comparison to in-ex vivo human skin samples. In combination with advanced computational/mechanical methods, these could offer many possibilities, such as optimised device design which would be used for effective and reproducible skin penetration in the clinical setting and for in vivo measurements.

To be able to carry out experimental cutting tests, physical models of skin were manufactured in the laboratory using silicone rubber. The mechanical properties of the physical models were examined experimentally by applying tensile and indentation tests to the test models using the Zwick universal testing machine and the Digital Image Correlation (DIC) System. To estimate the mechanical properties of the physical models and calculate the quantities, Poisson's ratio, Young's modulus and shear modulus -which were used later in computational cutting models - and inverse analyses were performed for each example of manufactured silicone rubber in the laboratory using the analytical study on indentation method, the curve fitting technique and DIC measurements. Then, the results were compared to the mechanical properties of human skin experimentally obtained in vivo/ ex vivo (from published studies).

A new large deformation cohesive zone formulation was implemented using contact mechanics, which allows easy definition of crack paths in conventional finite element models. This was implemented in the widely used open source FE package FEBio through modification of the classical contact model to provide a specific implementation of a mesh independent method for straightforward controlling of (non-linear) fracture mechanical processes using the Mixed Mode Cohesive-Zone method. Additionally, new models of friction and thermodynamically coupled friction were developed and implemented.

The computational model for the simulation of the cutting process (the finite element (FE) model of cutting) was reduced to the simplified model for the sharp interaction (triangular prisms wedge cutting), where the Neo Hookean hyperelastic material model was chosen to represent the skin layers for the FEM analysis.

Practical, analytical and experimental verification tests, alongside convergence analysis, were performed. Comparison of the computational results with the analytical and experimental results revealed that applying the modified contact algorithm to the fracture problem was effective in predicting and simulating the cutting processes.

Contents

List of Figures

List of Tables

Nomenclature

Roman Symbols

ε_N Normal penalty value

$< ... >$ Macaulay brackets

$\bar{R}^2$ Adjusted coefficient of determination

δg Virtual gap function

$\delta T^S, \delta T^M$ Virtual temperature variation of slave, master interfaces

δu Virtual displacement

δv Virtual velocity

δW Virtual work

$\dot{\xi}^\alpha$ Tangential relative velocity

ε Penalty factor

ε_T Friction penalty value

η_c Surface entropy

Γ_m Master boundary

Γ_s Slave boundary

κ Thermal conductivity

$\kappa_{\alpha\beta}$ Surface curvature tensor

λ Lagrangian multiplier

$\lambda_1, \lambda_2, \lambda_3$ Principal stretches

μ Friction factor

$\nabla(m)$ Material gradient

$\nabla(s)$ Spatial gradient

$\nabla.\sigma$ Divergence of Cauchy stress

$\nabla\Theta^s, \nabla\Theta^m$ Temperature gradients (slave and master interfaces)

Ω Domain of interest

$\partial\Omega_\Gamma$ Discontinuity boundary condition

$\partial\Omega_\sigma$ Neumann boundary condition

$\partial\Omega_u$ Dirichlet boundary condition

Π Potential function

Ψ Strain energy density function

ψ Surface free energy

$\Psi(F,\theta)$ Helmholtz free energy function

ρ Spatial mass density

σ Cauchy stress tensor

τ^α, τ_α Contra and co-variant base vectors)

$\varepsilon_n^{coh}, \delta_n^c$ Characteristic opening length (normal direction)

$\varepsilon_t^{coh}, \delta_t^c$ Characteristic opening length (tangential direction)

ξ_n^α Isoparametric coordinate of the projected slave node onto the master element

ζ Weighting function

C Right Cauchy–Green tensor

C^l Forth order elasticity tensor

$C_{cor}(u,v), C_{cor}^{norm}(u,v)$ Correlation coefficient and the normalized correlation coefficient

C_c Heat capacity per unit surface

$D_{\rho u} f(u)$ Directional derivative in the direction of the incremental displacement field

D_{mech} Mechanical dissipation

E Young's modulus

E_{total} Total energy balance

F Deformation gradient

G Shear modulus

$G_c[G_{Ic} \mid G_{IIc} \mid G_{IIIc}]$ Fracture energy per unit area

G_{ini}, G_{def} Intensity of a pixel of reference and deformed images

g_N Normal gap function

g_T Tangential gap function

$g_T^{elastic}, g_T^{inelastic}$ Elastic, inelastic parts of tangential gap

h Characteristic parameter size of a mesh

$H(g)$ Heaviside function

$H^1(\Omega)$ Hilbert space (one)

H_c^s, H_c^m Heat transfer coefficients (slave and master interfaces).

I_1, I_2, I_3 Strain invariants

J Determinant of the deformation gradien

$j(\eta_k)$ Jacobian of the transformation (at a Gauss Point)

$m_{\alpha\beta}$ Metric tensor

$N(\gamma_k)$ Shape function

$p(\Upsilon), \Gamma$ Discrete functions

q_c^s, q_c^m Heat fluxes across the contact interfaces

R, Q_N Heat source and heat supply flux normal to the boundary

T Temperature field

T_0 Reference temperature

T_c Interface characteristic temperature

T_n Normal opening traction

t_N^{max} Maximum normal opening traction

T_r Reaction force

T_t Tangentiall opening traction

t_T^{max} Maximum tangential opening traction

U Solution space

$u(x,t)_{t=0}$ Initial displacement condition

u^h Discrete solution

V Lyapunov's function

v Poisson's ratio

W Weighting space

$w[\zeta_k]$ Gauss/integration weight (at a Gauss Point)

$y_\gamma^\vdash, y_{\gamma\rho}^\vdash$ Component (current and previous) of the closest point

b   Body force

e   Exponential function

K   Tangent stiffness matrix

n   Vector normal

u   Unknown displacement field

Chapter 1

Introduction-literature review

The purpose of this study was to examine the mechanical characteristics of human skin with the aim of creating a sufficiently accurate physical model, while developing a non-linear fracture mechanics formulation applicable to the living tissues, with the purpose of building up a constitutive relationship for large deformation finite element models that allowed the accurate simulation of cutting and needle insertion into human skin by using common engineering modelling techniques.

Several studies have already begun to deal with a wide range of additional developments of various theoretical and numerical formulations of cutting and needle insertion by using (traditional) finite element methods [e.g. Azar and Hayward (2008), Groves (2008), Smolen and Patriciu (2009), Mahvash (2010)]. However, without being affected by the complex mechanical nature of soft solid penetration, it is worth saying that, unfortunately, the existing literature provides little insight into the underlying mechanisms of the penetration and cutting process. Generally, it indicates that deep penetration involves deformation and cracks, and in most cases with simplification of the complex problems (e.g. considering skin layers as linear, isotropic elastic materials) or without taking tissue deformation and friction into consideration, especially failing to take into account relevant considerations, such as the contact mechanics in the energy balance formulation Azar and Hayward (2008). Therefore, the aim, aside from studying the mathematical and physical characteristics of the mechanisms of needle insertion and cutting, and manufacturing a physical model of skin suitable for the cutting and needle insertion tests, was to develop a computational cutting-model and validate it.

To accomplish the goals of the project by making use of computational and physical techniques, such as image registration techniques-Digital Image Correlation (DIC) [which are generally used for accurate 2D and 3D measurements of deformation, displacement, strain], physical models of skin with the mechanical characteristics that could be the best fit with *in vivo* or *ex vivo* experimental data of skin which could be used to process cutting and needle in-

sertion into human skin, using silicone rubber in the laboratory, were generated and examined using the Zwick universal testing machine by applying tensile and indentation tests to the test models. To estimate the mechanical properties of the physical models and calculate the quantities, Poisson's ratio, Young's modulus and shear modulus, and inverse problem theory and methods were used.

The combined experimental and computational study and analysis of the cutting of a soft solid by making use of a tool with a sharp prismatic straight cutting edge (cutting blade) was proceeded by the development of a cohesive fracture model. This combined mathematical concepts of fracture mechanics and contact mechanics, where the modification of the classical contact to provide a specific implementation of a mesh independent method for straightforward modelling of a (non-linear) fracture mechanical process using a Mixed Mode Cohesive law, alongside thermodynamically coupled friction, formulated in one contact structure, was established. This was implemented using traditional finite element methods and the accuracy of the results was practically, analytically and experimentally verified.

It was possible to develop an accurate computational model of soft solid cutting which could open the possibility for the development of an advanced computational finite element skin cutting-needle insertion model that does not differ (or does not differ too much!) from experimental data which could provide information that could be very useful for surgical training, planning and navigation, and practical uses such as informing the development of optimised devices which could be used for effective and reproducible skin penetration in the clinical setting.

In the following sections, first, the relevant literature which has contributed to the aims and objectives of the project - in other words, a summary of some methods employed within biomechanical modelling of human skin, contact mechanics and cohesive zone models - will be reviewed. Then, a short review on techniques used in Digital Image Correlation (DIC) System, as a part of the specimen measurement devices, which was applied to the development of a physical model of human skin, will be provided. In the final section of this chapter the main aims and objectives of the research will be presented.

1.1 Biomechanical models of human skin

Fully understanding the known mechanical (biomechanical) properties of human skin can be particularly useful in fields such as the development of physical and computational models of skin [Nikooyanz and Zadpoor (2011), Thalmann *et al.* (2002), Adra *et al.* (2010)], or in general, tissue engineering for medical purposes [e.g. artificial skin Shirado *et al.* (2007)] where the development of products that can be used for improvement, restoration or maintenance of

Method	Shear\Young's modu.	Body region	Reference
Indentation	$E = 39.64 - 47.19(KPa)$	arm	Groves (2008)
	$E = 1.99.10^{-3}(MPa)$	male thigh	Bader and Bowker (1983)
	$E = 1.51.10^{-3}(MPa)$	male forearm	Bader and Bowker (1983)
	$E = 1.09.10^{-3}(MPa)$	female forearm	Bader and Bowker (1983)
Tensile	$E = 4.6 - 20(MPa)$	leg	Manschot (1985)
Torsion	$G = 0.58(MPa)$	arm	Grebenyuk and Utenkin (1994)
	$G = 0.84(MPa)$	thigh	Grebenyuk and Utenkin (1994)
	$G = 1.33(MPa)$	shin	Grebenyuk and Utenkin (1994)
	$G = 0.98(MPa)$	forearm	Grebenyuk and Utenkin (1994)
	$E = 0.42 - 0.85(MPa)$	dorsal forearm	Agache et al. (1980)
	$E = 1.12(MPa)$	ventral forearm	Escoffier et al. (1986)
Suction	$E = 13 - 26.10^{-2}(MPa)$	various regions	Barel et al. (1995)

Table 1.1: A summary of the experimentally obtained mechanical properties of human skin *in vivo/ ex vivo*

biological tissue functions or to replace the whole organ, can be improved by the employment of fully understood biomechanical concepts.

In the past few decades, modelling skin biomechanics has been the subject of several research studies [Lapeer et al. (2011), Bischoff et al. (2000), Retel et al. (2001)] where, due to the various type of applications, a wide range of problem solving approaches, methods and techniques have been developed Nunez (2014). An overview of existing techniques and recent scientific procedures in soft tissue modelling [Yidong and Dongmei (2015), Mendizabal et al. (2015), Wang et al. (2015)] and a comparison of the methods developed by different researchers revealed that, due to the complexity of living organ bio-mechanics, and in most cases, the simplified version of the complex problem and fragmented approaches to the real problems, the existing modelling approaches are in fact incapable of covering the entire spectrum of the complex biomechanical behaviour of soft tissue; in other words, there is no general modelling technique which could be used in all the fields of mechanical and medical applications.

In many applications in research, such as material development and testing, due to the repeatability and reproducibility of physical skin models in comparison to *ex vivo* human skin samples, the use of physical models is preferred to using real human skin Van Gele et al. (2011). Nevertheless, the accuracy of such physical skin models which can be used to replace real human skin (and can represent truly the mechanical characteristic of human skin and

deliver the same test results as the human skin *in vivo*), is an open question which can be answered with systematic investigation of the mechanical response of the materials used and exploration of the mechanical properties of the physical skin models and real human skin and finding their differences.

An overview of existing materials used for physical skin models, which are used to develop realistic models and to simulate the mechanical properties of human skin, revealed that the most commonly used materials are liquid, gelatinous substances, micro fillers, etc. which are described below according to Dabrowska *et al.* (2016) :

> **It was found that the most common materials used to simulate skin are liquid suspensions, gelatinous substances, elastomers, epoxy resins, metals and textiles. Nano- and micro-fillers can be incorporated in the skin models to tune their physical properties.**

Generally, studies have investigated two main aspects: the skin structure and the mechanical behaviour of skin [Silver *et al.* (2001), Annaidh *et al.* (2012), Holzapfel (2000a)]. As the starting point for the analysis, techniques such as ultrasound imaging Luo *et al.* (2015), MRI scans Sengeh *et al.* (2016) and digital image correlation Maiti *et al.* (2016) are used for the identification and measurement of the mechanical properties of skin structures. Then the collected data are used as the starting point for the numerical assumptions (the geometry and the boundary conditions). And finally, by applying an inverse finite element method Labanda *et al.* (2015), Groves (2008) [the determination of unknown by using known results (e.g. a load-displacement curve obtained through experimental test)] and using inverse problem theory and methods, the unknown material parameters (e.g. such as Young's moduli) are determined. Table 1.1 shows a summary of the experimentally obtained mechanical properties of human skin *in vivo/ ex vivo* (from literature)[Groves (2008), Bader and Bowker (1983), Manschot (1985), Grebenyuk and Utenkin (1994), Agache *et al.* (1980), Escoffier *et al.* (1986) *and* Barel *et al.* (1995)].

1.2 Contact mechanics

From a mechanical perspective, contact mechanics is the study of the interaction between bodies coming in touch with each other where - in the contact area between them - load, energy, heat flux or thermal flux, etc. are exchanged.

Contact mechanics is defined generally in the fields of theoretical solid mechanics, numerical mathematics and continuum mechanics, where the numerical treatment of contact problems, in most cases by using the finite element method (FEM), is established. It is worth adding that the study of the physics of contact, experimentally and computationally, where a

combination of solid mechanics and fluid mechanics are involved, can experience real difficulties in attempting to provide a consistent basis for the treatment of the contact problem.

The mechanics of contact involves geometrical discontinuity; this means that the contact is defined at the interface between two separated continuum bodies where the contact interface itself is supposed to have zero thickness. Also at the contact interface, contact constraints such as impenetrability or complementarity conditions cannot be formulated as ordinary boundary conditions defined on the contacting surfaces.

In this chapter, the initial focus is only on the existing literature that introduced established methods and solution techniques for the variational problem in large deformation contact theory, while in Chapter 4 an especially detailed method describing the physical ideas and the mathematical structure of large deformation kinematics (involving contact, friction and thermodynamically coupled friction) will be introduced.

The formulation and analysis of computational contact mechanics problems and extension of the special methods [e.g. the augmented Lagrangian method Serpa (2000), Auricchio (1996)] that are used to large sliding and large deformation by considering non linear materials where no limits are set to the amount of deformation, are introduced in some studies. For example, a three-dimensional solution of large deformation contact problems using the definition of the van der Waals interaction for both quasi-static and dynamic simulations is introduced by Fan and Li (2016) in a research paper where, to calculate the contact force, the so called double-layer surface integral, instead of traditional double volume integration method, has been applied to the problem. In another study a new computational contact formulation for large deformation frictional contact is presented in a paper by Sauer and DeLorenzis (2015), where a two-half-pass contact algorithm is used to formulate the two neighbouring contact surfaces. Furthermore, a three-dimensional FE contact model to the frictional heating problems is introduced in a study by Yevtushenko and Grzes (2016), where the effect of the sliding velocity, time-dependent contact pressure and temperature in the frictional-contact problem of a disc brake are investigated, which proposed methods and results generally could be useful for the analysis of frictional couple problems defined on contact surfaces with cohesive force. In the study of "A new computational approach to contact mechanics using variable-node finite elements" Kim *et al.* (2008) which was conducted in the area of contact mechanics, it has been shown that the employment of node-to-node contact formulation based on the closest point projection could provide accurate results even under non-conformable mesh. This is strongly considered in this study as a powerful choice for the Contact-Cohesive approach where in three-dimensional contact mechanics non-matching mesh elements could sometimes deliver undesirable results.

A review of the recent literature reveals that many mathematical/numerical difficulties

in contact mechanics are mostly due to the configuration of continuous interacting surfaces where the bodies which are in contact may penetrate each other or separate. On the one hand, this will result in difficulty finding corresponding contact points on the contact surfaces. On the other hand, difficulty with mesh distortion in large deformation problems such that a convergent solution cannot be succeeded at all successful, which are an active area of current research. There are also other mathematical difficulties such as complex variational inequalities (especially when involving friction) which arise in the study of contact problems. Like any other branch of continuum mechanics, the numerical-mathematical treatment of the problem is sometimes limited by the development of a completely linear boundary value problem or requires in most cases new solution approaches, more specifically, when studying the existence and uniqueness of solutions for frictional-contact problems, methods such as variational-hemivariational inequalities (more detail Chapter 4) [Kravchuk and Neittaanmäki (2007), Han et al. (2014)] need to be considered. In particular, the commonly used treatments (constitutive laws) are linear elasticity Villaggio (1980) and rate dependent plasticity Laursen (2003).

The treatment of the classical contact problem, frictional and thermodynamically coupled frictional contact problems for large deformation, in the framework of the FEM in this study, are mostly based on Laursen (2003), where the introduced frameworks for the development of numerical methods deal with all necessary aspects of numerical methods for contact mechanics and frictional contact mechanics for a wide range of application possibilities with supporting real complex problems involving dynamic large deformation.

1.3   Cohesive zone models

In connection with the numerical analysis of fracture mechanics processes and to approximate non-linear fracture behaviour, cohesive zone models have been introduced and widely studied over a period of years Hillerborg et al. (1976), Xu and Needleman (1993), Conroy et al. (2015), Xiao et al. (2016) etc.

The cohesive zone formulation, generally speaking, is the modelling of an interface by the placement of discrete elements (cohesive elements) between the two surfaces which are supposed to have zero separation in the initial condition. The constitutive formulation of the cohesive model inherits its definition from two different classes, namely potential based (the definition of the cohesive zone law is based on the definition of an interface potential Π which represents the work done to separate two opposing surfaces having contact at an interface Xu and Needleman (1993)) and non-potential based. While to get the traction–separation relationships, the first derivatives of an interface potential function need to be computed, in non-potential based, the traction–separation relationships are not derived from a potential function.

Therefore, the work done for mixed-mode separation is path-dependent [Parry *et al.* (2014)] cohesive models. Due to some limitations of the non-potential based cohesive interaction (e.g. all possible separation paths have not been considered under mixed mode conditions), and because potential- based cohesive formulation offers an effective and efficient mathematical and computational framework for handling fracture mechanics and to simulate any physical phenomenon associated with it, in this project, potential-based cohesive interaction has been chosen and studied. The different formulations of cohesive zones follow different laws which are commonly indicated as exponential Liu and Islam (2013), polynomial Yao *et al.* (2016), piece-wise linear Alfano *et al.* (2007) or rigid-linear Zhou *et al.* (2005) cohesive laws, where the parameters in the cohesive model are obtained by fitting the available experimental data Xu *et al.* (2016).

Finite element analysis of fracture processes in different materials using cohesive zone models is widely used and applied to the different classes of problems. However, FEM-cohesive zone formulations for large deformations and non-linear materials are the most interesting formulations in the study of the penetration problem (one of the primary methods of dealing with the cutting and needle insertion problem that was used in the present study).

One such formulation, using cohesive zone formulation, was presented by Fakhouri *et al.* (2015), where the puncture of soft materials was modelled; in particular, large-strain behaviour during deep indentation was analysed. Another interesting study that deals with rate-dependent visco-elastic properties, rate-independent behaviour as well as thermal features by large scale simulations, was presented by Kaliske *et al.* (2015). The use of cohesive elements for simulation of needle insertion was reported by Oldfield *et al.* (2013). Here the work presents a significant difference between the experimental and simulated force–displacements for complete penetration of a gelatine block where, in the generic energy balance formulation for the linear elastic model, using contact mechanics in the formulation has not been taken into consideration. Also the application of cohesive zone formulation to the needle insertion problem, by taking the needle tip geometric parameters into account, can be found in a study by Misra *et al.* (2008) where the cohesive zone model used to simulate the tissue cleavage process was based on linear traction-separation laws. However, the validation of such FE simulation models has not been demonstrated. A cohesive zone model (CZM) is treated in a particular way in the study of " Relating Cohesive Zone Models to Linear Elastic Fracture Mechanics" Wang (2010) where the researcher paid extra attention to the similarity of the result of the cohesive modelling to different cohesive laws (the accurate selection of the maximum traction of a CZM was examined). These results also show that, under certain circumstances, CZM analysis can be accepted as equivalent to LEFM analysis (e.g. the ratio of the cohesive zone length to crack length must be close to zero).

The advantages and disadvantages of cohesive models and a variety of issues related to the modelling are addressed by Needleman (2014). A summary of the addressed issues which are also the subjects of recent research studies can be formulated as:

-Determination of the cohesive parameter values to obtain a predictive theory (either using cohesive parameters to fit the experiments or deriving a cohesive constitutive relation from a physical model of the de-cohesion process).

-Cohesive surface location and orientation.

-Application of a cohesive formulation to ductile damage [cohesive model constitutive relation (tractions and displacements relation) cannot be used directly for the strong stress triaxiality dependence of ductile rupture],

where the advantages of applying such modelling techniques are:

- Computational efficiency.

-Applicability for a wide range of problems.

In the current study, the classification and treatment of fracture mechanics processes, based on the mixed mode cohesive zone model, corresponding to the cutting and needle insertion into human skin, are largely based on the particular ideas and the implementation method of a cohesive zone model to a non-linear finite element algorithm introduced by the following studies: De Morais (2014) [introducing methods which were used to develop piecewise linear mixed-mode I–II cohesive zone double cantilever beam models using separation-energy controlled damage formulation], Meo and Thieulot (2005) [presenting modelling techniques (CZM, tie-break contact and non-linear springs) which were used to develop the delamination failure mode in composite structures, where a comparison of the methods revealed that the tie-break contact was not able to achieve efficiently like other introduced methods for predicting the delamination growth], Harper and Hallett (2008) [demonstrating critical analysis of cohesive zone modelling technique by paying extra attention to the limitations of existing methods regarding the quality and quantity of interface elements within the cohesive zone], and Hillerborg *et al.* (1976) [introducing one of the types of finite element analysis of fracture mechanics developed in the last few where the relation between fracture energy per unit area (critical strain energy release rate), cohesive zone length, characteristic cohesive length, Young's modulus and interfacial strength were presented in a specific way].

To this end, it is worth mentioning that there are not many developed methods or general frameworks for large deformation and large sliding that are able to deal with contact and cohesive forces at the same time [e.g. Labanda *et al.* (2015), Yang *et al.* (2001)]. One such research study, which dealt with contact combined with cohesive forces, can be found in the research paper Doyen *et al.* (2010), where under consideration of also non-conformable mesh, suitable external load and boundary conditions, a simple form of the unilateral contact-cohesive for-
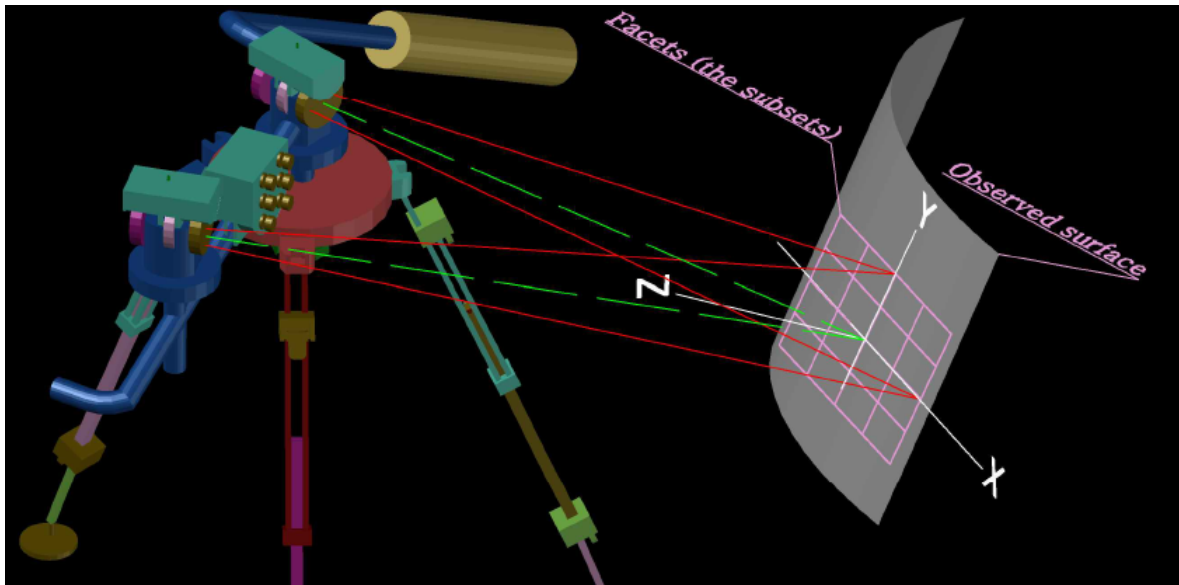
Figure 1.1: Digital Image Correlation (DIC) System

mulation with the nodal basis functions combined with two-three field augmented Lagrangian methods has been considered as minimisation of a non-convex functional which results show the dependency of cohesive law choice. In particular, to the author's knowledge there is no published papers which present the development of a cohesive fracture model through contact mechanics (formulated in one structure) which could deal with large deformation and large sliding, as this was performed by sophisticated algorithms in the present study.

1.4 Digital Image Correlation (DIC)

The DIC system traditionally uses two cameras and is a 3D, full field optical technique which can be used to measure deformation, vibration, strain, etc. (especially applicable to biological material) and is useful for a wide range of static and/or dynamic tests including compression, tensile, bending and such like.

The basic principle of the method is the tracking of the position of the same points in the image of the undeformed and deformed configurations of the object of interest. To make it possible, after the generation of a random intensity distribution, covering the object with painted speckles (a speckled pattern), the DIC system correlation algorithms are processed based on the identified square subset of the pixel around the point of interest on the image of the covered object of the undeformed and deformed configurations.

The algorithm makes it possible, by using the undeformed and deformed images, for the average grayscale over the identified subset to be calculated and compared. The measurement

principles of (DIC) can be described mathematically as follows according to the ISTRA 4D software from Dantec Dynamic (as a part of DIC-Equipment which was used to develop the tests in this study)[For more details see Appendix C part(3)]:

> **The correlation algorithm is based on the tracking of the grey value pattern** $G(x,y)$ **in small local neighbourhood facets. Due to a loading of the object this pattern is transformed into**
>
> $$G_t(x_t,y_t) = g_0 + g_1 G(x_t,y_t)$$
>
> **and**
>
> $$x_1 = a_0 + a_1 x + a_2 y + a_3 xy$$
>
> $$y_1 = a_4 + a_5 x + a_6 y + a_7 xy$$
>
> **Within the correlation algorithm the difference**
>
> $$\sum [G_t(x_t,y_t) - G(x,y)]^2$$
>
> **of these patterns is minimized.**
>
> **By varying the illumination parameters**
>
> $$(g_0, g_1)$$
>
> **and the parameters of the affine transformation**
>
> $$(a_0, ... a_7)$$
>
> **a matching accuracy of better than** 0.01 **pixel can be achieved.**

It is worth mentioning that the calibration of the DIC system plays a big role in the accuracy of the measured results. For instance, it helps the position and orientation of the cameras to be determined with respect to a word reference system and supports the transformation (rotation, translation) between the geometric and the image coordinate systems.

1.5   Aims and objectives

The aims of the study:

1. Development and testing of experimental models of human skin (Physical Skin Modelling) that can be suitable for the experimental cutting and needle insertion tests.

2. Estimation of the various mechanical properties of the manufactured physical models and comparison between the mechanical properties of the models and real human skin (ex vivo or in vivo) to find out whether or not the physical models can serve as an appropriate model for cutting and needle insertion tests.

3. Modification and implementation of large deformation contact mechanics using a mixed mode cohesive zone model (development of a cohesive fracture model through contact mechanics).

4. Incorporation of friction and frictional heat generation in the contact model (consideration of interfacial representations of total energy balance and entropy production).

To accomplish the goals of the project the following objectives were targeted:

1. **Experimental examination of the mechanical properties of the physical models:** Tensile and indentation tests were carried out on the manufactured physical models using Digital Image Correlation (DIC) to measure the deformation of the material.

2. **Inverse problems and inverse analyses, which deal with estimation of the mechanical properties of the physical models:** The calculation of the mechanical properties, Poisson's ratio, Young's modulus and shear modulus were performed for each manufactured silicone material in the laboratory using analytical study on indentation method, curve fitting technique and DIC measurements. Then, the results were compared to the experimentally obtained mechanical properties of human skin in vivo/ ex vivo from published studies.

3. **Implementation of the Modified Contact Mechanics using a traditional finite element method (FEM):** A modification of the classical contact to provide a specific implementation of a mesh-independent treatment for straightforward modelling of (non-linear) fracture mechanical processes using a mixed mode cohesive zone method, was obtained by determining the constitutive relationship within this framework, which consisted of a combination of both contact mechanics formulations and the Cohesive Law, together with friction and thermodynamically coupled friction, formulated in one contact structure. This was followed by implementation in the FEBio package, computational models, tests and practical, analytical and experimental verification.

4. **Development of a constitutive model for the penetration of a soft solid, specifically, needle insertion into human skin and cutting:** Under consideration of Griffith's theory, the internal and external mechanical and thermal energies (the work done by external and internal forces) and the cohesive fracture formulation through contact mechanics, the mathematical clarification of the mechanisms of cutting and needle insertion were performed and formulated as a general framework for the energy consistent treatment of the total system (the total energy balance of a globally conserved system). It was followed by the related algorithms, mathematical analysis and computational implementation of the theory.

Chapter 2

Human Skin: Layers, Structure and Function

2.1 Introduction

In order to understand the behaviour of the skin we need first to consider its anatomy. The skin has a complicated structure and microstructure which result in unusual behaviour and mechanical properties. In the following sections, firstly an overall view of the functionality of human skin will be provided, followed by a description of the skin layers in terms of the functions of the three primary layers of skin, namely the epidermis, the dermis and the hypodermis. Then, a detailed summary of the most recently employed methods for experimental and computational modelling of skin (the computational models of skin that have been clinically and experimentally validated) will be presented.

2.2 Skin Structure and Function

Human skin is a multi-layered thin membrane, with highly complex biological networks, which supports a variety of functions, such as protecting the body from a number of different kinds of damage and loss of water (acting as a resistant barrier to fluid loss), excreting waste, heat regulation, communication, storage, transport, etc. It is the largest organ in the human body.

The skin covers the surface of the human body. The area of skin of an average adult human is between 1.5-2.0 square metres, with the thickness of 2–3 mm. The average square centimetre (6.5 cm²) of skin also holds 650 sweat glands, 20 blood vessels, 60,000 melanocytes and more than 1,000 nerve endings [Bennett, Howard (2014-05-25)].
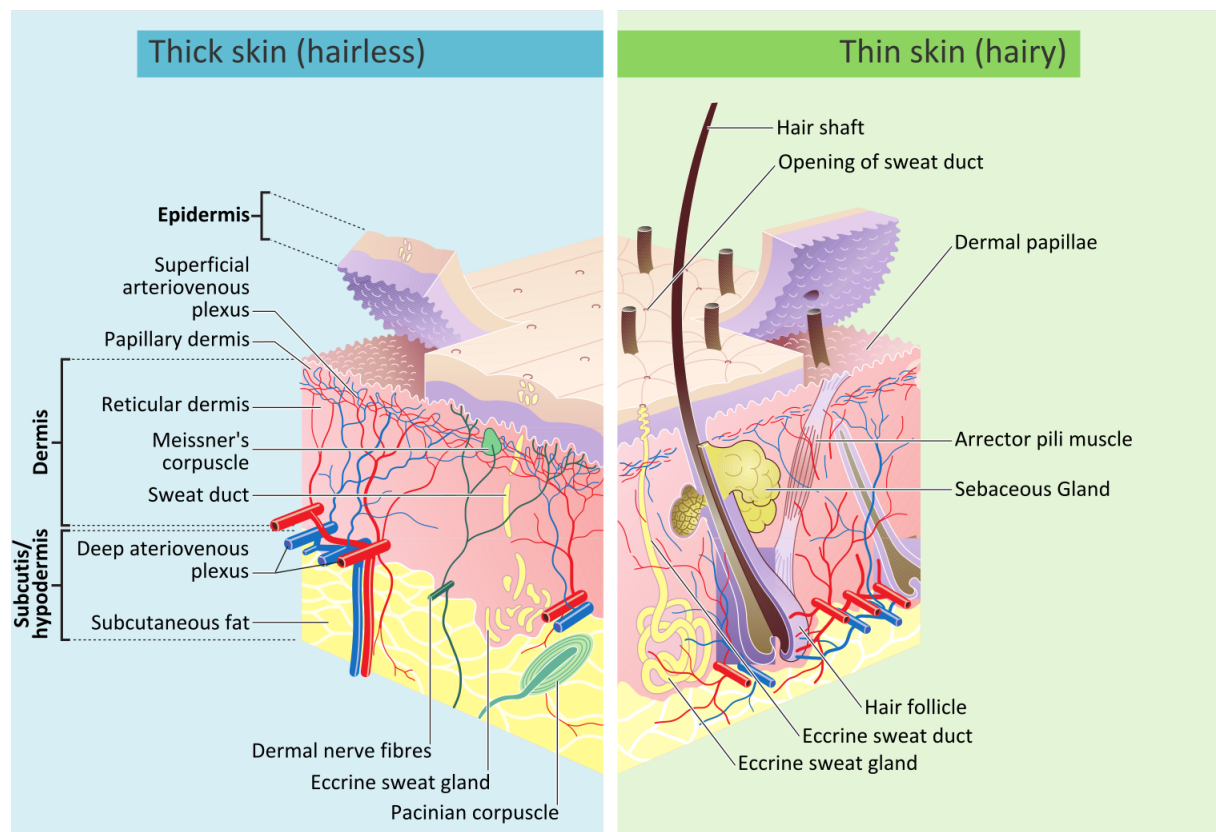
Figure 2.1: Human skin layers (source: https://en.wikipedia.org/wiki/Human_skin)

Important factors that affect skin thickness, structure and properties include age, the location on the body, medication, the environment etc., which can also affect skin colour.

As shown in Figure (2.1), the structure of skin is divided into three main layers and additionally into sub-layers as follows:

$$
\begin{cases}
Epidermis \begin{cases}
Stratum\ corneum \\
Stratum\ lucidum \\
Stratum\ granulosum \\
Stratum\ spinosum \\
Stratum\ germinativum
\end{cases} \\
Dermis \begin{cases}
Papillary\ region \\
Reticular\ region
\end{cases} \\
Hypodermis,
\end{cases}
$$
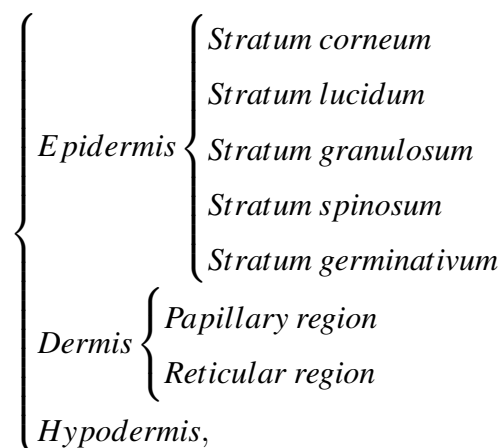
which will be discussed in terms of their functionality in detail in the following section.

2.3   Skin Layers

2.3.1   Epidermis

With 0.1mm thickness (in humans), the epidermal layer, the outermost layer of the skin, is made of several particular layers which are:

1. Stratum corneum: containing a network of keratin and acting as a barrier to infection and preventing fluid loss.

2. Stratum lucidum: containing several flattened and dead layers of keratinocytes and responsible for stretching and degeneration of skin cells.

3. Stratum granulosum: containing keratohyalin granules and acting as the waterproofing layer of the skin.

4. Stratum spinosum: containing polyhedral keratinocytes and helping to increase the flexibility of the skin.

5. Stratum germinativum: containing basal keratinocyte stem cells and helping the process of cell division (mitosis).

Generally speaking, the main duties and responsibilities of the epidermis layer (the keratinised layer of skin) are infection prevention, protection and the prevention of water loss from the body.

2.3.2   Dermis

Unlike the epidermis, which contains no blood vessels, the dermis contains blood vessels and it also contains the lymphatic vessels, sweat glands, hair follicles, sebaceous glands and apocrine glands.

The dermis layers, with a total thickness of approximately 1mm (in human), are:

1. Papillary region: containing loose connective tissue fibres (vertically arranged collagenous fibres, elastic fibres, reticular fibres) and connecting the reticular region to the epidermis.

2. Reticular region: containing a plane oriented irregular concentration of collagenous, elastic, and reticular fibres (a fibre matrix the direction of which is partly related to the orientation at which the skin is less flexible), allowing and providing elasticity and strength to the dermis.

The high flexibility (stretch and reorientation) of the dermis fibres allows this layer to undergo high levels of deformation with the aim of allowing freedom of movement while resisting perforation.

2.3.3   Hypodermis

Holding 50% of body fat, the hypodermis layer, the layer of skin beneath the dermis, contains areolar connective tissue (consists of elastin and collagen fibres and blood vessels, providing flexibility, cushioning, and serving as a store of water and salts and binding different tissue types together) and adipose tissue (stores nutrients and fats and plays a big role by serving as a reservoir of fats as potential energy reserves).

With approximately 8 to 20kg-15 to 30% of body weight, the thickness of the hypodermis is totally dependent on the location of the body (for example, it is thick on the buttocks and thin on the forehead).

The main purpose of the hypodermis layer, besides supplementing the skin with blood vessels and nerves, is to store nutrients and fat and to provide cushioning and protection.

2.4   Physics-Based Modeling, Analysis of Human Skin

Physics-based modelling of soft tissue has a long history. To be able to develop a biomechanical model of human skin based on the biological structure of skin we need to have an extensive knowledge in different scientific fields related to the modelling, namely numerical mathematical analysis, biology and biomechanics (the anatomy, physiology and mechanical properties of human skin) and mechanics (constitutive models of skin based on continuum mechanics).

In a common manner, the development of the modelling of deformable objects can be divided into two categories of modelling strategies, namely:

1. Physics-based Modelling: The modelling technique based on the analysis of the mechanical behaviour of materials under the effects of associated constraints by solving a continuum mechanics formulation applied to the problem [computationally a very expensive method, but mechanically and physically realistic].

2. Non Physics-based Modelling: The modelling technique based on a simplified version of the original physical principles or employment of a practical geometric method [the method attempts to achieve realistic effects of physical phenomena (e.g. body deformation) and it is computationally more efficient in comparison to the physical method].

Due to the popularity of the non physical modelling techniques (computationally low-cost methods), the past decade has seen increasing interest in the investigation of this modelling technique by a wide range of studies.

The techniques, such as spline technique [using Computer Aided Geometric Design technique (CAGD) for preparation and modification of complex geometries where, for example, methods like B-spline, Bezier curves, etc. can be used to modify the objects] or free-form deformation (FFD) technique [widely used in animation and geometric design where the deformation of the shape of the objects is based on the deformation of the space in which the objects are embedded by using, for example, the surface normal vector and transformation matrix] are examples of this modelling technique.

A brief overview of the methods used to develop non-physical models of human skin, mostly based on the theoretical human skin reflection model, by applying the standard physical or geometrical optics modelling technology to improved reflection models, revealed that although it has been claimed by the researchers that both qualitative and quantitative methods of their research provide a good approximation of experimental data, unfortunately, in most cases, important aspects of experimental verification have been ignored. One such model was presented by Li and Carmen (2009) where a multi-layer skin reflection model, based on optical principles and the bidirectional reflectance distribution function (BRDF), by using the Monte Carlo methods, has been developed by the researchers.

Unlike non-physical modelling techniques, the physical modelling technique provides realistic and accurate simulation of the deformation of the objects that is also visually realistic. In other words, to achieve accuracy (physical accuracy) in modelling and the simulation of complex systems, the physical modelling technique is the best choice.

There are a lot of issues related to the physical modelling technique, such as the speed and reliability of the algorithm that is used to solve the partial differential equations (describing the underlying process) or the complexity of the observed physical phenomena involving complicated dynamics.

In summary, and speaking generally, as the starting point for the analysis, techniques such as ultrasound imaging, MRI scans and digital image correlation are used to measure the mechanical behaviour of the skin, then the collected data are used as the starting point for the numerical assumptions (the geometry and the boundary conditions) and, finally, by applying an inverse finite element method or other techniques [the determination of unknown by using known results (e.g. load-displacement curve obtained through experimental test)] and using for example a stochastic optimisation process, the unknown parameters in the constitutive model are determined.
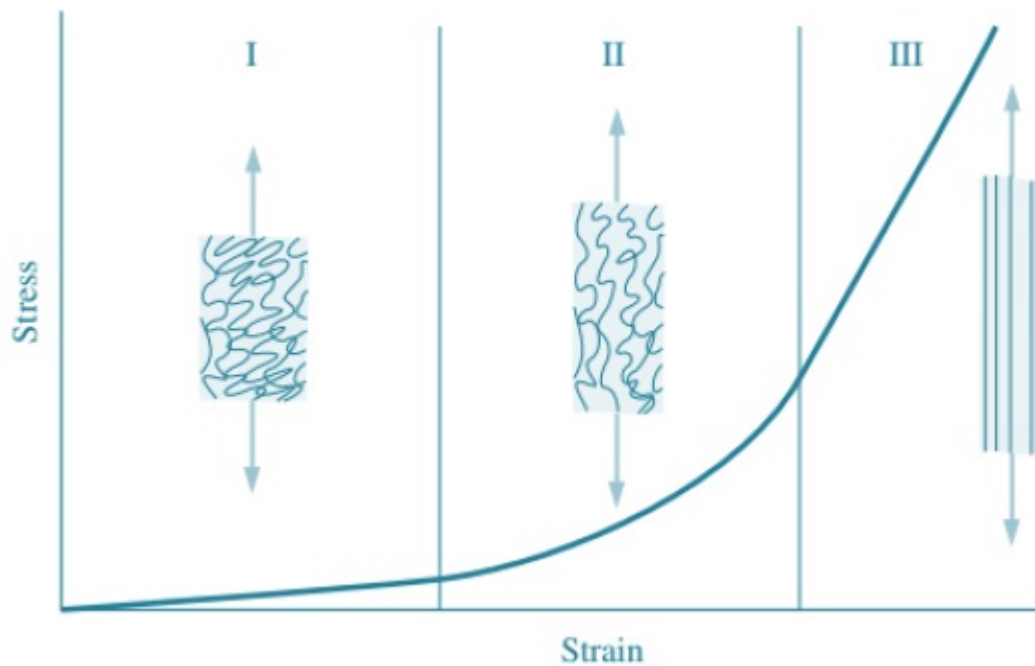
Figure 2.2: Stress-strain curve for skin [from Holzapfel (2000a)]

2.4.1 Anatomy, physiology and the mechanical properties of human skin

From the previous sections, we know that the human skin is a complex multilayer [as shown in Figure (2.1)] and multi-function organ, where each layer has nonlinear, inhomogeneous, viscoelastic Silver *et al.* (2001) [viscoelastic: showing both viscous and elastic behaviour by deformation] and anisotropic Annaidh *et al.* (2012) [anisotropic: change of the magnitude with respect to change of the direction of measurement], properties.

The elastic nature of skin makes the skin able to support body motion, while its flexibility and ability to return to its original shape (when an applied load is removed) help to support physically large deformations in order to fulfil the functional role of the body.

Due to the viscelastic nature of skin, human skin demonstrates the following behaviours, where the generation of the internal forces, due to deformation, aside from dependence on the amount of the deformation, are dependent on the deformation rate and/or duration:

   • Creep - Increasing strain with time under a constant load.

   • Hysteresis - The loading and unloading process produce different stress-strain curves.

   • Preconditioning - Different deformation results caused by repeatedly applied loads (same loads).

   • Stress relaxation - Reduction over time in stress under a constant strain.

It is also a fact that increasing or decreasing temperature can change the viscoelastic prop-

erties and consequently can affect the mechanical response of the skin. In addition to the temperature other environmental changes - such as chemical treatment, hydration etc. - can also influence the mechanical response of skin. For example, in a study by Jemec *et al.* (1990), the influence of superficial hydration on the mechanical response, "after applying tap water to the ventral aspect of the forearms of 18 healthy volunteers for 10 or 20 minutes and then measuring distensibility, elastic retraction, and hysteresis", significant increases in distensibility, resilient distensibility and hysteresis were reported.

The data and test results from many different research studies which tried to find out the mechanical properties of skin reveal that the constitutive equation of the skin, the stress-strain relationship, is nonlinear. The nonlinear stress-strain curve, as shown in Figure (2.2), based on the mechanical response of skin under tensile load, is divided generally into three main phases where the stress-strain relation is (approximately) linear (**Phase I**), increasing skin stiffness due to the straightening of collagen fibres (**Phase II**) and the linear response again at high strains (**Phase III**).

As was observed by Holzapfel (2000a) and other researchers:
Phase I. In the absence of load the collagen fibres, which are woven into rhombic-shaped patterns, are in a relaxed conditions and appear wavy and crimped. Unstretched skin behaves approximately isotropically. Initially, low stress is required to achieve large deformations of the individual collagen fibres without requiring stretch of the fibres. In phase I the tissue behaves like a very soft (isotropic) rubber sheet, and the elastin fibres (which keep the skin smooth) are mainly responsible for the stretching mechanism. The stress-strain relation is approximately linear, the elastic modulus of skin in phase I is low (0.1-2 MPa).
Phase II. In phase II, as the load is increased, the collagen fibres tend to line up with the load direction and bear loads. The crimped collagen fibres gradually elongate and they interact with the hydrated matrix. With deformation, the crimp angle in collagen fibrils leads to a sequential uncrimping of fibrils. Note, that the skin is normally under tension in vivo.
Phase III. In phase III, at high tensile stresses, the crimp patterns disappear and the collagen fibres become straighter. They are primarily aligned with one another in the direction in which the load is applied. The straightened collagen fibres resist the load strongly and the tissue becomes stiff at higher stresses. The stress-strain relation becomes linear again. Beyond the third phase the ultimate tensile strength is reached and fibres begin to break.

It is worth mentioning that the results can be affected by different Factors, such as age, and can differ from person to person.

Aside from testing the mechanical properties of skin *in vivo* [Agache *et al.* (1980), Liang
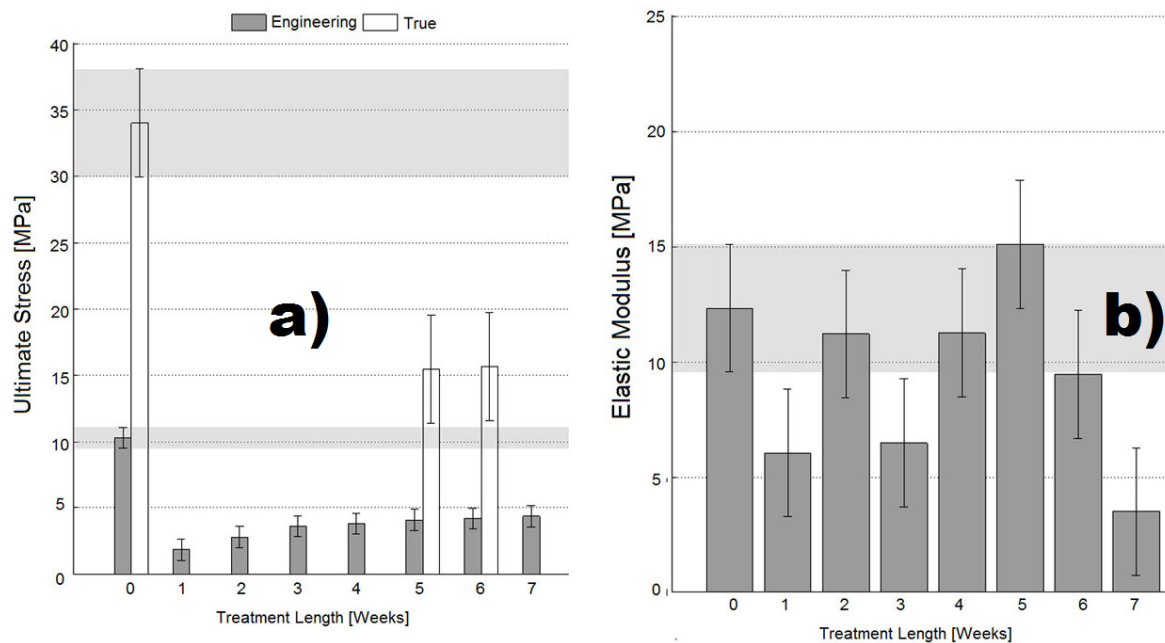
Figure 2.3: The results obtained on the examination of human skin in some studies : a) and b) ultimate stress and elastic modulus versus treatment duration Terzini *et al.* (2016)

and Boppart (2010), Evans and Holt (2009), Hendriks (2005) etc.], there are also several *ex vivo* approaches. There are many reasons for conducting an analysis of the mechanical behaviour of *ex vivo* human skin. In other words, due to the fact that the *ex vivo* model implies a wide range of possible analysis methods for exploring the mechanical characteristics of skin in comparison to *in vivo*, and sometimes for reasons of convenience, the *ex vivo* model is mostly preferred. The most common reason for *ex vivo* test is, for example, destructive tensile and failure tests (Destructive Physical Analysis) on the removed tissue samples of the animal or human skins.

Experiments applying *ex vivo* methods are reported in a number of different research studies. In a study by Terzini *et al.* (2016) several tensile tests, on decellularised and native tissues, were performed. They found hints that the decellularisation treatment results in getting a lower value for the ultimate stress and the elastic modulus and the duration of the treatment can be critical to preserve the mechanical properties of the tissue [see Figure (2.3)]. Using statistical methods, multi-scale mechanical measurements on *ex vivo* murine skin are reported by Bancelin *et al.* (2015), where the relationship between the microstructure of two different samples of skin - namely, normal and diseased skins - and their macroscopic mechanical properties were investigated [see Figure (2.4)- This shows: toe region with no significant force, increasing stiffness, linear behaviour with constant stiffness and skin breaking]. Based on *ex vivo* methods, and considering the rate dependency and anisotropic nature of skin, char-
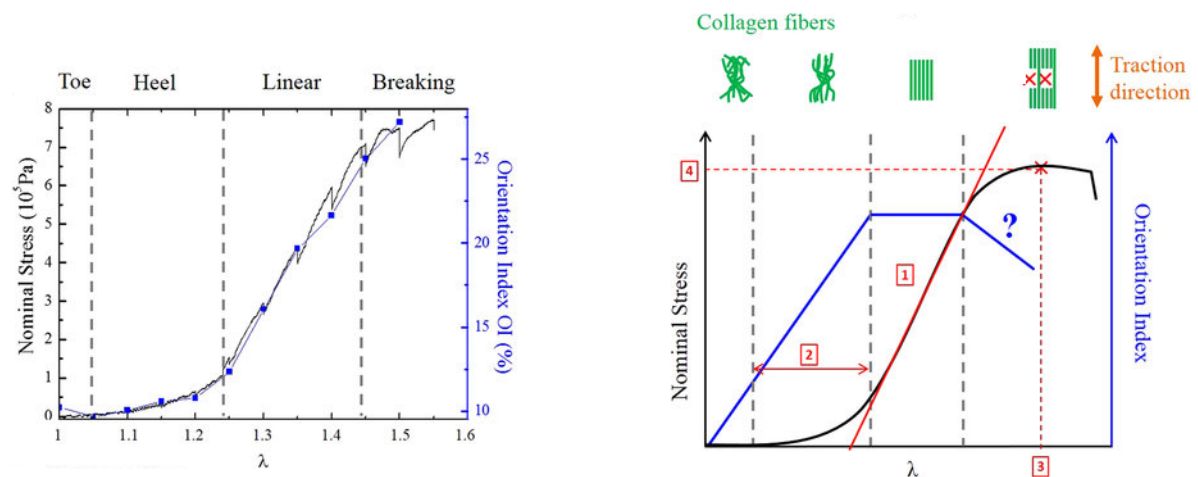
Figure 2.4: Nominal stress and orientation index variations as a function of the global stretch applied to the skin sample Bancelin *et al.* (2015)

acterisation techniques have been used to determine the failure mechanisms of human skin by Annaidh *et al.* (2012). Using *ex vivo* method, the non-linear, inhomogeneous, viscoelastic and anisotropic properties of skin have been also shown in many other studies. For example, in the determination of the subcutaneous fat layer viscous properties (the stress relaxation and the frequency dependent behaviour at constant temperature) was taken into account in a study by Geerligs *et al.* (2008).

2.4.2 Constitutive model of skin based on continuum mechanics

Finding appropriate constitutive laws which can describe the complex mechanical behaviour of skin is a very challenging process, but the outcomes of such a process, the mathematical formulation of the skin's mechanical characteristics, could be extremely useful.

There are several nonlinear models which are capable of describing the nonlinear mechanical properties of skin. The most popular models are the hyperelastic material models, in which it is assumed that the stress is independent of time or previous loading history. The stress and stiffness are defined by a strain energy function which is a function only of deformation and is independent of time. The stress and stiffness are found by differentiating the strain energy function with respect to the strain.

The constitutive hyperelastic models which are widely used to develop the modelling nonlinear mechanical behaviour of skin are listed as follows, but before describing the models, the following definitions need to be made [recall the definitions from Laursen (2003) and Holzapfel (2000b):

Displacement Gradient Tensor:

$$u \otimes \nabla, \; notated \; as \; \nabla u, \tag{2.1}$$

is a tensor with component $\frac{\partial u_i}{\partial x_j}$.

Deformation gradient :

$$F := \frac{\partial [\varphi_t(X) = x]}{\partial X} = \nabla u + I, \tag{2.2}$$

is a quantity frequently used to measure the quantity of strain in a large deformation.

Deformation tensors :

$$C = F^T F, \; b = F F^T, \tag{2.3}$$

are the right and left Cauchy-Green tensors.

Jacobian determinant:

$$J = det F, \; dx_1 dx_2 dx_3 = J dX_1 dX_2 dX_3, \tag{2.4}$$

is the determinant of the transformation between reference and current coordinates.

Green-lagrange strain tensor:

$$E = \frac{1}{2}(C - I) = \frac{1}{2}(F^T F - I), \tag{2.5}$$

is a strain tensor for large deformations which is used to measure the difference between Cauchy-Green tensor C and identity tensor I (is used to quantify the changes in length of a material fibre in a deformable body).

Stretch: λ is a measure of how much a unit vector $n = \frac{Y-X}{|Y-X|}$ has stretched.

Principal stretches:

$$\lambda_1, \lambda_2, \lambda_3$$

are the eigenvalues of right or left Cauchy-Green tensors or deformation gradient F [$det(F - \lambda_i I) = 0$].

2.4.2.1   The constitutive hyperelastic models:

-Neo-Hookean: The model is used to describe the non-linear mechanical behaviour of the compressible and the incompressible materials, and is an extended form of Hooke's law for large deformation. The strain energy density function for the compressible and the incom-

pressible neo-Hookean models are given by:

$$\Psi = \frac{G}{2} \left(\overbrace{I_1}^{\lambda_1^2 + \lambda_2^2 + \lambda_3^2} - 3 \right) - p(J-1) \ [Incompressible] \tag{2.6}$$

$$\Psi = \frac{G}{2}(I_1 - 3) - Gln \overbrace{J}^{(\lambda_1.\lambda_2.\lambda_3)=det(F)} + \frac{\kappa}{2}(lnJ)^2 \ [Compressible], \tag{2.7}$$

where $G, \kappa, (\lambda_1, \lambda_2, \lambda_3), I_1, p, J$ are the shear modulus, the bulk modulus, the principal stretches, the first invariant of the right Cauchy-Green deformation tensor, pressure and the determinant of the deformation gradient F.

[Dijk (2007), Su *et al.* (2009)]

-Ogden: The model is used to describe the non-linear, isotropic mechanical response of rubber like materials, where the principal stretches are used to describe the strain energy density as:

$$\Psi(\lambda_1, \lambda_2, \lambda_3) = \sum_{i=1}^{N} \frac{\mu_i}{m_i^2} \left(\lambda_1^{m_i} + \lambda_2^{m_i} + \lambda_3^{m_i} - 3 - m_i lnJ \right) + \overbrace{U(J)}^{\frac{1}{2}c_p(J-1)^2} \ [OgdenUnconstrained], \tag{2.8}$$

where $\lambda_1, \lambda_2, \lambda_3$ are the principal stretches of the left-Cauchy-Green tensor and μ_i, m_i, c_p are the material parameters and the term $U(J)$ corresponds to the volumetric component.

[Mahmud *et al.* (2013)]

-Mooney–Rivlin: The model is used to describe the non-linear, isotropic and incompressible (Nearly-Incompressible) mechanical response of rubber like material defined by the following strain energy function

$$\Psi = c_1(I\prime_1 - 3) + c_2(I\prime_2 - 3) + \frac{1}{2}K(lnJ)^2 \ [NearlyIncompressibleMooneyRivlin], \tag{2.9}$$

where c_1 and c_2 are the Mooney-Rivlin material coefficients, $I\prime_1$ and $I\prime_2$ are the invariants of the deviatoric part of the right Cauchy-Green deformation tensor ($\bar{C} = \bar{F}^T \bar{F}$, where $\bar{F} = [det(F)]^{\frac{-1}{3}} F$, and F is the deformation gradient), and K is a material constant.

[Lopes *et al.* (2006)]

-Yeoh model: The model is used to describe the non-linear, isotropic and incompressible mechanical response of rubber like material which uses the following strain energy function

(a reduced polynomial model)

$$\Psi = \sum_{i=1}^{N} C_i \left(\overbrace{\lambda_1^2 + \lambda_2^2 + \lambda_3^2}^{I_1} - 3 \right)^i - p(J-1), \tag{2.10}$$

where the shear modulus in relation to C is given by $C_1 = \frac{\mu}{2}$.

[Tenga *et al.* (2015)]

-Arruda–Boyce model: The model is used to describe the non-linear and incompressible mechanical response of rubber like material. It is formulated as an eight polymer chain of macromolecular network and is based on the statistical mechanics which uses the inverse Langevin function to formulate the following strain energy function

$$\Psi = C_1 [\frac{1}{2}(I_1 - 3) + \frac{1}{20N}(I_1^2 - 9) + \frac{11}{1050N^2}(I_1^3 - 27) + \frac{19}{7000N^3}(I_1^4 - 81) + \frac{519}{673750N^4}(I_1^5 - 243)], \tag{2.11}$$

where $C1, N, I_1 = 3\lambda^2$ are the material constant, the measure of the limiting network stretch and the first strain invariant. [Arruda and Boyce (1993)]

To add the viscoelastic and anisotropic mechanical properties of skin to the constitutive models, material models that represent a single fibre direction or a or family of fibre directions, the constitutive models such as Transversely Isotropic Hyperelastic (represents single preferred fibre direction), Elliptical Fibre Distribution (represents ellipsoidal fibre distribution), Fibre with Exponential Power Law (represents family of fibre based on exponential power law strain energy function), Fung Orthotropic (represents orthotropic constitutive model - a subset of anisotropic materials that greatly in their three mutually-orthogonal axes of rotational symmetry) and Viscoelasticity (represents viscoelastic material), can be applied to the model Gasser *et al.* (2005), Annaidh *et al.* (2014).

2.4.3   Numerical mathematical analysis methods

In general (and practically), the common numerical methods, based on the physical modelling technique, can be divided into four categories of numerical modelling strategy, namely the Spring-Mass-Damper system (SMD), the Boundary Element Method (BEM), the Finite Difference Method (FDM) and the Finite Element Method (FEM). Of these, the SMD and FEM approaches are most commonly used for soft tissue modelling.

2.4.3.1 The Spring Mass Damper System (SMD):

The physical object is modelled by using a set of connected mass points (connected by springs) where, due to tension-compression load, the forces created [(linear-Hookean) spring force $F = -ku$ where u is displacement and k is spring constant] by the presence of a mass displacement and consequently applied to the neighbouring points, a combination of mathematics and physical laws [i.e. the equation $M\frac{d^2u}{dt^2} + D\frac{du}{dt} + Ku = F_{ext}$ where M is mass, K is stiffness matrix, D is damping and F_{ext} is external force (the Newton equation of motion defined for the system of n mass points)] that approximate the deformation of the physical body can be used for soft-tissue modelling.

In the paper by Nikooyanz and Zadpoor (2011), several mass-spring–damper models, classified as active or passive methods, to study the human body's behaviour (in the case of collision with the ground during running, trotting and hopping), are proposed. In another study Zhang *et al.* (2009), based on the Mass-Spring system, a deformable model for soft tissue simulation in real-time is developed. It has been argued that the accuracy of simulation can be influenced by the density of springs.

2.4.3.2 The Boundary Element Method (BEM):

The general idea of this method is formulation of the given partial differential equations PDE (for solving boundary value problems) as integral equations over the whole domain of interest Ω^i where the so formulated integral equations, under certain conditions (homogeneity of the materials and zero volumetric forces), can be modified and defined over the boundary $\partial\Omega^i$, and as a result we need only to discretise the boundary of the integration domain (and this will also have an advantage in the dimensionality of the resulting system of equation in comparison to the discretisation of the total volume).

An example of dealing with modelling the deformation behaviour of soft tissue by applying the boundary element method is given in the research paper by Koppel *et al.* (2008), where the research indicates the time complexity of the algorithm as "an almost linear time complexity of O($n^{1.14}$), a significant speed up comparing to the traditional O(n^3) schemes employing brute-force linear-algebra solution methods based on Finite-Element Method (FEM) formulations." Using the boundary element method for modelling the soft tissue is also reported in a study by Tang (2010) where the researcher, by applying BEM in such a way (determination of the fields displacement at each vertices of the skin model) to model human skin deformation, claims that the deformation of the skin layer can be shown at interactive frame rates.

2.4.3.3   The Finite Difference Method (FDM):

The basic concept of this method, under consideration of initial and boundary conditions, is the replacement of the continuous derivatives (at each point of the domain of interest) with finite difference approximation (i.e. $f(u+h) \approx f(u) + \frac{df(u)}{du}h$ and $\frac{d^2 f(u)}{du^2} \approx \frac{f(u+h)-2f(u)+f(u-h)}{h^2}$, where h is the characteristic dimension of the discretisation), where the assembled linear system of the equations (the resulting system of the equations) can be solved by different solving techniques such as iterative methods or direct method. From the computational complexity point of view, and in the case of irregularity in the geometry due to the discretisation of the objects, FDMs main drawback is using extensive computational resources for processing the data; in order to get around this limitation we can use, for example, parallel processing techniques.

Using the McCormack finite difference method, and based on the Galerkin finite element method, a coupled FDM-FEM approach can be found in the paper by Mithraratne *et al.* (2009), where a simulation of a computational model of a 3D soft tissue continuum and a one-dimensional transient blood flow network were reported.

2.4.3.4   The Finite Element Method (FEM):

To deal with all (almost all) limitations, such as the problem with the complex geometry, the boundary conditions, the material types etc., and to prove a more accurate method in solving (continuum mechanics) problems, the finite element method (FEM) is widely used. One of the major differences between the SMD and FDM methods and the FEM method is that the SMD and FDM approximate the continuous equilibrium equation (resultant equation due to minimisation of the energy functional) over the discretised equation at the mesh nodes, whereas the FEM algorithms, after dividing the object into a set of elements, approximate the equilibrium equation over each element [where the algorithms can be simply divided into the following steps: first, defining the continuous equilibrium equation and finding the suitable finite elements and the shape function or the interpolation function, then dividing the objects into the elements and interpolating all appropriate variables by using the shape function and computing, then applying the boundary condition and assembling the set of the equations into the global system of equations and, finally, solving the equations for the unknowns (e.g. unknown displacement)].

Due to the fact that the FEM is widely used for a physics-based approach to model soft tissue, especially to model the human skin, we can find a lot of studies that deal with all types of linear and non-linear elastic finite element approaches. For example, a finite element approach, based on linear elastic modelling of soft (facial) tissue in craniofacial surgery, can

be found in the paper by Gladilin (2002), where a simulation with a simple artificial model consisting of two nested cylinders, the inner cylinder for muscle and the outer cylinder for the remaining soft tissue, was reported. Furthermore, in a study by Lapeer *et al.* (2011), a non-linear FE model of human skin has been developed with applications in real time surgical simulation, where making use of GPU allowed large nonlinear dynamic explicit FE meshes to be used in their model in real time as is required for modelling most biological soft tissues. However, these models relied on Poisson's ratio value, adapted from another research study, which could also have an effect on the accuracy of the results. In another study by Bischoff *et al.* (2000), based on statistical mechanics, the development of a human skin model by applying a non-linear elastic constitutive model is reported, where the non-linearity of the mechanical stress-strain response of skin due to the collagen network in skin is investigated. However, as was reported in this study, viscoelastic properties of skin could not be modelled with the introduced constitutive model.

2.5 Computational models of human skin

Depending on the application, in the last few decades several computational multi-layer models of skin for studying the mechanical properties of skin have been developed. A few techniques are briefly described in the following texts.

Considering skin layers as linear, isotropic elastic materials, in a study by Thalmann *et al.* (2002) a three layer computational model of skin was developed for studying the changes in the appearance and characteristics and mechanical properties of the skin due to skin ageing. The researchers claim to have an accurate computational model of skin compared to clinical observations and laboratory tests. However, when dealing with an extremely non-linear mechanical problem such as skin, making use of an isotropic, linear elastic material model is unlikely to deliver really accurate results. Consequently, it cannot be useful for accurate simulation of needle insertion into human skin and cutting.

Using the agent-based modelling (ABM) technique [a computational modelling technique which is used to simulate the actions and interactions of so-called autonomous agents (such as cells, organs, molecules, etc.) where the modelling approach additionally provides a significant degree of flexibility (e.g. there is no more need for the linearity or smoothness assumption of a system) for the generation of complex behaviour from simple behaviour], are reported in many research studies (and especially largely in biology are employed to study complex biological systems). As such, in the paper entitled "Development of a Three Dimensional Multiscale Computational Model of the Human Epidermis", an agent-based model, by using the agent-based modelling framework FLAME (Flexible Large Scale Agent Modelling Envir-

onment) and COPASI (a software application for the simulation and analysis of biochemical networks), was developed by Adra *et al.* (2010) to simulate the behaviour of the human epidermis, where the 3D multiscale model of the human epidermis consisted of cells, tile (for modelling the interaction of cells with substrate) and physical solver agents (responsible for resolving forces between cells).

Based on the Monte Carlo technique [computational algorithms based on repeated random sampling], Meglinsky and Matcher (2000) developed an experimentally validated multi-layered computational model of skin (claimed by the developers) which was used to simulate the reflection skin spectra, where the simulation technique was based on a three dimensional photon packets tracking strategy where the absorption properties of the modelled skin layers (seven layers model) were "related to the real absorption spectra of pure oxy- and deoxy-haemoglobin, and water, and include a different rate of blood oxygen saturation and hematocrit".

In a research paper by Buganza Tepole *et al.* (2014) a computational model of skin, based on stress profiles of skin flaps, was introduced where the models were used to explore the evolution of tissue tension during flap (with parallel and perpendicular to fibres directions) advancement, which, they claim, in connection with reconstructive surgery, can be used to "minimise stress, accelerate healing, minimise scarring, and optimise tissue use". They also claim that their results (the mechanical analysis of skin flaps and related simulations) are very useful for accurate preoperative planning in plastic surgery. However, because the skin flaps typically undergo large deformation, the introduced algorithms and nonlinear constitutive models were not verified to be accurate in predicting the stress response.

In order to simulate transdermal drug delivery, the penetration of the drugs and chemicals into dermal tissue which are applied to skin, Dancik (2004), by using finite difference method, introduced a computational model that claimed to be useful for describing the transportation process of the chemical collection through/in each tissue layer.

With regard to the fracture mechanic modelling strategy, and in order to study the mechanical characteristics of needle insertion into soft tissue, a simple model [without taking tissue deformation and friction into consideration, specially failure to take into account relevant considerations such as the contact mechanic in the energy balance formulation] based on quasi-static analysis of the penetration force, was developed by Azar and Hayward (2008).

One of disadvantages of the above introduced methods is that they cannot be applied to the skin-cutting or needle penetration models because, either due to simplification of the complex problems (e.g. considering non-linear, anisotropic and viscoelastic properties of skin layers as linear, isotropic elastic materials) or the presented models not being based on the constitutive relations of continuum mechanics which provide an idealised description of materials.

To this end, as listed in the following table (2.1), a brief summary of existing findings and related literature (current knowledge of skin penetration) which deals with computational (soft solid) skin models used for simulation of cutting and needle penetration, and which aims to help to develop a clear sense of direction early on in this study, has been provided.

Paper	Application	Objective-aim	Methodology
Groves (2008)	To optimise microneedle device design	Quantifying the mechanical properties of skin and developing microneedle array designs	Experimental observations (in vivo and ex vivo) and development of multilayer FEM models of human skin indentation and skin under tension
Bodhale *et al.* (2010)	To the transdermal drug delivery (TDD) through Skin	Simulation of structural and CFD analysis on three-dimensional model of microneedle array	Finite element (FE) and computational fluid dynamic (CFD) analysis using ANSYS-design of hollow, out-of-plane polymeric microneedle with cylindrical side-open holes
Shergold and Fleck (2004)	To the injection and wounding of skin	Investigating the mechanisms of deep penetration of soft solids	Development of micromechanical models for the deep penetration of a soft solid by a flat–bottomed and by a sharp–tipped cylindrical punch.
Mahvash (2010)	To medical needle interventions	Investigating the mechanisms of rupture events that involve large forces and tissue deformations	Development of nonlinear viscoelastic Kelvin model to predict the relationship between the deformation of tissue and the rupture force at different velocities.
Mahvash and Hayward (2001)	To predict effectively the deterministic behaviour of cutting in terms of material fracture toughness	Haptic real time simulation of Cutting	Cutting simulation of shaped prismatic samples of two different biomaterials: potato and calf liver
Buitrago *et al.* (2015)	To control correctly robot-assisted surgeries and to avoid compromising the patient's vital organs	Simulation of cutting on the skin and estimate of the range of forces that can safely be applied with it during a surgery	Finite element analysis of the skin incision and puncture when using a scalpel

Table 2.1: A brief summary of some of computational (soft solid)skin-cutting and needle penetration models

Chapter 3

Development of a physical model for skin

3.1 Introduction

From the literature and the previous chapter we know that human skin has non-linear, aniso-tropic and viscoelastic properties which makes measuring its properties very difficult. Fur-thermore, we also know that the mechanical behaviour of skin can be affected by different factors such as age, the environment, etc. For these reasons, and others such as observational error, random and/or system errors, etc., the various laboratory tests using *ex vivo* human skin samples or clinical *in vivo* tests cannot be both accurate and precise and the tests can also be problematic, especially those that involve cutting or needle insertion into the skin. When test-ing the human skin or particularly when doing cutting and needle insertion tests, because of many reasons such as being at increased risk of acquiring infection when handling human (or animal) skin or the difficultly of needle insertion tests or the virtual impossibility of successful cutting *in vivo* test*s, ex vivo* tests, in comparison with clinical *in vivo* tests, are preferable.

   Furthermore, as mentioned earlier, due to age or environment-related and other changes in the mechanical properties of human skin, sometimes even *ex vivo* human skin samples might not be the perfect candidates for highly specific tests. In other words, they cannot be used to cover every variety of tests. Thus, in many applications in research, such as material devel-opment and testing, due to the repeatability and reproducibility of the reliable physical skin models in comparison to *ex vivo* human skin samples, researchers prefer to use physical mod-els instead of using real human skin. Nevertheless, the accuracy of such physical skin models which can be used to replace real human skin (and can represent the mechanical character-istics of human skin truthfully and deliver the same test results as the human skin *in vivo*), are an open question which can be answered with systematic investigation of the mechanical response of the material applied to the physical skin models and exploration of the mechanical properties of the physical skin models and real human skin and finding their differences.

The main aim of this chapter is to describe and demonstrate the method used to create a physical model of skin suitable for the cutting and needle insertion tests. In the following sections, the manufacturing process of the materials (i.e. silicone rubber) that were used to develop the physical model of human skin in this study will be described in detail. Then, very briefly, the specimen measurement devices, the testing machine and Digital Image Correlation (DIC) System, will be introduced. Next, the tensile and indentation tests on the models produced in the laboratory, by using previously mentioned specimen measurement devices, will be described. And finally, the process of evaluation of the test results will be discussed.

3.2 Methods

3.2.1 Specimen preparation-silicone moulding

Using a custom mould made by a different researcher at Cardiff University, the manufacturing process began by mixing two parts liquid silicone[1] [after metering unit for the A and B components (9:1)-specified by the manufactures] which were used to make the specimens. After mixing they were degassed (so all the air bubbles in the mixture were removed). The time to do this varied between specimens and was deemed to be complete when there were no more visible air bubbles in the mixture. After that, the mixture was poured into the mould. The mould was clamped shut, and then the silicone was cured in an oven. The temperature of the oven was dependent on what silicone was made.

Additionally, when making samples - such as fat samples - a thin layer of silicone was used to make skin. This was laid down first and then the fat was poured onto it. For other samples, like the muscle sample, it was poured directly into the mould. The mould was coated with a wax releasing agent prior to pouring in the silicone to try and ensure that the silicone was easy to remove from the mould.

3.2.2 Mechanical testing procedure

3.2.2.1 Zwick universal testing machine

Three different tests were carried out: tensile tests on rectangular specimens (with initial width: 10.1 mm, height: 60 mm, depth: 4.2 mm), compression tests on cylindrical speci-

---

[1]Due to the fact that the liquid silicone has a different viscosity and curing temperature from other types, it has the advantage of being able to change the shape easily (in other words, it can easily fit in any mould and is ideal for complex moulds and is highly appropriate for the production of parts). The specimens were manufactured by moulding of liquid silicone rubber.

	Maximum force $2.8 - 34.7\,N$	
tensile test	Deformation at maximum force $65.1 - 99.9\,mm$	
indentation test	Maximum force $37.3 - 93.9\,N$	
	Deformation at maximum force $3.1 - 3.7\,mm$	
Test Speed	$10 - 100\,mm/min$	

Table 3.1: The range of the measured maximum forces and deformations during tensile and indentation tests and the test speed configurations (Zwick machine)

mens and indentation tests. The tests were run at three different crosshead speeds, namely $10\,mm/min$, $50\,mm/min$, $100\,mm/min$.

The tests (three tests on each material) were carried out using a Zwick Z050 testing machine with a 2kN load cell. Load and displacement data were recorded on the machine and also output as analogue voltages which were recorded by the DIC system.

3.2.2.2   Tensile test

In order to perform the tensile test, the sample (the silicon rubber manufactured in the laboratory) was attached to the Circular Bollard Grips which were mounted to the Zwick testing machine.

The testing protocol involved uniaxial tensile tests at three different constant speeds, namely $10\,mm/min$, $50\,mm/min$, $100\,mm/min$. Two high-speed video cameras were mounted in front of the testing sample to collect image-video data of the specimen stretching or being stretched with/without breaking, and the load and the displacement signals (analogue signals) from the the Zwick machine were sent to the DIC system. The software (Istra 4D) was used to store camera data, which was located in a laptop (part of DIC System equipment). The captured image data was automatically loaded into the Istra 4D DIC analysis software where the measurements (strain measurements), testing, analysis and evaluation proceeded. Each Zwick testing machine has its own software which was used in the tensile testing to manage the individual test data. The test data and conditions are shown in Tables 3.1 and 3.2.

3.2.2.3   Indentation test

The materials used for the experimental study of indentation tests were again silicon rubbers [the samples (with initial width: 10.1 mm, height: 60 mm, depth: 4.2 mm)], where each indentation test involved the following steps:

-The indenter approached the surface of the specimen until sensing contact.

Measuring instruments	Zwick universal testing machine
	DIC system
DIC Analysis	software Istra 4D
Calibration plate	size: 105 x 148 mm²
Imaging Speed	500 - 1000 frames/sec
Grip	Circular Bollard Grip
Measuring	Force, displacements and strains

Table 3.2: Test conditions

-The indenter was pressed at a rate of $10mm/min$ into the sample. It continued to deepen until a maximum depth of about $3.8 - 4mm$ was reached.

-The indenter was detached from the specimen completely, and the sample was prepared for the next indentation tests involving two different test rates, namely $50mm/min$, $100mm/min$.

By making use of a flat-bottomed, circular cross section punch [cylindrical indenter which was attached to the Circular Bollard Grips which were mounted to the Zwick testing machine, allowing the tool to perform indentation test in the direction orthogonal to the surface of the specimen where the sample was joined (freely sliding) by one face to a solid metallic plate (a solid part of the machine)], a series of indentation tests were accomplished.

In addition to the Zwick universal testing machine, an optical measuring system, Digital Image Correlation system, described previously, was used to measure the displacement. This is necessary because it is not possible to attach a conventional extensometer to the specimens to measure the strain during the test, and so an optical method is necessary.

The necessary control conditions were included entirely which were important to be considered [before and after the collection of information and data (during tests)].

The machine crosshead was programmed to have constant velocity of $10mm/min$ [the rate of the first test] where the displacement of the arm was controlled by implementation of the limit. The resulting force-displacement, for different values of the test rates and loads, was recorded by the machine's software, The test data and conditions are shown in Table 3.1 and 3.2.

Simultaneously, to collect more accurate 2D and/or 3D measurements, the DIC measurement was proceeded where the flat-bottomed indenter was covered with painted speckles allowing more accurate DIC measurement of the displacement of the tool.

The DIC measurements of the entire process of the indentation tests, as shown in Figure (3.2), were based on the displacement field of the surface of the indenter.

3.2.3   Processing-data analysis

3.2.3.1   DIC data

The calculation of Poisson's ratio [*Assuming $v = -\frac{d\varepsilon_x}{d\varepsilon_y} = -\frac{d\varepsilon_z}{d\varepsilon_y}$, stretched in the $y - direction$*] were performed for each manufactured silicone rubber in the laboratory.

To achieve more accurate results, the following mathematical formulation was used.

$$v = -\frac{1}{3}\Big[\frac{1}{l}\sum_{i=1}^{l}\frac{d\varepsilon_x^i}{d\varepsilon_y^i} + \frac{1}{m}\sum_{j=1}^{m}\frac{d\varepsilon_x^j}{d\varepsilon_y^j} + \frac{1}{n}\sum_{k=1}^{n}\frac{d\varepsilon_x^l}{d\varepsilon_y^l}\Big], \tag{3.1}$$

where l, m, n refer to the number of the DIC measured engineering strains of three line pairs, as shown in Figure (3.1). Note that, the increasing of the accuracy is related to the number of line pairs.

Using the above mathematical relation, and the results from DIC measurements which were imported into Microsoft Excel, the Poisson's ratio for each sample was calculated.

3.2.3.2   Zwick machine data

To extract the general characteristics of the tested samples and compare them, the recorded load-displacement data from the Zwick machine for both tests, the indentation and the tensile tests, were examined.

The load-displacement curves for the tensile tests were converted to stress-strain curves where engineering stress σ was defined as force per unit area $\sigma = \frac{F}{A}$ (where F is force and A is the cross sectional area of the specimen) and the engineering strain was defined as the change in length $l - L = \Delta L$ per unit of the original length L of a line element$\varepsilon = \frac{l-L}{L}$. The so calculated stress-strain curves were used for curve fitting as described in Section (3.2.3.3).

Considering the following previously developed mathematical relations, the indentation data was processed.

The mathematical formulation of the normal penetration of the boundary of a half space by a flat-ended cylindrical punch has been developed by a wide range of studies. One such formulation, based on the axisymmetric Boussinesq problem [Selvadurai (2001)] and using the theory of Hankel transformation, can be found in the paper by Sneddon (1965), where the researcher found that the total load P required to produce a penetration d by a flat-ended cylindrical punch of radius a can be formulated as

$$P = 2\pi\int_0^a p\sigma_{zz}(p,0)dp = \frac{4Gad}{1-v}, \tag{3.2}$$

where G, v are the shear modulus and the Poisson's ratio.
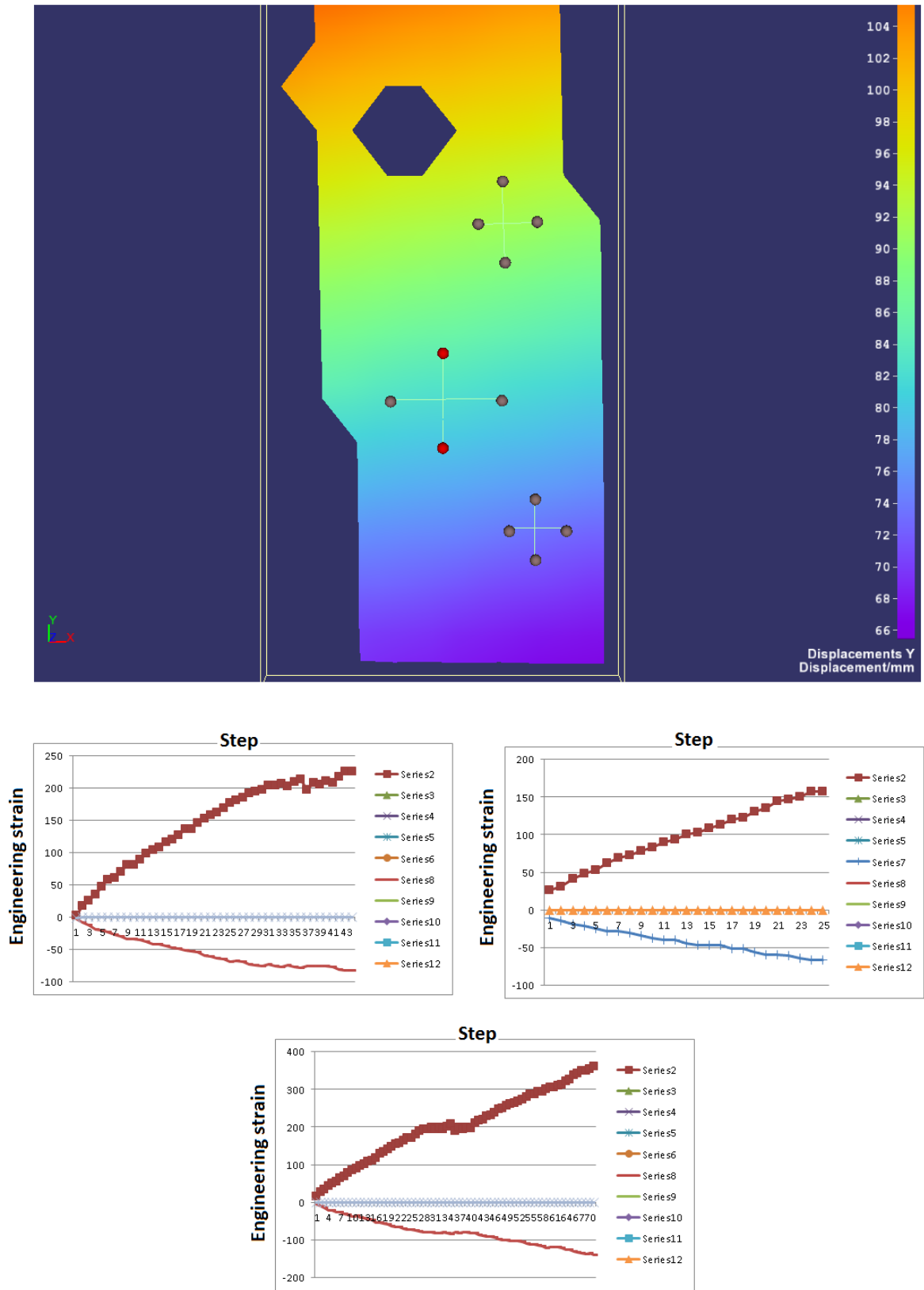
Figure 3.1: Top: The selected three line pairs on the specimen, Bottom: (Engineering) strain distribution as a function of time of the line pairs and the result of division (imported data from DIC database to Excel)

The pressure distribution σ_{zz} and the displacement u_z are given by

$$\sigma_{zz}(p,0) = -\frac{2Gd}{\pi(1-v)}(a^2-p^2)^{\frac{-1}{2}}, \quad 0 \le p < a \tag{3.3}$$

$$u_z(p,0) = \frac{2d}{\pi}sin^{-1}(\frac{a}{p}), \quad p > a \tag{3.4}$$

It is worth mentioning that the equation (3.2), in the other study Hayes *et al.* (1970), using Boussinesq-Papkovitch potential function and Fredholm integral equation of the second kind[2], has been slightly differently expressed, namely:

$$P = 2\pi \int_0^a \varphi(t)dt \tag{3.5}$$

$$\frac{P(1-v)}{4Gad} = \kappa = \int_0^1 \omega_1(\tau)d\tau, \tag{3.6}$$

where

$$\xi = \frac{x}{a}, \ \tau = \frac{t}{a}, \ \alpha = \lambda h, \ \varphi(x) = \frac{2Gd}{\pi(1-v)}\omega_1(\xi) \tag{3.7}$$

$$\omega_1(\xi) = 1 - \frac{1}{\pi}\int_0^1 \omega_1(\tau)[K(\tau+\xi)+K(\tau-\xi)]d\tau \tag{3.8}$$

$$K(u) = \frac{a}{h}\int_0^\infty \{\frac{(3-4v)h\alpha e^{-\alpha}-[\alpha(1+\alpha)+4(1-v)^2]}{(\alpha)^2+4(1-v)^2+(3-4v)h^2\alpha}\} \times cos[\alpha(\frac{a}{h})u]d\alpha, \tag{3.9}$$

where at $z = h$, $u_z = u_r \mid_{0 \le r < \infty} = 0$

Although it has been proven by Hayes *et al.* (1970) that the indentation data (e.g. the quantity κ) is dependent on the area aspect ratio $\frac{a}{h}$ (e.g. the edge effect can be neglected in the case of large indenter compared to thickness of the specimen), nevertheless, in the present study the indentation tests were developed under consideration of the fixed contact area and the fixed thickness of the specimens [and consequently fixed value for the quantity κ in equation (3.6)] where the equation (3.2) was directly used to determine the shear modulus G.

3.2.3.3 Curve fitting

The curve fitting technique is used to determine mathematically the material model's parameters or constants by finding and constructing a best fit curve based on the experimental

---

[2]$\varphi(x) + \frac{1}{\pi}\int_0^1 \varphi(t)[H(t+x)+H(t-x)]dt = F(x), \ 0 \le x \le a$

(measured stress-strain) data for the material where the results of the (curve-fitting) method follow the test data within the range of interest. Curve fitting will not deliver an exact fit to the test data where, due to variations in the material and tests, in most situations, a high degree of precision in the curve-fitting cannot be achieved.

The Neo-Hookean incompressible material curve fitting technique involves the following steps (which is generally the same technique for different hyperelastic material models):

- Acceptable stress-strain curves need to be considered and made suitable to requirements or conditions

- A constitutive Neo-Hookean hyperelastic material model needs to be chosen

- Regression analysis (least squares method and definition of an error criterion)

- Comparison of the curve fitting results with the measured stress-strain data (the best approach to solving the problem using different softwares)

Mathematically, the curve fitting method for the Neo-Hookean incompressible material (usually used as a constitutive hyperelastic material model for silicone rubber) is described as follows:

Recall the equation (2.6), the incompressible Neo-Hookean material

$$\Psi(\lambda_1, \lambda_2, \lambda_3) = \frac{G}{2} \left(\overbrace{I_1}^{\lambda_1^2 + \lambda_2^2 + \lambda_3^2} - 3 \right) - p(J-1) \; [Incompressible], \qquad (3.10)$$

where p, J are pressure and the determinant of the deformation gradient F and the strain invariants I_1, I_3 in term of the principal stretches $\lambda_1, \lambda_2, \lambda_3 (\lambda_{i \in [1,2,3]} = \underbrace{\overbrace{l_i}^{deformedlength}}_{undeformedlength})$ are defined as

$$\begin{cases} I_1 = & \lambda_1^2 + \lambda_2^2 + \lambda_3^2 \\ I_3 = & \lambda_1^2 . \lambda_2^2 . \lambda_3^2 = 1 \quad [Incompressibility \; condition] \end{cases} \qquad (3.11)$$

Assuming the stretch $\lambda = \lambda_1$ is parallel to the tensile stress and $\lambda_2 = \lambda_3$, by using the incompressibility condition, the first and third strain invariant I_1, I_3 can be re-expressed as:

$$\begin{cases} I_1 = & \lambda^2 + 2\lambda^{-1} \\ I_3 = & \lambda_1^2 . \lambda_2^2 . \lambda_3^2 = 1 \overset{\lambda_2 = \lambda_3}{\Longleftrightarrow} \lambda_2 = \lambda_3 = \lambda^{\frac{-1}{2}} \end{cases} \qquad (3.12)$$

Furthermore, the relation between the strain energy $\Psi(\lambda_1, \lambda_2, \lambda_3)$ and the first Piola-Kirchhoff

stress $P(\lambda, G)$ is given by

$$P(\lambda, G) = \frac{\partial \Psi(\lambda_1, \lambda_2, \lambda_3)}{\partial \lambda_{i \in [1,2,3]}} = \frac{\partial \Psi(\lambda_1, \lambda_2, \lambda_3)}{\partial I_1} \frac{\partial I_1}{\partial \lambda_1} + \underbrace{\frac{\partial \Psi(\lambda_1, \lambda_2, \lambda_3)}{\partial I_2} \frac{\partial I_2}{\partial \lambda_2}}_{=0} + \underbrace{\frac{\partial \Psi(\lambda_1, \lambda_2, \lambda_3)}{\partial I_3} \frac{\partial I_3}{\partial \lambda_3}}_{=0},$$

$$(3.13)$$

after substitution of the equations (3.1) and (3.2) into the equation (3.3), and under the assumption of perfect incompressibility, the first and second Piola-Kirchhoff stress expressions for the cases of uniaxial (ux) $[P_1 = \lambda S_1, \sigma_1 = \lambda^2 S_1, S_2 = S_3 = 0]$ [and equibiaxial (bx)$[\lambda_1 = \lambda_2, \lambda_3 = \lambda^{-2}]]$ deformation are given by

$$\begin{cases} P_{ux}(\lambda, G) = G(\lambda - \lambda^{-2}) \Longrightarrow S(\lambda, G) = G(1 - \lambda^{-3}) \\ [P_{bx}(\lambda, G) = G(\lambda - \lambda^{-5})], \end{cases} \quad (3.14)$$

which can be used (in this study only the uniaxial first Piola-Kirchhoff is used) to measure stress versus stretch relation for the analytical expressions (the first Piola-Kirchhoff stress-stretch relation for tension and compression of the incompressible Neo-Hookean material).

The next step of analysis is usually associated with the regression analysis where, as shown in equations (3.15) or (3.16), by making use of so called least squares method which uses the sum of the squares of the difference of the functions [e.g. the stress model function $P_{ux}(\lambda, G)$ and the (experimentally) measured nominal stress function $\sigma_N(\lambda) = P_N$] and minimises the overall solution, we can find the approximate solution of overdetermined systems.

$$\varepsilon rror = \sum_{i=1}^{n} [\sigma_N(\lambda_i) - P_{ux}(\lambda_i, G)]^2 \to min, \ (n, number\ of\ data\ pairs) \quad (3.15)$$

$$\varepsilon rror_{norm} = \sum_{i=1}^{n} \frac{[\sigma_N(\lambda_i) - P_{ux}(\lambda_i, G)]^2}{[\sigma_N(\lambda_i)]^2} \to min, \ (normalized) \quad (3.16)$$

which assumed to have the ideal solution $\sigma_N(\lambda_i) = P_{ux}(\lambda_i, G) \mid_{\forall i}$ in the case of having identified curves.

At this point it is worth mentioning that in the case of non linear least square problem [when the model function $P(X_i, \alpha_j)$ (where X_i is an independent variable-found by observation and α_j is a model parameter) is not linear in the parameters (if the derivatives of the model function with respect to the parameters $\frac{\partial P(X_i, \alpha_j)}{\partial \alpha_j}$ is not constant), the sum of squares must be

minimised by an iterative procedure. Using Taylor series expansion we will get

$$P^{(k+1)}(X_i, \alpha_j) = P^{(k)}(X_i, \alpha_j) + \sum^{\forall j} \frac{\partial P(X_i, \alpha_j)}{\partial \alpha_j} \overbrace{(\alpha_j^{(k+1)} - \alpha_j^{(k)})}^{\triangle \alpha_j}, \qquad (3.17)$$

where k is an iteration number, and to minimise the sum of squares after setting the gradient of squared residuals $[Y_i - P(X_i, \alpha_j), Y_i$ is a dependent variable found by observation] to zero we will get

$$\sum^{\forall i} [\underbrace{Y_i - P^{(k)}(X_i, \alpha_j) - \sum^{\forall j} \frac{\partial P(X_i, \alpha_j)}{\partial \alpha_j} \overbrace{(\alpha_j^{(k+1)} - \alpha_j^{(k)})}^{\triangle \alpha_j}}_{r_i}] \frac{\partial r_i}{\partial \alpha_j} = 0, \qquad (3.18)$$

which can be solved in an iterative procedure for $\triangle \alpha_j$. The non linear least squares problem occurs when, for example, trying to fit the curve for the Ogden models and has no analytic solution, where the analysis continues with the definition of a convergence criterion which can be defined as

$$\left| \frac{\varepsilon rror^{(k+1)} - \varepsilon rror^{(k)}}{\varepsilon rror^{(k)}} \right| < limit \quad or \quad \left| \frac{parm^{(k+1)} - parm^{(k)}}{parm^{(k)}} \right| < limit, \qquad (3.19)$$

where $\varepsilon rror^{(k)}, parm^{(k)}$ are the kth iteration of the sum of squares (the error) and the non linear model parameters.

Also the goodness of fit which is typically used to measure the similarity between measured values and the values of the model in a problem, can be evaluated using the following equation [Rackl (2015)]

$$\bar{R}^2 = 1 - \frac{n-1}{n-p-1} [(1 - \underbrace{\frac{\sum_{i=1}^{n} [f_E(\beta_i) - f(\beta_i, C)]^2}{\sum_{i=1}^{n} [f_E(\beta_i) - \overline{f_E(\beta_i)}]^2}}_{R^2}) - 1] \qquad (3.20)$$

where $\bar{R}^2$ is the adjusted coefficient of determination which, in the case of having a value close to 1 (ideally 1 for perfect fit), indicates a good fit, and $p, f_E(\beta_i), \overline{f_E(\beta_i)}, f(\beta_i, C)$ are the number of model parameters, the function of measured values, the average of the measured values and the model function.

3.2.3.4 Results

Figure (3.2 and 3.3) shows the result of experimental tensile tests, indentation tests and the DIC measurements obtained in tensile-indentation testing of silicon rubber specimens (from the start of the tensile test to the point that some of the specimen breaks where the influence of the different testing speed was also investigated - for example, more accurate DIC measurements at low speed test). The images were extracted in a typical time course analysis from two DIC cameras. The appearance of colouring in the images corresponds to the strain distribution in the specimen where the colour maps in Figure (3.2) show the distribution of strain in the direction of the highest degree of strain over the specimen. The certain quantity of strain that occurs in the specimen corresponds to the degree of the colour temperature, where the areas of the images that show brighter colour, such as white green-orange-red, indicate a greater degree of strain and the areas of darker colour, such as blue-black, indicate low strain.

Using MATLAB, in order to fit the constitutive model (Neo-Hookean hyperelastic material model) to the experimentally measured stress–strain data (to obtain the model parameter), the first Piola-Kirchhoff stress function P ($P = FS$) was calculated (where F, S are the deformation gradient and the second Piola-Kirchhoff stress tensor).

The results of curve fitting using MATLAB are shown in Figure (3.3), where the stress (MPa) - strain data was calculated directly from the experimentally measured force-displacement. Using the equation (3.14), a function was defined as an input for curve fitting where, by proceeding the goodness of fit analysis, determination of the sum of squared errors of prediction [$SSE = \sum_{i=1}^{n} w_i(y_i - \hat{y}_i)^2$, where w_i is the (i th) weighting applied to each data point, y_i is the i th observed data value and $\hat{y}_i$ is the i th predicted value from the fit, a value closer to 0 indicates that the model has a smaller random error component, and that the fit will be more useful for prediction (MATLAB)], root-mean-square error [$RMSE = sqrt(mean((y_i - \hat{y}_i)^2))$, a value closer to 0 indicates a fit that is more useful for prediction (MATLAB)], R-square and the adjusted coefficient[3], the unknown G, the shear modulus, was determined for each sample data. Note that the measured data was fitted against the appropriate stress measure; in other words, the measured data against the analytical expressions for the uniaxial first Piola-Kirchhoff stress expressions.

Table 3.3 shows the material property Young's modulus E and Goodness of fit obtained in

---

[3]Interactive curve fitting using MATLAB code: [stress(y) , strain(x)]
mynormresid3 = sum(resids3.^2)^(1/2) (norm-of-residuals)
mynormresid3 =0.3248
SStotal = (length(y)-1) * var(y); (the sum of the squared diff. of each value from the mean of the variable y)
SSpop =61.3061
rsqlinear = 1 - mynormresid3^2 / SSpop
rsqlinear =0.9983 ← R^2
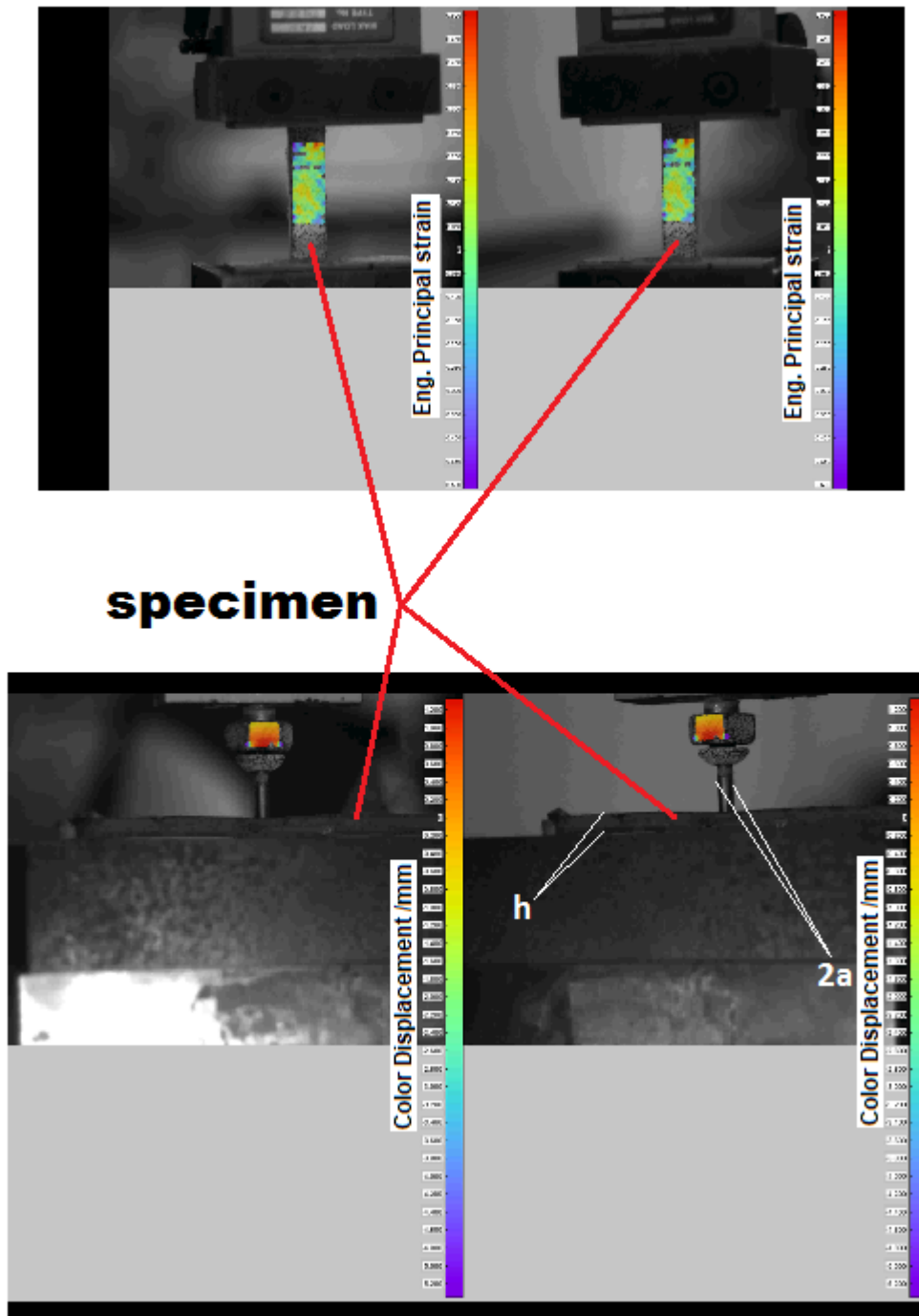
Figure 3.2: Tensile-indentation tests using Zwick testing machine and DIC measurements
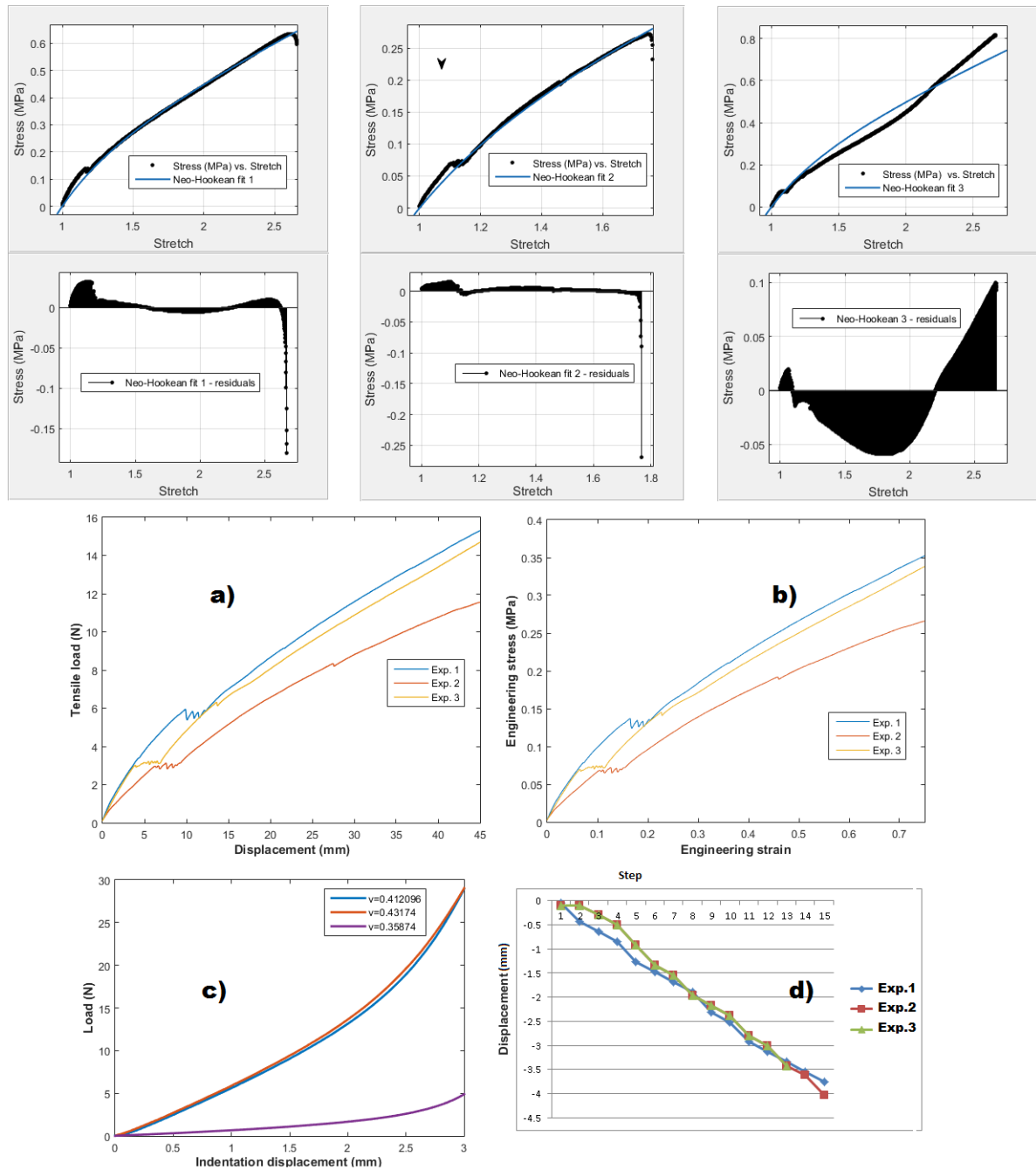
Figure 3.3: Top: Curve fitting using the measured stress (MPa) - strain data and MATLAB [Stress vs.Stretch] Bottom: a) Force-Displacement curve for tensile tests of the manufactured silicon rubbers, b) the resulting stress-strain curve. Indentation tests, c) Load-Indentation displacement curve d) DIC measurements (indentation displacement versus step) [Zwick testing machine measurements]

$f(\lambda) = G(\lambda - \lambda^{-2})$ $\mid$ $G = \frac{E}{2(1+v)}(MPa)$	SSE	R-square	Adj. R-square	RMSE
$E = 0.723$	0.2565	0.9931	0.9931	0.01453
$E = 0.813$	0.2573	0.9584	0.9584	0.04598
$E = 0.527$	2.1057	0.9703	0.9703	0.01366

Table 3.3: Young's modulus E and Goodness of fit of the input function, incompressible Neo-Hookean, used for curve fitting in MATLAB
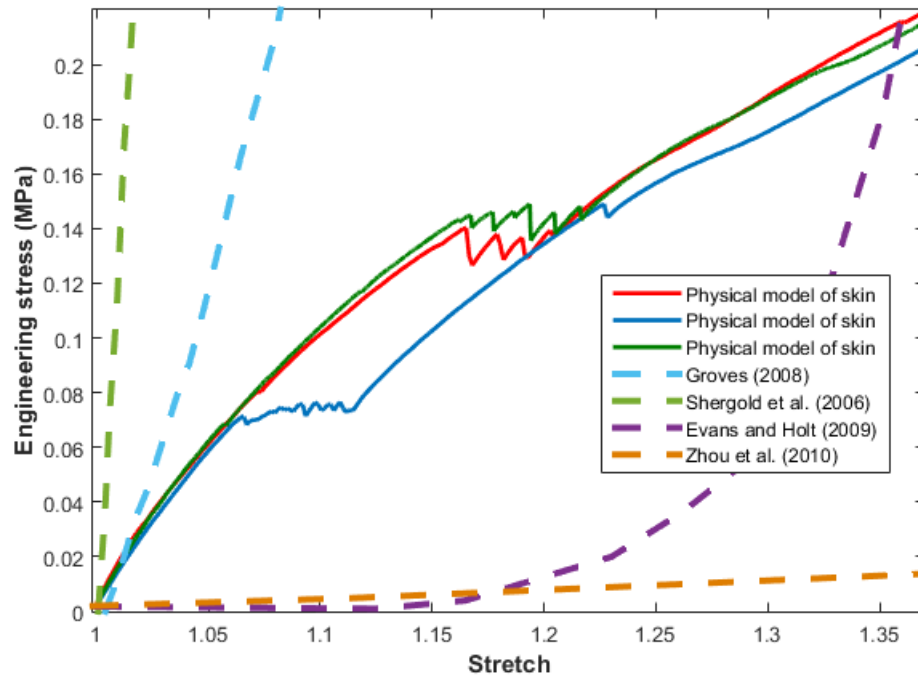
Figure 3.4: Stress stretch curves for the generated physical models of skin in comparison with literature data for real skin [Zhou *et al.* (2010), Evans and Holt (2009), Shergold *et al.* (2006), Groves (2008)]

incompressible Neo-Hookean curve fitting in MATLAB using calculated stress-strain (stretch = strain+1) curves from experimental tests.

Furthermore, Table 3.4 presents the average values of the shear modulus $G = \frac{E}{2(1+v)}$ for the plane-ended cylindrical indentation (for different specimens).

3.3 Conclusion/Discussion

The aim of the work presented in this chapter was the use of existing methods which were adapted to the development of a physical model of human skin suitable for cutting test and needle insertion into human skin where the methods allowed accurate measurement of the

Shear modu.	$a = 1.6mm$	$h = 4.2mm$	$f^{max}(37.3621 - 93.9111\,N)$	$d^{max}(3.8 - 4mm)$
$G(v_1)$			$0.437557\,\frac{N}{mm^2}$	
$G(v_2)$			$0.446646\,\frac{N}{mm^2}$	
$G(v_3)$			$0.270886\,\frac{N}{mm^2}$	

Table 3.4: Average values of the shear modulus G for the plane-ended cylindrical indenter, ($Poisson's\,ratio$, $v_1 = 0.412096, v_2 = 0.43174, v_3 = 0.35874$)

mechanical properties of the physical model.

This study applied tensile tests and indentation measurement to the silicon rubber manufactured in the laboratory by using the Zwick compression-tensile testing machine and the Digital Image Correlation (DIC) technique to characterise the mechanical properties of the sample.

Using the Digital Image Correlation technique and applying the powerful DIC Functions, such as strain and displacement mapping to the test analysis methodology, have made this study capable of accurate measurement of the mechanical properties of the samples (such as shear modulus, Young's modulus etc.). Although the full 3D DIC has been proven to be capable of handling more accurate deformation analysis than the conventional methods, besides experimental condition and issues, additional work, such as improvement of the DIC data processing hardware-software, can be investigated to improve the DIC results.

In this study, the mechanical characteristics of several physical models of skin were extracted and compared with the data obtained from existing research studies *(in vivo/ ex vivo* measurements). In Figure (3.4), the quality of the results obtained in this study in comparison with literature data for real skin [Zhou *et al.* (2010), Evans and Holt (2009), Shergold *et al.* (2006), Groves (2008)], is presented, which shows the considerable difference between (stress stretch curves for) so generated physical models of skin and real skin. To overcome this problem, based on the results, this study suggests, adding fibres to silicone rubber could improve the tensile strength of silicone properties (tensile strength of fibres/silicone rubber composites) and provide more quantitative and qualitative fit with experimental data. It needs to be said that the variations in the mechanical characteristics of the physical model of skin in comparison to the real skin model are not just limited to the physical model of skin. It has also been shown by some researchers that even *in vivo* and *ex vivo* measurements of the mechanical properties of skin vary. An overview of such *in vivo* and *in vitro* experiments revealed that, in most of these experimentally performed tests, the complexity of the mechanical properties of skin is reduced and regarded, for example, as a homogeneous non-linear elastic solid where mostly quite simple constitutive equations are used for highlighting the fundamental principles and straightforward nature of the mechanical behaviour of skin.

As mentioned earlier, due to the complex mechanical properties of the skin tissue, additional work is required to develop a new physical model using various materials that could potentially provide a more accurate model (a physical model whose extracted material parameters could be the best fit with experimental data), where the process can be repeated until the issues have been reduced to an acceptable level, meaning that each time a measurement is taken, it could be compared with the results of the existing literature and it could be repeated over and over again until the required precision is achieved.

3.4   Summary

A summary of the methods which were used to develop a physical model for skin (in this study) is shown in Figure (3.5).
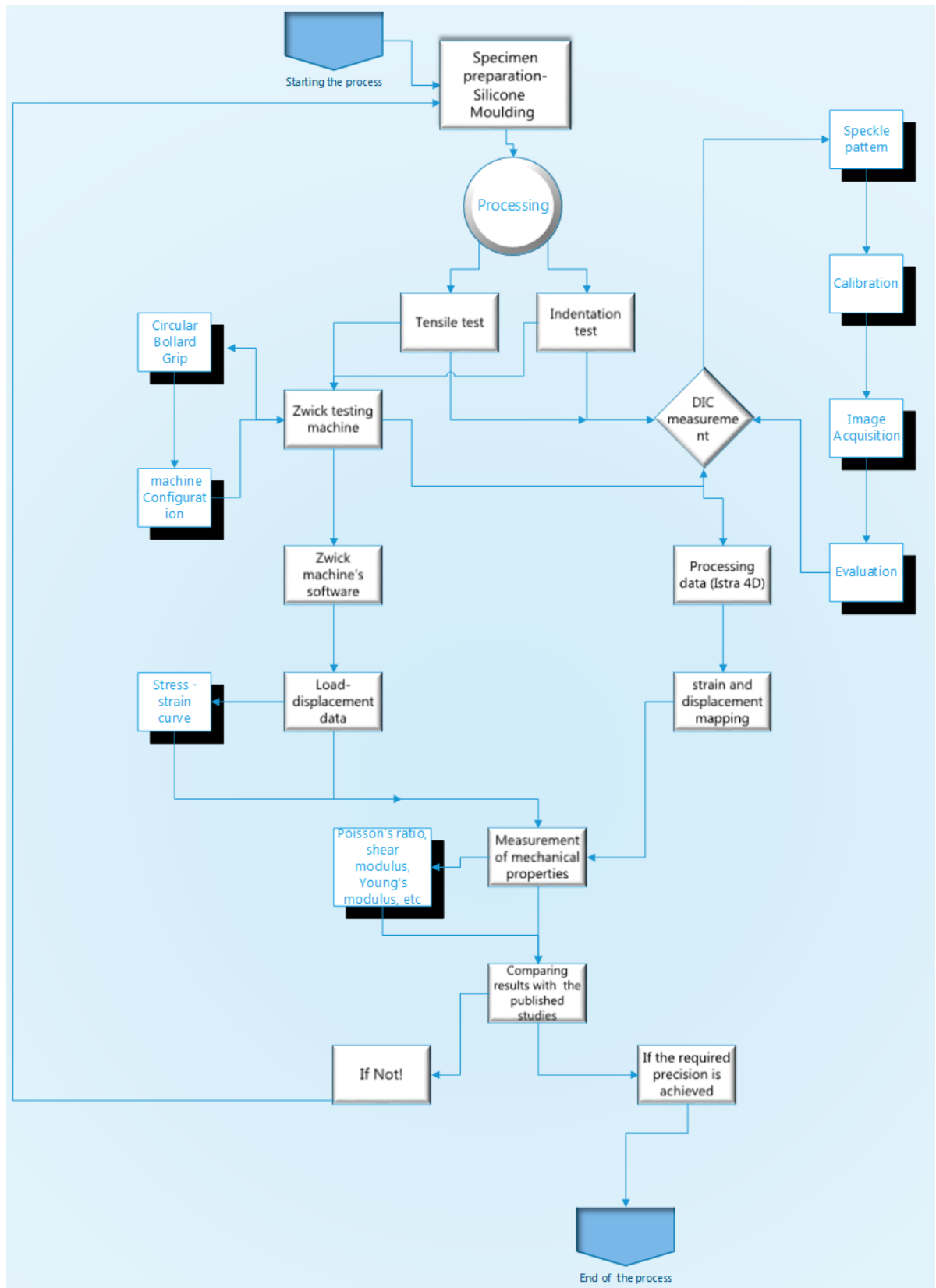
Figure 3.5: A summary of the methods used to develop a physical model for skin

Chapter 4

Implementation of a Cohesive Fracture Model through Contact Mechanics

4.1 Introduction

Various theoretical and numerical formulations of Cohesive Modelling and Contact mechanics with/without cohesive forces have been widely studied and applied for the different problem classes with the traditional Finite Element Method (FEM).

Modifying the classical contact mechanics (modification of classical contact constraints based on Kuhn-Tucker conditions) to provide a specific implementation of a mesh independent method for straightforward controlling of (non-linear) fracture mechanical processes using Mixed Mode Cohesive-Zone method - in other words, a new large deformation cohesive zone formulation alongside thermodynamically coupled friction (based on the Coulomb friction law), formulated in one contact structure - was the idea of this project, which has been implemented using FEM. Then the accuracy of the implemented algorithms has been analytically, practically and experimentally verified.

In order to process the development of this project, the first step was the classification of computational and mechanical-mathematical problems related to modelling which were clearly separated into those with the implementation of the clarified underlying theory and those problems with optimisation using advanced computational and mechanical optimisation algorithms and methods.

The treatment of the modified contact given here, specially the treatment of the classical contact, friction and thermodynamic, follows in the footsteps of some previous research studies [Laursen *et al.* (2004) and Laursen (2003)]. The numerical implementation of the algorithms of modified contact is based on the open source code FEBio with modification

and re-development of existing source code, while the theoretical-mathematical framework of modified contact inherits its definition from mixed mode cohesive law and the partial divergence of the standard definition of the classical contact formulation (based on Lagrange multiplier and penalty factor and gap function). In other words, the constitutive models within this framework consist of a combination of both classical contact mechanics and cohesive fracture formulations where the boundary value formulation of modified contact mechanics is based on the modification of the long-established contact-boundary value formulation (the traditional way of the Contact-Calculus Variation formulation) in combination with the Strong Cohesive Law. Additionally, constitutive relations that govern the constitutive model of the thermodynamically coupled friction boundary value problems in solid and structural mechanics have been taken into account. To enable switching between the classical contact part of modified contact and the cohesive fracture part of modified contact, the algorithm of the modified contact, optimised with inequality constraints (the Kuhn-Tucker conditions), enforces the contact constraints within a strong Mixed Mode Cohesive Law formulation which clearly takes the place of the classical contact constraints formulation and, in the case of the physical requirement of impenetrability and compressive interaction between two bodies, enforces the classical contact constraints. The theoretical-practical presentation of the numerical methods of modified contact in solid and structural mechanics and the accuracy of the constitutive models for practical engineering problems and the applicability of algorithms have been treated in the following sections.

The formulation begins with an overall description of the problem, global variation formulation of the problem. [In this chapter, the focus is only on the contact and frictional-thermomechanical contact problem, while the fully thermomechanical initial non-linear boundary value problem IBVP (considering all thermodynamic parameters of a system) will be treated in the next chapter in relation to cutting modelling]. It follows with the definition of mathematical models of the cohesive model and classical contact mechanics, then it continues with the development of mathematical models of the modified contact and thermodynamically coupled frictional contact problem, followed by convergence analysis. Finally, it presents the implementation (modifying FEBio-package), computational models and verification tests.

4.2 Constitutive models

4.2.1 Global Variation Principle (total virtual work)

Considering the general problem statement for the treatment of the thermomechanical non-linear dynamic contact interaction of two finitely deformable bodies ($\Omega_{(1)}, \Omega_{(2)}$), introduced
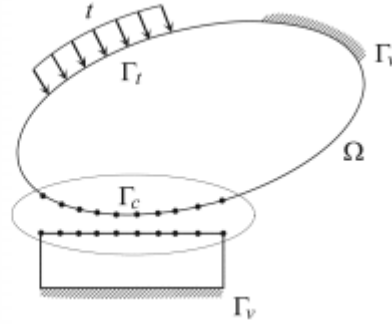
Figure 4.1: Illustration of solid body Ω with boundaries $\Gamma_c = \partial\Omega_\Gamma, \Gamma_v = \partial\Omega_u, \Gamma_t = \partial\Omega_\sigma$ [source: Xuan *et al.* (2016)]

previously in Laursen (2003), the thermomechanical initial non-linear boundary value problem (a finite strain IBVP including contact), during a time interval $\top = [0, t]$, and for the given boundary conditions: $\partial\Omega_\Gamma, \partial\Omega_u, \partial\Omega_\sigma, \partial\Omega_T, \partial\Omega_q$ discontinuity, Dirichlet, Neumann, temperature and heat flux (prescribed) boundary conditions with:

$$\forall contact\, interfaces \mid \partial\Omega_\Gamma \cup \partial\Omega_u \cup \partial\Omega_\sigma = \partial\Omega = \partial\Omega_\Gamma \cup \partial\Omega_T \cup \partial\Omega_q \; and$$

$$\partial\Omega_\Gamma \cap \partial\Omega_u = \partial\Omega_\Gamma \cap \partial\Omega_\sigma = \partial\Omega_\sigma \cap \partial\Omega_u = \partial\Omega_T \cap \partial\Omega_q = \partial\Omega_\Gamma \cap \partial\Omega_q = \emptyset, \qquad (4.1)$$

formulated as the following:

Given the following boundary conditions on traction, body force, boundary displacement, heat source and temperature boundary:

$$\begin{cases} b_{(i)} : \Omega_{(i)} \times \top \to \mathbb{R}^m, & [i = 1, 2] \\ R_{(i)} : \Omega_{(i)} \times \top \to \mathbb{R} \\ t_{(i)}^\sigma : \partial\Omega_{(i)\sigma} \times \top \to \mathbb{R}^m \\ \psi_{(i)}^u : \partial\Omega_{(i)u} \times \top \to \mathbb{R}^m \\ T_{(i)}^T : \partial\Omega_{(i)T} \times \top \to \mathbb{R} \end{cases} \qquad (4.2)$$

find the motions $\psi_{(i)} : \overline{\Omega_{(i)}} \times \top \to \mathbb{R}^m [\overline{\Omega_{(i)}} = \Omega_{(i)} \cup \partial\Omega_{(i)}, the\, closure\, of\, \Omega_{(i)}]$ and temperature fields $T_{(i)} : \overline{\Omega_{(i)}} \times \top \to \mathbb{R}$ such that (*m* the number of the dimension of the problem)

$$\begin{cases} \nabla.P_{(i)} + b_{(i)} = \rho_0^{(i)} \frac{\partial^2}{\partial t^2} \psi_{(i)} & on \quad \Omega_{(i)} \times \top \quad Momentum\ Balance\ equation(MB) \\ \frac{\partial}{\partial t}\mid_{t=0} \psi_{(i)} = v_0^{(i)} & in \quad \overline{\Omega_{(i)}} \\ \psi_{(i)|t=0} = \psi_{(i)}^0, T_{(i)|t=0} = T_{(i)}^0 & in \quad \overline{\Omega_{(i)}} \\ \psi_{(i)} = \psi_{(i)}^u & on \quad \partial\Omega_{(i)u} \times \top \\ P_{(i)}N_{(i)} = t_{(i)}^\sigma & on \quad \partial\Omega_{(i)\sigma} \times \top \\ T_{(i)} = T_{(i)}^T & on \quad \partial\Omega_{(i)T} \times \top \\ Q_{(i)}N_{(i)} = q_{(i)} & on \quad \partial\Omega_{(i)q} \times \top, \end{cases} \tag{4.3}$$

where $\psi_{(i)}, \psi_{(i)}^0, v_0^{(i)}, T_{(i)}^0, \nabla.P_{(i)}, N_{(i)}, b_{(i)}, \rho_0^{(i)}, t_{(i)}^\sigma, Q_{(i)}, R_{(i)}$ are the unknown displacement field, initial displacement field, initial velocity field, initial temperature field, the divergence of first Piola-Kirchhoff stress tensor, outward normal, body force, the initial mass density of the material, traction field, heat flux and heat source which are to hold [$\forall t \in \top$] at each material point of deformable bodies ($\Omega_{(1)}, \Omega_{(2)}$).

Using the following definitions [(4.4), (4.5), (4.6), (4.7)], the above problem can also be expressed in terms of the following total virtual work formulation (weak form of the large deformation frictional-thermomechanical contact with cohesive force problem):

$$U^i = \left\{ \psi_{(i)} \in H^1(\Omega_{(i)}) : \overline{\Omega_{(i)}} \to \mathbb{R}^m \mid \psi_{(i)} = \psi_{(i)}^u \ in \ \partial\Omega_{(i)u} \right\} \tag{4.4}$$

$$W^i = \left\{ \psi_{(i)}^w \in H^1(\Omega_{(i)}) : \overline{\Omega_{(i)}} \to \mathbb{R}^m \mid \psi_{(i)}^w = 0 \ in \ \partial\Omega_{(i)u} \right\} \tag{4.5}$$

$$T^i = \{ T_{(i)} : \overline{\Omega_{(i)}} \to \mathbb{R} \mid T_{(i)} > 0, T_{(i)} = T_{(i)}^T on \quad \partial\Omega_{(i)T} \} \tag{4.6}$$

$$TW^i = \{ T_{(i)}^w : \overline{\Omega_{(i)}} \to \mathbb{R} \mid T_{(i)}^w = 0, on \quad \partial\Omega_{(i)T} \}, \tag{4.7}$$

where $H^1(\Omega^i)$ introduce Square integrable (derivative) functions space (H1 Hilbert space) and the weighting spaces W^i, TW^i and the solution spaces U^i, T^i are given with respect to the

reference configuration of each deformable bodies ($\Omega_{(i)}$, $i = 1.2$).

$\forall t \in \top \mid find\ \psi_i^t \in U^i, T^t \in \cup T^i, \forall v_i \in W^i\ and\ \forall \delta T \in \cup T W^i [\psi^t \in \cup U^i, v \in \cup W^i]$ such that[1]

$$\delta W_{Total}(\psi^t, v, T^t, \delta T) \quad = \quad \sum_{i=1}^{2}[\delta W_{int}(\psi_i^t, v_i) - \delta W_{ext}(\psi_i^t, v_i)] + \delta W_{friction}(\psi^t, v) +$$

$$\delta W_{thermodynamic}(\psi^t, v, T^t, \delta T) + \delta W_{contact}(\psi^t, v) = 0, \tag{4.8}$$

where $\delta W_{Total}(\psi^t, v, T^t, \delta T)$ is the total virtual work expressed in term of internal and external virtual works $\delta W_{int}(\psi_i^t, v_i), \delta W_{ext}(\psi_i^t, v_i)$, friction virtual work $\delta W_{friction}(\psi^t, v)$, thermodynamic virtual work $\delta W_{thermodynamic}(\psi^t, v, T^t, \delta T)$ and modified contact virtual work (which is a combination of the classical contact and the contact with cohesive force) $\delta W_{contact}(\psi^t, v)$.

Before demonstrating the above virtual works in integral form and to avoid adding too many new symbols, the following discrete functions $\Gamma(\mu, \varepsilon_f, \varepsilon_n^{coh}, g_N)$ and $p(\Upsilon)$ are defined first:

$$\Gamma(\mu, \varepsilon_T, \varepsilon_n^{coh}, g_N) \quad = \quad \begin{cases} 1 & \mu, \varepsilon_n^{coh}\ and\ \varepsilon_T > 0, \begin{cases} g_N > 0 & only\ stick \\ g_N \leqq 0 & stick\ and\ slip \end{cases} \\ 0 & otherwise, \end{cases} \tag{4.9}$$

where μ, ε_T are the friction coefficient and the friction penalty factor, and $p(\Upsilon)$ defined by:

$$p(\Upsilon) : \quad = \quad \begin{cases} T_n(\lambda, g) = \lambda_n + \varepsilon_n g_N(X) & Classical(sliding)Contact\ if\ g_N > 0 \\ T_n(\alpha) = t_N^{max}.(\frac{g_N(X)}{\varepsilon_n^{coh}}).e^{(1 - (\frac{g_N(X)}{\varepsilon_n^{coh}}))} e^{-(\frac{(g_T(X))^2}{(\varepsilon_t^{coh})^2})} & if\ g_N \leq 0 \\ T_t(\beta) = 2\sqrt{\frac{1}{2}}e.t_T^{max}.(\frac{g_T(X)}{\varepsilon_t^{coh}}).(1 + \frac{g_N(X)}{\varepsilon_n^{coh}}).e^{-(\frac{g_N(X)}{\varepsilon_n^{coh}} + \frac{(g_T(X))^2}{(\varepsilon_t^{coh})^2})} & if\ g_N \leq 0, \end{cases} \tag{4.10}$$

where λ_n, ε_n are the Lagrange multiplier and penalty factor and

---

[1]Commonly Momentum Balance equation (MB) will be multiplied by a smooth function, so-called test function or weighting function $v_i := \delta v$ or virtual weighting function with $v_i = 0$ on the boundary surface $\partial \Omega_u$ and after some algebra (e.g. applying the product rule$(\nabla.\sigma).\zeta + \sigma : \nabla \zeta = \nabla(\sigma.\zeta))$ leads to the virtual work formulation

$$\begin{cases} \alpha = (\varepsilon_n^{coh}, g_N, g_T, t_N^{max}, \varepsilon_t^{coh}) \\ \beta = (\varepsilon_n^{coh}, g_N, g_T, t_T^{max}, \varepsilon_t^{coh}), \end{cases}$$

and $\varepsilon_t^{coh}, \varepsilon_n^{coh}, g_N, t_T^{max}, t_N^{max}, g_T, \delta v$ are the characteristic opening length of the tangential direction, the characteristic opening length of the normal direction, the normal gap function, the maximum allowed tangential traction before propagation of cracks, the maximum allowed normal traction before propagation of cracks, the tangential gap function, virtual velocity and $\frac{\partial \Psi}{\partial C}$ is the derivative of stored strain energy function or elastic potential per unit of undeformed volume with respect to the right Cauchy–Green tensor.

It is worth adding that Ψ can be established as the work done by the stress from the initial to the current position and can depend on F(deformation gradients) or C(right Cauchy–Green tensor) or on the invariants of C(I_C,II_C,III_C)as :

$$\Psi(F(X),X) \;=\; \Psi(C(X),X) = \Psi(I_C, II_C, III_C, X), \tag{4.11}$$

and is different from material to material, for example [recall the equation (2.7)] compressible neo-Hookean material

$$\Psi = \frac{G}{2}(I_1 - 3) - Gln \overbrace{J}^{(\lambda_1.\lambda_2.\lambda_3)=det(F)} + \frac{\kappa}{2}(lnJ)^2 \tag{4.12}$$

So, the internal, external, friction, thermodynamic and modified contact virtual works in integral form are given by (which will be described in more detail in the sections following):

$$\delta W_{int}(\psi^t, v) \;=\; \sum_{i=1}^{2} \int_{\Omega_i} \frac{\partial \Psi_i}{\partial C} : DC[\delta v_i]d\Omega_i \qquad [v_i = \delta v_i] \tag{4.13}$$

$$\delta W_{ext}(\psi^t, v) \;=\; \sum_{i=1}^{2} (\int_{\Omega_i} b_{(i)}\delta v_i d\Omega + \int_{\delta\Omega_i} t_{(i)}.\delta v_i d\delta\Omega_i) \tag{4.14}$$

$$\delta W_{friction}(\psi^t, v) = \int_{\Gamma_s} t_f.\Gamma(\mu, \varepsilon_T, \varepsilon_n^{coh}, g_N).\overbrace{\tau^\gamma \{\delta\varphi(X) - \delta\varphi(\bar{Y}(X))\}}^{\delta g_T}d\Gamma_s \tag{4.15}$$

$$\delta W_{thermodynamic}\left(\psi^t, v, T^t, \delta T\right) = \int_{\Gamma_s} \Gamma(\mu, \varepsilon_T, \varepsilon_n^{coh}, g_N)(q_c^{slave}\delta T^S + q_c^{master}\delta T^M)d\Gamma_s \quad (4.16)$$

$$\delta W_{contact}\left(\psi^t, v)\right) = \int_{\Gamma_s} p(\Upsilon).\delta g_\Upsilon d\Gamma_s, \quad (4.17)$$

where $\Psi, C, t, b, q_c^{slave}, q_c^{master}, t_f, \Gamma_s, DC[\delta v], \delta T, \delta g_\Upsilon[\delta g_N \mid \delta g_T]$ are the stored strain energy function or elastic potential per unit of undeformed volume, the right Cauchy–Green tensor, the traction, body force, the heat fluxes across the contact interfaces (slave and master), the friction traction, contact boundary, virtual temperature, the directional derivative of virtual velocity and virtual gap function.

4.2.2   Cohesive Zone Model (CZM)

In connection with numerical analysis of the fracture mechanical (failure and delamination) processes and to approximate non-linear fracture behaviour, cohesive zone models have been introduced and widely studied over a period of years. Even recently, there has been growing interest in the field among many scientists.

In general, a cohesive element formulation is the interface modelling with the definition of discrete elements between the two surfaces, which are supposed to have zero separation in initial condition. As the cohesive surfaces separate, cohesive traction first increases until a maximum value is reached, and then it reduces to zero (complete separation).

As mentioned in an earlier chapter, the constitutive formulation of the cohesive model inherits its definition from two different classes, namely the potential and non-potential based cohesive model. Due to some limitations of the non-potential based cohesive interaction (e.g. all possible separation paths have not been considered under mixed mode conditions), and because potential-based cohesive formulation offers an efficient computational framework for handling fracture mechanics, in this project, potential based cohesive interaction has been chosen and studied.

The most important characteristics of cohesive constitutive relationships are (see Figure 4.2) :

1. The work done by creating a new surface, the fracture energy, is the area under a traction separation curve.
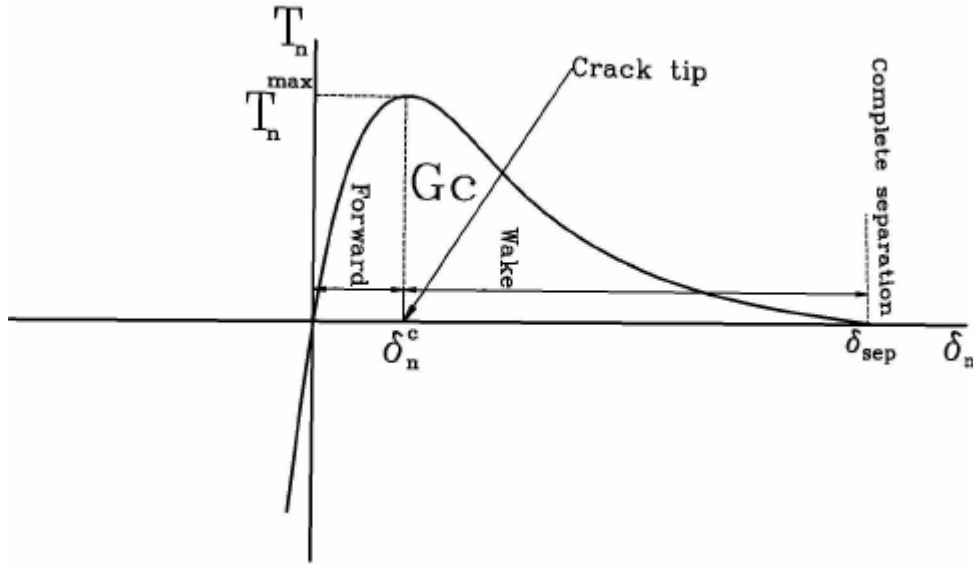
Figure 4.2: Two dimensional illustration of the normal opening traction versus normal opening(pure normal opening)

Cohesive Law	Traction function	Parameters
Exponential	$T_{\alpha \in \{n,t\}} = T_\alpha^{max}(\frac{\delta_\alpha}{\delta_{c\alpha}})exp(1 - \frac{\delta_\alpha}{\delta_{c\alpha}})$	δ_α opening direction
	$T_{\alpha \in \{n,t\}}^{max}$ maximum normal/tangential traction	$\delta_{c\alpha}$ characteristic op. length
Polynomial	$T_{\alpha \in \{n,t\}} = T_\alpha^{max}(\frac{\delta_\alpha}{\delta_{c\alpha}})f(d), d = \sqrt{\Sigma_\alpha(\frac{\delta_\alpha}{\delta_{c\alpha}})^2}$	
Piece-wise linear	$T_t^{max} = T_n^{max}(\frac{\delta_n}{t})$	
Rigid-linear	$T_{\alpha \in \{n,t\}} = T_\alpha^{max}(1 - \frac{\delta_\alpha}{\delta_{c\alpha}})$	

Table 4.1: Cohesive Zone Laws

2. The cohesive traction decreases to zero while the separation increases, which results in the complete separation.

3. Different fracture energy for different opening modes (mode I,II,III).

4. The (unloading-reloading) energy dissipation is not dependent on the potential.

The different formulation of cohesive zone follows different laws, which are commonly indicated as Cohesive Laws (exponential, polynomial, piece-wise linear, rigid-linear as described in the Table 4.1).

The most popular cohesive zone law is exponential cohesive law where, in the case of mixed mode, the normal and tangential traction functions are the functions of both normal and

tangential openings. Due to some advantages of the exponential law[2] compared to the other laws. In this study, the formulations are based on the exponential mixed mode cohesive law defined by (see Figure 4.3):

$$
\begin{cases}
\Pi(\delta_n, \delta_t) = \Pi_0[1 - (1 + \frac{\delta_n}{\delta_n^c}).exp[-(\frac{\delta_n}{\delta_n^c} + \frac{\delta_t^2}{(\delta_t^c)^2})]] \\
T_n(\delta_n, \delta_t) = \frac{\partial \Pi}{\partial \delta_n} |_{\Pi_0 = \Pi_n} = \frac{\Pi_n}{\delta_n^c}.(\frac{\delta_n}{\delta_n^c}).exp[-(\frac{\delta_n}{\delta_n^c} + \frac{\delta_t^2}{(\delta_t^c)^2})] \\
T_t(\delta_n, \delta_t) = \frac{\partial \Pi}{\partial \delta_t} |_{\Pi_0 = \Pi_t} = 2\frac{\Pi_t}{\delta_t^c}.(\frac{\delta_t}{\delta_t^c}).(1 + \frac{\delta_n}{\delta_n^c}).exp[-(\frac{\delta_n}{\delta_n^c} + \frac{\delta_t^2}{(\delta_t^c)^2})] \\
\delta_n^c = \frac{\Pi_n}{T_n^{max}.exp(1)}, \ \delta_t^c = \frac{\Pi_t}{T_t^{max}.\sqrt{\frac{1}{2}exp(1)}},
\end{cases}
\tag{4.18}
$$

where $T_n, T_t, T_n^{max}, T_t^{max}, \delta_n^c, \delta_t^c, \Pi(\delta_n, \delta_t), \delta_n, \delta_t$ are the normal opening traction (coupled mode I cracks), the tangential opening traction (coupled mode II,III cracks), the maximum normal opening traction, the maximum tangential opening traction, the characteristic opening length of the normal direction, the characteristic opening length of the tangential direction, the potential function, the relative displacement of normal opening and the relative displacement of tangential opening.

As shown in the equation (4.18), the normal traction is calculated by differentiating the potential $\Pi(\delta_n, \delta_t)$ with respect to the normal opening δ_n for the work of separation of the pure normal opening ($\Pi_0 = \Pi_n$) and the tangential traction is calculated by differentiating the potential $\Pi(\delta_n, \delta_t)$ with respect to the tangential opening δ_t for the work of separation of the pure tangential opening ($\Pi_0 = \Pi_t$).

Also the total work of separation (per unit surface area) defined by

$$
Work^{total} = \underbrace{\int_0^\infty T_n(\delta_n, \delta_t) d\delta_n}_{work^{normal}} + \underbrace{\int_0^\infty T_t(\delta_n, \delta_t) d\delta_t}_{work^{tangential}},
\tag{4.19}
$$

Using the above definitions, $t_N^{coh}, t_{T_\alpha}^{coh}$ the normal and tangential cohesive traction have been calculated based upon the following determination (described in more detail in the following

---

[2]Due to the fact that the tractions and their derivatives are continuous, the exponential mixed mode cohesive law has been selected as cohesive law and applied to the problem
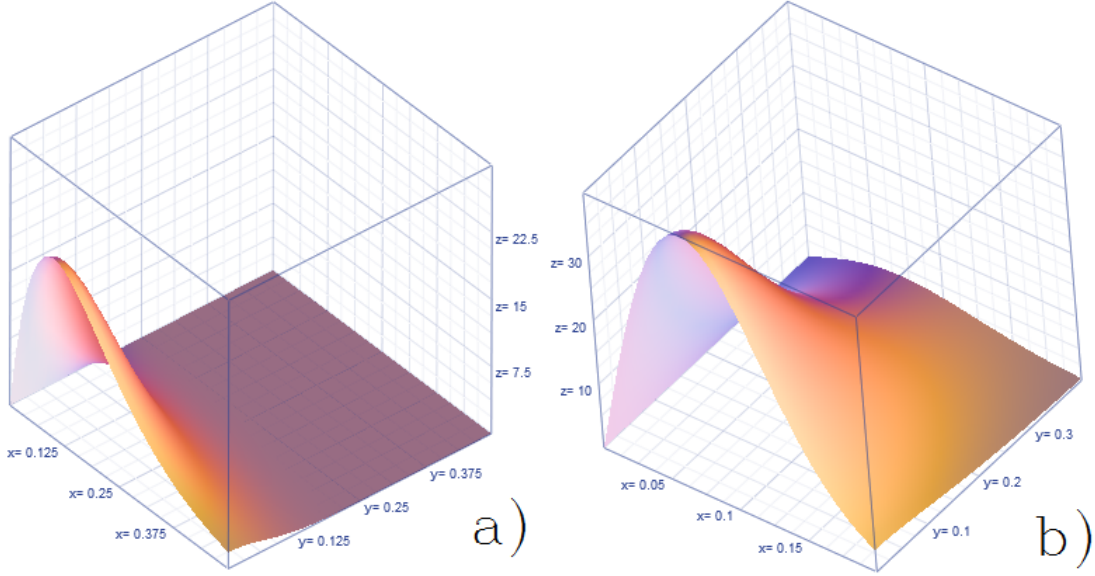
Figure 4.3: Three dimensional illustration of the normal and tangential traction-opening $[a]$: $T_n(\delta_n, \delta_t) = z, \delta_n = x, \delta_t = y, \; b) : T_t(\delta_n, \delta_t) = z, \delta_n = y, \delta_t = x$]

section)

$$
\begin{cases}
t_N^{coh} = t_N^{max} . \left(\frac{g_N(X)}{\varepsilon_n^{coh}} \right) . e^{\left(1 - \left(\frac{g_N(X)}{\varepsilon_n^{coh}} \right) \right)} e^{-\left(\frac{(g_T(X))^2}{(\varepsilon_t^{coh})^2} \right)} \\
t_T^{coh} = 2\sqrt{\frac{1}{2}e} . t_T^{max} . \left(\frac{g_T(X)}{\varepsilon_t^{coh}} \right) . \left(1 + \frac{g_N(X)}{\varepsilon_n^{coh}} \right) . e^{-\left(\frac{g_N(X)}{\varepsilon_n^{coh}} + \frac{(g_T(X))^2}{(\varepsilon_t^{coh})^2} \right)} \\
t_{T_\alpha}^{coh} = 2\sqrt{\frac{1}{2}e} . t_T^{max} . \left(\frac{g_T^\alpha(X)}{\varepsilon_t^{coh}} \right) . \left(1 + \frac{g_N(X)}{\varepsilon_n^{coh}} \right) . e^{-\left(\frac{g_N(X)}{\varepsilon_n^{coh}} + \frac{(g_T^\alpha(X))^2}{(\varepsilon_t^{coh})^2} \right)} ,
\end{cases}
\tag{4.20}
$$

where $g_N(X)[-v.(\varphi^{(1)}(X) - \varphi^{(2)}(\bar{Y}(X)))], \; g_T(X)[g_T^\alpha = m_{\alpha\beta}(\xi_{n+1}^\beta - \xi_n^\beta)]$ are the normal and tangential gap functions, t_N^{max}, t_T^{max} are the maximum normal tangential opening tractions, $\varepsilon_n^{coh}, \varepsilon_t^{coh}$ are the characteristic opening length of the normal and the tangential directions.

In order to calculate the amount of irreversible cohesive energy which is normally indicated by damage factor W, we need to compute the characteristic opening length of the normal (tangential) direction (defined by $\delta_c = \varepsilon_n^{coh} \mid \varepsilon_t^{coh}$) and the maximum separation value (maximum gap value) reached until time evaluation t ($\delta_{max,t} = gap_{max,t}(X, \bar{Y}(X))$), which in general is shown as (linear case):

$$
W \quad = \quad \frac{\delta_{max,t}}{\delta_c} ,
\tag{4.21}
$$

where, $\forall time \quad gap_{max,t}(X, \bar{Y}(X)) \geq gap(X, \bar{Y}(X))$.

Furthermore, the observation of the loading and unloading behaviour of the cohesive model needs to be considered where the unloading, after the achievement of the undeformed state, is fully successful (decreasing stress to zero and leading to the vanishing of separation).

Following the idea of the history parameter δ_{Max}, in the case of coupling mode formulation (normal and tangential loading), we have

$$\delta_{Max} = max\{\underbrace{\sqrt{[g_N(X)]^2 + \beta[g_T(X)]^2}}_{\delta_{effective}}\} \quad with\,\beta = (0,\infty), \tag{4.22}$$

where $\delta_{effective}$ refers to the effective opening displacement, $\beta^2 = (G_{II}/G_I)$ is a measure of the strain energy release rate ratio (Mode I and II) [Galvanetto and Aliabadi (2009)] and δ_{Max} satisfies the Kuhn-Tucker condition

$$\delta_{Max} - \delta_{effective} \geq 0, \quad \frac{\partial \delta_{Max}}{\partial t} \geq 0, \quad \frac{\partial \delta_{Max}}{\partial t}(\delta_{Max} - \delta_{effective}) = 0 \tag{4.23}$$

Thus, the tractions defined by the equation (4.20), are modified as follows

$$\begin{cases} t_N^{coh^{lu}} = \frac{\delta_{effective}}{\delta_{Max}} t_N^{coh}(\frac{\delta_{effective}}{\delta_{Max}} g_N(X), \frac{\delta_{effective}}{\delta_{Max}} g_T(X)) \\ t_T^{coh^{lu}} = \frac{\delta_{effective}}{\delta_{Max}} t_T^{coh}(\frac{\delta_{effective}}{\delta_{Max}} g_N(X), \frac{\delta_{effective}}{\delta_{Max}} g_T(X)), \end{cases} \tag{4.24}$$

where the openings $g_N(X), g_T(X)$, are first scaled by a factor $\frac{\delta_{effective}}{\delta_{Max}}$ and then the associated tractions are computed [as shown in equation (4.24)]. Note that the associated stiffness needs to be modified as well.

To demonstrate the use of the above traction separation relationships in the implementation of the irreversible phenomena formulated for the coupled mode, we use the following equation

$$t^{coh} = \begin{cases} t_N^{coh}, t_T^{coh} & (Loading) \quad if \quad \delta_{effective} > \delta_{Max}^i, \quad i \quad is\,time\,increment \\ t_T^{coh^{lu}}, t_T^{coh^{lu}} & (Reloading/Unloading) \quad otherwise \end{cases} \tag{4.25}$$

Using introduced methods for the calculation of the damage by Galvanetto and Aliabadi (2009) and Lucchini (2013), the following two scalar quantities are defined ($\forall i$, $D_i^{normal|tangential} \in [0,1]$)

$$D_i^{normal} := \begin{cases} 1 - \frac{t_N^{coh}}{g_N(X)} \frac{\varepsilon_n^{coh}}{t_N^{coh}(\varepsilon_n^{coh})} & if \quad g_N(X) > 0 \, and \, \frac{t_N^{coh}}{g_N(X)} < \frac{t_N^{coh}(\varepsilon_n^{coh})}{\varepsilon_n^{coh}} \\ D_{i-1}^{normal} & otherwise \end{cases} \tag{4.26}$$

$$D_i^{tangential} := \begin{cases} 1 - \dfrac{t_T^{coh}}{g_T(X)} \dfrac{\varepsilon_t^{coh}}{t_T^{coh}(\varepsilon_t^{coh})} & if \quad \dfrac{t_T^{coh}}{g_T(X)} < \dfrac{t_T^{coh}(\varepsilon_t^{coh})}{\varepsilon_t^{coh}} \\ D_{i-1}^{tangential} & otherwise; \end{cases} \tag{4.27}$$

where the damage parameter varies between zero (undamaged) and one (complete failure).

4.2.3 Mechanics of Classical Contact

In this section, the development of the friction-less classical contact problem is based on the original work by Laursen (2003). The definition of the sliding interfaces (so called master and slave surfaces), as shown in Figure (4.4); in other words, the mathematical formulation of the classical (sliding) contact boundary condition in a form of contact integral defined on two deformable bodies is given by:

$$\delta W_{classical contact}\left(\psi^t, \delta v\right) = \int_{\Gamma_s} t_c^s . \delta v_s d\Gamma_s + \int_{\Gamma_m} t_c^m . \delta v_m d\Gamma_m$$

$$\overset{-t_c^s = t_c^m \, Newton's \, second \, law}{=} \int_{\Gamma_s} t_c^s . (\delta v_s - \delta v_m) d\Gamma \tag{4.28}$$

$$(in \, compact \, form) \quad \delta W_{classical contact}\left(\psi^t, \delta g\right) = \int_{\Gamma_s} t_N . \delta g_N d\Gamma \tag{4.29}$$

$$(\Gamma_s, \Gamma_m \, are \, the \, contact \, boundaries),$$

where $\delta W_{classical contact}\left(\psi^t, \delta g\right)$ corresponds to the virtual work of the sliding contact (frictionless) of two different bodies which are in contact with each other. ψ^t is the unknown in the problem which will be solved for all $t \in time$ such that,

$$\begin{cases} X \, is \, a \, point \, in \, reference \, description \\ \psi^t(X) = x \, is \, a \, point \, in \, spatial \, description \end{cases}$$

$t_N, \delta v(\delta g)$ are the contact pressure and the (virtual) weighting function (virtual gap function δg) defined as the following.

The contact pressure t_N is formulated as the following expression:

$$(t_N . v = t_c)[t_N = \lambda_N + \varepsilon_N g_N], \tag{4.30}$$
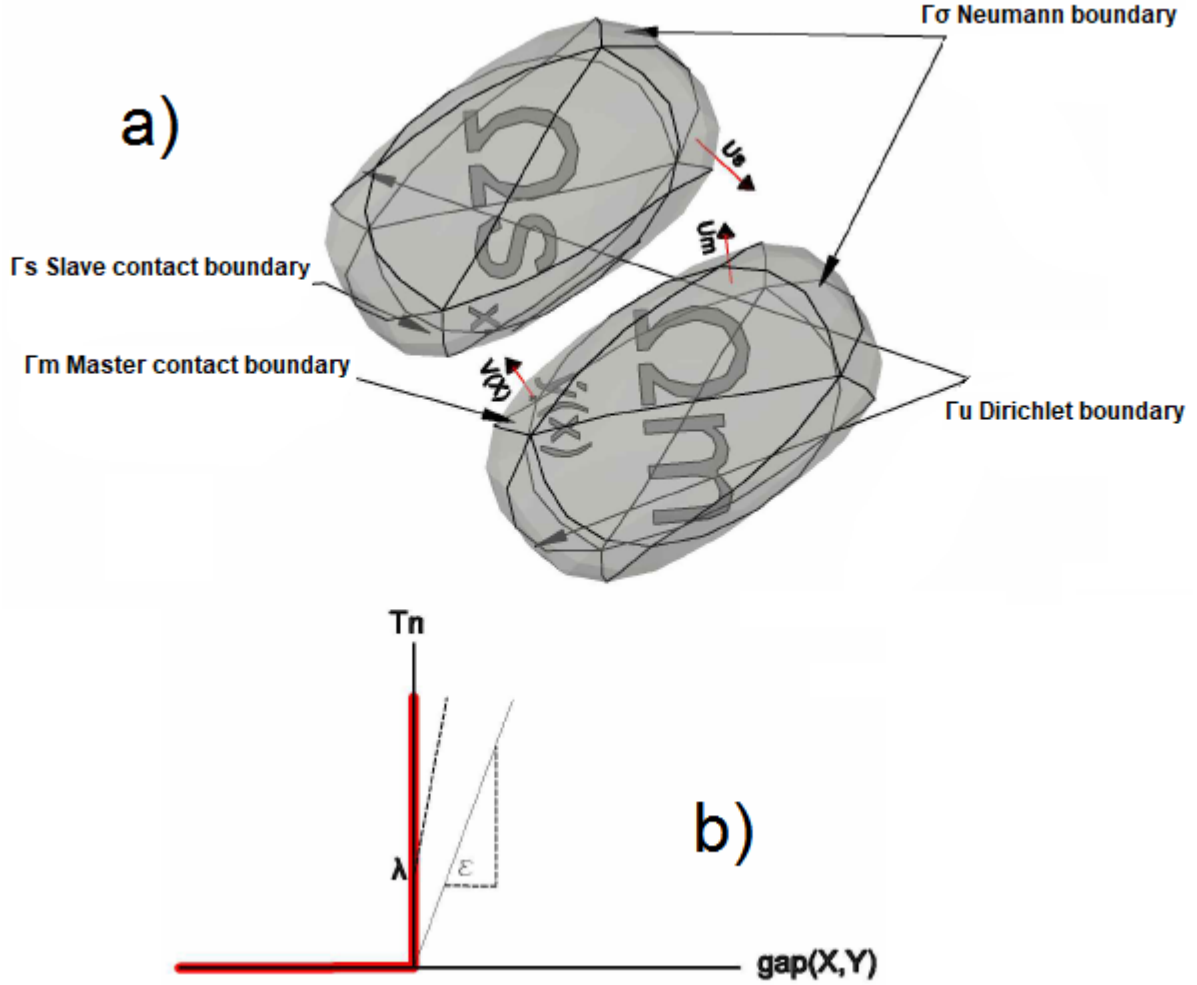
Figure 4.4: a) Contact problem of two bodies Ω_s, Ω_m with boundaries, b) Kuhn-Tucker conditions (contact inequality constraints)

where ε_N, λ_N are the penalty factor and Lagrange multiplier (enable exact representation of contact constrains) and $t_c(t_c^s, t_c^m)$ correspond to the contact traction.

g_N (as shown in Figure 4.5), is the contact normal gap function defined as scalar product of master normal vector v with the closest point (projection onto master surface). It measures the (normal) distance between a given point $X \in \Gamma_s$ on the slave reference contact surface and $\bar{Y}(X) \in \Gamma_m$, the closest point to X on the master contact surface, expressed as

$$g_N(X, \bar{Y}(X)) = -v.\{\psi_s(X_i) - \psi_m(\bar{Y}(X))\}, \tag{4.31}$$

where $\psi_m(\bar{Y}(X)) = \psi_m(inf\|\psi(X_j) - \psi(X_i)\|_{Xj \in \Gamma_s, X_i \in \Gamma_m})$.

To calculate the linearisation $(\delta_{\delta\varphi} f(\varphi) := \frac{d}{d\varepsilon} f(\varphi + \varepsilon\delta\varphi)\mid_{\varepsilon=0})$ of g_N we could refer dir-
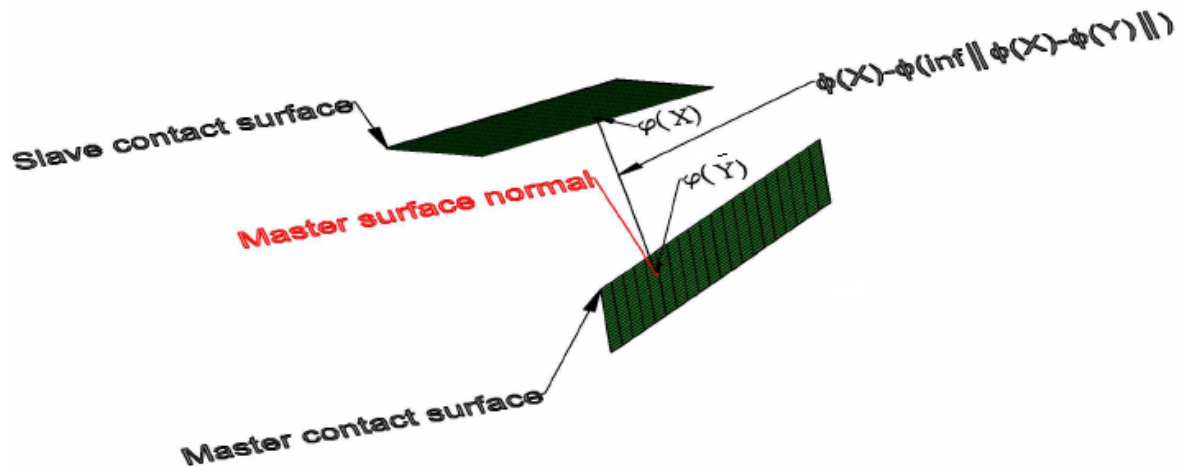
Figure 4.5: 3D illustration of the normal gap functions

ectly to the equation (4.31) and compute δg_N

$$\delta g_N(X, \bar{Y}(X)) = \delta[-v.\{\psi_s(X_i) - \psi_m(\bar{Y}(X)))\}] = -v.\{\delta \psi_s(X_i) - \delta \psi_m(\bar{Y}(X))\} \quad (4.32)$$

The contact condition optimised with inequality constraints: the Kuhn-Tucker conditions [as shown in Figure 4.4 b)]

$$\forall X \in \Gamma_s, \Gamma_m \ such \ that, \ \begin{cases} t_N(\lambda, g) \geqq 0 \\ g_N(X, \bar{Y}(X)) \leqq 0 \\ t_N(\lambda, g) g_N(X, \bar{Y}(X)) = 0, \end{cases} \quad (4.33)$$

where $t_N(\lambda, g) \geqq 0$ implies that the contact interactions are all compressive, $g_N(X, \bar{Y}(X)) \leqq 0$ refers to the impenetrability condition and $t_N(\lambda, g) g_N(X, \bar{Y}(X)) = 0$ is the condition requiring the development of the contact stress only under certain condition namely, $g_N(X, \bar{Y}(X)) = 0$ (for example if $g_N(X, \bar{Y}(X)) > 0$ it requires that $t_N(\lambda, g) > 0$.

At this point it is worth mentioning that the impenetrability condition [as shown in Figure 4.4 b)] cannot be perfectly represented because of some limited penalty value ε_N (e.g. obtained by setting $\lambda_N = 0$)

$$t_N = \lambda_N + \varepsilon_N g_N \overset{\lambda_N=0}{\Longleftrightarrow} \varepsilon_N = \frac{t_N}{g_N} \overset{g_N \to 0}{\Longleftrightarrow} \varepsilon_N \to \infty, \quad (4.34)$$

which is practically impossible in this case having a penalty value.

Due to the fact that the most popular algorithms for the solution of non-linear discrete
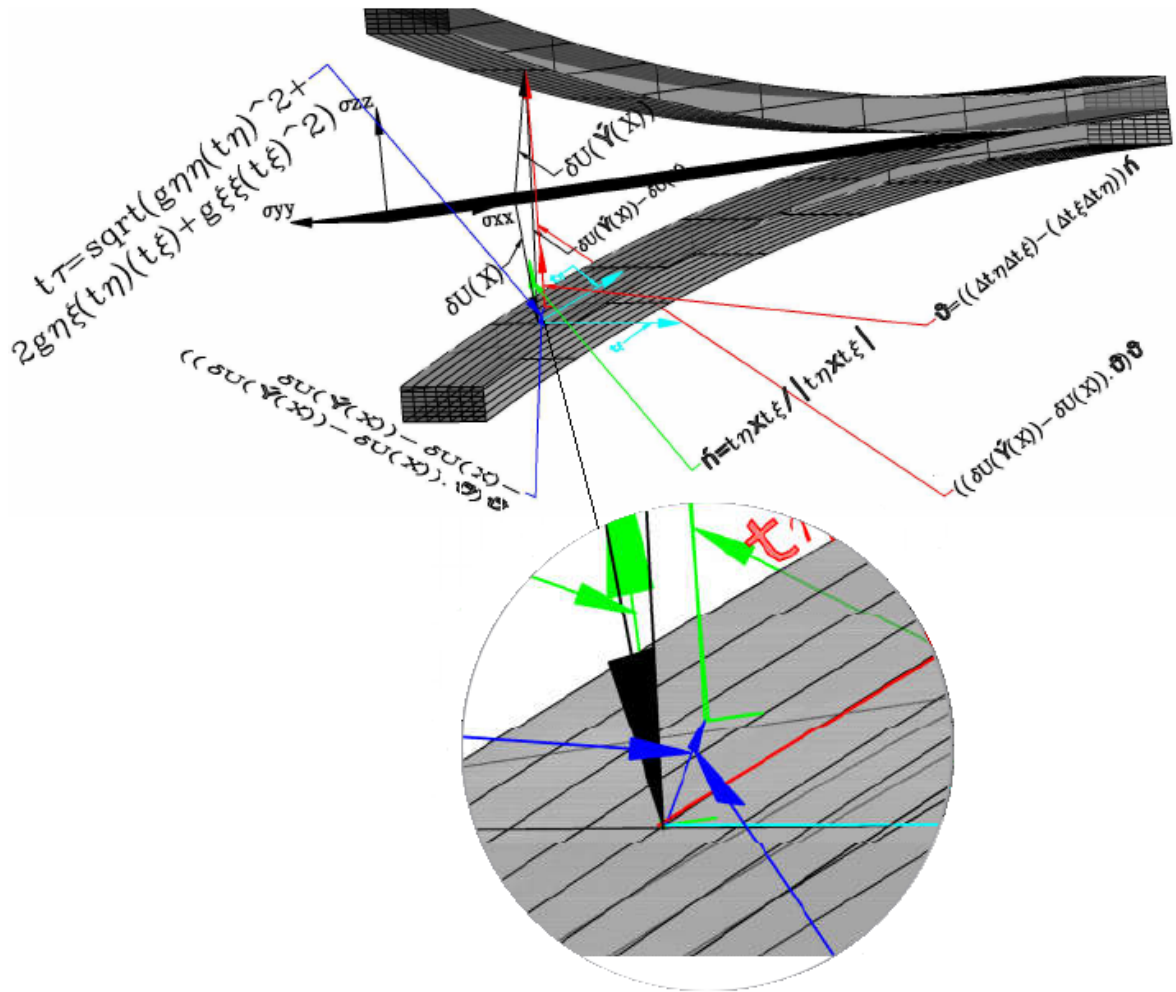
Figure 4.6: 3D illustration of the tangential gap functions

equations are based on the Newton-Raphson method, where the algorithm requires the linearised problem, we will next focus on linearisation of the contact integral.

The directional derivative in the direction of the incremental (displacement or velocity) field $\Delta := D_{\rho u} f(u) = \frac{d}{d\varepsilon} f(u + \varepsilon \rho u) \mid_{\varepsilon=0}$ [linearisation] of the equation (4.29) is given by the following equation

$$\Delta \delta W_{classical contact} \left(\psi^t, \delta g \right) = \Delta \int_{\Gamma_s} t_N . \delta g_N d\Gamma = \int_{\Gamma_s} \Delta t_N . \delta g_N d\Gamma + \int_{\Gamma_s} t_N . \Delta \delta g_N d\Gamma, \qquad (4.35)$$

where

$$\Delta t_N = \Delta(\lambda_N + \varepsilon_N g_N) = \varepsilon_N \Delta(g_N) = \varepsilon_N \frac{\partial <g_N>}{\partial g_N} \Delta g_N = \varepsilon_N H(g_N) \Delta g_N, \tag{4.36}$$

where $\Delta g_N = -v.\{\Delta \psi_s(X_i) - \Delta \psi_m(\bar{Y}(X))\}$ and $< ... >$ is the Macaulay brackets ($<x> =$ $\begin{cases} x & if\, x \geq 0 \\ 0 & if\, x < 0 \end{cases}$) and $H(...)$ is the Heaviside function ($H(x) = \begin{cases} 1 & if\, x \geq 0 \\ 0 & if\, x < 0 \end{cases}$).

Where also the quantity $\Delta \delta g_N$ is formulated in Appendix A (part 1).

The next step is the discretisation of the equation (4.29), the contact integral and the equation (4.35), the contact stiffness, expressed as the following equations.

Discretisation of the contact Integral:

$$\delta W_{classicalcontact}\left(\psi^h, \delta g^h\right) \approx \sum_{e=1}^{n_{sel}} \{\sum_{k=1}^{n_{int}} W_k j(\eta_k) t_N^h(\eta_k) \delta g^h(\eta_k)\}, \tag{4.37}$$

where $\psi^h, \delta g^h$ are the finite dimensional counterparts of $\psi, \delta g$, n_{sel} is the number of surface elements (i.e., the slave surface elements), n_{int} is the number of integration points, W_k is the quadrature weight corresponding to local quadrature points k and $j(\eta_k) = \| \frac{\partial X^h(\eta_k)}{\partial \eta_\alpha} \times \frac{\partial X^h(\eta_k)}{\partial \eta_\beta} \|$ is the Jacobian of the transformation at each point η_k.

The equation (4.37) can be also expressed as follows

$$\delta W_{classicalcontact}\left(\psi^h, \delta g^h\right) \approx \sum_{e=1}^{n_{sel}} \{\sum_{k=1}^{n_{int}} W_k j(\eta_k) \delta \Phi_k^c . f_k^c\}, \tag{4.38}$$

where $\delta \Phi^c = \begin{bmatrix} C_s^{(1)} \\ C_1^{(2)} \\ . \\ . \\ C_{mnode}^{(2)} \end{bmatrix}$, $f^c = t_N \mathbf{N}$ are the vector of nodal variations (slave and master nodes) and the local contact force vector corresponding to local quadrature points .The *mnode* refers to the number of nodes per element on the master surface (e.g. for a quadrilateral surface element we have *mnode* = 4)

Where $\mathbf{N}$ refers to the vectors $\mathbf{N} = \begin{bmatrix} v \\ -N_1(\bar{Y}(X))v \\ . \\ . \\ -N_{mnode}(\bar{Y}(X))v \end{bmatrix}$.

And the discretization of the contact Stiffness:

$$\triangle \delta W_{classical contact}\left(\psi^h, \delta g^h\right) \approx \sum_{e=1}^{n_{sel}}\{\sum_{k=1}^{n_{int}} W_k j(\eta_k)[\triangle t_N^h(\eta_k)\delta g^h(\eta_k) + t_N^h(\eta_k)\triangle \delta g^h(\eta_k))]\} =$$

$$\sum_{e=1}^{n_{sel}}\{\sum_{k=1}^{n_{int}} W_k j(\eta_k)\delta \Phi_k^c . k_k^c \triangle \Phi_k^c\}, \tag{4.39}$$

where $\triangle\Phi^c = \begin{bmatrix} \triangle d_s^{(1)} \\ \triangle d_1^{(2)} \\ . \\ . \\ \triangle d_{mnode}^{(2)} \end{bmatrix}$, k_N^c are the vector of local nodal values and the global contact

stiffness is defined in Appendix B.

4.2.4 Mechanics of Modified Contact

With a definition of the classical contact mechanics in hand, the treatment of the modified contact mechanics within this section takes the place, where the modification of the existing contact definition, generally speaking, is based on the modification of the classical contact inequality constraints: the Kuhn-Tucker conditions [equation (4.33), as shown in Figure 4.4 b)].

Before we proceed to the development of the modified contact mechanics, we need to define the tangential gap function $g_T(X, \bar{Y}(X))$, as shown in Figure (4.6), that measures the (tangential) distance between a given point $X \in \Gamma_c^{(1)}$ on the slave reference contact surface and $\bar{Y}(X) \in \Gamma_c^{(2)}$, the closest point to X on the master contact surface, expressed as

$$\begin{cases} g_T(X, \bar{Y}(X)) = m_{\alpha\beta}(y_\gamma^\vdash - y_{\gamma\rho}^\vdash) & \gamma \in \{\alpha, \beta\} \\ g_t^\alpha = \xi_{n+1}^\alpha - \xi_n^\alpha & (shorthand\, notation), \end{cases} \tag{4.40}$$

where $\alpha, \beta = 1, ..., d-1$ with d for the dimension in the problem, $m_{\alpha\beta}$ is the metric tensor ($m_{\alpha\beta} = \tau_\alpha.\tau_\beta$, $\tau^\alpha = m^{\alpha\beta}\tau_\beta$, $\tau_\alpha = \psi_t(\bar{Y}(X)),_\alpha = \frac{\partial \psi_t(\bar{Y}(X))}{\partial \alpha}$, τ^α, τ_α the contra and co variant base vectors) and $y_\gamma^\vdash - y_{\gamma\rho}^\vdash$ are the component (current and previous) of the closest point. ξ_n^α is the isoparametric coordinate of the projected slave node onto the master element.

The relative tangential motion $\chi_t(X)$ of a given point $X \in \Gamma_c^{(1)}$ on the slave surface to the closest point to X on the master contact surface can also be expressed as

$\chi_t(X) = \chi(X) - \chi(\bar{Y}(X)) - [(\chi(X) - \chi(\bar{Y}(X))).v]v$
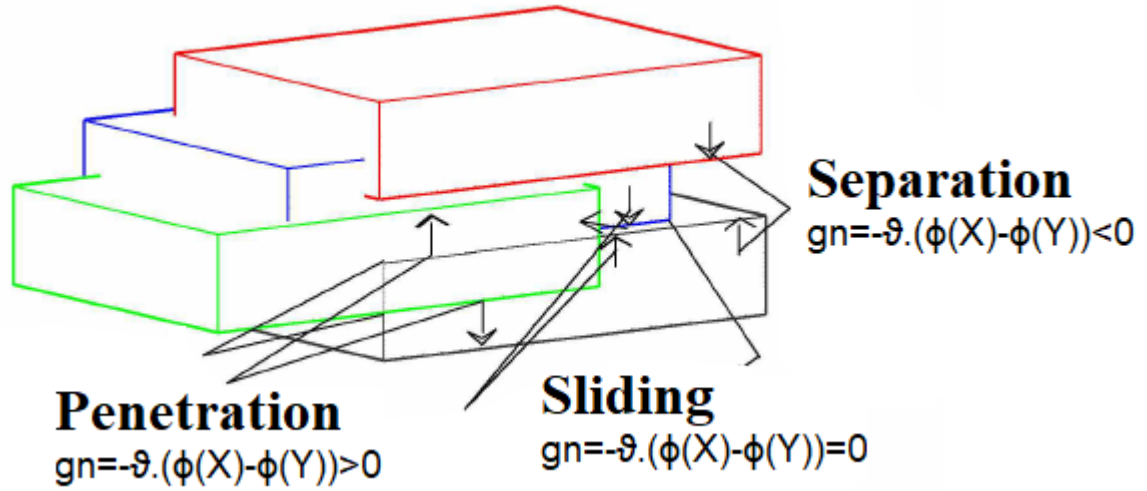
Figure 4.7: Illustration of the contact tractions with respect to gap functions

Keeping this in mind, the tangential contact traction can be formulated as: $t_{t\gamma}.\tau^\gamma = t_t$ with $t_{t\gamma}$ as tangential contact nodal pressure and τ^γ as contra variant base.

Recall the equation (4.20) where $t_N^{coh}, t_{T_\alpha}^{coh}$ the normal and tangential cohesive tractions have been calculated based on mixed mode cohesive law and using the definition of the normal and tangential gap functions, the modified contact integral, defined on two bodies, can be shown as

$$
\delta W_{modifiedcontact}\left(\psi^t, \delta g\right) = \underbrace{\int_{\Gamma_s} t_N \delta g d\Gamma}_{[classicalcontact]g_N(X)>0} + \underbrace{\overbrace{\int_{\Gamma_s} t_N^{coh} \delta g d\Gamma + \int_{\Gamma_s} t_{T_\alpha}^{coh} \delta \xi^\alpha d\Gamma}^{\int_\Gamma G_c[G_{Ic}|G_{IIc}|G_{IIIc}]d\Gamma (totalworkofseparation)}}_{[contactcohesiveinteraction]g_N(X)\leq 0} ,
$$

(4.41)

where $G_c[G_{Ic} \mid G_{IIc}]$ are the fracture energy (mode I, mode II) per unit area due to the creation of the new crack surface, δg is the variation of the normal gap function defined by the equation (4.32) and $\delta \xi^\alpha$ the variation of the tangential gap function is given by the following determination:

Due to the fact that,

$$
\underbrace{[\psi_s(X) - \psi_m(\bar{Y}(X)))]}_{closestpointprojection}.\underbrace{\frac{\partial \psi_t(\bar{Y}(X))}{\partial \alpha}}_{tangentbasisvector} = 0,
$$

(4.42)
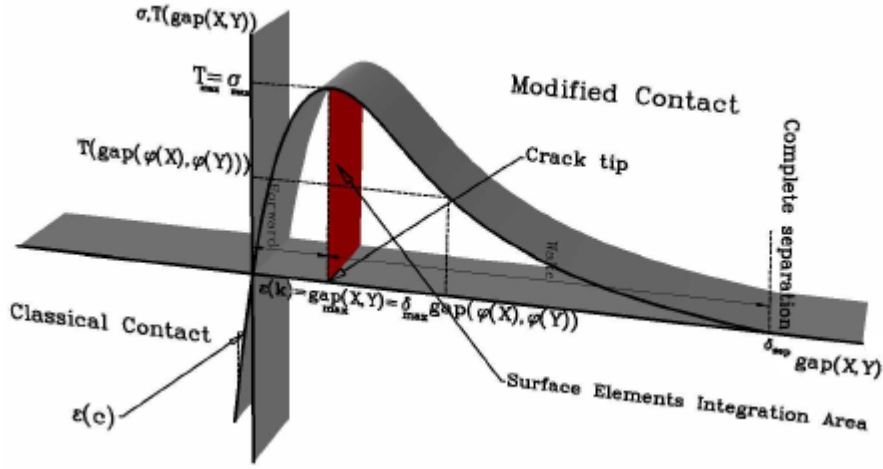
Figure 4.8: Modified-Classical Contact Mechanics combined structure

after taking the directional derivative of the equation (4.42) and some algebra we get

$$A_{\alpha\beta}\delta\xi^{\alpha} = [\delta\psi_s(X) - \delta\psi_m(\bar{Y}(X))].\tau_{\alpha} - gv.[\frac{\partial\delta\psi_m(\bar{Y}(X))}{\partial\alpha}], \qquad (4.43)$$

where $A_{\alpha\beta} = m_{\alpha\beta} + g_N\kappa_{\alpha\beta}$, $\kappa_{\alpha\beta} = v.\psi_m(\bar{Y}(X))_{,\alpha\beta}$ is the curvature of the surface at $\psi_m(\bar{Y}(X))$.

Recall additionally the discrete function $p(\Upsilon)$ defined by the equation (4.10), the classical-modified contact integral (4.41), in a compact form, is given by the following expression

$$\delta W_{modifiedcontact}\left(\psi^t, \delta g\right) = \int_{\Gamma_s} p(\Upsilon).\delta g_{\Upsilon}d\Gamma, \qquad (4.44)$$

where $\delta g_{\Upsilon} = [\delta g_N \mid \delta g_T = \delta\xi^{\alpha}]$.

The linearisation of the equation (4.41) is given by the following equation

$$\triangle\delta W_{modifiedcontact}\left(\psi^t, \delta g\right) = \triangle\int_{\Gamma_s} t_N\delta g d\Gamma + \triangle\int_{\Gamma_s} t_N^{coh}\delta g d\Gamma + \triangle\int_{\Gamma_s} t_{T_{\alpha}}^{coh}\delta\xi^{\alpha}d\Gamma =$$

$$\int_{\Gamma_s}(\triangle t_N\delta g + t_N\triangle\delta g)d\Gamma + \int_{\Gamma_s}(\triangle t_N^{coh}\delta g + t_N^{coh}\triangle\delta g)d\Gamma + \int_{\Gamma_s}(\triangle t_{T_{\alpha}}^{coh}\delta\xi^{\alpha} + t_{T_{\alpha}}^{coh}\triangle\delta\xi^{\alpha})d\Gamma =$$

$$\underbrace{\int_{\Gamma_s} (\triangle t_N \delta g + t_N \triangle \delta g) d\Gamma}_{equation (3.25)} + \int_{\Gamma_s} [(\frac{\partial t_N^{coh}}{\partial g_N}.\triangle g_N + \frac{\partial t_N^{coh}}{\partial g_T}.\triangle g_T)\delta g + t_N^{coh} \triangle \delta g)] d\Gamma +$$

$$\int_{\Gamma_s} [(\frac{\partial t_T^{coh}}{\partial g_N}.\triangle g_N + \frac{\partial t_T^{coh}}{\partial g_T}.\triangle g_T)\delta \xi^\alpha + t_{T_\alpha}^{coh} \triangle \delta \xi^\alpha] d\Gamma, \tag{4.45}$$

where the quantities $\triangle \delta g, \triangle \delta \xi^\alpha$ are given in Appendix A. $\triangle t_N^{coh}, \triangle t_{T_\alpha}^{coh}$ are defined as follows

$$\triangle t_{N|T}^{coh} := \begin{cases} \frac{\partial t_N^{coh}}{\partial g_N}.\triangle g_N = \{t_N^{max}.e^{-(\frac{(g_T(X))^2}{(\varepsilon_t^{coh})^2})}[(\frac{e^{(1-(\frac{g_N(X)}{\varepsilon_n^{coh}}))}}{\varepsilon_n^{coh}}) + (\frac{g_N(X)}{\varepsilon_n^{coh}})(\frac{-1}{\varepsilon_n^{coh}})e^{(1-(\frac{g_N(X)}{\varepsilon_n^{coh}}))}]\}\triangle g_N \\[2mm] \frac{\partial t_N^{coh}}{\partial g_T}.\triangle g_T = \{t_N^{max}.(\frac{g_N(X)}{\varepsilon_n^{coh}}).e^{(1-(\frac{g_N(X)}{\varepsilon_n^{coh}}))}[(\frac{-2g_T(X)}{(\varepsilon_t^{coh})^2})e^{-(\frac{(g_T(X))^2}{(\varepsilon_t^{coh})^2})}]\}\triangle g_T \\[2mm] \frac{\partial t_T^{coh}}{\partial g_N}.\triangle g_N = \{2\sqrt{\frac{1}{2}e}.t_T^{max}.(\frac{g_T(X)}{\varepsilon_t^{coh}}).e^{-(\frac{(g_T(X))^2}{(\varepsilon_t^{coh})^2})}[(\frac{e^{-(\frac{g_N(X)}{\varepsilon_n^{coh}})}}{\varepsilon_n^{coh}}) + \\ (1 + \frac{g_N(X)}{\varepsilon_n^{coh}}).(\frac{-1}{\varepsilon_n^{coh}}).e^{-(\frac{g_N(X)}{\varepsilon_n^{coh}})}]\}\triangle g_N \\[2mm] \frac{\partial t_T^{coh}}{\partial g_T}.\triangle g_T = \{2\sqrt{\frac{1}{2}e}.t_T^{max}.(1 + \frac{g_N(X)}{\varepsilon_n^{coh}}).e^{-(\frac{g_N(X)}{\varepsilon_n^{coh}})}[(\frac{e^{-(\frac{(g_T(X))^2}{(\varepsilon_t^{coh})^2})}}{\varepsilon_t^{coh}}) + \\ (\frac{g_T(X)}{\varepsilon_t^{coh}}).(\frac{-2g_T(X)}{(\varepsilon_t^{coh})^2}).e^{-(\frac{(g_T(X))^2}{(\varepsilon_t^{coh})^2})}]\}\triangle g_T, \end{cases}$$

$$\tag{4.46}$$

in matrix form

$$\triangle t_{N|T}^{coh} := \begin{bmatrix} \frac{\partial t_N^{coh}}{\partial g_N} & \frac{\partial t_N^{coh}}{\partial g_T} \\ \frac{\partial t_T^{coh}}{\partial g_N} & \frac{\partial t_T^{coh}}{\partial g_T} \end{bmatrix} . \begin{bmatrix} \triangle g_N \\ \triangle g_T \end{bmatrix}, \tag{4.47}$$

where $[setting \, \Delta \, for \, \delta]$

$$\begin{cases} \triangle g_N = -\nu.\{\Delta\psi_s(X) - \Delta\psi_m(\bar{Y}(X))\} \\ \triangle g_T^\alpha = \Delta m_{\alpha\beta}(\xi_{n+1}^\beta - \xi_n^\beta) = \Delta m_{\alpha\beta}(\xi_{n+1}^\beta - \xi_n^\beta) + m_{\alpha\beta}\Delta(\xi_{n+1}^\beta - \xi_n^\beta) = \\ [((\tau_\beta \frac{\partial^2 \psi_m(\bar{Y}(X))}{\partial\alpha\partial\gamma}) + (\tau_\alpha \frac{\partial^2 \psi_m(\bar{Y}(X))}{\partial\beta\partial\gamma}))\tau^\gamma(\Delta\psi_s(X) - \Delta\psi_m(\bar{Y}(X))) + (\tau_\beta \frac{\Delta\partial\psi_m(\bar{Y}(X))}{\partial\alpha}) + \\ (\tau_\alpha \frac{\Delta\psi_m(\bar{Y}(X))}{\partial\beta})](\xi_{n+1}^\beta - \xi_n^\beta) + m_{\alpha\beta}\tau^\beta(\Delta\psi_s(X) - \Delta\psi_m(\bar{Y}(X))) \end{cases}$$

$$\tag{4.48}$$

The discretisation of the equation (4.41), the modified contact integral, is given by the following expression

$$\delta W_{modifiedcontact}\left(\psi^h,\delta g^h\right) \approx \sum_{e=1}^{n_{sel}}\{\sum_{k=1}^{n_{int}} W_k j(\eta_k)[t_N^h(\eta_k)\delta g^h(\eta_k)+$$

$$t_N^{coh^h}(\eta_k)\delta g^h(\eta_k)+t_{T_\alpha}^{coh^h}(\eta_k)\delta\xi^{\alpha^h}(\eta_k)]\} = \sum_{e=1}^{n_{sel}}\{\sum_{k=1}^{n_{int}} W_k j(\eta_k)\delta\Phi_k^c.f_k^c\}, \qquad (4.49)$$

where $\delta\Phi^c = \begin{bmatrix} C_s^{(1)} \\ C_1^{(2)} \\ . \\ . \\ . \\ C_{mnode}^{(2)} \end{bmatrix}$, $f^c = t_N\mathbf{N}+ \underbrace{t_N^{coh}\mathbf{N}}_{t_{N_\alpha}^{coh}\mathbf{N}+t_{N_\beta}^{coh}\mathbf{N}} +t_{T_\alpha}^{coh}D_\alpha+t_{T_\beta}^{coh}D_\beta$ are the vector of nodal

variations(slave and master nodes) and the local contact force vector corresponding to local quadrature points .

Where $D_1,D_2(D_\alpha,D_\beta)$ and $\mathbf{N}$ have been defined in Appendix B.

The discretisation of the equation (4.45), the modified contact stiffness, can be written as the following expression

$$\triangle\delta W_{modifiedcontact}\left(\psi^h,\delta g^h\right) \approx \sum_{e=1}^{n_{sel}}\{\sum_{k=1}^{n_{int}} W_k j(\eta_k)[(\triangle t_N^h(\eta_k)\delta g^h(\eta_k)+t_N^h(\eta_k)\triangle\delta g^h(\eta_k))+$$

$$((\frac{\partial t_N^{coh^h}}{\partial g_N}(\eta_k).\triangle g_N^h(\eta_k)+\frac{\partial t_N^{coh^h}}{\partial g_T}(\eta_k).\triangle g_T^h(\eta_k))\delta g^h(\eta_k)+t_N^{coh^h}(\eta_k)\triangle\delta g^h(\eta_k))+$$

$$((\frac{\partial t_T^{coh^h}}{\partial g_N}(\eta_k).\triangle g_N^h(\eta_k)+\frac{\partial t_T^{coh^h}}{\partial g_T}(\eta_k).\triangle g_T^h(\eta_k))\delta\xi^{\alpha^h}(\eta_k)+t_{T_\alpha}^{coh^h}(\eta_k)\triangle\delta\xi^{\alpha^h}(\eta_k))]\} =$$

$$\sum_{e=1}^{n_{sel}}\{\sum_{k=1}^{n_{int}} W_k j(\eta_k)\delta\Phi_k^c.k_k^c\triangle\Phi_k^c\}, \qquad (4.50)$$

where $\triangle \Phi^c = \begin{bmatrix} \triangle d_s^{(1)} \\ \triangle d_1^{(2)} \\ . \\ . \\ \triangle d_{mnode}^{(2)} \end{bmatrix}$, $k^c = k_N^c + k_N^{coh^c} + t_{T_\alpha}^{coh} A^{\alpha\beta} k_{T_\beta}^{coh^c} + k_T^{coh^c}$ are the vector of local

nodal values and the global contact stiffness have been also defined in Appendix B.

4.2.5 Friction mechanics

The definition of the friction mechanics in this section [without taking into account the role of thermodynamics in the treatment of the (thermodynamically coupled) frictional problem (which is the subject of the next section)], is too close to the original works Laursen (2003) on which the development of the frictional modelling framework is based on the Coulomb friction law. The difference between the definition here and the original definition [Laursen (2003)], is the various definitions of the friction traction based on the modified version of contact (various definitions of the contact normal traction), where there are two cases of the problem which need to be dealt with, namely the contact normal traction definition due to the classical contact part of the modified contact and due to the cohesive fracture part of the modified contact.

The frictional contact integral defined between surfaces (master and slave) is given by

$$\delta W_{friction}\left(\psi^t, \delta g\right) = \int_{\Gamma_s} t_{T_\alpha} \delta \xi^\alpha d\Gamma, \tag{4.51}$$

where t_{T_α} is the frictional traction calculated based upon the following determination

$$t_{T_\alpha}^{n+1} = \begin{cases} T_{T_\alpha}^{n+1} = t_{T_\alpha}^n + \varepsilon_T m_{\alpha\beta}(\xi_{n+1}^\beta - \xi_n^\beta) & if \ \| T_T^{n+1} \| - \mu t_N^{n+1} \leq 0 \, (stick) \\ \mu t_N^{n+1} \frac{T_{T_\alpha}^{n+1}}{\|T_T^{n+1}\|} & otherwise \, (slip), \end{cases} \tag{4.52}$$

where ε_T the friction penalty value (is different from normal penalty value ε_N), $\| T_T^{n+1} \| = [t_{T_\alpha} m^{\alpha\beta} t_{T_\beta}]^{\frac{1}{2}}$, μ the friction coefficient, $m^{\alpha\beta}$ defined in previous section, $\delta \xi^\alpha$ the variation of the tangential gap function is given by the equation (4.43).

Note that, in this study, the frictional modelling framework, based on Coulomb friction law, relates the frictional traction to the single-valued tangential displacement defined by:

$g_T = \gamma t_T$ with $\begin{cases} \gamma = 0 & \| t_T \| < \mu t_N \\ \gamma \geq 0 & \| t_T \| = \mu t_N \end{cases}$, where using additionally the friction penalty value
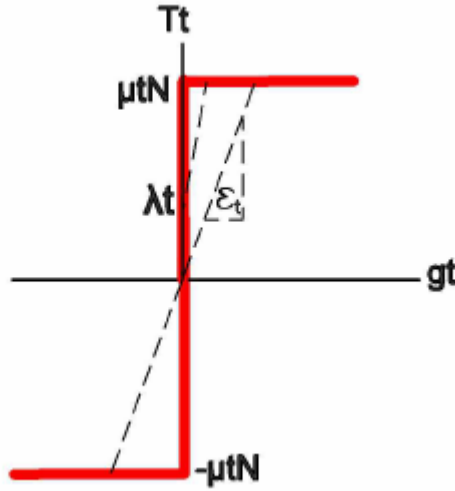
Figure 4.9: The unregularized and regularized Coulomb friction law

ε_T removes this effect but, as before, the perfect representation of the Coulomb friction law can be achieved only when $\varepsilon_T \to \infty$.

While this presentation is convenient for the classical frictional sliding contact formulation, in the case of the consideration of the cohesive force (combined classical and modified contact), to be able to use this method, we recall the discrete functions $\Gamma(\mu, \varepsilon_T, \varepsilon_n^{coh}, g_N)$ defined by the equation (4.9) and rewrite the equation (4.51) as the following

$$\delta W_{friction}\left(\psi^t, \delta g\right) = \int_{\Gamma_s} \Gamma(\mu, \varepsilon_T, \varepsilon_n^{coh}, g_N) t_{T_\alpha} \delta \xi^\alpha d\Gamma, \tag{4.53}$$

where, in the case of penetration ($g_N > 0$), the friction formulation is based on the classical frictional contact and otherwise ($g_N \leq 0$), computation of friction formulated under cohesive interaction. Note that the contact vector for tangential traction will be calculated only if both the friction coefficient and friction penalty factor are non-zero. Also note that the quantity t_N^{n+1} in equation (4.52) must be replaced with $\begin{cases} t_N^{n+1} & g_N > 0 \\ t_N^{n+1(coh)} & g_N \leq 0 \end{cases}$.

The linearisation of the equation (4.53) is given by the following equation

$$\triangle \delta W_{friction}\left(\psi^t, \delta g\right) = \Gamma(\mu, \varepsilon_T, \varepsilon_n^{coh}, g_N)\{\triangle \int_{\Gamma_s} t_{T_\alpha} \delta \xi^\alpha d\Gamma\} =$$

$$\Gamma(\mu, \varepsilon_T, \varepsilon_n^{coh}, g_N)\{\int_{\Gamma_s} [\triangle t_{T_\alpha} \delta \xi^\alpha + t_{T_\alpha} \triangle(\delta \xi^\alpha)]d\Gamma\}, \tag{4.54}$$

where

$$
\triangle t_{T_\alpha}^{n+1} =
\begin{cases}
\triangle T_{T_\alpha}^{n+1} = \varepsilon_T \{ m_{\alpha\beta} \triangle \xi^\beta + [(\varphi_t^{(2)}(\bar{Y}(X))_{,\alpha\gamma}.\tau_\beta + \varphi_t^{(2)}(\bar{Y}(X))_{,\beta\gamma}.\tau_\alpha) \triangle \xi^\gamma + \\
\quad \triangle \varphi_t^{(2)}(\bar{Y}(X))_{,\alpha}.\tau_\beta + \triangle \varphi_t^{(2)}(\bar{Y}(X))_{,\beta}.\tau_\alpha](\xi_{n+1}^\beta - \xi_n^\beta) \} \quad (stick) \\
\mu p_{T_\alpha} \begin{cases} \varepsilon_N H(g) \triangle g & g_N > 0 \\ \triangle t_N^{coh} & g_N \leq 0 \end{cases} + \mu \frac{\triangle T_{T_\beta}^{n+1}}{\|T_T^{n+1}\|}[\delta_\alpha^\beta - p_T^\beta p_{T_\alpha}] \begin{cases} t_N^{n+1} & g_N > 0 \\ t_N^{n+1(coh)} & g_N \leq 0 \end{cases} + \\
\mu p_T.[\triangle \varphi_t^{(2)}(\bar{Y}(X))_{,\beta} + \triangle \varphi_t^{(2)}(\bar{Y}(X))_{,\beta\gamma} \triangle \xi^\gamma] p_T^\beta p_{T_\alpha} \begin{cases} t_N^{n+1} & g_N > 0 \\ t_N^{n+1(coh)} & g_N \leq 0 \end{cases} \quad (slip),
\end{cases}
$$

$$(4.55)$$

where $p_{T_\alpha} = \frac{T_{T_\alpha}^{n+1}}{\|T_T^{n+1}\|}$ and $\delta_\alpha^\beta = \begin{cases} 0 & \alpha \neq \beta \\ 1 & \alpha = \beta \end{cases}$ stands for the Kronecker delta and where the quantities $\triangle \delta \xi^\alpha$ is given in Appendix A.

The discretisation of the equation (4.53) can be written as the following expression

$$
\delta W_{friction}\left(\psi^h, \delta g^h\right) \approx \Gamma(\mu, \varepsilon_T, \varepsilon_n^{coh}, g_N) \sum_{e=1}^{n_{sel}} \{ \sum_{k=1}^{n_{int}} W_k j(\eta_k) t_{T_\alpha}^h(\eta_k) \delta \xi^{\alpha h}(\eta_k) \},
$$

$$
= \Gamma(\mu, \varepsilon_T, \varepsilon_n^{coh}, g_N) \sum_{e=1}^{n_{sel}} \{ \sum_{k=1}^{n_{int}} W_k j(\eta_k) \delta \Phi_k^c.f_k^c \}, \tag{4.56}
$$

where $\delta \Phi^c = \begin{bmatrix} C_s^{(1)} \\ C_1^{(2)} \\ . \\ . \\ . \\ C_{mnode}^{(2)} \end{bmatrix}$, $f^c = t_{T_\alpha} D_\alpha + t_{T_\beta} D_\beta$ are the vector of nodal variations (slave and master nodes) and the local contact force vector corresponding to local quadrature points and D_α, D_β have been defined in Appendix B.

The discretisation of the equation (4.54) can be written as the following expression

$$
\triangle \delta W_{friction}\left(\psi^h, \delta g^h\right) \approx \Gamma(\mu, \varepsilon_T, \varepsilon_n^{coh}, g_N) \sum_{e=1}^{n_{sel}} \{ \sum_{k=1}^{n_{int}} W_k j(\eta_k)[\triangle t_{T_\alpha}^h(\eta_k) \delta \xi^{\alpha h}(\eta_k) +
$$

$$t_{T_\alpha}^h(\eta_k)\triangle\delta\xi^{\alpha^h}(\eta_k)]\} = \Gamma(\mu,\varepsilon_T,\varepsilon_n^{coh},g_N)\sum_{e=1}^{n_{sel}}\{\sum_{k=1}^{n_{int}} W_k j(\eta_k)\delta\Phi_k^c.k_k^c\triangle\Phi_k^c\}, \qquad (4.57)$$

where $\triangle\Phi^c = \begin{bmatrix} \triangle d_s^{(1)} \\ \triangle d_1^{(2)} \\ . \\ . \\ \triangle d_{mnode}^{(2)} \end{bmatrix}$, $k^c = k_{direct}^c + t_{T_\alpha}A^{\alpha\beta}k_{T_\beta}^c$ are the vector of local nodal values

and the global contact stiffness have been defined in Appendix B.

4.2.6 Thermodynamics of Contact Interfaces

In this section, focus is on the mathematical-mechanical formulation of the thermodynamics of the contact interfaces for the treatment of two body thermomechanical frictional contact problem (thermodynamically coupled frictional problem), and as mentioned in the previous section, here again the formulation is based on the original works by Laursen (2003) and the modified version of contact.

The formulation begins with the definitions: heat fluxes (assumed to be positive if the heat flow out of the contacting body into the interface region and zero in the case of the out of contact), the entropy evolution on the contact interfaces and the mechanical dissipation.

The constitutive relation of heat fluxes across the contact interfaces, based on FourierÕs law which relates the local heat flux to the temperature gradient, can be shown as:

$$\begin{cases} q_c^s = H_c^s\nabla\Theta^s & slave\,interface \\ q_c^m = H_c^m\nabla\Theta^m & master\,interface, \end{cases} \qquad (4.58)$$

where $\nabla\Theta^s,\nabla\Theta^m,H_c^s,H_c^m$ temperature gradients and heat transfer coefficients(slave and master interfaces).

The entropy evolution [supposed to be positive all the time due to the thermodynamically consistent formulation (of the problem)] is given by

$$\aleph_c = \frac{C_c(T_c - T_0)}{T_0}, \qquad (4.59)$$

where C_c, T_c, T_0 are the heat capacity per unit surface, interface characteristic temperature and reference temperature.

At this point, it is worth mentioning that the formulation of the heat fluxes across the

contact interfaces (q_c^s, q_c^m), depends on the normal pressure t_N, can be done by replacement of the quantities H_c^s, H_c^m with $t_N h_c^s, t_N h_c^m$ and the quantity $\nabla \Theta$ with $(T^{s|m} - T_c)$ in the equation (4.58), where $T^{s|m}[T^s, T^m]$ stands for the temperature of two bodies (which the master and slave interfaces belong to) at the contact activation stage (contact approach time).

Using the definition of the frictional traction and the time derivative of tangential relative displacement (tangential relative velocity), one obtains the following expression for the mechanical dissipation

$$
D_{mech} = | \overbrace{t_{T_\alpha}}^{frictional\,traction} \cdot \underbrace{\frac{\partial(\xi^\alpha)}{\partial t}}_{tangential\,relative\,velocity} | \approx | t_{T_\alpha} \cdot \frac{(\xi_{n+1}^\alpha - \xi_n^\alpha)}{\Delta t} |, \tag{4.60}
$$

where, in the case of non perfect sliding$(gap_N \neq 0)$, the tangential relative velocity term $\frac{\partial(\xi^\alpha)}{\partial t} = \dot{\xi}^\alpha$ in the equation (4.60) should be calculated as follows:

After taking the material time derivative of the equation (4.42) and some algebra we get

$$
A_{\alpha\beta} \frac{\partial(\xi^\alpha)}{\partial t} = \underbrace{[V_s(X) - V_m(\bar{Y}(X))]}_{relative\,material\,velocity} \cdot \tau_\alpha - gv.[\frac{\partial V_m(\bar{Y}(X))}{\partial \alpha}], \tag{4.61}
$$

where again $A_{\alpha\beta} = m_{\alpha\beta} + g_N \kappa_{\alpha\beta}$, $\kappa_{\alpha\beta} = v.\psi_m(\bar{Y}(X))_{,\alpha\beta}$ is the curvature of the surface at $\psi_m(\bar{Y}(X))$.

Also the thermal dissipation (due to the irreversible part of heat transfer development) can be expressed as

$$
D_{thermal} = \frac{q_c^s(T^s - T_c)}{T^s} + \frac{q_c^m(T^m - T_c)}{T^m} \tag{4.62}
$$

The relation between free energy function $\Psi(g_N, g_T^{elastic}, T_c)$ and the local energy balance defined on the contact interfaces, based on the contact tractions, gaps, entropy, interface characteristic temperature and the relative velocities, is given by

$$
\frac{d\Psi(g_N, g_T^{elastic}, T_c)}{dt} = \frac{de_{contact}^{stored\,energy}}{dt} - \frac{d\aleph_c}{dt}T_c - \frac{dT_c}{dt}\aleph_c \iff \underbrace{\frac{\partial\Psi}{\partial g_N}}_{t_N}\frac{dg_N}{dt} + \underbrace{\frac{\partial\Psi}{\partial g_T^{elastic}}}_{t_T}\frac{dg_T^{elastic}}{dt} +
$$

$$\underbrace{\frac{\partial \Psi}{\partial T_c}}_{-\aleph_c} \frac{dT_c}{dt} = t_N \frac{dg_N}{dt} + t_T \frac{dg_T^{elastic}}{dt} + t_T \frac{dg_T^{inelastic}}{dt} + q_c^s + q_c^m - \frac{d\aleph_c}{dt} T_c - \frac{dT_c}{dt} \aleph_c, \qquad (4.63)$$

where $g_T = g_T^{elastic} + g_T^{inelastic}$ are the elastic and inelastic parts of tangential gap. Note that, the free energy $\Psi(g_N, g_T^{elastic}, T_c)$ is not depend on the inelastic slip.

After some algebra, the equation (4.63) leads to the following equation

$$t_N \frac{dg_N}{dt} + t_T \frac{dg_T^{inelastic}}{dt} + q_c^s + q_c^m = \frac{d\aleph_c}{dt} T_c \qquad (4.64)$$

Combining the definition of the frictional stresses, the entropy evolution, the mechanical dissipation, the equation (4.64) and the local energy balance on the contact interfaces, the heat fluxes equation for the contact interfaces can be expressed as:

$$\begin{cases} q_c^s = t_N R(T^s - T^m) + (R1)D_{mech} + t_N[(R3)T^s - (R4)] \\ q_c^m = t_N R(T^s - T^m) + (R2)D_{mech} + t_N[(R5)T^m - (R6)], \end{cases} \qquad (4.65)$$

where

$$\begin{cases} R = \frac{h_c^s h_c^m}{F_1 + h_c^s + h_c^m} \, ; R1 = \frac{R}{h_c^m} \, ; R2 = \frac{R}{h_c^s} \, ; \\ R3 = F_1 R1 \, ; R4 = F_2 R1 \, ; R5 = F_1 R2 \, ; R6 = F_2 R2 \, ; \\ F_1 = \frac{C_c T_{c(s|m)}}{\Delta t T_0} \, ; F_2 = F_1 T_{c(s|m)} \\ t_N \text{ contact pressure} \\ h_c^s, h_c^m \text{ heat transfer coefficients} \end{cases} \qquad (4.66)$$

Using the above definitions and recalling the discrete functions $\Gamma(\mu, \varepsilon_T, \varepsilon_n^{coh}, g_N)$, the thermodynamic integral defined between master and slave surfaces is given by:

$$\delta W_{thermodynamic}\left(\psi_c^t, T^t, \delta T\right) = \Gamma(\mu, \varepsilon_T, \varepsilon_n^{coh}, g_N) \int_{\Gamma_s} \{q_c^{slave} \delta T^S + q_c^{master} \delta T^M\} d\Gamma =$$

$$\Gamma(\mu, \varepsilon_T, \varepsilon_n^{coh}, g_N) \int_{\Gamma_s} \{\underbrace{t_N R(T^s - T^m)(\delta T^S - \delta T^M)}_{conduction} - \underbrace{D_{mech}(R1\delta T^S + R2\delta T^M)}_{dissipation} +$$

$$\underbrace{t_N[(R3T^S + R4)\delta T^S - (R5T^M + R6)\delta T^M]}_{heat\,sinks}\}d\Gamma, \tag{4.67}$$

where $\delta T^S, \delta T^M$ are the (virtual) temperature variation of slave and master interfaces.

Note that, due to the contact inequality constraints, the Kuhn-Tucker conditions [equation (4.33)], in the case of the out of contact $t_N = 0$, the conduction, the heat sinks and the dissipation integral will tend to be zero, which will imply zero heat fluxes across the interfaces.

The linearisation of the equation (4.67) is given by the following equation

$$\triangle \delta W_{thermodynamic}\left(\psi_c^t, T^t, \delta T\right) = \Gamma(\mu, \varepsilon_T, \varepsilon_n^{coh}, g_N) \int_{\Gamma_s} \triangle\{q_c^{slave}\delta T^S + q_c^{master}\delta T^M\}d\Gamma =$$

$$\Gamma(\mu, \varepsilon_T, \varepsilon_n^{coh}, g_N) \int_{\Gamma_s} \{\triangle t_N R[(T^s - T^m)(\delta T^S - \delta T^M)] + t_N R[\triangle(T^s - T^m)(\delta T^S - \delta T^M)]+$$

$$t_N R[(T^s - T^m)\triangle(\delta T^S - \delta T^M)] - \triangle D_{mech}(R1\delta T^S + R2\delta T^M)-$$

$$D_{mech}\triangle(R1\delta T^S + R2\delta T^M) + \triangle t_N[(R3T^S + R4)\delta T^S - (R5T^M + R6)\delta T^M]+$$

$$t_N[\triangle(R3T^S + R4)\delta T^S - \triangle(R5T^M + R6)\delta T^M]\}d\Gamma_s, \tag{4.68}$$

where

$$\begin{cases}
\triangle t_N = \begin{cases} \varepsilon_N H(g)\triangle g & g_N > 0 \\ \triangle t_N^{coh} & g_N \le 0 \end{cases} \\
\triangle(T^s(X) - T^m(\bar{Y}(X))) = \triangle T^s(X) - \triangle T^m(\bar{Y}(X)) - T^m(\bar{Y}(X)),_\alpha \triangle \xi^\alpha \\
\triangle(\delta T^S(X) - \delta T^M(\bar{Y}(X))) = -\delta T^M(\bar{Y}(X)),_\alpha \triangle \xi^\alpha \\
\triangle D_{mech} = (\triangle t_{T_\alpha}\frac{\partial(\xi^\alpha)}{\partial t} + t_{T_\alpha}\triangle\frac{\partial(\xi^\alpha)}{\partial t})sign(t_{T_\alpha}.\frac{\partial(\xi^\alpha)}{\partial t}) \\
\triangle(R1\delta T^S + R2\delta T^M) = -R2\delta T^M(\bar{Y}(X)),_\alpha \triangle \xi^\alpha \\
\triangle(R3T^S + R4)\delta T^S - \triangle(R5T^M + R6)\delta T^M = \triangle R3T^S\delta T^S - R5[\triangle T^M\delta T^M+ \\
T^M(\bar{Y}(X)),_\alpha \triangle\xi^\alpha\delta T^M] - (R5T^M - R6)\delta T^M(\bar{Y}(X)),_\alpha \triangle\xi^\alpha
\end{cases} \tag{4.69}$$

The discretisation of the equation (4.67) can be written as the following expression

$$\delta W_{thermodynamic}\left(\psi_c^h, T^h, \delta T^h\right) \approx \Gamma(\mu, \varepsilon_T, \varepsilon_n^{coh}, g_N) \sum_{e=1}^{n_{sel}} \{\sum_{k=1}^{n_{int}} W_k j(\eta_k)[t_N(\eta_k)R(T^s(\eta_k)-$$

$$T^m(\eta_k))(\delta T^S(\eta_k) - \delta T^M(\eta_k)) - D_{mech}(\eta_k)(R1\delta T^S(\eta_k) + R2\delta T^M(\eta_k)) + t_N(\eta_k)((R3T^S(\eta_k)+$$

$$R4)\delta T^S(\eta_k) - (R5T^M(\eta_k) + R6)\delta T^M(\eta_k))]\} = \Gamma(\mu, \varepsilon_T, \varepsilon_n^{coh}, g_N) \sum_{e=1}^{n_{sel}} \{\sum_{k=1}^{n_{int}} W_k j(\eta_k)\delta\Phi_k^c . fther_k^c\},$$

$$(4.70)$$

where $\delta\Phi^{c^T} = [\; C_\varphi^{(1)} \quad C_T^{(1)} \quad --- \quad C_{\varphi 1}^{(2)} \quad C_{T1}^{(2)} \quad -- \quad C_{\varphi mnode}^{(2)} \quad C_{Tmnode}^{(2)} \;]$, $fther_k^c$ are the vector of nodal variations(slave and master nodes) and the thermal part of the local contact force vector corresponding to local quadrature point k.

Where also

$$T^h := T^{s|m^h}(\eta) = \sum_{i=1}^{n_{int}} N_i(\eta)T_i^{s|m}(t) \tag{4.71}$$

,

$$\delta T^h := \delta T^{s|m^h}(\eta) = \sum_{i=1}^{n_{int}} N_i(\eta)c_i^{s|m} \tag{4.72}$$

$$\psi^h := \psi^{s|m^h}(\eta) = \sum_{i=1}^{n_{int}} N_i(\eta)d_i^{s|m}(t), \; \delta\psi^h := \delta\psi^{s|m^h}(\eta) = \sum_{i=1}^{n_{int}} N_i(\eta)C_i^{s|m}, \tag{4.73}$$

where $T_i^{s|m}(t), d_i^{s|m}(t)$ are nodal values, $N_i(\eta)$ denotes a standard shape function and $c_i^{s|m}, C_i^{s|m}$ stand for the time independent nodal values of the associated variational fields.

The thermal part of the contact contribution to the residual can also be expressed as

$$fther^c = -\underbrace{Rt_N(\mathbf{a.c})\mathbf{a}}_{conduction} + \underbrace{D_{mech}\mathbf{b}}_{dissipation} + \underbrace{t_N[(R3(\mathbf{e.c}) - R4)\mathbf{e} - (R5(\mathbf{f.c}) - R6)\mathbf{f}]}_{heat sinks}, \tag{4.74}$$

where the temperature vectors $\mathbf{a}, \mathbf{b}, \mathbf{c}, \mathbf{e}, \mathbf{f}$ have been defined in Appendix B.

The discretisation of the equation (4.68) is given by

$$\triangle \delta W_{thermodynamic} \left(\psi_c^h, T^h, \delta T^h \right) \approx \Gamma(\mu, \varepsilon_T, \varepsilon_n^{coh}, g_N) \sum_{e=1}^{n_{sel}} \{ \sum_{k=1}^{n_{int}} W_k j(\eta_k) [\triangle t_N(\eta_k) R((T^s(\eta_k) -$$

$$T^m(\eta_k))(\delta T^S(\eta_k) - \delta T^M(\eta_k))) + t_N(\eta_k) R(\triangle(T^s(\eta_k) - T^m(\eta_k))(\delta T^S(\eta_k)$$

$$- \delta T^M(\eta_k))) + t_N(\eta_k) R((T^s(\eta_k) - T^m(\eta_k)) \triangle(\delta T^S(\eta_k) - \delta T^M(\eta_k))) -$$

$$\triangle D_{mech}(\eta_k)(R1 \delta T^S(\eta_k) + R2 \delta T^M(\eta_k)) - D_{mech}(\eta_k) \triangle(R1 \delta T^S(\eta_k) + R2 \delta T^M(\eta_k)) +$$

$$\triangle t_N(\eta_k)((R3 T^S(\eta_k) + R4) \delta T^S(\eta_k) - (R5 T^M(\eta_k) + R6) \delta T^M(\eta_k)) +$$

$$t_N(\eta_k)(\triangle(R3 T^S(\eta_k) + R4) \delta T^S(\eta_k) - \triangle(R5 T^M(\eta_k) + R6) \delta T^M(\eta_k))] \} =$$

$$\Gamma(\mu, \varepsilon_T, \varepsilon_n^{coh}, g_N) \sum_{e=1}^{n_{sel}} \{ \sum_{k=1}^{n_{int}} W_k j(\eta_k) \delta \Phi_k^c . kther_k^c \triangle \Phi_k^c \}, \tag{4.75}$$

where $\triangle \Phi^c = \begin{bmatrix} \triangle d_s^{(1)} \\ \triangle T_s^{(1)} \\ --- \\ \triangle d_1^{(2)} \\ \triangle T_1^{(2)} \\ . \\ . \\ \triangle d_{mnode}^{(2)} \\ \triangle T_{mnode}^{(2)} \end{bmatrix}$, $kther^c = k_{conduction}^c + k_{dissipation}^c + k_{heatsinks}^c + k_{direct}^c$ are the

vector of local nodal values and the global contact stiffness have been defined in Appendix B.

4.2.7 Assembly

Next, we create a standard frame base assembly using the previously defined equations and $\delta W_{int,ext}^{(e)}(u, N_i \delta u_i), \Delta_{N_j u_j}^{(e)} \delta W_{int,ext}(u, N_i \delta u_i)$ the discretised internal and external virtual work and the discretised linearised internal and external virtual work (linearised in the direction

$N_j u_j$-change in force at node i due to change in the current position of node j) over an individual element e given by

$$\delta W^{(e)}_{int,ext}(u, N_i \delta u_i) \;=\; [\underbrace{\int_{\Omega} \sum_k \sigma_k \nabla N_i d\Omega}_{T_i} - \underbrace{\int_{\Omega} b.N_i d\Omega - \int_{\partial\Omega_\sigma} \bar{t}.N_i d_{\partial\Omega_\sigma}}_{F_i}].\delta u_i \tag{4.76}$$

$$\Delta^{(e)}_{N_j u_j} \delta W_{int,ext}(u, N_i \delta u_i) \;=\;$$

$$\underbrace{\sum_k \int_{\Omega} [\nabla N_i \delta u_i : \nabla N_j u_j \sigma_k + \nabla N_i \delta u_i : C_k : \nabla N_j u_j] d\Omega}_{\delta u_i^T .(k_c^{ij}+k_\sigma^{ij})u_j}, \tag{4.77}$$

where
$$\begin{cases} x(t) = \sum_{i=1}^n N_i(\gamma_1, \gamma_2, \gamma_3)x_i(t) \\ N_i(\gamma_1, \gamma_2, \gamma_3 \mid \gamma_k, local\ coordinate\ system) \\ v = \frac{dx(t)}{dt} = \sum_{i=1}^n N_i(\gamma_1, \gamma_2, \gamma_3)\frac{dx_i(t)}{dt} = \sum_{i=1}^n N_i(\gamma_1, \gamma_2, \gamma_3)v_i \\ \delta v = \frac{d\delta x(t)}{dt} = \sum_{i=1}^n N_i(\gamma_1, \gamma_2, \gamma_3)\frac{d\delta x_i(t)}{dt} = \sum_{i=1}^n N_i(\gamma_1, \gamma_2, \gamma_3)\delta v_i \end{cases}$$
and

$$\begin{cases} u = \sum_{i=1}^n N_i(\gamma_1, \gamma_2, \gamma_3)u_i,\ \delta u = \sum_{i=1}^n N_i(\gamma_1, \gamma_2, \gamma_3)\delta u_i \\ \delta\iota = \frac{1}{2}[\nabla \sum_{i=1}^n N_i(\gamma_1, \gamma_2, \gamma_3)\delta u_i + \nabla \sum_{i=1}^n N_i(\gamma_1, \gamma_2, \gamma_3)\delta u_i] \\ F = \frac{dx}{dX} = \sum_{i=1}^n \frac{dN_i x_i}{dX} = \sum_{i=1}^n N_i(\gamma_1, \gamma_2, \gamma_3)\nabla x_i + \sum_{i=1}^n x_i \otimes \nabla N_i(\gamma_1, \gamma_2, \gamma_3) = \sum_{i=1}^n x_i \otimes \nabla N_i \\ X = \sum_{i=1}^n N_i(\gamma_1, \gamma_2, \gamma_3)X_i \qquad n, number\ of\ nodes, \end{cases} \tag{4.78}$$

which can also be written in terms of nodal equivalent forces $T_i, F_i \mid T_i - F_i- = R_i$:

$$\delta W^{(e)}_{int,ext}(u, N_i \delta u_i) \;=\; [T_i^{(e)} - F_i^{(e)} = R_i^{(e)}]\delta u_i \tag{4.79}$$

$$\Delta^{(e)}_{N_j u_j} \delta W_{int,ext}(u, N_i \delta u_i) \;=\; \delta u_i^T .(k_c^{ij(e)} + k_\sigma^{ij(e)})u_j \tag{4.80}$$

So, the assembled equation for individual element e can be expressed as [with $\delta u_i^T, u_j$ replaced with $\delta \Psi_i^T, \Delta \Psi_j$-with additional temperature degree of freedom] (Equilibrium state $\delta W_{Total} = 0$) :

$$0 = \delta \Psi_i^T . (k_c^{ij(e)} + k_\sigma^{ij(e)} + k_{ij(e)}^{thermodynamic} + k_{ij(e)}^{friction} + k_{\Upsilon[ij(e)]}^{modifiedcontact}) \Delta \Psi_j +$$

$$\delta \Psi_i^T . [T_i^{(e)} - F_i^{(e)} + .f_{thermodynamic}^i + f_{friction}^i + f_{\Upsilon(i)}^{modifiedcontact} = R_i^{(e)}], \qquad (4.81)$$

and the assembled process for all nodes

$$\sum_{i=1}^{\forall n | n, \, nodes} \sum_{j=1}^{\forall j | j, i \, connected} \sum_{e=1}^{\forall e | i, j \in e} \{ \delta \Psi_i^T . (k_c^{ij(e)} + k_\sigma^{ij(e)} + k_{ij(e)}^{thermodynamic} +$$

$$k_{ij(e)}^{friction} + k_{\Upsilon[ij(e)]}^{modifiedcontact}) \Delta \Psi_j = -\delta \Psi_i^T . [R_i^{(e)}] \}, \qquad (4.82)$$

or in simple notation

$$\delta \Psi^T . (k \quad | \quad k, \, the \, assembled \, stiffness \, matrix) \Delta \Psi = -\delta \Psi^T . (R), \qquad (4.83)$$

which can be solved with an iterative method such as Newton–Raphson method.

4.3   Convergence analysis

To provide the convergence analysis of the methods used to describe contact interactions, in other words, to prove whether or not the previously defined methods (used to describe modified contact mechanics), in general, facilitate the convergence of the described numerical methods and what might be the rate of convergence, the methods of the so-called mortar finite element analysis for contact mechanics Laursen (2003), variational inequality (based on monotonicity, convexity and subdifferential)[Mircea and Andaluzia (2009)] and hemivariational inequality (based on Clarke-subdifferential, locally Lipschitz function, convexity or/and nonconvexity)[Han *et al.* (2014)] have been used to develop the convergence analyse of unilateral contact problem, frictional contact problem and frictional-contact-cohesive problem where the idea of the $inf - sup$ conditions for the convergence analysis of the finite element method over conforming/nonconforming domain using L2 energy norm or broken energy norm has been taken into account.

Prior to the process of the development of the weak statement of the above mentioned problems of the two body (Ω^i, $i = 1, 2$) contact problem, it is necessary to define the weighting

space W^i and solution space U^i given by:

$$U_t^i = \left\{ u_t^i \in \underbrace{H^1(\Omega^i)}_{Square\,integrable\,(derivative)\,functions\,set} : \bar{\Omega}^i \to R^\kappa \mid u_t^i = \bar{u}_t^i \; in \; \partial\Omega_u^i \right\} \qquad (4.84)$$

$$W^i = \left\{ w^i \in \underbrace{H^1(\Omega^i)}_{Square\,integrable\,(derivative)\,functions\,set} : \bar{\Omega}^i \to R^\kappa \mid w^i = 0 \; in \; \partial\Omega_u^i \right\}, \qquad (4.85)$$

where $H^1(\Omega^i)$ [3] refers to Hilbert space, the set of square integrate derivative functions on Ω^i (set of all vector valued functions over Ω^i whose values and first derivatives are square integrable), $\partial\Omega_u^i$ the (prescribed) Dirichlet boundary condition, u_t^i time dependent unknown displacements, w^i time independent weighting functions, $\bar{\Omega}^i$ denotes the closure of the open set Ω^i.

Using the above definitions, the weak statement of momentum balance of each of the bodies in a general form can be shown as

$$P(u^i, w^i) := \underbrace{\int_{\Omega^i} [(\sigma(u_l^i) = C^l \varepsilon(u_l^i))] \varepsilon(w_l^i) d\Omega^i}_{a(u,w)} + \int_{\Omega^i} \rho^i w_l^i \frac{\partial^2 u_l^i}{\partial t^2} d\Omega^i -$$

$$\underbrace{\left(\int_{\Omega^i} w_l^i f_l d\Omega^i + \int_{\partial\Omega_\sigma^i} w_l^i t_l d\partial\Omega_\sigma^i + \int_{\partial\Omega_c^i} w_l^i t_l^c d\partial\Omega_c^i \right)}_{L(w)} = 0, \; \forall w^i \in W^i, \qquad (4.86)$$

where C^l stands for a symmetrical forth order tensor, $\sigma(u_l^i), \varepsilon(w_l^i), \rho^i$ are the stress, strain tensors and the density, f_l, t_l, t_l^c denote the body force, the traction for the points on the Neumann boundary $\partial\Omega_\sigma^i$ and the contact traction.

For the sake of simplicity, the domains of interest (Ω^i, $i = 1,2$) are considered as linear elastic domains where the inertial effects are not taken into account.

Detailed convergence analysis (Unilateral Contact problem, Frictional Contact problem and Frictional-Contact-Cohesive problem) are contained in Appendix A (part 2).

---

[3] $for \; k \in N_0 \quad H^k(\Omega) = \{v \in L^2(\Omega) ; \frac{\partial^{|\alpha|} v}{\partial x_1^{\alpha_1} \partial x_2^{\alpha_2} ... \partial x_n^{\alpha_n}} \in L^2(\Omega), |\alpha| \le k\} \; with \, \alpha = (\alpha_1, \alpha_2, ... \alpha_n), |\alpha| = \sum \alpha_i \in N_0$

4.4 Implementation

The numerical implementation of the explained theories has been performed in the open source code FEBio (Non-linear finite element solver for biomechanical applications)[4] by the modification of the existing contact algorithm in FEBio. Major changes in algorithms and definitions which affect the contact conditions and enforce new conditions based on mixed mode cohesive law, have been proceeded by re-implementing the previously existing implementation of Contact Forces and the Contact Stiffness (by redefinition of nodal contact traction and, consequently, the variation of contact traction). Additionally, for solving the problem of the frictional heating at the contact interface (thermodynamically coupled frictional contact), new algorithms have been added to the existing one (to the existing contact interface implementation).

Based on the Mixed Mode cohesive law [which is itself dependent on the normal-tangential gap functions, normal-tangential characteristic opening length, and the value of the maximum normal-tangential tractions (maximum value of traction before propagation of cracks)], the process of the redefinition and declaration of the contact tractions has been carried on the existing algorithms of the nodal contact traction.

Then, the implementation of the contact nodal stiffness followed the same rule as before for the nodal contact traction where the algorithm has been extended with an additional existing control function, heavy-side function ($HEAVYSIDE(x)((x) = 1\,if\,x \geqq 0\,and = 0\,else$).

To enforce the classical contact constraints [in the case of the physical requirement of impenetrability and compressive interaction between (two) bodies], the existing contact algorithms of the nodal contact traction which was originally defined based on the gap function, penalty value and the Lagrange multiplier, has also been added to the new algorithms where, due to the different value of gap function ($gab \leqq, >, = 0$), different contact algorithms have been performed [to enable the algorithm, in combination with the gap function, for independently switching between modified and classical contact, where in the case of $gab > 0$, the algorithms of the existing classical contact formulation (original FEBio implementation) has been performed and in the case of $gab \leqq 0$, the modified contact algorithms has been proceeded (the criteria detailed in Appendix D)].

Because

$lim_{gap_N(x_n,y_n) \to \infty,\ gap_T(x_n,y_n) \to \infty} T_n \to 0,\ T_t \to 0,$

but we could just calculate

$lim_{gap_N(x_n,y_n) \to tolerance,\ gap_T(x_n,y_n) \to tolerance} T_n \to 0,\ T_t \to 0,$

in words, for the reason that, the interface cohesive tractions are computed according to

---

[4]Finite elements for biomechanics, http://febio.org/

a exponential mixed mode law, dependent on the normal-tangential openings (gap functions), the upper and lower limit of the normal and tangential openings g_N, g_T, from the numerical point of view, must have been given prior to the analysis. Otherwise, the complete separation ($T_n, T_t = 0$) will not be achieved unless $g_N, g_T \to \infty$ which is practically impossible. Therefore, the implementation of the control algorithms must be considered.

Consequently, the control algorithms has been implemented in FEBio by using *Macauley bracket* $MBRACKET(x)((x) = x\,if\,x \geqq 0\,and = 0\,else$,

and calculating the value of the (normal and tangential)gap tolerance [the directional derivative of the traction functions in the direction of the normal-tangential gaps with respect to the initial gaps]. Additionally, the definition of the criteria for out-of-contact has been modified.

The developed hierarchy of the Unit Tests (the fragment test of the individual units of source code), in a special form (specification and test of the behaviour of the methods/functions for the different range of values where the detected program bugs could depend on the internal/external library), determined the stability of the algorithms.

The modified and classical contact algorithms expressed in pseudo code is given in Appendix D.

4.5   Computational Models

To demonstrate the applicability of the above described numerical frameworks, a series of computational models are generated and analysed using the (modified) finite element code FEBio. The computational experiments are organized under three following sections. The first section describes contact-cohesive problems that are related to Mode I crack – opening, the second section presents the related problems to Mode II crack – opening, and the third section demonstrates the study of the mechanism of (heating) temperature evaluation on the frictional contact interfaces. Importantly, the set of all tests given here are three dimensional calculations (employing hexahedral and quadrilateral elements).

4.5.1   Mode I opening

In order to represent potential application of the large deformation framework that has been developed in this study, the primary test was a tear test where in order to investigate the complete failure of the material that already contains a predefined fracture [two deformable bodies (width: 10 mm, height: 20 mm, depth: 10 mm, element type regular linear hexahedral, the parameters of the mesh nx = 20, ny = 10, nz = 10, x-ratio=1.1, y-ratio=1, z-ratio=1), Mooney–Rivlin solid as a Hyperelastic material model with bulk modulus $k = 0.48$
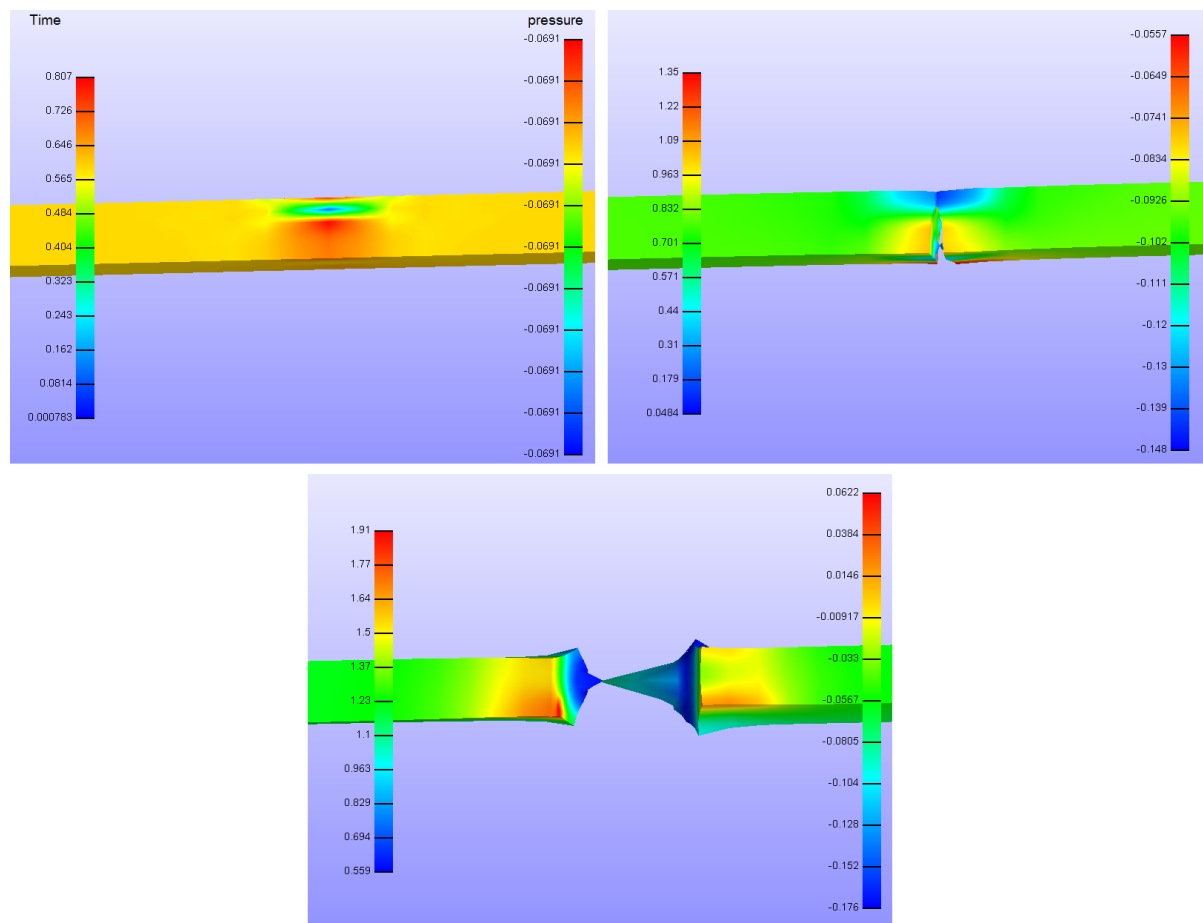
Figure 4.10: Very large deformation tear test using modified contact- Mooney–Rivlin solid as a Hyperelastic material model with bulk modulus $k = 0.48$ and $C_1, C_2 = 1$, interfacial normal/tangential strength 200 MPa

and $C_1, C_2 = 1$, interfacial normal/tangential strength 200 MPa, characteristic opening length $0.0001\,mm$, penalty 8000], equal and opposite forces are applied at both ends of the material, as shown in Figure (4.10), where the three dimensional tear test problem [shown in Figure (4.10) at three state of the system under analysis] combines the phenomena of nearly incompressible non-linear material models in the large deformation (Mooney–Rivlin Hyperelastic material) and contact-cohesive problem (modified contact). As can be seen, virtually the specimens go very large deformation before tearing which demonstrates applicability and efficiency of the proposed modified contact technique.

The secondary test intention was the double cantilever beam DCB test and double box test where the (force) traction versus the displacement (Coupled Mode I opening) has been measured (Figure 4.11). Table (4.2) shows the mechanical properties of the double cantilever beam and the two elastic boxes [Young modulus $E = 50GPa$, Poisson's ratio $v = 0.48$, Interfacial

normal strength $2.5(MPa)$].

As shown in Figure (4.11), an isotropic elastic DCB specimen (width: 20 mm, length: 125 mm, depth: 4 mm) with matching mesh elements (nodes: 3751, faces: 1400, elements: 3000), subjected to prescribe relative displacement in $z = 0.0025$ and $-z = 0.0025$ directions at both ends of the objects, fixed/zero displacement-rotation boundary condition (constraint all available degrees of freedom) and assigned with the modified contact (a prior placement of cohesive zone at known path), based on the static structural mechanic analysis method, has been implemented in a finite element scheme and the performance has been examined. As can be seen in Figure (4.11), the modified contacts are not applied to entire master and slave surfaces where just the intersect surfaces were active during analysis. The resulting force-displacement (Mode I opening) curves are shown in Figure (4.11) [based on random selected master or slave surface element nodes]. Figure (4.12) shows a class of irreversible cohesive exponential law where the ability of the method (used in this study) is demonstrated through the simulation of an isotropic elastic DCB specimen (same as the above: width: 20 mm, length: 125 mm, depth: 4 mm). The structure contains two types of loading and the corresponding loading, unloading and reloading paths, as shown in Figure (4.12).

The third isotropic elastic double cantilever beam Mode I opening test [width l=20 mm, length b=125 mm, depth h=4 mm, structural mechanics analysis (quasi-static)] was carried out, as shown in Figure (4.11), by attaching two rigid bodies to the free end of a cantilever beam (width L=20 mm, length b=3.3 mm, depth h=1 mm) where each rigid body was subjected to applied force F.

The following mathematical formulations based on beam theory are generally used to determine the relationships between the force F, the strain energy U, the crack opening length and the critical strain energy release rate Kundu (2008):

$$G_c \;=\; \frac{dU_t}{d_{\partial\Omega_\Gamma}} = \frac{Fd\delta c}{bd\delta n} = \frac{F^2 dC}{bd\delta n} = \frac{F^2}{b}\cdot\frac{dC}{d\delta n} =$$

$$\frac{F^2}{b}\cdot\frac{12\delta n^2}{Ebh^3} = \frac{12F^2\delta n^2}{Eb^2h^3} \Rightarrow \delta n = \sqrt{\frac{G_c E b^2 h^3}{12F^2}}, \tag{4.87}$$

where $\delta c, \delta n$ are the crack opening length at the free end and the crack length, $G_c = \frac{dU_t}{d_{\partial\Omega_\Gamma}}\big|_{F=F_{critical}}$ is the critical strain energy release rate, the coefficient C, the compliance, defined by $FC = \delta c \Rightarrow C = \frac{\partial(\delta c)}{\partial F}$, and $d_{\partial\Omega_\Gamma} = b\delta n$ is the crack area/surface. Note that the function of
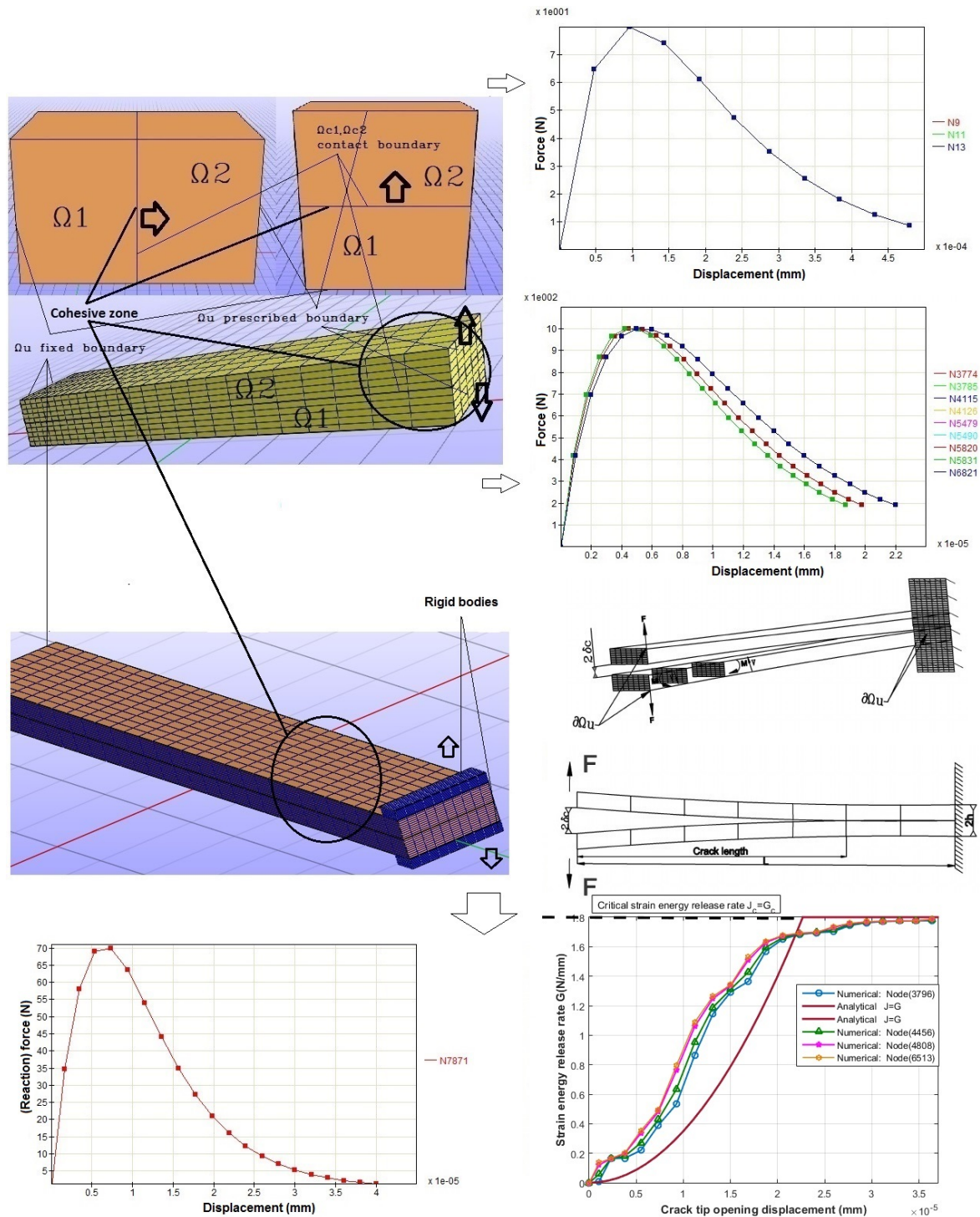
Figure 4.11: Coupled Mode I opening: Force (*N*) versus displacement (*mm*) [based on random selected master or slave surface element nodes and rigid body nodes] and strain energy release rate *G*(*N*/*mm*) versus crack tip opening displacement (*mm*)
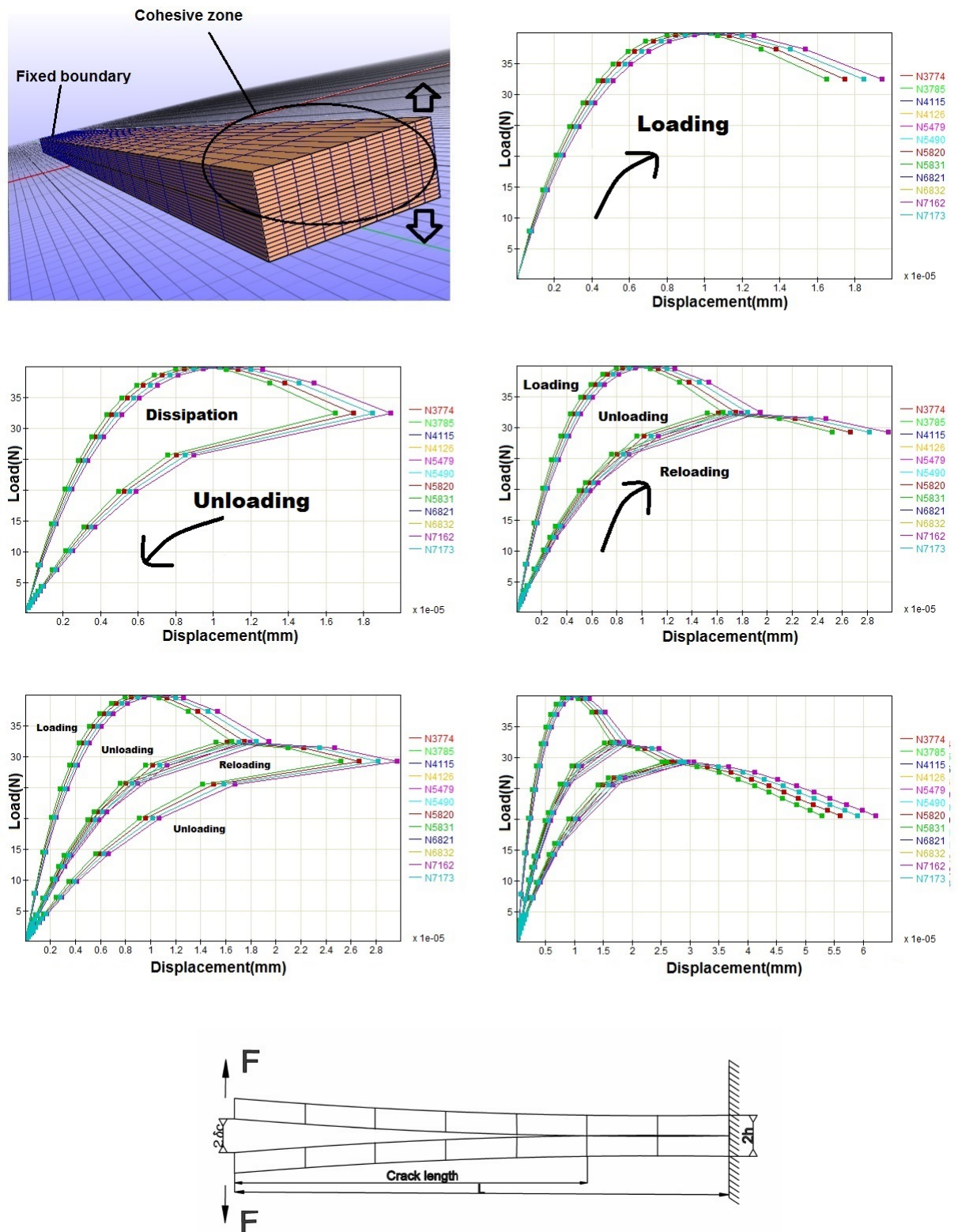
Figure 4.12: Corresponding loading, unloading and reloading paths through the simulation of an isotropic elastic DCB specimen

the deflection at any point of the beam's x axis is given by

$$y = \frac{Fx^2}{6EI}(3L - x) \; so \; I = \int_b \int_h y^2 dA[dydz] = \frac{1}{12}bh^3, \qquad (4.88)$$

and consequently, for a fully developed crack length $x = \delta n$, we will have

$$\delta c = \frac{F\delta n^3}{3EI} = \frac{4F\delta n^3}{Ebh^3} \Rightarrow \frac{dC}{d\delta n} = \frac{12\delta n^2}{Ebh^3}, \qquad (4.89)$$

On the other hand, Kundu (2008), using the concept of $J-$integral (an integral expression that was originally proposed by Rice (1968) which can be used to compute strain energy release rate - another way of calculating the potential energy release rate), introduced the following relationships between the critical strain energy release rate $G_c = J_c$, (critical) $J-$integral and the crack tip opening displacement δc [for the fixed force or fixed grip loading]

$$\begin{cases} J = G = K(\delta c)^2 & [J_c = G_c] & in \, linear \, range \, of \, load \, displacement \, curve \\ J = G = K(\delta c), & & in \, nonlinear \, range \, of \, load \, displacement \, curve \end{cases} \qquad (4.90)$$

where K is a proportionality constant related to the fracture toughness, the Poisson's ratio, the Young's modulus of the material, cohesive length and thickness of the DCB specimen. Note that, relating the $J-$integral to the strain energy release rate G in general is true, under quasi-static conditions, and for linear elastic materials. The resulting (reaction) force-displacement (Mode I opening) and the critical strain energy release rate $J_c = G_c$ versus crack tip opening displacement curves are shown in Figure (4.11) [based on random selected rigid body element nodes and master or slave surface element nodes].

The next test was carried out on a double elastic box, where two isotropic elastic boxes (width: 10 mm, height: 10 mm, depth: 10 mm), as shown in Figure (4.11), subjected to the prescribed displacement, the fixed displacement and the modified contact, were analysed. The force-displacement curve is shown in Figure (4.11) which is again based on random selected master or slave surface element nodes.

To investigate more tests, a computational model of a three-point bend specimen (L=100 mm, B=10 mm, W=20 mm), assigned with the modified contact and subjected to prescribe displacement $-z = 0.00155$ directions and an initial cracks a (9 mm), as shown in Figure (4.13), was analysed. The diagram of the specimen with all its dimensions is shown in Figure (4.13) and the Table (4.2) shows the mechanical properties of the three-point bend specimen.

To calculate analytically the stress intensity factor K_F at failure of the specimen (plane strain failure), the following mathematical formulation, presented by Kundu (2008), was used,
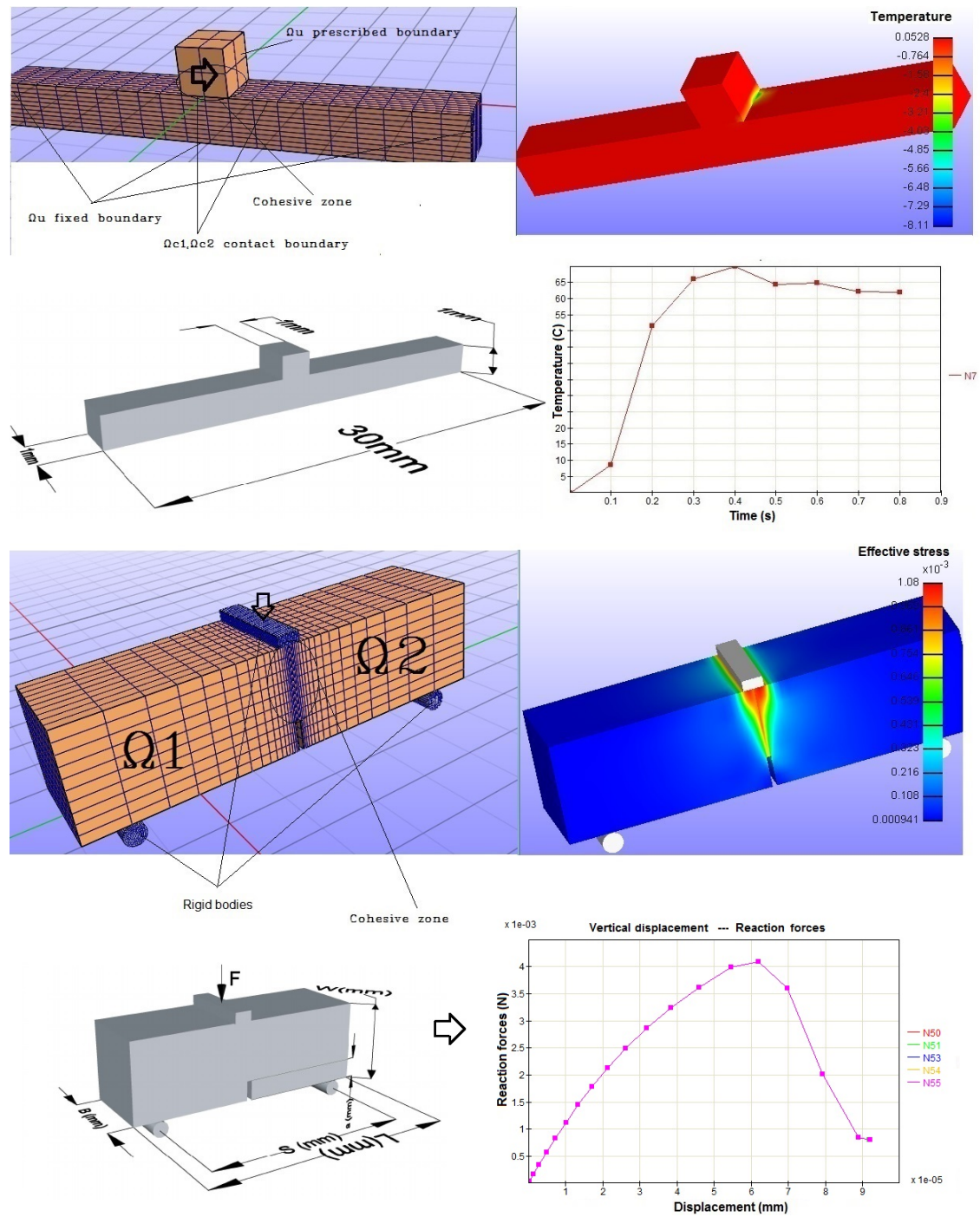
Figure 4.13: Notched beam with initial cracks and a prior cracks path (determination and analysis of coupled mode I crack near cracktip). Contact interface temperature evalution (a sliding elastic block over a longer fixed block)

Type of material	Isotropic elastic	Element types	$HEX8$
Density	$1\frac{kg}{m^3}$	Time steps	$10-100$
Young modulus	$E=(50-90)GPa$	Step size	0.1
Poisson's ratio	$v=0.48$	Max step	$1-10$
Interfacial normal/tangential strength	$(2-2.5)MPa$	Min step	0.1
Critical strain energy release rate(G_c)	$(28.3-50)N/mm$	Max refs	1500
Optimal iterations	40	Max retries	25
Nonlinear solution method	$Full-Newton$	Disp. tolerance	0.0001
Auto timestep-controller	$checked$	Energy tolerance	0.001
Characteristic opening length	$0.001\,mm$	Gap tolerance	0

Table 4.2: Mechanical properties of the DCB and the boxes (coupled Mode I opening) and the test conditions

where the conditions $\frac{W}{4} \leq B \leq \frac{W}{2}$ and $0.45W \leq a \leq 0.55W$, $a,B \geq 2.5\pi R$,(R is the plastic zone size), were taken into account.

$$K_F = \frac{F_F S}{BW^{\frac{3}{2}}} f(\frac{a}{W}), \tag{4.91}$$

where F_F is the failure load (obtained by numerical or experimental procedure), $S \approx 4W$ and

$$f(\frac{a}{W}) = 2.9(\frac{a}{W})^{\frac{1}{2}} - 4.6(\frac{a}{W})^{\frac{3}{2}} + 21.8(\frac{a}{W})^{\frac{5}{2}} - 37.6(\frac{a}{W})^{\frac{7}{2}} + 38.7(\frac{a}{W})^{\frac{9}{2}}, \tag{4.92}$$

which only covers the interval $0.45 \leq \frac{a}{W} \leq 0.55$ [and consequently $2.28 \leq f(\frac{a}{W}) \leq 3.15$]. Alternatively, for the function $f(\frac{a}{W})$ we have the following expression

$$f(\frac{a}{W}) = \frac{3\sqrt{\frac{a}{W}}[1.99 - (\frac{a}{W})(1-\frac{a}{W})(2.15 - 3.93\frac{a}{W} + 2.7\frac{a^2}{W^2})]}{2(1+2\frac{a}{W})(1-\frac{a}{W})^{\frac{3}{2}}}, \tag{4.93}$$

which covers entire range of $\frac{a}{W}$.

Furthermore, using the following mathematical relation [Hellan (1984)]

$$G = \frac{dU}{dA} = \alpha\frac{K_I^2}{E} + \alpha\frac{K_{II}^2}{E} + (1+v)\frac{K_{III}^2}{E}, \tag{4.94}$$

where

$$\alpha = \begin{cases} 1 & for\,plane\,stress,\ \sigma_{33}=0 \quad E,Young's\,modulus \\ 1-v^2 & for\,plane\,strain,\ \varepsilon_{33}=0 \quad v,Poisson's\,ratio \end{cases} \tag{4.95}$$

Type of material	Isotropic elastic	Element types	$HEX8$
Density	$1\frac{kg}{m^3}$	Time steps	$10-100$
Young modulus	$E=50GPa$	Step size	0.1
Poisson's ratio	$v=0.48$	Max step	$1-10$
Interfacial normal/tangential strength	$(2-1.5)MPa$	Min step	0.1
Critical strain energy release rate(G_c)	$(28.3-40)N/mm$	Max refs	3500
Optimal iterations	40	Max retries	50
Nonlinear solution method	$Full-Newton$	Disp. tolerance	0.00001
Auto timestep-controller	$checked$	Energy tolerance	0.0001
Characteristic opening length	$0.001\,mm$	Gap tolerance	0

Table 4.3: Mechanical properties of the DCB and the boxes (coupled Mode II, III openings) and the test conditions

[which relates the strain energy release rate G to the stress intensity factor K_I (where for pure normal opening $K_{II}=K_{III}=0$)], the strain energy release rate G of the specimen was computed.[5]

The resulting (reaction) force-displacement curve of the numerical analysis of the three-point bend specimen is plotted in Figure (4.13).

4.5.2   Mode II opening

The secondary test has been done with the same isotropic elastic DCB and the double box models (Young modulus $E=50GPa$,Poisson's ratio $v=0.48$ and same geometry as the previous problems) to investigate and friction-less analysis of the coupled mode (II, III), where the models were subjected to the prescribe displacement in different directions, fixed displacement-rotation boundaries, Interfacial tangential strength $(2-2.5)MPa$, and the modified contact, as shown in Figure (4.14). The resulting (force) tangential traction- total displacement (Mode II,III openings) curves are shown in Figure (4.14) [based on randomly selected master or slave surface element nodes]. All results are based on frictionless tests with different mesh scenarios (confirming and non conforming mesh).

---

[5]The stress intensity factor K_F at failure and the strain energy release rate G of the three-point bend specimen in Figure (4.12):

$\frac{a}{W}=0.45, f(\frac{a}{W})=2.28, E=90000(N/m^2), v=0.48, Interfacial\,normal/tangential\,strength=1900(N/m^2)$

$K_F=\frac{F_F S}{BW^{\frac{3}{2}}}f(\frac{a}{W})=\frac{0.075*4*2}{1*2^{\frac{3}{2}}}*2.28=0.484(N/mm^{\frac{3}{2}})$

$G=\frac{1-v^2}{E}K_F^2=\frac{1-0.48^2}{9*10^{-2}}*(0.484)^2=2.003(N/mm)$
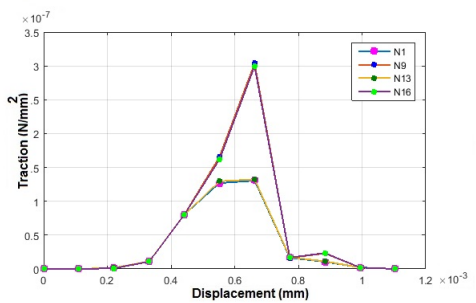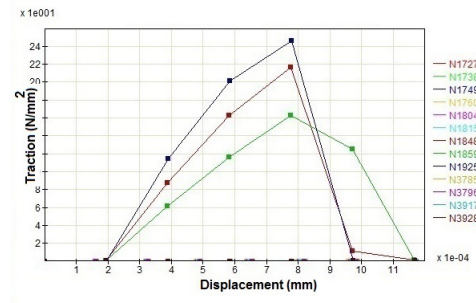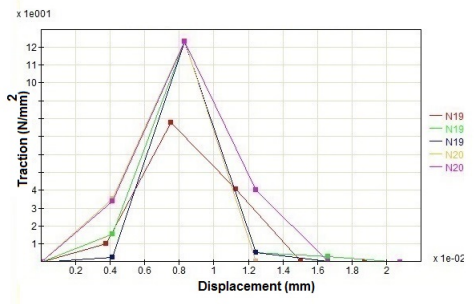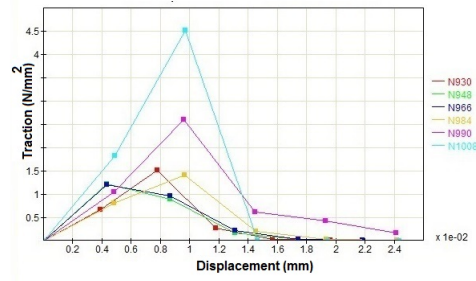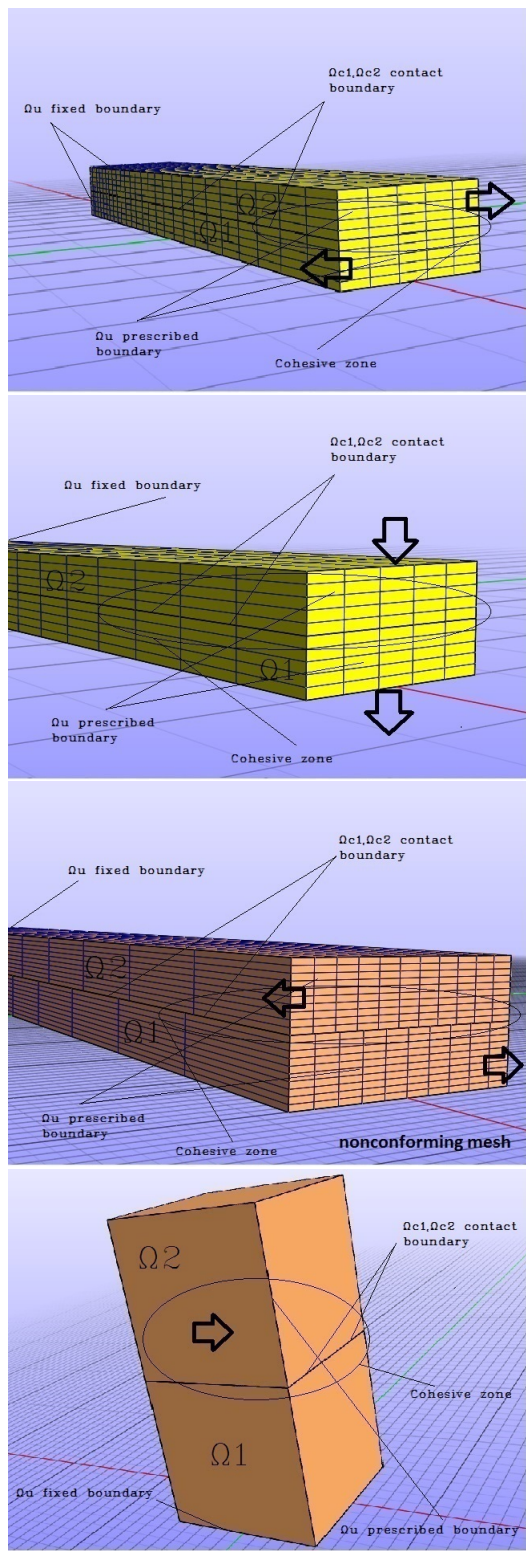
Figure 4.14: Analysis of coupled mode II, III [traction(N/mm^2) versus displacement (mm)]

type of materials	Young modulus	Poisson's ratio	Interfacial normal/tangential strength		
isotropic elastic	$E = 5.10^6 MPa$	$v = 0.48$	$1.2 MPa$		
Fric. coefficient	Fric. penalty	Ini. temp.	Heat capacity	Heat transfer coefficients	
$\mu = 0.1$	$\varepsilon_f = 0.1$	$T_0 = 0^o C$	$C_c = 100 m^2/s^2 K$	$h_c^s = h_c^m = 1.0 W N^{-1} K^{-1}$	
Density	Time steps	Step size	Disp. tolerance	Energy tolerance	
$1\frac{kg}{m^3}$	10	0.1	0.001	0.01	

Table 4.4: The test parameters for the frictional dissipation problem

4.5.3 Frictional heating

To study the mechanism of (heating) temperature evaluation on the (frictional) contact interfaces (with cohesive forces), an elastic model (width: 10 mm, length: 10 mm, depth: 10 mm) which slides over a longer fixed block (width: 10 mm, length: 100 mm, depth: 10 mm), where the system and its finite element discretisation are shown in Figure (4.13), has been modelled and analysed. The initial temperatures were the same at all nodes ($0^o C$) and the upper body was subjected to the prescribed displacement in x direction. The boundaries, all except the contact boundary, were thermally insulated and all the frictional work was supposed to be dissipated as heat. The parameters used for this test are given in Table (4.4) $[E = 5.10^6 MPa, ,v = 0.48 ,\mu = 0.1 ,\varepsilon_f = 0.1 ,C_c = 100 m^2/s^2 K ,h_c^s = h_c^m = 1.0 W N^{-1} K^{-1}]$. The plotted result, given in Figure (4.13), shows the temperature evaluation/map versus time [based on random selected node on contact surfaces].

Note that the test analysis was based on the (quasi) static analysis method, where for a dynamic analysis case, additionally, complex problems involving large (plastic) deformation, coupled thermo-elasto-plastic response in bulk media, etc. can also be considered.

Aside from carefully chosen parameters (contact boundary parameters, the mesh density, the material type, etc.), it has been highlighted that the solution can quickly diverge (if the friction has been taken into account) and it could jump to an unexpected equilibrium point.

At this point it is worth adding that the tests of convergence have proceeded under consideration of both the available non-linear iterative solution methods implemented in FEBio package, which are the Full Newton method and the Broyden–Fletcher–Goldfarb–Shanno (BFGS) method (the run-time and convergence are slightly different from Newton's method). The results of the examination of the structural mechanic problems under consideration the modified contact algorithms, show the difficulty of obtaining a converged FE solution when using the BFGS method (which depends totally on the parameters such as maximum BFGS updates, etc.) and also in some cases Newton's method will not converge at all unless we choose, for example, a high value for the maximum matrix reformations.

4.6   Verification test (analytical)

In order to study in detail and understand the different types of contact interaction that have been previously defined and which enable one to understand the behaviour of the complex system under different contact configurations, in the following sections we provide certain mathematical-computational formulations on each of the two different parts of the modified contact configurations, namely the classical contact part and the cohesive fracture part. Additionally, frictional and thermodynamically coupled frictional contact problems will be taken into account.

To make it possible, the first step in the analysis will be finding an analytical solution to the compressive contact interaction problem, where using Hertzian Contact Theory will allow us to be able to obtain an analytical solution for the classical contact part of the modified contact, and then make a comparison between numerical and analytical solution models. Then, the centre of interest will be the analytical predictions of the contact with cohesive force formulation, by choosing a convenient method for the analytical expression of the interfacial stress distribution, where, due to the complex non-linear formulation of the interfacial normal and tangential stiffness, for reasons of simplicity the formulation will be based on the infinitesimal change in the opening direction, which will allow us to have a linear relationship between (normal, tangential) stress and the opening. Then, after finding a general solution to the problem using integral theorem, we will find a general formula, which will be used later to make a comparison between the numerical and analytical solution methods.

4.6.1   Elastic contact between a sphere and a half space

The original aspect of this test was the systematic analytical study of the elastic contact between a rigid sphere and a half space based on the long-established technical approaches.

Given a rigid sphere with radius $R = 20mm$ (width: 20 mm, height: 20 mm, depth: 20 mm, element type hexahedral, properties parts=1, faces=4, edges=6, nodes=4), applied force F (Prescribed Rigid constraint=-0.01), deformable body [an elastic half space, width: 100 mm, height: 100 mm, depth: 10 mm, element type hexahedral, properties parts=1, faces=6, edges=12, nodes=8], subjected to fixed boundary condition, determine the relation between applied force F and the displacement of the contact surface area points (especially the displacement at the centre and the boundary of the circular contact area).

The modelling of the previously mentioned problem is shown in Figures (4.15) and (4.16).

[The displacement equations (at any point in the solid) under the influence of the force F acting on the surface of the half-space and the stress equations (where the normal stress component in the z-direction σ_{zz} of the stress tensor σ is of the 'real' interests in the analytical
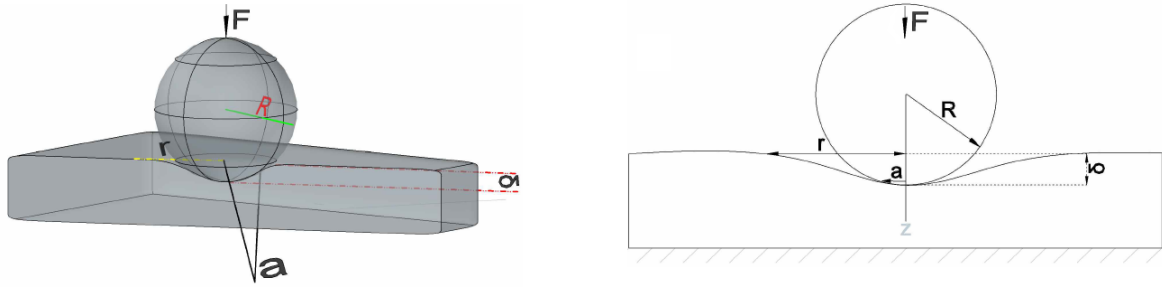
Figure 4.15: Contact between a sphere and a half space

Type of material (elastic half space)	Isotropic elastic	Element types	$HEX8$
Density (rigid body and elastic half space)	$1\frac{kg}{m^3}$	Time steps	10
Young modulus	$E = 4000\,Pa$	Step size	0.1
Poisson's ratio	$v = 0.35$	Max step	1
Radius(rigid sphere)	$20mm$	Min step	0.1
Augmented lagrangian	*checked*	Max refs	1500
Optimal iterations	25	Max retries	15
Nonlinear solution method	$Full-Newton$	Disp. tolerance	0.001
Auto timestep-controller	*checked*	Energy tolerance	0.01
Penalty	100	Gap tolerance	0

Table 4.5: Mechanical properties of the rigid body and elastic half space and the test conditions

solution), have been described in Appendix C part(1)]

Due to Hertzian Contact Theory we have

$$p(r) = p_0\left(1-\frac{r^2}{a^2}\right)^{\frac{1}{2}} \quad (a)\,as\,significant\,dimension\,of\,the\,contact\,area \qquad (4.96)$$

So, for all points along z-axis (in the case of coincidences of the principal axes with co-ordinate axes), the σ_{zz} can be expressed as

$$\sigma_{zz} = -p_0\left(1+\frac{z^2}{a^2}\right)^{-1} \quad and \quad \bar{\sigma}_{zz} = -p(r) = -p_0\left(1-\frac{r^2}{a^2}\right)^{\frac{1}{2}}$$

and $\sigma_{xx} = \sigma_{yy} = -p_0[(1+v)\left(1-\frac{z}{a}arctan(\frac{a}{z})\right) - \frac{1}{2}\left(1+\frac{z^2}{a^2}\right)^{-1}]$

Also, the relation between force F, distributed pressure p (exerted on a circle shaped area due to applied force F), and the maximum pressure p_0(pressure in the middle of circular contact surface), can be expressed as
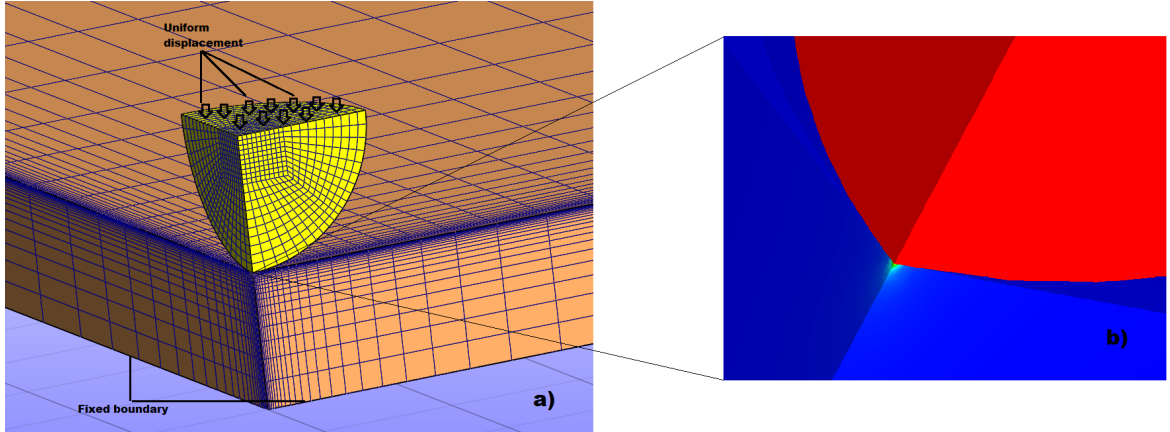
Figure 4.16: a) The (Geometrical/Computational) Finite Element (FE) Preprossessing model, b) the Finite Element Postprossessing model

$$F = \int_0^a p(r)2\pi r dr = \int_0^a p_0 \left(1 - \frac{r^2}{a^2}\right)^{\frac{1}{2}} 2\pi r dr = \pi p_0 [\frac{-\left(1-\frac{r^2}{a^2}\right)^{\frac{3}{2}}}{\frac{3}{2}(\frac{1}{a^2})}|_0^a] = \frac{2}{3}a^2\pi p_0 \quad (I)$$

So, the resulting vertical displacement (the displacement of the points of the contact surface area) is given by[6]

$$\delta - \frac{r^2}{2R} = u_z = \frac{\pi p_0}{4E^*a}(2a^2 - r^2) = \frac{\pi a p_0}{2E^*} - \frac{r^2}{\frac{4E^*a}{\pi p_0}} \quad , \quad \frac{1}{E^*} = \frac{1-v_1^2}{E_1} + \frac{1-v_2^2}{E_2} \quad (II)$$

$$(\delta = \frac{\pi a p_0}{2E^*} \Rightarrow p_0 = \frac{2E^*\delta}{\pi a} , 2R = \frac{4E^*a}{\pi p_0} \Rightarrow a = \frac{\pi p_0 R}{2E^*}) \Longrightarrow \frac{a}{\delta} = \frac{R}{a} \quad , p_0 = \frac{2E^*}{\pi}\sqrt{\frac{\delta}{R}},$$

where E_1, E_2, v_1, v_2 are known Young modulus and Poisson ratios.

Furthermore, the force F, in terms of δ, R, E^*, is given by

---

[6]In the case of distributed pressure $p(x,y)$, the displacement is given: $u_z = \frac{1}{\pi E^*}\int\int p(x,y)\frac{dxdy}{r}$ with $r = \sqrt{(X-x)^2 + (Y-y)^2}$

also

$u_z = \delta - (\frac{r^2}{2R_1} + \frac{r^2}{2R_2})$ with R_1, R_2 principal radii of the curvature of the surface at the origin

$u_z = \frac{p_0}{2E^*a}\int_0^{\frac{\pi}{2}}(a^2 - r^2\sin^2\alpha)d\alpha = \frac{p_0}{2E^*a}\cdot\frac{\pi(2a^2-r^2)}{2}$

$\frac{1}{E^*} = \frac{1}{E_1} + \frac{1}{E_2}$ with $E_1 | E_2 = \frac{E_1|E_2}{1-v_1^2|v_2^2}$ (plane strain modulus)

$$F = \frac{2}{3}a^2\pi p_0 = \frac{2}{3}R\delta\pi\frac{2E^*}{\pi}\sqrt{\frac{\delta}{R}} = \frac{4}{3}E^*\delta^{\frac{3}{2}}R^{\frac{1}{2}} \tag{4.97}$$

Sometimes it is convenient to re-express the a, δ, p_0 in other forms, namely

$$a = \frac{\pi p_0 R}{2E^*} \overset{p_0 = \frac{3}{2a^2\pi}F}{\Longrightarrow} (a = \frac{\pi(\frac{3}{2a^2\pi}F)R}{2E^*} = \frac{3FR}{4a^2E^*}) \Longrightarrow a = \left(\frac{3FR}{4E^*}\right)^{\frac{1}{3}} \tag{4.98}$$

$$\delta = \frac{a^2}{R} \overset{a=\left(\frac{3FR}{4E^*}\right)^{\frac{1}{3}}}{\Longrightarrow} \delta = \left(\frac{9F^2}{16RE^{*2}}\right)^{\frac{1}{3}} \tag{4.99}$$

$$p_0 = \frac{3}{2a^2\pi}F \overset{a=\left(\frac{3FR}{4E^*}\right)^{\frac{1}{3}}}{\Longrightarrow} p_0 = \left(\frac{6FE^{*2}}{\pi^3 R^2}\right)^{\frac{1}{3}} \tag{4.100}$$

To carry out the analysis of the theory explained above, by using the finite element method, based on only one quarter of the rigid sphere axial section, a computational model as shown in Figure (4.16) has been created and analysed (only one quarter due to stress intensity factors which could lead to numerical instability). Mechanical properties of the rigid body and elastic half space and the test conditions (the parameters used for this test) are given in Table (4.5).

The plotted numerical results, analytical versus numerical, as shown in Figure (4.17), are based on applied force as a function of the displacement of the point (the node) placed in the centre of the contact area and the stress distribution along the z-axis as a function of r.

The difficulty by the FEM analysis was first, the determination of the radius r, because there is no formula, based on a given parameter, which could be used to determine the value of r at any analysis step. Another difficulty was the fact that, unlike the analytical method, the contact area in finite element analysis cannot be presumed to have a circular area with radius a. Also, due to the occurrence of extreme local stresses, instead of applying concentrated load on the top point of the sphere, uniformly and linearly increasing prescribed axial displacement has been applied.
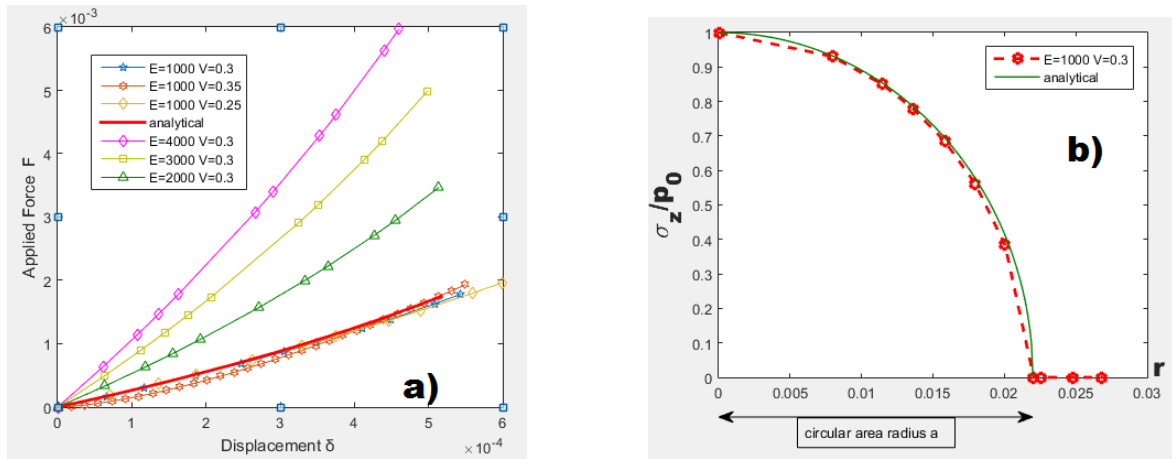
Figure 4.17: a) The applied force $F(N)$ versus the displacement $\delta(mm)$[analytical: $E = 1000Pa$, $v = 0.25$], b) Stress distribution along the axis of symmetry$\sigma_z(Pa)$ at the contact area versus circular area radius $a(mm)$ (due to Hertz pressure)[analytical: $E = 1000Pa$, $v = 0.3$]

4.6.2 Frictional Contact-Cohesive problem between linear elastic bodies (Two Boxes)

In this section, to verify the numerical finite element cohesive fracture model using modified contact against an analytical cohesive model based on similar assumptions, using the analytical and applicable idea to cohesive modelling, established through the work of Lorenzis and Zavarise (2009).

The major difference between this study and Lorenzis and Zavarise (2009) is that the mode-I and mode-II cohesive laws used in Lorenzis and Zavarise (2009) are based on mixed mode bilinear cohesive law for analytical analyses of the interfacial stresses (distributions of the normal and shear tractions) where in opposite current study uses the mixed mode exponential cohesive law (implemented in modified contact) and provides second order differential equations for the stress distribution of interfacial normal and tangential stresses.

The analytical elastic contact (with cohesive force) problem combined with coulomb friction problem, defined at the interface between two (dis)similar elastic solids, and formulated for two different classes of problems, namely mode I and mode II fracture, are developed as follows.

Given two elastic bodies Ω_1, Ω_2 (width: 10 mm, height: 10 mm, depth: 10 mm, hexahedral elements, the parameters of the mesh nx = 1, ny = 1, nz = 1), as shown in Figure (4.18), pre-defined sliding contact interface between them where the Coulomb friction with constant friction coefficient $\mu_f = 0.3$ acts at their interface, subjected to the boundaries $\partial\Omega_c, \partial\Omega_u$ [discontinuity and Dirichlet boundary conditions (applying different constraint to
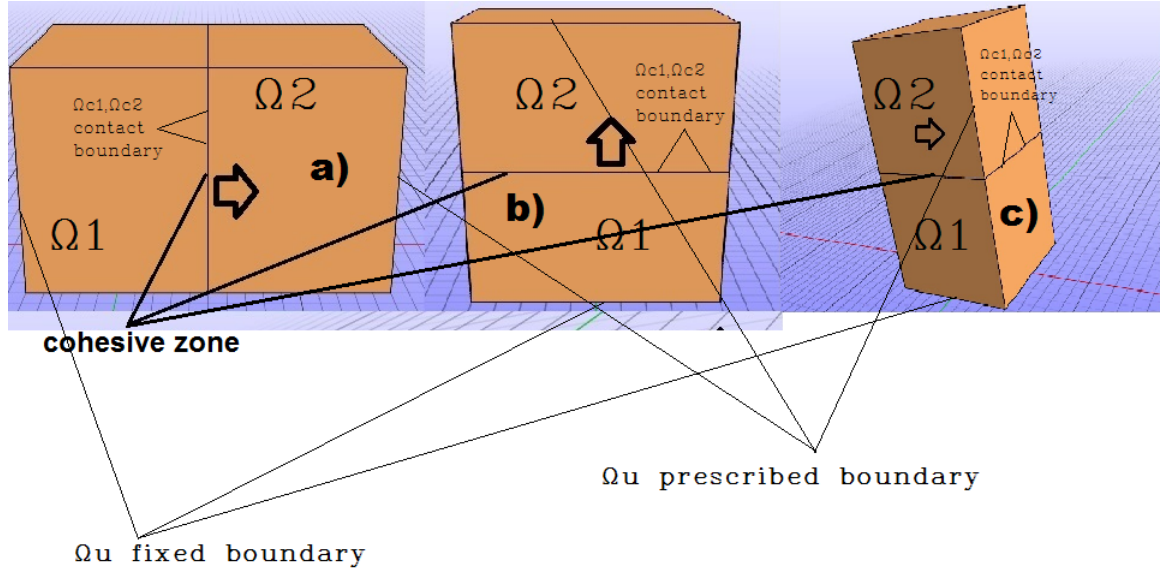
Figure 4.18: [a) , b) normal opening (mode I)] , c) tangential opening (mode II)

x,y,z,Rx,Ry,Rz degree of freedoms)], Young's modulus $E_1, E_2 = 5.10^6 (MPa)$ and the Poisson's ratio $v_1, v_2 = 0.48$, determine the relation between applied force F (for two different classes of the problem, prescribed displacement=0.00048) and the displacement (opening). Mechanical properties of the double boxes and the test conditions (the parameters used for the tests) are given in Table (4.6).

First test case (normal opening)[see Figure (4.18 a, b)]:

The normal stress σ_n (at the interface), as a function of normal and tangential opening δ_n, δ_t (due to mixed mode cohesive law formulation), in relation to the interfacial function (interfacial normal stiffness K_n), can be expressed as

$$\sigma_n(\delta_n, \delta_t) = \underbrace{\frac{\partial \sigma_n(\delta_n, \delta_t)}{\partial \delta_n}}_{interfacial\,normal\,stiffness\,K_n(\delta_n, \delta_t)} [U_v^2(x) - \underbrace{U_v^1(x)}_{=0(if\,fixed\,displacement)} = \delta_n] \quad (4.101)$$

where $U_v^2(x), U_v^1(x)$ are the vertical components of the displacements respectively and the non-linear normal stiffness K_n is given by

(with $\delta_n = g_N(X)$, , $\delta_t = g_T(X)$)

$$K_n(\delta_n, \delta_t) = \{t_N^{max}.e^{-(\frac{(g_T(X))^2}{(\varepsilon_t^{coh})^2})}[(\frac{e^{(1-(\frac{g_N(X)}{\varepsilon_n^{coh}}))}}{\varepsilon_n^{coh}}) + (\frac{g_N(X)}{\varepsilon_n^{coh}})(\frac{-1}{\varepsilon_n^{coh}})e^{(1-(\frac{g_N(X)}{\varepsilon_n^{coh}}))}]\}\triangle g_N +.$$

$$\{t_N^{max}.(\frac{g_N(X)}{\varepsilon_n^{coh}}).e^{(1-(\frac{g_N(X)}{\varepsilon_n^{coh}}))}[(\frac{-2g_T(X)}{(\varepsilon_t^{coh})^2})e^{-(\frac{(g_T(X))^2}{(\varepsilon_t^{coh})^2})}]\}\triangle g_T, \tag{4.102}$$

where the parameters $t_N^{max}, \varepsilon_n^{coh}, \varepsilon^{coh}, g_N(X), g_T(X)$ have been defined in previous sections.

Taking the first derivative of the stress $\sigma_n(\delta_n, \delta_t)$ with respect to the x-axis of Cartesian, we will get (due to the assumption that the opening is along z or x axis/direction, thus $\partial \delta_n = \partial z \mid \partial x$ -*[see Figure 4.18 a), b)]*)

$$\frac{\partial \sigma_n(\delta_n, \delta_t)}{\partial x} = [\frac{K_n(\delta_n, \delta_t)}{\partial x} = \frac{\partial^2 \sigma_n(\delta_n, \delta_t)}{\partial x^2}][U_v^2(x) - U_v^1(x)] + K_n(\delta_n, \delta_t)[\frac{\partial U_v^2(x)}{\partial x} - \frac{\partial U_v^1(x)}{\partial x}] =$$

$$\frac{\partial^2 \sigma_n(\delta_n, \delta_t)}{\partial x^2}[U_v^2(x) - U_v^1(x)] + K_n(\delta_n, \delta_t)[\varepsilon_2(x) - \varepsilon_1(x)] \tag{4.103}$$

Due to Hooke's law for isotropic materials, the strains$\varepsilon_2(x), \varepsilon_1(x)$ (in terms of Young's modulus and Poisson's ratio- $\varepsilon_{ij} = \frac{1}{E}(\sigma_{ij} - v[\sigma_{kk}\delta_{ij} - \sigma_{ij}])$), can be expressed as

$$\varepsilon_{11} = \varepsilon_2(x) = \frac{\partial U_v^2(x)}{\partial x} = \tfrac{1}{E_2}[\sigma_{11} - v_2(\sigma_{22} + \sigma_{33})] \tag{4.104}$$

$$\varepsilon_{11} = \varepsilon_1(x) = \frac{\partial U_v^1(x)}{\partial x} = \tfrac{1}{E_1}[-\sigma_{11} - v_1(\sigma_{22} + \sigma_{33})] \tag{4.105}$$

So, after substitution, the stress function $\sigma_n(\delta_n, \delta_t)$ now shown as

$$\frac{\partial \sigma_n(\delta_n, \delta_t)}{\partial x} = K_n(\delta_n, \delta_t)(\tfrac{1}{E_2}[\sigma_{11} - v_2(\sigma_{22} + \sigma_{33})] - \tfrac{1}{E_1}[-\sigma_{11} - v_1(\sigma_{22} + \sigma_{33})]) +$$

$$\frac{\partial^2 \sigma_n(\delta_n, \delta_t)}{\partial x^2}[U_v^2(x) - U_v^1(x)] = \sigma_n(\delta_n, \delta_t)K_n(\delta_n, \delta_t)([\tfrac{1}{E_2} + \tfrac{1}{E_1}]) +$$

$$K_n(\delta_n, \delta_t)((\sigma_{22} + \sigma_{33})[\tfrac{v_1}{E_1} - \tfrac{v_2}{E_2}]) + \frac{\partial^2 \sigma_n(\delta_n, \delta_t)}{\partial x^2}[U_v^2(x) - U_v^1(x)], \tag{4.106}$$

where $\sigma_{11} = \sigma_n(\delta_n, \delta_t)$ [see Figure (4.19)].
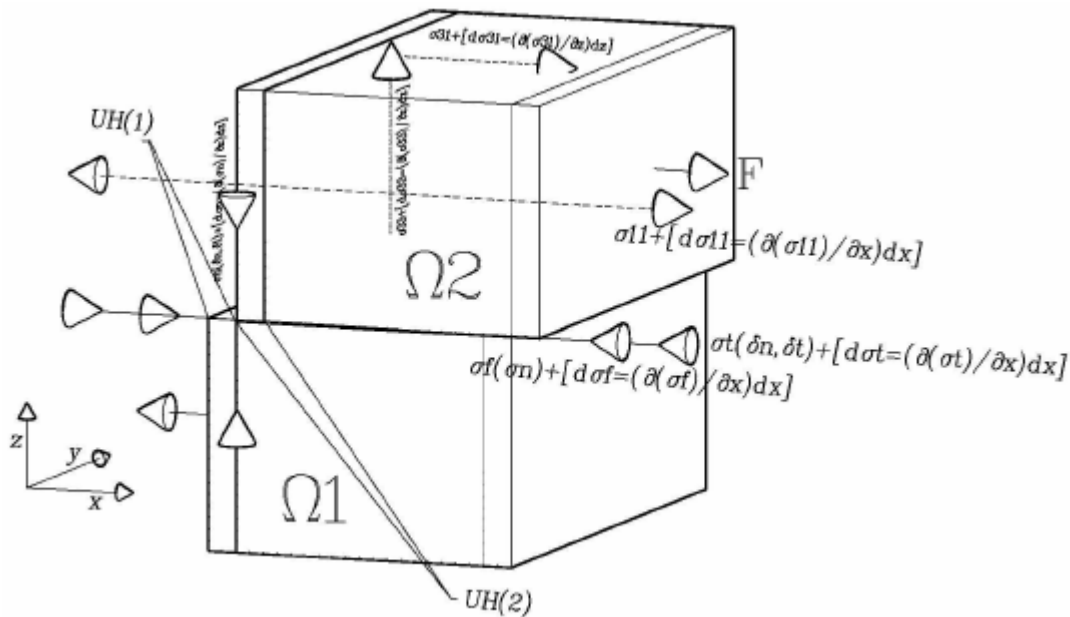
Figure 4.19: Free body diagram

Finally, we will have a (partial) second order non-homogeneous differential equation

$$q_0(x)y''(x) - y'(x) + p_0(x)y(x) = f(x), \tag{4.107}$$

where

$f(x) = -K_n(\delta_n, \delta_t)((\sigma_{22} + \sigma_{33})[\frac{v_1}{E_1} - \frac{v_2}{E_2}]), q_0(x) = [U_v^2(x) - U_v^1(x)]$
and $p_0(x) = K_n(\delta_n, \delta_t)\left([\frac{1}{E_2} + \frac{1}{E_1}]\right)),$

and in special cases ($E_1 = E_2$ and $v_1 = v_2 \implies f(x) = 0$), we will get the corresponding homogeneous equation which has the general (complementary) solution

$$[\sigma_n(x) = \sigma_n(\delta_n, \delta_t) = y(x)] = e^{\lambda x}(C_1^{//} \sin\mu x + C_2^{//} \cos\mu x) \tag{4.108}$$

Remark 4.1: ....

Note that the equation (4.108) *is formulated based on the infinitesimal change in the opening direction, and if we want to get a general formula, first, we take the derivative of the equation* (4.108) *with respect to opening direction*

$$\frac{\partial \sigma_n(\delta_n, \delta_t)}{\partial \delta_n} = \frac{\partial e^{\lambda x}(C_1 \sin\mu x + C_2 \cos\mu x)}{\partial x} = \lambda e^{\lambda x}(C_1^{//} \sin\mu x + C_2^{//} \cos\mu x) +$$

$$e^{\lambda x}(C_1^{//}\mu cos\mu x - \mu C_2^{//} sin\mu x) = e^{\lambda x}(C_1^{/} sin\mu x + C_2^{/} cos\mu x) \tag{4.109}$$

Substituting the equation (4.109) *into the equation* (4.101) *and integrating,*

$$\int e^{\lambda x}(C_1^{/} sin\mu x + C_2^{/} cos\mu x)dx, \tag{4.110}$$

by using the following integral formula

$$\int e^{\lambda x}(sin\mu x)dx = \frac{e^{\lambda x}}{\lambda^2 + \mu^2}(\lambda sin\mu x - \mu cos\mu x) + C \tag{4.111}$$

$$\int e^{\lambda x}(cos\mu x)dx = \frac{e^{\lambda x}}{\lambda^2 + \mu^2}(\mu sin\mu x + \lambda cos\mu x) + C, \tag{4.112}$$

finally, we get

$$\sigma_n(\delta_n, \delta_t) = e^{\lambda x}(C_1 sin\mu x + C_2 cos\mu x) \tag{4.113}$$

....

Due to the fact that, $\sigma_n(0) = 0 \implies 0 = e^0(C_1 sin(0) + C_2 cos(0) \Rightarrow C_2 = 0)$, and when $g_N(X) = \varepsilon_n^{coh}$, we get the maximum allowed displacement (normal stress) before propagation of cracks, namely $\sigma_n(x = \varepsilon_n^{coh}) = t_N^{max}$ (pure normal opening $g_T(X) = 0$), therefore, $\sigma_n(\varepsilon_n^{coh}) = t_N^{max} = C_1 sin(\mu \varepsilon_n^{coh})e^{\lambda \varepsilon_n^{coh}} \implies C_1 = \frac{t_N^{max}}{sin(\mu \varepsilon_n^{coh})e^{\lambda \varepsilon_n^{coh}}}$.

Thus,

$$\sigma_n(\delta_n, \delta_t) \quad = \quad \sigma_n(x) = e^{\lambda x}\left(\frac{t_N^{max}}{sin(\mu \varepsilon_n^{coh})e^{\lambda \varepsilon_n^{coh}}}\right) sin\mu x \tag{4.114}$$

The plotted graphical results, analytical versus numerical, are shown in Figure (4.20 a), which demonstrate a very good agreement between the analytical and numerical models. Note that the mathematical procedure for the determination of the quantities λ, μ is related to the fact $\frac{\partial \sigma_n(x)}{\partial x}|_{x=\sigma_n^{-1}(t_N^{max})} = 0$ and the pre-defined upper limit of the normal (and tangential) openings.

Second test case (frictional tangential opening)[see Figure (4.18 c)]:

The (total) tangential stress σ_T (as a function of normal and tangential opening δ_n, δ_t), is

the result of tangential opening stress $\sigma_t(\delta_n, \delta_t)$ and frictional stress σ_f, which can be shown as

$$
\sigma_T(\delta_n, \delta_t) \quad = \quad \underbrace{\frac{\partial \sigma_t(\delta_n, \delta_t)}{\partial \delta_t}}_{interfacial\,tangential\,stiffness\,K_t(\delta_n,\delta_t)} \quad [U_H^2(x) - \underbrace{U_H^1(x)}_{=0(if\,fixed\,displacement)}
$$

$$
= \delta_t] + [\sigma_f = \mu_f . \sigma_n(\delta_n, \delta_t)\{\frac{(U_H^2(x) - U_H^1(x))}{\| (U_H^2(x) - U_H^1(x)) \|}\} \quad if\,(U_H^2(x) - U_H^1(x)) \neq 0(slip)], \quad (4.115)
$$

where $U_H^2(x), U_H^1(x)$ are the horizontal components of the displacements respectively, μ_f friction coefficient, $\sigma_f = \sigma_n(\delta_n, \delta_t) = \lambda_f + \varepsilon_f \| (U_H^2(x) - U_H^1(x)) \|$ *if stick* and the non-linear tangential stiffness K_t is given by

$$
K_t(\delta_n, \delta_t) \quad = \quad \{2\sqrt{\frac{1}{2}}e.t_T^{max}.(\frac{g_T(X)}{\varepsilon_t^{coh}}).e^{-(\frac{(g_T(X))^2}{(\varepsilon_t^{coh})^2})}[(\frac{e^{-(\frac{g_N(X)}{\varepsilon_n^{coh}})}}{\varepsilon_n^{coh}})+
$$

$$
(1 + \frac{g_N(X)}{\varepsilon_n^{coh}}).(\frac{-1}{\varepsilon_n^{coh}}).e^{-(\frac{g_N(X)}{\varepsilon_n^{coh}})}]\}\triangle g_N + \{2\sqrt{\frac{1}{2}}e.t_T^{max}.(1 + \frac{g_N(X)}{\varepsilon_n^{coh}})
$$

$$
.e^{-(\frac{g_N(X)}{\varepsilon_n^{coh}})}[(\frac{e^{-(\frac{(g_T(X))^2}{(\varepsilon_t^{coh})^2})}}{\varepsilon_t^{coh}}) + (\frac{g_T(X)}{\varepsilon_t^{coh}}).(\frac{-2g_T(X)}{(\varepsilon_t^{coh})^2}).e^{-(\frac{(g_T(X))^2}{(\varepsilon_t^{coh})^2})}]\}\triangle g_T, \quad (4.116)
$$

where again the parameters $t_T^{max}, \varepsilon_n^{coh}, \varepsilon_t^{coh}, g_N(X), g_T(X)$ have been defined in previous sections.

Note that the tangential slip is collinear with frictional stress (exerted by the point $p \in \partial\Omega_{c1}$ (during sliding) on the opposing surface).

Taking the derivative of stress $\sigma_T(\delta_n, \delta_t)\{\sigma_T = \sigma_t + \sigma_f\}$ with respect to tangential opening direction [for more details see Appendix C part(2)] and applying again Hooke's law for isotropic materials, after substitution ($\frac{\partial^2 \sigma_t(\delta_n, \delta_t)}{\partial x^2} = \frac{\partial^2 \sigma_T(\delta_n, \delta_t)}{\partial x^2} - \frac{\partial^2 \sigma_f}{\partial x^2}$), we will get

$$
\frac{\partial^2 \sigma_T(\delta_n, \delta_t)}{\partial x^2} \underbrace{[U_H^2(x) - U_H^1(x)]}_{q_0(x)} - \frac{\sigma_T(\delta_n, \delta_t)}{\partial x} + \sigma_T(\delta_n, \delta_t) \underbrace{[K_t(\delta_n, \delta_t)[\frac{1}{E_2} + \frac{1}{E_1}]]}_{p_0(x)} +
$$

Type of material	Isotropic elastic	Element types	$HEX8$
Density	$1\frac{kg}{m^3}$	Time steps	100
Young modulus	$E = 5.10^6 MPa$	Step size	0.1
Poisson's ratio	$v = 0.48$	Max step	10
Interfacial normal/tangential strength	$200 N/mm^2$	Min step	0.1
Critical strain energy release rate(G_c)	$28.3 N/mm$	Max refs	2500
Optimal iterations	60	Max retries	50
Nonlinear solution method	$Full-Newton$	Disp. tolerance	0.00001
Auto timestep-controller	$checked$	Energy tolerance	0.0001
Characteristic opening length	$0.001 mm$	Gap tolerance	0

Table 4.6: Mechanical properties of the double boxes and the test conditions

$$\underbrace{\{\frac{\partial^2 \sigma_f}{\partial x^2}[U_H^1(x) - U_H^2(x)] + \frac{\partial \sigma_f}{\partial x}[K_t(\delta_n, \delta_t)(\frac{1}{E_2} + \frac{1}{E_1} + 1)]}_{f(x)_1}$$

$$\underbrace{+K_t(\delta_n, \delta_t)(\sigma_{22} + \sigma_{33})[\frac{v_1}{E_1} - \frac{v_2}{E_2}]\}}_{f(x)_2} = 0 \tag{4.117}$$

$f(x) = f(x)_1 + f(x)_2,$
where $\frac{\partial \sigma_f}{\partial x} = \mu_f.\{K_n(\delta_n, \delta_t)[\frac{\partial U_v^2(x)}{\partial x} - \frac{\partial U_v^1(x)}{\partial x}]\}.$
Finally, we will get a (partial) second order non-homogeneous differential equation

$$q_0(x)y''(x) - y'(x) + p_0(x)y(x) = f(x), \tag{4.118}$$

with general solution

$$\sigma_T(\delta_n, \delta_t) = y(x) = y_c(x) + Y, \tag{4.119}$$

where Y is any specific function that satisfies the non-homogeneous equation and $y_c(x)$ is the corresponding complementary solution expressed as

$$y_c(x) = e^{\lambda x}(C_1 sin\mu x + C_2 cos\mu x) \tag{4.120}$$

First, we break the non-homogeneous differential equation into 3 parts and solve them separately ($Y = Y_1 + Y_2 + Y_3$)

I: $q_0(x)y''(x) - y'(x) + p_0(x)y(x) = \frac{\partial^2 \sigma_f}{\partial x^2}[U_H^1(x) - U_H^2(x)] = \mu_f.K_n(\delta_n, \delta_t)\frac{\partial \sigma_{31}}{\partial x}[\frac{2(1+v_2)}{E_2} + \frac{2(1+v_1)}{E_1}][U_H^1(x) - U_H^2(x)]$

II: $q_0(x)y''(x) - y'(x) + p_0(x)y(x) = \frac{\partial \sigma_f}{\partial x}[K_t(\delta_n, \delta_t)(\frac{1}{E_2} + \frac{1}{E_1} + 1)]$

III: $q_0(x)y''(x) - y'(x) + p_0(x)y(x) = K_t(\delta_n, \delta_t)(\sigma_{22} + \sigma_{33})[\frac{v_1}{E_1} - \frac{v_2}{E_2}]$

So, after some algebra, we will get

$$Y_1 = \frac{\mu_f.K_n(\delta_n, \delta_t)\frac{\partial \sigma_{31}}{\partial x}[\frac{2(1+v_2)}{E_2} + \frac{2(1+v_1)}{E_1}][U_H^1(x) - U_H^2(x)]}{-1 + [K_t(\delta_n, \delta_t)\frac{\partial \sigma_{31}}{\partial x}\left([\frac{1}{E_2} + \frac{1}{E_1}]\right)[U_H^1(x) - U_H^2(x)]} \tag{4.121}$$

$$Y_2 = \frac{\frac{\partial \sigma_f}{\partial x}(\frac{1}{E_2} + \frac{1}{E_1} + 1)}{\left([\frac{1}{E_2} + \frac{1}{E_1}]\right)} \tag{4.122}$$

$$Y_3 = \frac{(\sigma_{22} + \sigma_{33})[\frac{v_1}{E_1} - \frac{v_2}{E_2}]}{\left([\frac{1}{E_2} + \frac{1}{E_1}]\right)} \tag{4.123}$$

Thus,

$$\sigma_T(x) = \sigma_T(\delta_n, \delta_t) = e^{\lambda x}(C_1 \sin\mu x + C_2 \cos\mu x) + Y_1 + Y_2 + Y_3 \tag{4.124}$$

Using boundary condition, we can determine the coefficients C_1, C_2. Due the fact that, $\sigma_T(0) = 0 \implies 0 = e^0(C_1 \sin(0) + C_2 \cos(0) + Y_1 + Y_2 + Y_3 \Rightarrow C_2 = -(Y_1 + Y_2 + Y_3)$ and assuming ($\varepsilon_n^{coh} = \varepsilon_t^{coh}$) if $\varepsilon_n^{coh} = \varepsilon_t^{coh} = g_N(X) = g_t(X)$ (the maximum allowed normal and tangential displacement before propagation of cracks), then, we will have $\sigma_n(x = \varepsilon_n^{coh}) = e^{-1}t_N^{max}$, $\sigma_t(x = \varepsilon_t^{coh}) = 4e^{-2}\sqrt{\frac{e}{2}}t_T^{max}$, and consequently the (total) tangential stress σ_T has the value

$$\sigma_T(x = \varepsilon_n^{coh} = \varepsilon_t^{coh}) = \mu_f e^{-1}t_N^{max} + 4e^{-2}\sqrt{\frac{e}{2}}t_T^{max} = e^{\lambda \varepsilon_t}(C_1 \sin\mu\varepsilon_t^{coh} + -Y\cos\mu\varepsilon_t^{coh}) + Y \implies$$
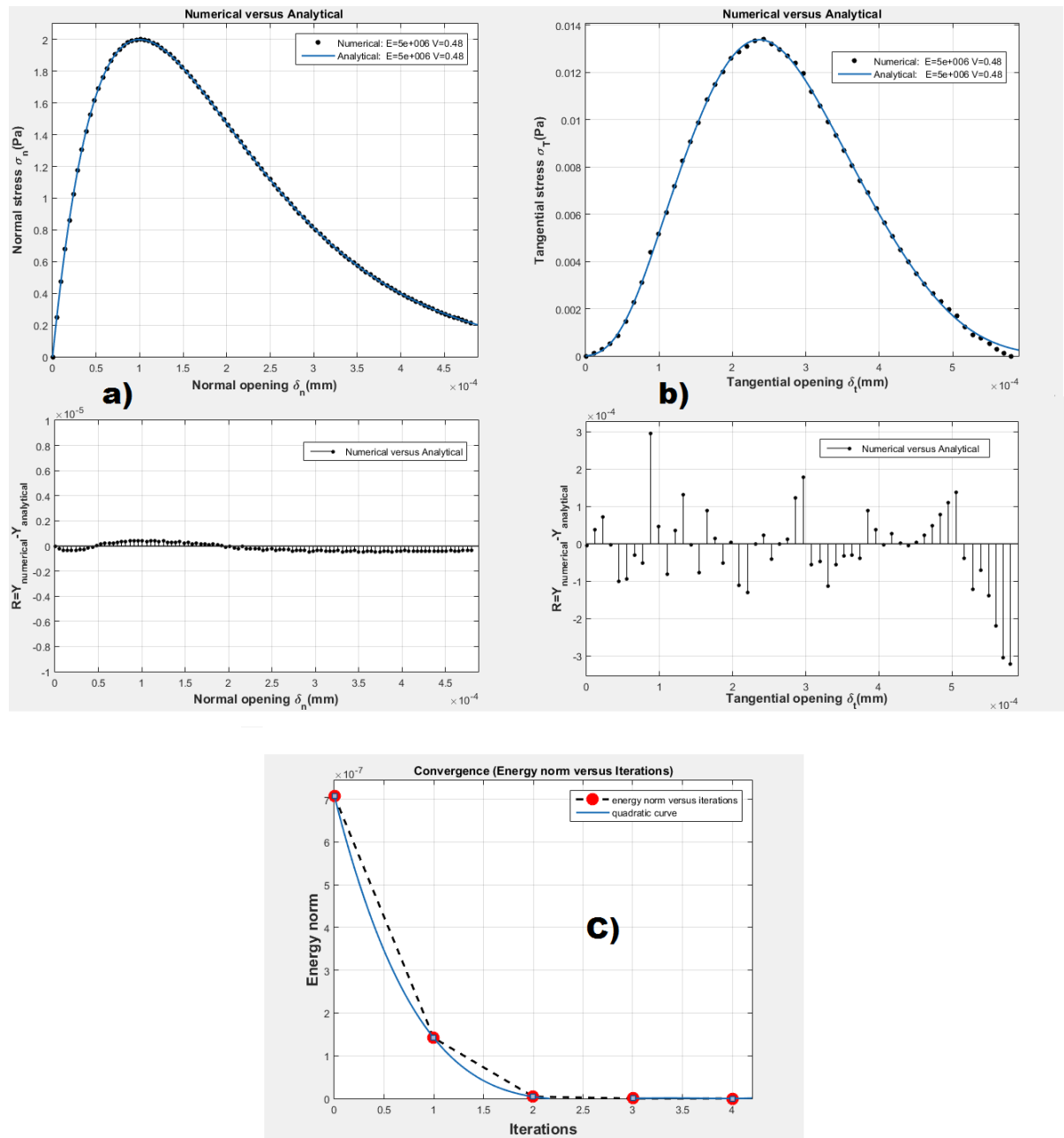
Figure 4.20: (a) Normal stress $\sigma_n(Pa)$ versus normal opening $\delta_n(mm)$ (Numerical versus Analytical), $R = Y_{numerical} - Y_{analytical}$ versus normal opening)[Young's modulus $E(Pa)$ and the Poisson's ratio v], normal interfacial strength $t_N^{max} = 200 N/mm^2$, (b) The (total) tangential stress $\sigma_T(Pa)$ versus tangential opening $\delta_t(mm)$ (Numerical versus Analytical, $R = Y_{numerical} - Y_{analytical}$ versus tangential opening){[Young's modulus $E(Pa)$ and the Poisson's ratio v], normal and tangential interfacial strength $t_N^{max}, t_T^{max} = 200 N/mm^2$}, (c) Energy norm versus Iterations for one typical load step of the given problems [see Table (4.7)].

$$C_1 = \frac{\mu_f e^{-1} t_N^{max} + 4e^{-2}\sqrt{\frac{e}{2}} t_T^{max} - Y + Ye^{\lambda \varepsilon_t^{coh}} cos\mu \varepsilon_t^{coh}}{e^{\lambda \varepsilon_t^{coh}} sin\mu \varepsilon_t^{coh}} \tag{4.125}$$

Finally, after substitution of these coefficients C_1, C_2 into the general solution (4.124), the stress $\sigma_T(\delta_n, \delta_t)$ can be expressed as

$$\sigma_T(x) = e^{\lambda x}\Big(\frac{\mu_f e^{-1} t_N^{max} + 4e^{-2}\sqrt{\frac{e}{2}} t_T^{max} - Y + Ye^{\lambda \varepsilon_t^{coh}} cos\mu \varepsilon_t^{coh}}{e^{\lambda \varepsilon_t^{coh}} sin\mu \varepsilon_t^{coh}}$$

$$sin\mu x - Ycos\mu x\Big) + Y_1 + Y_2 + Y_3 \tag{4.126}$$

The plotted graphical results, numerical versus analytical, is shown in Figure [4.20 b)], moreover, as seen in Figure [4.20 c)], the graph of Energy norm versus Iterations for one typical load step of the given problems [see Table (4.7)] demonstrates the quadratic rate of the convergence within a Newton-Raphson equation solving strategy[7] where if the current energy norm drops below the required value (*initial energy norm* × *energy tolerance*), the analysis will consider the time step converged and move on to the next time step [see Algorithm (4.1)].

As can be seen in Figure [4.20 a) b)], the numerical method gives us approximate solution and not exact solution, where in the case of normal opening numerical and analytical models coincide and in the case of the tangential opening a good agreement is to be noted between analytical results and the finite element computations.

Although the introduced numerical algorithmic approach could produce better numerical results, but a simple calculation of the error in the above approximation using either absolute error method ($e_{abs} = \| u_{exact} - u_{approximation} \|$, where u_{exact} is the exact solution and $u_{approximation}$ is the approximate solution), or relative error method ($e_{rel} = \frac{\| u_{exact} - u_{approximation} \|}{\| u_{exact} \|}$), reveals acceptable percentage error ($= \frac{maximum\,error \times 100\%}{value\,of\,the\,measurement}$) [less than 5%], which measures the degree of accuracy-precision of the above introduced methods and determines that the methods can be accepted as reliable.

Nonetheless, this study suggests, to improve accuracy by 1%, the (coarse) simple mesh that is used in this study (two elastic boxes each with one hexahedral element) can be appropriately refined to a suitable finite element meshes (without changing the material property), where the difference between the analytical solution and numerical solution can be directly influenced by the number of mesh elements and geometry size, on the other hand, the above difference can

---

[7]All problems discussed in this PhD project exhibited quadratic rate of the convergence within Newton-Raphson equation solving strategy

Algorithm 4.1 Algorithm to solve the nonlinear FE equations

1: Beginning time step n
2: **while** not converged **do**
3:     **if** $Mmn < m \vee Nitn < l$ **then** goto End
4:     **end if**
5:     $S^{converge} \leftarrow true$
6:     Solve the equations for $d_{n+\alpha}^l, T_{n+\alpha}^l$:
7:     $I : \quad R^{global}[d_{n+\alpha}^l] = F_{ext}^{mech}(t_{n+\alpha}) + F_{ext}^{ther}(t_{n+\alpha}) - M[\ddot{d}_{n+\alpha}^l \mid a_{n+\alpha}^l] - Cd_{n+\alpha}^l - F_{int}^{mech}[d_{n+\alpha}^l] - F_{int}^{ther}[d_{n+\alpha}^l] - F^C[d_{n+\alpha}^l]$
8:     $II : d_{n+\alpha}^l = d_n + v_n(t_{n+\alpha} - t_n) + \frac{1}{2}[2\beta a_{n+\alpha}^l + (1 - 2\beta)a_n](t_{n+\alpha} - t_n)^2$
9:     $III : v_{n+\alpha}^l = v_n + [\gamma a_{n+\alpha}^l + (1 - \gamma)a_n](t_{n+\alpha} - t_n)$
10:     $IV : T_{n+\alpha}^l = \frac{[D_{mechanical dissipation}^{(n+\alpha)^l} + R_{d_{n+\alpha}^l} - DIV(Q_{d_{n+\alpha}^l})]}{[\eta_{n+\alpha}^l - \eta_n]}(t_{n+\alpha} - t_n)$
11:     $V : T_{n+\alpha}^{contact^l}(T_{n+\alpha}^{contact^l} - T_n^{contact}) = \frac{T_0[\xi \|t_f^{(n+\alpha)^l}\| + t_N^{(n+\alpha)^l} h_c^m \theta_m^{(n+\alpha)^l} + t_N^{(n+\alpha)^l} h_c^s \theta_s^{(n+\alpha)^l}]}{C_{contact}^{heatsink}}$
12:     $L(s) \leftarrow d_{n+1}^T R(d_{n+1}^l + s\triangle d)$ [perform a linesearch]
13:     **if** $\mid L(s) \mid \geq Tol \mid L(0) \mid \vee L(0)L(1) < 0$ **then**
14:         Iterate $for s \in (0,1), such that \mid L(s) \mid \leq Tol \mid L(0) \mid$
15:     **else**
16:         $s \leftarrow 1$ [Update(geometry), Update(residual)]
17:     **end if**
18:     **if** $\frac{R^{global}(d_{n+1}^l + s\triangle d) * R^{global}(d_{n+1}^l + s\triangle d)}{R^{global}(d_{n+1}^l) * R^{global}(d_{n+1}^l)} > R^{tol} \wedge R^{tol} > 0$ **then**
19:         $S^{converge} \leftarrow false$
20:     **end if**
21:     **if** $\frac{(s\triangle d)*(s\triangle d)}{(d_{n+1}^l + s\triangle d)*(d_{n+1}^l + s\triangle d)} > d^{tol} * d^{tol} \wedge d^{tol} > 0$ **then**
22:         $S^{converge} \leftarrow false$
23:     **end if**
24:     **if** $\frac{s*\mid \triangle d * R^{global}(d_{n+1}^l + s\triangle d)\mid}{\mid \triangle d * R^{global}(d_{n+1}^l)\mid} > E^{tol} \wedge E^{tol} > 0$ **then**
25:         $S^{converge} \leftarrow false$
26:     **end if**
27:     **if** $s < LineS_{min}^{stp} \wedge LineS^{tol} > 0$ **then**
28:         $S^{converge} \leftarrow false$
29:     **end if**
30:     **if** $s* \mid \triangle d * R^{global}(d_{n+1}^l + s\triangle d) \mid > \mid \triangle d * R^{global}(d_{n+1}^l) \mid$ **then**
31:         $S^{converge} \leftarrow false$
32:     **end if**
33:     **if** $S^{converge} \leftarrow false$ **then**
34:         **do**
35:         $m \leftarrow m + 1$ [ReformStiffness()]
36:         **if** $Mmn < m$ **then**
37:             **break**
38:         **end if**
39:     **end if**
40:     $l \leftarrow l + 1$
41: **end while**
42: **if** converged **then**
43:     update the total displacements
44:     $n \leftarrow n + 1$ [move on to the next step]
45: **end if**

Iterations	Converg. norms	INITIAL	CURRENT	REQUIRED
1	Energy	$7.086406e-007$	$1.417000e-007$	$7.086406e-009$
	Displacement	$4.376051e-013$	$2.387279e-014$	$1.660441e-019$
	Residual	$1.702439e+000$	$1.246976e+000$	$1.000000e-015$
2	Energy	$7.086406e-007$	$4.278462e-009$	$7.086406e-009$
	Displacement	$4.376051e-013$	$3.158365e-013$	$1.660441e-019$
	Residual	$1.702439e+000$	$7.549132e-005$	$1.000000e-015$
3	Energy	$7.086406e-007$	$3.689671e-013$	$7.086406e-009$
	Displacement	$4.376051e-013$	$2.533324e-017$	$1.660441e-019$
	Residual	$1.702439e+000$	$6.568224e-009$	$1.000000e-015$
4	Energy	$7.086406e-007$	$4.218806e-017$	$7.086406e-009$
	Displacement	$4.376051e-013$	$4.087037e-021$	$1.660441e-019$
	Residual	$1.702439e+000$	$6.594945e-016$	$1.000000e-015$

Table 4.7: Energy, displacement and residual norms in a typical load step for the contact-cohesive problem between linear elastic bodies (two boxes)

be also decreased by choosing real high value for the elastic modulus of the elastic materials (with the same simple mesh).

4.6.3 Frictional heating and temperature evaluation on contact interfaces

As a final topic in this chapter, analytical methods for the analysis of the temperature evaluation and heat fluxes through the frictional contact interfaces of two thermally insulated and materially identical elastic bodies (also assuming equally heat transfer coefficients $\gamma_{c1} = \gamma_{c2}$ and thermal conductivity $\kappa_1 = \kappa_2$)[based on the methods presented in Laursen (2003), have been developed and applied.

Given two elastic bodies Ω_1, Ω_2 [an elastic model (width: 10 mm, length: 10 mm, depth: 10 mm, hexahedral elements, the parameters of the mesh nx = 2, ny = 2, nz = 2) which slides over a longer fixed block (width: 10 mm, length: 100 mm, depth: 10 mm, hexahedral elements, the parameters of the mesh nx = 20, ny = 10, nz = 10)], as shown in Figure (4.21), a pre-defined sliding contact interface between them where Coulomb friction with constant friction coefficient μ_f acts at their interface, subjected to the boundaries $\partial\Omega_c, \partial\Omega_u$ (discontinuity and Dirichlet boundary conditions), Young's modulus $E_1, E_2 = 5.10^7 (MPa)$ and the Poisson's ratios $v_1, v_2 = 0.48$, initial temperatures $\theta_1, \theta_2 = 0^oC$, determine the contact temperature evaluation T_c (due to change of normal pressure) as time evaluated. Mechanical properties and the test parameters of the sliding elastic block and the fixed elastic block are given in Table (4.8).
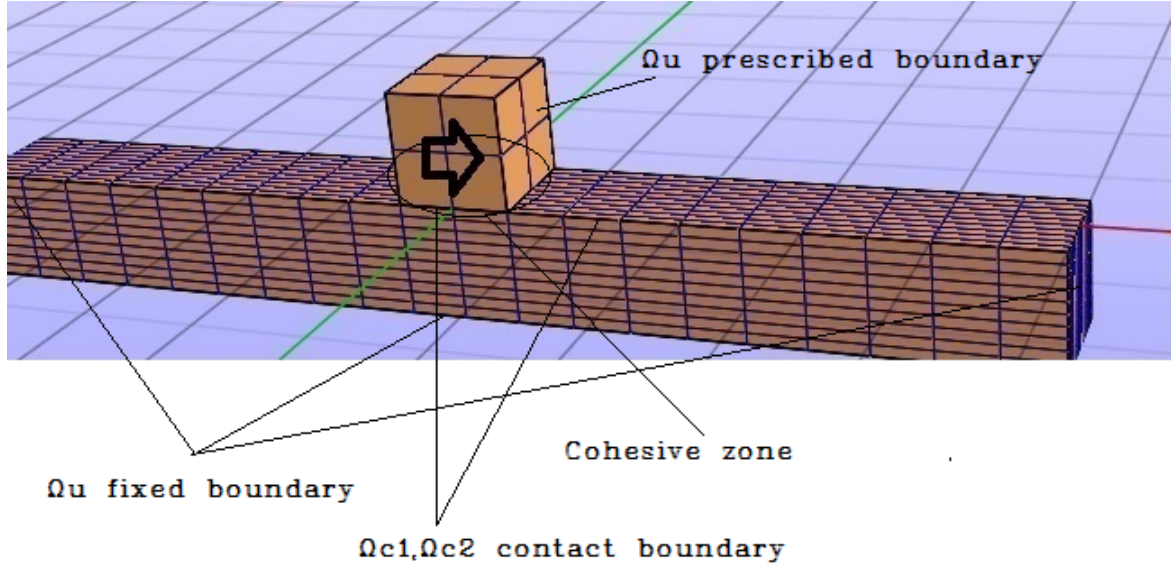
Figure 4.21: An sliding elastic block over longer fixed elastic block

To allow an exact approach, first, the general heat conduction formulation due to Fourier's law which related the local heat flux Q to the temperature gradient ∇T using thermal conductivity in the bodies κ, given by

$$Q = -\kappa \nabla T, \tag{4.127}$$

has been taken into account.

The formulation of heat flux across the contact interface q_{c1}, q_{c2} follows then the fact that the time derivative of the surface density of internal energy is in one way dependent on the contact of normal and tangential traction, relative normal and tangential velocities and heat fluxes given by

$$\frac{\partial Se}{\partial t} = t_N \cdot \frac{\partial g_N(X)}{\partial t} + t_T \cdot \left(\frac{\partial g_T^e(X)}{\partial t} + \frac{\partial g_T^p(X)}{\partial t} \right) + q_{c1} + q_{c2}, \tag{4.128}$$

and in another way, it is related to the time derivative of surface entropy η_c and free energy ψ expressed as

$$\frac{\partial Se}{\partial t} = \frac{\partial \psi}{\partial g_n} \cdot \frac{\partial g_N(X)}{\partial t} + \frac{\partial \psi}{\partial g_t^e} \cdot \frac{\partial g_T^e(X)}{\partial t} + \frac{\partial \psi}{\partial T_c} \cdot \frac{\partial T_c}{\partial t} + \frac{\partial \eta_c}{\partial t} \cdot T_c + \eta_c \frac{\partial T_c}{\partial t} \tag{4.129}$$

Combining these two last equations and using the equation of entropy evolution

$$\eta_c = \frac{C_c(T_c - T_0)}{T_0}, \tag{4.130}$$

type of materials	Young modulus	Poisson's ratio	Interfacial normal/tangential strength	
isotropic elastic	$E = 5.10^7 MPa$	$v = 0.48$	1.8MPa	
Fric. param.	Thermal cond.	Ini. temp.	Heat capacity	Heat transfer coefficients
$\mu = 0.1, \varepsilon_f = 0.1$	$\kappa = 100 N/sK$	$T_0 = 0^o C$	$C_c = 100 m^2/s^2 K$	$h_c^s = h_c^m = 1.0 W N^{-1} K^{-1}$
Density	Time steps	Step size	Disp. tolerance	Energy tolerance
$1\frac{kg}{m^3}$	10	0.1	0.001	0.01

Table 4.8: The test parameters of the sliding elastic block and the fixed elastic block

where C_c, T_c, T_0 are the heat capacity per unit surface, interface characteristic temperature and reference temperature, one can obtain the following equation [under the assumption that the free energy is independent of inelastic slip $g_T^p(X)$]

$$\begin{cases} I: t_T . \frac{\partial g_T^p(X)}{\partial t} + q_{c1} + q_{c2} = \frac{C_c(T_c)}{T_0} . \frac{\partial T_c}{\partial t} \\ II: q_{c1} = \gamma_{c1} t_N(T_1 - T_c), \quad q_{c2} = \gamma_{c2} t_N(T_2 - T_c), \end{cases} \tag{4.131}$$

where the thermal dissipation formulation

$$\frac{q_{c1}(T_1 - T_c)}{T_1} + \frac{q_{c2}(T_2 - T_c)}{T_2} = \frac{\gamma_{c1} t_N(T_1 - T_c)^2}{T_1} + \frac{\gamma_{c2} t_N(T_2 - T_c)^2}{T_2}, \tag{4.132}$$

has been used to formulate the second equation II [equation (4.131)].

Using the equations above, one can develop the following constitutive relationship for the contact temperature evolution and the normal traction

$$\kappa_1(T_{c1} - T_2) + \kappa_2(T_{c1} - T_2) = 2\kappa(T_{c1} - T_2) = q_{c1} + q_{c2} = \gamma_{c1} t_N(T_1 - T_{c1}) +$$

$$\gamma_{c2} t_N(T_2 - T_{c1}) = \gamma_{c1} t_N T_1 + \gamma_{c2} t_N T_2 - \gamma_{c1} t_N T_{c1} - \gamma_{c2} t_N T_{c1} = \gamma_{c1} t_N T_1 + \gamma_{c1} t_N T_2 - 2\gamma_{c1} t_N T_{c1}$$

$$T_{c1} = \frac{\gamma_{c1} t_N T_1 + (2\kappa + \gamma_{c1} t_N) T_2}{2\kappa + 2\gamma_{c1} t_N}, T_{c2} = \frac{\gamma_{c1} t_N T_2 + (2\kappa + \gamma_{c1} t_N) T_1}{2\kappa + 2\gamma_{c1} t_N} \tag{4.133}$$

Due to the modified contact formulation (classical contact combined with the contact with cohesive force), the normal traction t_N in the case of stick and slip takes two different values,
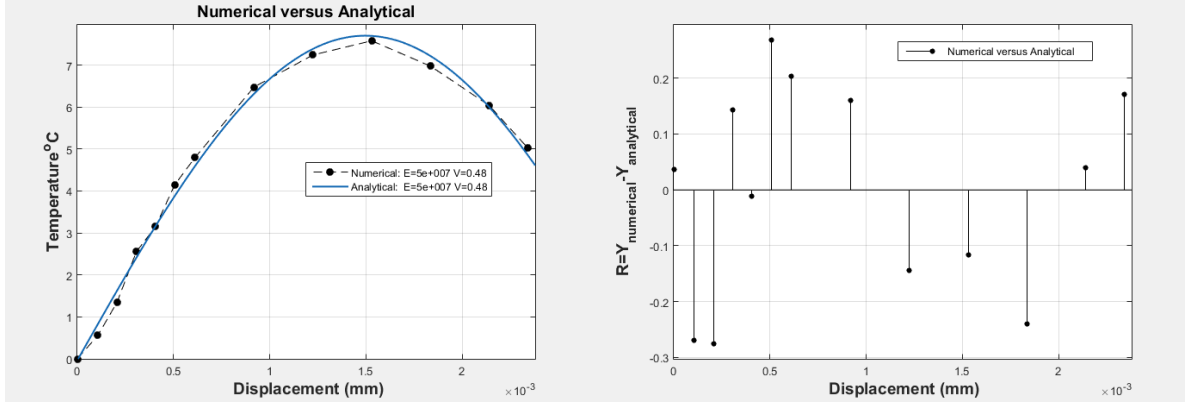
Figure 4.22: Temperature$^o C$ versus displacement $\delta_t(mm)$[Young's modulus E and the Poisson's ratio v, $\gamma_{c1} = \gamma_{c2} = 1.0WN^{-1}K^{-1}$, $\kappa = 100N/sK$] and $R = Y_{numerical} - Y_{analytical}$ versus displacement

namely

$$t_N = \begin{cases} t_N^{slip} = t_N^{max} \cdot (\frac{g_N(X)}{\varepsilon_n^{coh}}).e^{(1-(\frac{g_N(X)}{\varepsilon_n^{coh}}))} e^{-(\frac{(g_T(X))^2}{(\varepsilon_t^{coh})^2})} & if\, g_N \leqq 0 \\ t_N^{stick} = \lambda_n + \varepsilon_N g_N(X) & if\, g_N > 0, \end{cases}$$ (4.134)

where the parameters $t_N^{max}, \varepsilon_n^{coh}, \varepsilon_t^{coh}, g_N(X), g_T(X), \lambda_n, \varepsilon_N$ have been in earlier sections.

Using abstract function $\varpi(x) = \begin{cases} 1 & x \geq 0 \\ 0 & x < 0 \end{cases}$, we can rewrite the equation (4.133) in the following form

$$T_{c1} = (\frac{\gamma_{c1} t_N^{slip} T_1 + (2\kappa + \gamma_{c1} t_N^{slip})T_2}{2\kappa + 2\gamma_{c1} t_N^{slip}})\varpi(U_v^2(x) - U_v^1(x))+$$

$$(\frac{\gamma_{c1} t_N^{stick} T_1 + (2\kappa + \gamma_{c1} t_N^{stick})T_2}{2\kappa + 2\gamma_{c1} t_N^{stick}})\varpi(U_v^1(x) - U_v^2(x)),$$ (4.135)

where for T_{c2}, we can develop a similar expression and $U_v^2(x), U_v^1(x)$, are the vertical components of the displacements respectively.

The plotted graphical results, temperature-normal opening, numerical versus analytical, are shown in Figure (4.22). As can be seen in Figure (4.22), the numerical method gives us approximate solution and again not exact solution, where the observed difference between analytical method and numerical method in temperature evaluation on the contact interfaces, beside the assumption that all frictional work is dissipated as heat (which could influence the results), is highly related to relatively coarse mesh in the finite element mesh [note that

the difference could be also due to the boundary condition, the coefficient of friction and material property but the key issues in this frictional contact problem are the (systematically improvable) influence of the contact constrains and the frictional stress on the stick and slip regions of the contact interface]. Nonetheless, the analytical result has good agreement with the simulation result and the error of approximation we obtain with numerical solution is acceptable.

Although there is a good agreement between the analytical results and finite elements calculations, it is worth mentioning that verification process, analytical method versus numerical method, have limitations in case of non-linear problem, specially in the study of the frictional heating problem where additionally, some problems related to contact mechanics such as the sensibility of the algorithm to impenetrability condition of the contact formulation, could make the analysis and verification processes more difficult.

However, this study suggests, to improve accuracy, reducing element sizes (e.g. using the finite element mesh that having different aspect ratios) in places where large deformations, elastic stresses or possible instabilities take place, making careful choice of the material property and the friction coefficient, and using the concept of state variable and viscoplastic regularization method for frictional model [Laursen (2003)], could allow for highly accurate results, also (to get more degree of precision) more iterations with smaller time steps could also have positive effect on the results.

4.7 Conclusion/Discussion

This chapter has shown that, with modified contact definition, the so-called discontinuities can be modelled in different complex geometry and analysed in a sophisticated way. It has been also been proved that the redefinition of contact mechanics in this way fulfils the condition of the cohesive zone law and additionally supports the physical ideas and mathematical structures of the classical contact mechanics. The achieved results of the various tests and modelling scenarios (e.g. models with different material types; namely, Compressible, Nearly-Incompressible and In-compressible) also showed the ability of modified contact as well as the potential accuracy and enhanced quality in solving large deformation fracture mechanics problems.

In support of successful algorithms and programs and their constituents, the practical and analytical test methods of classical contact, contact with cohesive forces, thermodynamically coupled frictional problem were taken into account. The convergence analysis of the methods was also provided. Three different classes of verification by examining the existing literature on model validation [Lorenzis and Zavarise (2009), Laursen (2003)] have been considered

namely: Elastic contact between a sphere and a half space, Frictional Contact-Cohesive problem between linear elastic bodies (two boxes) and Frictional heating and temperature evaluation on contact interfaces. Comparison the proposed finite element algorithm for the above mentioned problems with analytical data was made for all the analytical results obtained for the various models and good agreement was to be noted in general. At this point it's important to add that although the introduced numerical algorithmic approach mainly could produce better numerical results, but it has been highlighted to get more both quantitative and qualitative fit with analytical data, beside the optimal choice for finite element analysis (FEA) parameters, the boundary condition, the coefficient of friction and material property, the reduction of the non smoothness of the contact interactions (using smoothing techniques such as Gregory patches) with the aim of making the numerical approach more robust, also improvement of the result in terms of cohesive fracture formulation, and other factors such as (adaptive) mesh refinement need to be considered.

One of the important observation in this research study was due to the classical contact mechanics definition (contact constraint based on the Kuhn Tucker condition). On the one hand, we assume it will have non zero surface tractions in zero separation, and on the other hand, we assume the surface tractions are zero in the case of using cohesive interface. Thus, using the classical contact and the cohesive interfaces simultaneously, defined at the same interfaces [which are implemented in a wide range of previous studies for the analysis of the fracture mechanics process Labanda *et al.* (2015), Yang *et al.* (2001), etc.], could automatically create an issue, which, in the case of using modified contact, can be easily overcome (was overcome in this study) where in zero separation only contact surface cohesive interaction is enforced (the classical contact constrains enforcement only in the case of positive gap function $gap > 0$, $gap \neq 0$- non zero separation - in other words, in the case of the physical requirement of impenetrability and compressive interaction between two bodies, enforcement of the classical contact constrains).

Furthermore, the placement of cohesive zones can presenting a problem (the placement of cohesive elements at any orientation independent of the finite element mesh), in other words, due the fact that the interface elements are aligned with elements boundaries [taking the location of the cohesive surfaces to coincide with element boundaries is problematic in several respects Needleman (2014)], the orientation of cracks is restricted and limited which makes the placement of cohesive interfaces between all continuum not completely mesh independent van der Zwaag (2007), where any not so careful (qualitative or quantitative) change or re-positioning of the discrete cohesive elements, because of their dependence on factors such as global deformation, could lead to unexpected results, therefore, to overcome this problem, this study suggests, making use of the modified contact approach could be very helpful.

There were several important issues (detected or not detected) on dealing with large deformation problems related to modified contact formulation which depends on the different applications which, naturally, need to be considered.

Besides the convergence issue for large deformations because of several difficulties related to mesh distortions, an especially significant issue related to modified contact was the geometry of the models where any wrong geometrical information (e.g. projection to surface and gap function was extremely dependent on correct geometry) had a direct result on unsuccessful termination of FEBio [the issue related to some existing software issue in PreView-Finite Element (FE) preprocessor]. Another case of great significance was the right selection of the (material, contact, etc.) parameters (parameters such as interfacial strength, characteristic length, penalty factor, etc. which in general could also open the possibility for the disadvantageous divergence from desired results).

Although it has been verified that the modification of contact formulation in this way has no negative effect on the result, the non-linearity of fracture mechanical processes combined with computational complexity conditions sometimes produces limitations in desired and successful results. The future work of modified contact mechanics, besides fixing existing issues (e.g. solving difficulties such as "negative Jacobian" , etc.), effective mesh refinement, and improvement of the accuracy of solutions by the finite-element method, would be the integration of the idea and the definition of modified contact into so-called auto contact mechanic where it will not be necessary to have a pre-defined contact area (master and slave contact surfaces) prior to FE analysis.

Chapter 5

Mechanical description and engineering analysis of cutting and needle insertion

5.1 Introduction

This chapter describes the development of a mathematical and computational model of cutting of soft solids undergoing large deformations. This is a very complex problem which is not easily amenable to mathematical analysis. Firstly the basic mechanics of cutting and penetration will be described, followed by the development of a mathematical analysis of the process. A cohesive zone model was developed to simulate the process, with consideration of the effects of large deformations on the process. This was then implemented in a novel way using a modified contact formulation in which the crack path must be defined in advance. Using a contact formulation this is very easy to do in a finite element model. Finally, examples and validation tests for the model will be presented.

There have been several studies of cutting and needle penetration of human skin. Groves *et al.* (2012) studied the indentation and penetration of skin in order to design an optimised micro-needle device for drug delivery. This completely depends on understanding human skin biomechanics under large deformations. After doing a series of optimised laboratory developed tests and using a much more precise model (considering the skin as a multilayer composite) by applying the multilayer finite element model(the results of which show a remarkable degree of success), Groves *et al.* (2012) argue that the problem with the precise approach and optimum development of numerical-experimental procedure and modelling of the very complex mechanical behaviour of human skin would require first the perfect understanding of the dependence and independence of parts or elements of the skin combined with a mechanical description which could be used later for computational modelling.

At this point it is worth mentioning that there were two main studies which helped in developing this project. The first was the study by Shergold and Fleck (2004) about the analysis of the deep penetration of a soft solid by a flat-bottomed and by a sharp-tipped cylindrical punch, using a one term Ogden strain energy function and considering the skin as an incompressible hyperelastic, isotropic solid. The second one was the study Mahvash and Hayward (2001) about the development of the haptic rendering of cutting with the clarification of the geometry and the mechanism of the interaction of the tools and the sample.

There are also other studies [Buitrago et al. (2015), Bodhale et al. (2010)] which deal with a wide range of additional developments of various theoretical and numerical formulations for cutting and needle insertion by using the (traditional) finite element methods. Without being affected by the complex nature of soft solid penetration, it is worth saying that the existing literature unfortunately does not provide much insight into the underlying mechanisms of penetration and cutting. Generally they indicate that deep penetration involves deformation and cracks and in most cases without taking the existence of (sliding) friction into account. Therefore, this chapterÕs goal is to keep focused on what is of most importance, namely the mathematical and physical clarification of the mechanisms of penetration and the cutting processes, followed by the related algorithms and computational implementation of the theory.

5.2 Constitutive models

5.2.1 Mechanics of needle insertion

Several researchers have studied the force required to penetrate a solid and some of the constitutive models have been developed for the penetration of a soft solid (e.g. flat bottomed and sharp tipped punches). Unfortunately, none of these studies could establish a constitutive model for the penetration of a soft solid, in particular needle insertion into human skin.

The constitutive model for needle insertion into a soft solid, described in detail in the following, as shown in Figure (5.1), is based on the work done by external and internal forces, where the external work is the sum of the work done by the indenter (needle) and the body force, and the internal work is the work done in changing the strain energy that is stored in the solid (the work done by the deformation before penetration and the potential energy stored after expansion), the work done by creating cracks and the work done by friction.

To begin we introduce the following global variational statement (the total work)

$$\delta W_T \quad = \quad \delta W_F + \delta W_D + \delta W_C - \delta W_{ext} \tag{5.1}$$
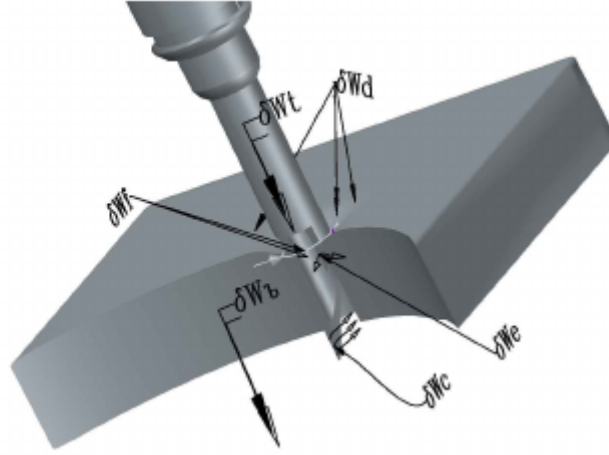
Figure 5.1: The δWt and δW_b represent the external work δW_{ext} (work due to the body force and the traction), and the notations $\delta Wf, \delta Wd, \delta We, \delta Wc$ represent the internal work δW_{int}

$$\delta W_T \quad = \quad \delta W_{int} - \delta W_{ext}, \tag{5.2}$$

where

$$\delta W_{int} \quad = \quad \delta W_C + \delta W_F + \delta W_D, \tag{5.3}$$

where $\delta W_C, \delta W_F, \delta W_D$ are the work done by crack, friction and deformation, and

$$\delta W_{ext} \quad = \quad \int_V f.\delta v dv + \int_S t.\delta v ds, \tag{5.4}$$

where $\delta W_{ext}, \delta W_{int}$ are (the sum of) the external and the internal works, f, t are the body force and the traction (of $\Omega_{indenter}, \Omega_{softsolid}$), $S = \delta V$ is the traction boundary and δv is the velocity (an increment in velocity).

Briefly, with this technique, which relates the change of elastic energy in the soft solid to the variation of the global stress field, we can describe (cutting) the needle insertion into a soft solid as a process (irreversible work done by the fracture) which takes place when the stress (needed to fracture) created by the indenter reaches a limit (the magnitude or intensity that must be exceeded for a crack extension). Note that, in the case of equilibrium, the total work δW_T is zero.

5.2.1.1 Deformation before penetration (due to external and internal forces)

The recoverable part of the work done by the indenter, during the penetration process, can be expressed in terms of the following work equation [which will be used later as the basis for
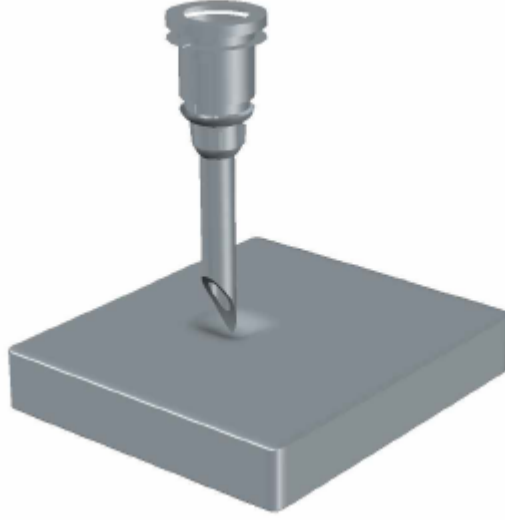
Figure 5.2: Deformation before the penetration of the needle

the finite element discretisation]:

$(\Omega_{softsolid} = V)$

$$\delta W_D = \int_V \frac{\partial \Psi}{\partial C} : DC[\delta v] dV - \int_V f.\delta v dv - \int_S t.\delta v ds, \tag{5.5}$$

which can be divided into two parts

$$\delta W_S = \int_V \frac{\partial \Psi}{\partial C} : DC[\delta v] dV \tag{5.6}$$

$$\delta W_{ext} = \int_V f.\delta v dv + \int_S t.\delta v ds, \tag{5.7}$$

where δW_{ext} is the external work of the soft solid and δW_S is the internal work done by the stress of the solid, and $\frac{\partial \Psi}{\partial C}, DC[\delta v]$ are the derivatives of stored strain energy function or elastic potential per unit undeformed volume with respect to the right Cauchy–Green tensor, the directional derivative of the right Cauchy–Green tensor in the direction of an increment in displacement (or velocity).

In general, if the soft solid material in our model is made from two or more constituent

materials with (significantly) different physical properties (different material types), which are in contact with each other (the different parts connected in various ways), the work equation (5.5), by using the definition of the contact mechanics (defined in previous Chapter), takes the following form:

$$\delta W_D\left(\Psi_1, \Psi_2, ..., \Psi_n; \delta v\right) = \sum_{i=1}^{n} \int_{V_i} \frac{\partial \Psi_i}{\partial C} : DC[\delta v] dV - \sum_{i=1}^{n} (\int_{V_i} f_i . \delta v dv +$$

$$\int_{S_i} t_i . \delta v ds) - \sum_{j=1}^{m} \sum_{a,b} \int_{\delta \Gamma_c} t_a . \delta g d\Gamma, \tag{5.8}$$

where $\Psi_1, \Psi_2, ..., \Psi_n$ are the strain energy density functions of n different material types, the first term in the right hand side corresponds to the sum of the work δW_S for n bodies, f_i, t_i are the body force and the traction of n different bodies, and the last term corresponds to the total contact work of n bodies with m connection between n bodies where a and b corresponds to two bodies which are connected with each other (surface connection between any two bodies).

One important practical example of having different material type in our model is the case study for modelling human skin, where we could need as many as eight different material types in our model for eight different human skin layers (human skin, as described in Chapter 2, is composed of three primary layers: the epidermis, the dermis and the hypodermis (fat layer) plus sub-layers, which together make up 8 layers in human skin).

Conveniently, the material models, chosen for a 5 layer epidermis, are a compressible neo-Hookean material [recall the equations (2.7), (2.8), (2.9)]

$$\Psi = \frac{\mu}{2}\left(I_C - 3\right) - \mu ln J + \frac{\lambda}{2}\left(ln J\right)^2, \tag{5.9}$$

and the materials for 2 layers dermis, are Ogden Hyperelastic (This form of the Ogden strain-energy is consistent with that used by FEBio for FEM analysis)

$$\Psi\left(\lambda_1, \lambda_2, \lambda_3\right) = \sum_{i=1}^{N} \frac{\mu_i}{m_i^2}\left(\lambda_1^{m_i} + \lambda_2^{m_i} + \lambda_3^{m_i} - 3 - m_i ln J\right) + \overbrace{U\left(J\right)}^{\frac{1}{2}c_p(J-1)^2} \quad [Ogden Unconstrained] \tag{5.10}$$

where $\lambda_1, \lambda_2, \lambda_3$ are the principal stretches and μ_i and m_i are material parameters. The term $U\left(J\right)$ corresponds to the volumetric component and J is the determinant of the deformation
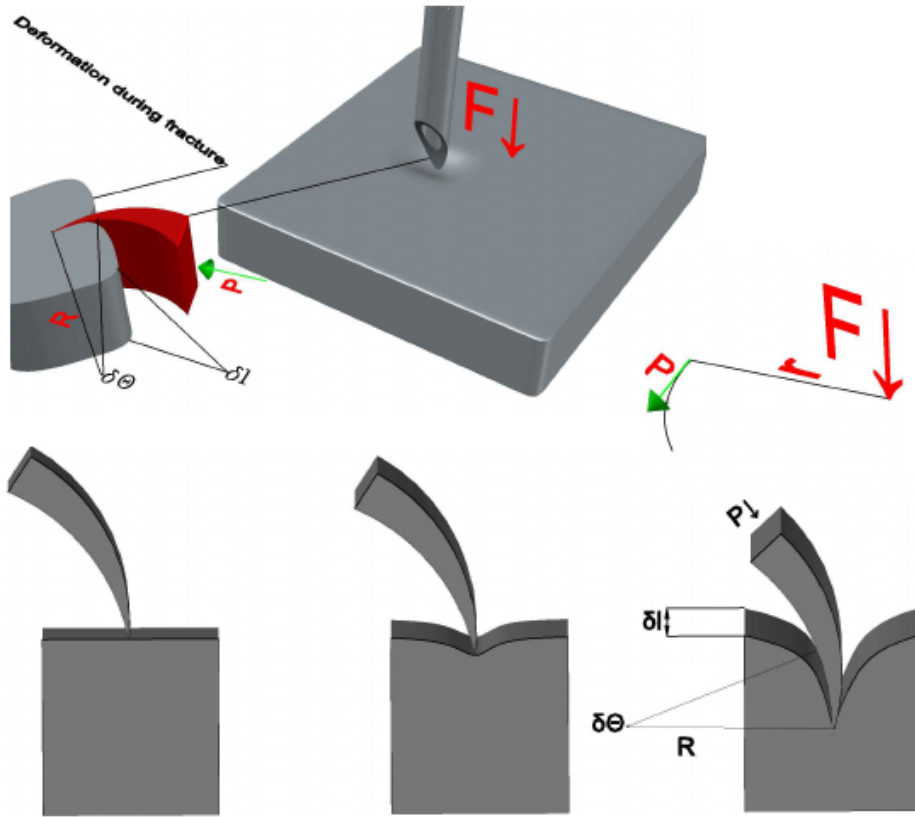
Figure 5.3: Geometrical definition of the penetration process

gradient, and the hypodermis layer is modelled as a nearly-incompressible Mooney-Rivlin material:

$$\Psi = c_1 \left(I\prime_1 - 3 \right) + c_2 \left(I\prime_2 - 3 \right) + \frac{1}{2} K \left(lnJ \right)^2 , \qquad (5.11)$$

where c_1 and c_2 are the Mooney-Rivlin material coefficients, $I\prime_1$ and $I\prime_2$ are the invariants of the deviatoric part of the right Cauchy-Green deformation tensor ($\bar{C} = \bar{F}^T \bar{F}$, where $\bar{F} = [det(F)]^{\frac{-1}{3}} F$, and F is the deformation gradient), and K is a material constant.

Thus, the equation (5.8), formulated for 8 different human skin layers, can be expressed as:

$$\delta W_D \left(\Psi_1, \Psi_2, ..., \Psi_8 \right) = \underbrace{\sum_{i=1}^{5} \int_{V_i} \frac{\partial \Psi_i}{\partial C} : DC[\delta v] dV}_{Epidermis} + \underbrace{\sum_{j=1}^{2} \int_{V_j} \frac{\partial \Psi_j}{\partial C} : DC[\delta v] dV}_{Dermis} +$$

$$\underbrace{\int_{V_h} \frac{\partial \Psi_h}{\partial C} : DC[\delta v]dV}_{Hypodermis} - \underbrace{\sum_{i=1}^{n}(\int_{V_i} f_i.\delta v dv + \int_{S_i} t_i.\delta v dS)}_{\delta W_{ext}} - \underbrace{\sum_{j=1}^{m}\sum_{a,b}\int_{\delta \Gamma_c} t_a.\delta g d\Gamma}_{Contacts} \qquad (5.12)$$

5.2.1.2 Work done by creating the cracks

For the sake of simplicity, by assuming friction-less contact interaction (or negligible frictional contact interaction), the formulation of the work done by the injector needle (steel needle) for the penetration of the soft solid, determined by a planar mode-I crack at the tip (sharp edge) in a circular form, from initial to final step, where the soft solid tears and opens at the sharp tip of the punch (opening of the crack by the advancing punch at different time steps), can be divided into two parts.

The first part, as shown in Figure (5.3), involved the deformation during the period of time preceding crack which will occur in a body before a crack is created by cutting, and the second part is the fracture itself which is the creating of the crack and the displacement of the tool which is assumed to be friction-less.

The following work equation describes the process of the total work done by creating the cracks Shergold and Fleck (2004)

$$W_C = W_{Crack} + W_{SC} - W_{D_t}, \qquad (5.13)$$

where W_{D_t} is the work done by the displacement of the tool, W_{Crack} is the non-reversible work of fracture and W_{SC} is the strain energy stored due to deformation of the body.

The work done by the displacement of the tool is given by:

$$W_{D_t} = F\delta l \quad, \qquad (5.14)$$

in integral form

$$W_{D_t} = \int_{0}^{l_{\Psi_i}} F\delta l, \qquad (5.15)$$

where $F, \delta l, l_{\Psi_i}$ are the load, the axial displacement and the depth of different bodies in our model.

To calculate the W_{SC}, we use again the work equation (5.12) [in a compact form]
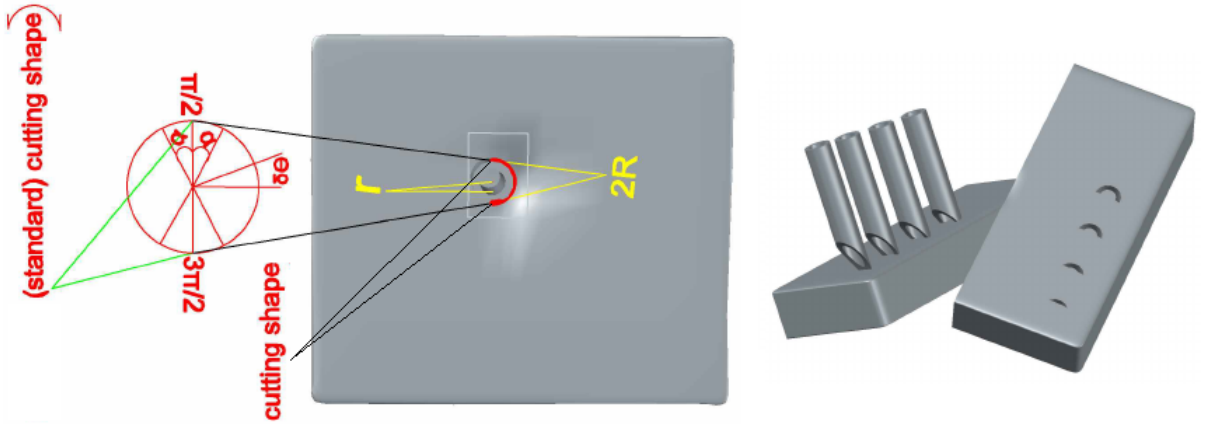
Figure 5.4: Illustration of cutting shape

$$
\delta W_{SC}(\Psi_i) \;=\; \underbrace{\int_{V_i} \frac{\partial \Psi_i}{\partial C} : DC[\delta v]dV \;-}_{internal\,stresses\,work}
$$

$$
\overbrace{-\sum_{i=1}^{n}\Big(\underbrace{\int_{V_i} f_i.\delta v dv + \int_{\delta V_i} t_i.\delta v da\Big) - \sum_{j=1}^{m}\sum_{a,b}\int_{\delta\Gamma_c} t_a.\delta g d\Gamma}_{Contacts} - \underbrace{\sum_{j=1}^{m}\sum_{a,b}\int_{\delta\bar\Gamma_c} \bar t_a.\delta g d\bar\Gamma}_{Contacts\,after\,fracture}}^{included\,in\,equation(4.12)}}_{\delta W_{ext}} , \qquad (5.16)
$$

where the contact interactions at the punch tip and the body forces and the tractions are included in the equation (5.12), but we still need to define new contact between the indenter and the soft solid after cracks (due to the creation of new surfaces).

The non-reversible work done by fracture is related to the fracture toughness of the body $J_c(\Psi_i)$ and to the size of a crack extension of length $\delta\theta$ and depth δl [see Figure (5.3)]

$$
\delta W_{Crack}(\Psi_i) \;=\; J_c(\Psi_i)R\delta l\delta\theta, \qquad (5.17)
$$

in integral form
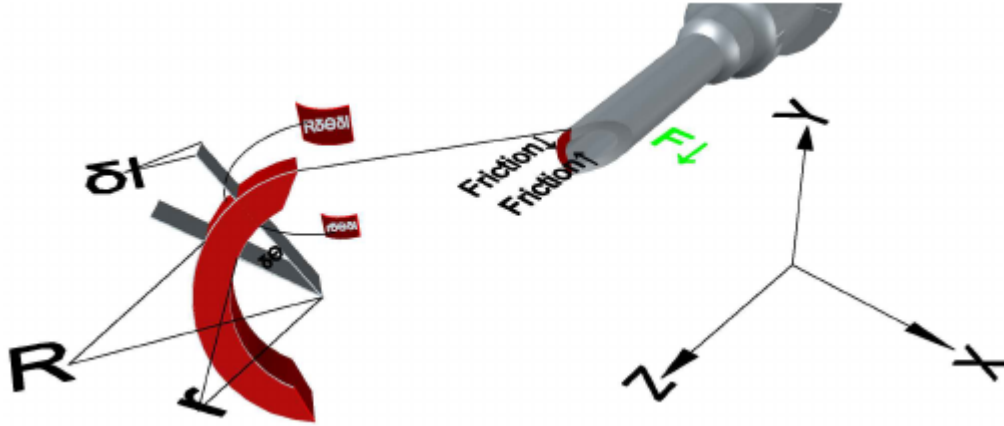
Figure 5.5: Definition of Area of Frictional Contact during cutting-penetration process

$$\delta W_{Crack}(\Psi_i) \;=\; 2 \int_0^{\frac{\pi}{2} \pm \alpha} \int_0^{l_{\Psi_i}} J_c(\Psi_i) R \delta l \delta \theta, \tag{5.18}$$

The reason for having α in the equation (5.18) is, in the case of non standard tools, the total extended length of the crack. Unlike standard tools (by which the total extended crack length is a half circle), these could be bigger or smaller than the standard length. Therefore, they need to be taken into account [see Figure (5.4)].

Now we turn our attention to the special case of a complex situated in a cutting process where the existence of the frictional contact interactions between the indenter and the soft solid will be taken into account.

The work done by friction δW_{F_C} of the size of a crack extension of length $\delta\theta$ and depth δl during the fracture process can be calculated as

$$\delta W_{F_C}(\Psi_i) \;=\; 2 \int_0^{\frac{\pi}{2} \pm \alpha} \int_0^{l_{\Psi_i}} \underbrace{\mu_{\Psi_i}.\bar{t}_a.}_{F_{f_c}(\Psi_i)} (R+r) \delta l \delta \theta \tag{5.19}$$

where μ_{Ψ_i} the friction coefficient of different materials, $\bar{t}_a$ contact pressure, and $F_{f_c}(\Psi_i)$ is the friction traction.

Thus, the total work done by creating the cracks is given by
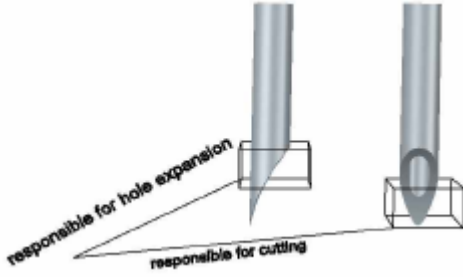
Figure 5.6: Needle head functionality (Expansion versus Cutting)

$$\delta W_C = 2\int_0^{\frac{\pi}{2}\pm\alpha}\int_0^{l_{\Psi_i}} J_c(\Psi_i)R\delta l\delta\theta + \int_{V_i}\frac{\partial\Psi_i}{\partial C}:DC[\delta v]dV - \sum_{j=1}^{m}\sum_{a,b}\int_{\delta\bar{\Gamma}_c}\bar{t}_a.\delta gd\bar{\Gamma} -$$

$$\int_0^{l_{\Psi_i}} F\delta l - 2\int_0^{\frac{\pi}{2}\pm\alpha}\int_0^{l_{\Psi_i}} F_{f_c}(\Psi_i).(R+r)\delta l\delta\theta, \tag{5.20}$$

5.2.1.3   Work done by the friction force

Now we consider the frictional work done by advancing the punch (by the displacement of the rest of the tool), as shown in Figure (5.7), which is the result of the negative work of kinetic friction, in the opposite direction to the motion, given by:

$$\delta W_F(\Psi_i) = \int_0^{l_{\Psi_i}} \underbrace{\mu_{\Psi_i}.\bar{t}_a}_{F_{f_c}(\Psi_i)}.2\pi R\delta l \tag{5.21}$$

where μ_{Ψ_i} the friction coefficient of different materials and $F_f(\Psi_i)$ the friction traction which is related to $\bar{t}_a$ contact pressure, which is itself related to the strain energy stored due to the hole expansion.

5.2.1.4   Assembly

Next, we create a standard frame base assembly using the previous defined equations, by substitution of the different components of the total work δW_T into the equation (5.1), which can be shown as the following expression
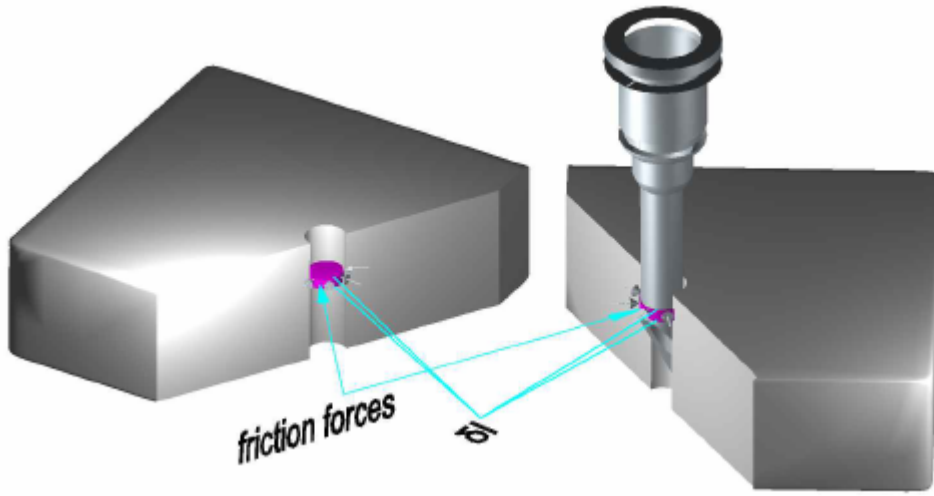
Figure 5.7: Definition of the area of the frictional contact

(formulated on the basis of human skin structure)

$$\delta W_T = \sum_{i=1}^{5} \int_{V_i} \frac{\partial \Psi_i}{\partial C} : DC[\delta v] dV + \underbrace{\sum_{j=1}^{2} \int_{V_j} \frac{\partial \Psi_j}{\partial C} : DC[\delta v] dV}_{\text{}} + \underbrace{\int_{V_h} \frac{\partial \Psi_h}{\partial C} : DC[\delta v] dV}_{\text{}} +$$

$$\underbrace{}_{Epidermis} \qquad \underbrace{}_{Dermis} \qquad \underbrace{}_{Hypodermis}$$

$$2 \int_{0}^{\frac{\pi}{2} \pm \alpha} \int_{0}^{l_{\Psi_i}} J_c(\Psi_i) R \delta l \delta \theta + 2 \int_{0}^{\frac{\pi}{2} \pm \alpha} \int_{0}^{l_{\Psi_i}} F_{f_c}(\Psi_i).(R+r) \delta l \delta \theta - \sum_{j=1}^{m} \sum_{a,b} \int_{\delta \bar{\Gamma}_c} \bar{t}_a . \delta g d\bar{\Gamma} +$$

$$\int_{0}^{l_{\Psi_i}} \underbrace{\mu_{\Psi_i} . \bar{t}_a}_{F_{f_c}(\Psi_i)} . 2\pi R \delta l - \sum_{j=1}^{m} \sum_{a,b} \int_{\delta \Gamma_c} t_a . \delta g d\Gamma -$$

$$\int_{0}^{l_{\Psi_i}} F \delta l - \{ \underbrace{\sum_{i=1}^{n} (\int_{V_i} f_i . \delta V dv + \int_{S_i} t_i . \delta V ds)}_{\delta W_{ext}} \} \quad Problem(NI) \tag{5.22}$$

Now, with the problem (*NI*), the non-linear system equation (5.22), can be formed first by linearising the equation and then discretising it using a suitable numerical scheme.

Remark 5.1: ....

The complicated expression (5.22) can be reduced to a simpler one, in other words, we can express the steady-state penetration process in terms of the work done in advancing the indenter (as a part of the external work δW_{ext}) and the work done in creating the crack(s)

(GcA where A is the new crack area) plus the strain energy stored in the soft solid [S(Ψ_i)], by using the existing contact algorithm ($\sum_{j=1}^{m} \sum_{a,b} \int_{\delta\Gamma} t_a.\delta g d\Gamma$), and the friction definition ($\sum_{\forall i,j,\beta} \int_{\partial\Omega_\Gamma} t_f^i.\tau^\beta (u_j^\beta - u_i^\beta) d_{\partial\Omega_\Gamma}$), but the trouble is, we should be able to define (automatically during the cutting process) new contact between the indenter and the soft solid after cracks (due to the creation of new surfaces), which is currently not (supported) defined in the existing contact algorithms (the algorithm of so-called auto contact mechanic where it will not be necessary to have a pre-defined contact area (master and slave contact surfaces) can solve this problem).

However, this can be calculated for an arbitrary geometry using existing techniques, but we need a cohesive zone fracture implementation. In other words, this problem can be overcome by using the modified contact algorithm defined in a previous chapter where the contact definition between the indenter and the soft solid before and after cracks stays the same.

....

5.2.2   Mechanics of cutting

In this section, by using the constitutional model of the cohesive fracture formulation through contact mechanics, the mathematical formulation of the mechanisms of cutting will be demonstrated.

The complicated mechanics of the cutting process, involving many different factors such as the stress and the deformation distributions/productions throughout the deformable solid, as shown in Figure (5.8), due to the applied (normal and tangential) forces to the deformable body by the cutting tool, and which in examination of the total energy balance E_{total} (globally conserved for the current system) [Holzapfel (2000b)], based on the global conservation law Laursen (2003), and under consideration of Griffith's theory Kundu (2008), can be considered as a total variational equation, mathematically, split into several parts; namely, the internal and external mechanical and thermal energies (applied mechanical energy, total strain energy and applied thermal energy), the friction energy, the contact energy, the fracture energy, the heat energy, the work done by the sharp tool motions and the kinetic energy, which can be formulated as the following general framework for the energy consistent treatment of the total system:

$$\frac{DE_{total}}{Dt} = \frac{D}{Dt}\{\sum_{\forall i|\forall\Omega|\forall\partial\Omega_\sigma}(\underbrace{\int_\Omega U_i^t d_\Omega}_{Total strain energy} \underbrace{- \int_\Omega b_i.u_i d_\Omega - \int_{\partial\Omega_\sigma} t_\sigma^i.u_i d_{\partial\Omega_\sigma}}_{Applied energy}) + \sum_{\forall\partial\Omega_\Gamma}[$$
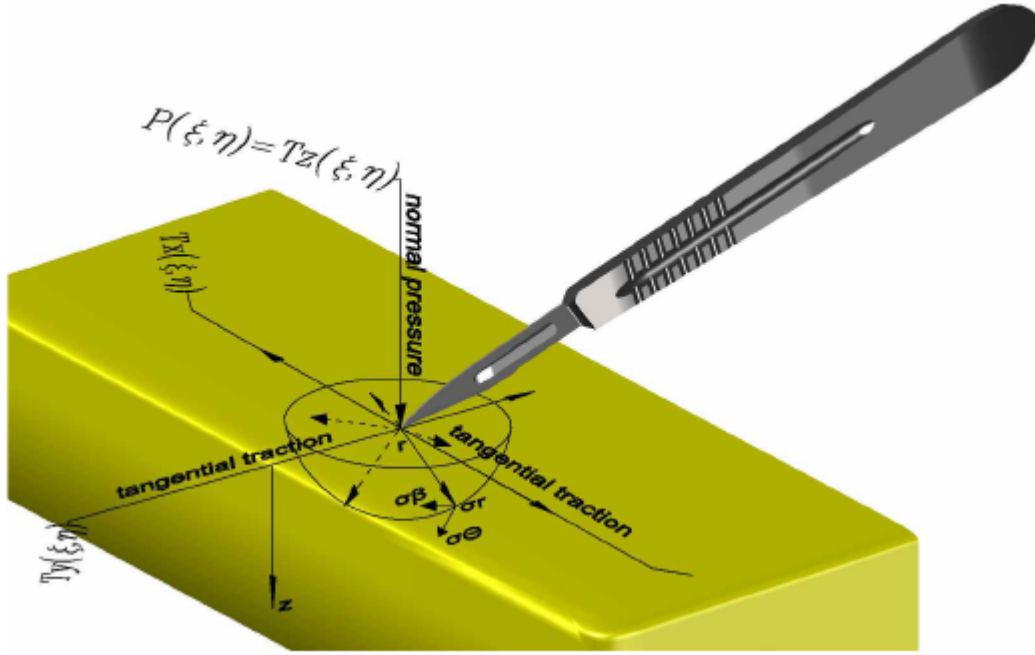
Figure 5.8: Geometrical description of Cutting process

$$\underbrace{\sum_{\forall i,j,\beta}\int_{\partial\Omega_\Gamma} t_f^i.\tau^\beta(u_j^\beta - u_i^\beta)d_{\partial\Omega_\Gamma}}_{Fracture Surface-Friction energy} - \underbrace{\sum_{\forall s,m}\int_{\partial\Omega_\Gamma}(q_c^s + q_c^m)_t d_{\partial\Omega_\Gamma}}_{Fracture Surface-Thermodynamic energy} - \underbrace{\sum_{\forall i,j}\int_{\partial\Omega_\Gamma} T_N^i(u_i^* - u_j^*)d_{\partial\Omega_\Gamma}]}_{Contact} -$$

$$\underbrace{\sum_{\forall\partial\Omega_\Gamma}(\int_{\partial\Omega_\Gamma} T_x\{u_i\}d_{\partial\Omega_\Gamma} + \int_{\partial\Omega_\Gamma} T_y\{u_i\}d_{\partial\Omega_\Gamma} + \int_{\partial\Omega_\Gamma}[P=T_z]\{u_i\}d_{\partial\Omega_\Gamma})}_{\iint_s Tx(\xi,\eta)\phi d\xi d\eta + \iint_s Ty(\xi,\eta)\phi d\xi d\eta + \iint_s[P(\xi,\eta)=Tz(\xi,\eta)]\phi d\xi d\eta} +$$

$$\underbrace{\sum_{\forall\partial\Omega_\Gamma}\int_{\partial\Omega_\Gamma} G_c[G_{Ic} \mid G_{IIc} \mid G_{IIIc}]d_{\partial\Omega_\Gamma}}_{Fracture energy} + \underbrace{\sum_{\forall\Omega}(\int_\Omega C(T_{current} - T_{initial})\rho d_\Omega}_{Heat energy} +$$

$$\sum_{\forall i|\forall\Omega|\forall\partial\Omega}[\underbrace{\int_\Omega\frac{1}{2}\rho(\frac{\partial u_i}{\partial t})(\frac{\partial u_i}{\partial t})d_\Omega}_{Kinetic energy} - \underbrace{\int_\Omega R^t d_\Omega + \int_{\partial\Omega} Q^t N d_{\partial\Omega}]}_{Applied Thermal energy}\} = 0, \quad Problem(MOC) \quad (5.23)$$

[assumption:

- $\frac{DE_{total}}{Dt} = 0$ [(for more detailed information see appendix C part (5)]
- Contact condition is frictional]

Where

$$Q_{supply} = \underbrace{\sum_{\forall s,m} \int_{\partial\Omega_\Gamma} (q_c^s + q_c^m) d_{\partial\Omega_\Gamma}}_{Fracture Surface-Thermodynamic power} + \underbrace{\sum_{\forall\Omega}(\int_\Omega R d_\Omega - \int_{\partial\Omega} Q_N d_{\partial\Omega})}_{Applied Thermal power}, \tag{5.24}$$

is the heat supply to the system per unit time, $Tx(\xi,\eta), Ty(\xi,\eta), [P(\xi,\eta) = Tz(\xi,\eta)]$ with $(\{u_i\} = u_i^* - u_j^*)$ are the tangential and the normal traction-pressure [as shown in Figure (5.9)], R is the heat source, $Q_N = \kappa\nabla T.N$ is the heat supply flux normal to the boundary $\partial\Omega_i$, ρ is the mass density, $G_c[G_{Ic} \mid G_{IIc} \mid G_{IIIc}]$ are the fracture energy per unit area due to the creation of the new crack surface (mode I,II,III), U_i the strain energy per unit volume of different materials, $W_t = \sum_{\forall i}(\int_\Omega b.u_i d_\Omega + \int_{\partial\Omega_\sigma} \bar{t_\sigma}.u_i d_{\partial\Omega_\sigma})$ the total work done by applied loads, ∇T temperature gradient, C heat specific value and κ is heat conductivity and T_N^i, t_f^i are the contact traction (t_N^i contact pressure) and the friction traction.

Note that, due to the assumption that the heat enters the body, we have

$$Q_N(x,t,N) = -Q_N(x,t).N, \tag{5.25}$$

in other words, inward normal flux (opposite to N outward normal to the $\partial\Omega$).

With the above formulation of the cutting process in terms of the total energy balance E_{total} [Problem (MOC)] in hand, we can now develop the weak formulation [conversion into the work expression $\delta W_T(v_i, T_i, \delta v, \delta T)$-constitute minimal] of E_{total} by using the definition of the directional derivative [$\Delta := D_{[\delta u,\delta v]}f(u) = \frac{d}{d\varepsilon}f(u+\varepsilon[\delta u,\delta v])|_{\varepsilon=0}$ the directional derivative in the direction of the incremental (displacement or velocity) field $\delta u, \delta v$], which is formulated with the following expression[2]

$$\delta W_T(v_i, T_i, \delta v, \delta T) = \sum_{\forall i|\forall\Omega|\forall\partial\Omega_\sigma}[\underbrace{\int_\Omega \frac{\partial U_i}{\partial e} : De[\delta v] d_\Omega}_{Internal work \delta W_{int}^{mech}} - \underbrace{\int_\Omega b_i.\delta v d_\Omega - \int_{\partial\Omega_\sigma} t_\sigma^i.\delta v d_{\partial\Omega_\sigma}}_{External work \delta W_{ext}^{mech}}] -$$

$$\underbrace{\sum_{\forall\partial\Omega_\Gamma}(\int_{\partial\Omega_\Gamma} T_x\delta g_N d_{\partial\Omega_\Gamma} + \int_{\partial\Omega_\Gamma} T_y\delta g_T d_{\partial\Omega_\Gamma} + \int_{\partial\Omega_\Gamma} [P = T_z]\delta g_T d_{\partial\Omega_\Gamma})}_{D_{\delta v}(\iint_s Tx(\xi,\eta)\phi d\xi d\eta + \iint_s Ty(\xi,\eta)\phi d\xi d\eta + \iint_s [P(\xi,\eta)=Tz(\xi,\eta)]\phi d\xi d\eta) = \delta W_{trac}} + \sum_{\forall\partial\Omega_\Gamma}($$

$$\underbrace{\sum_{\forall i,j,\beta}\int_{\partial\Omega_\Gamma} t_f^i.\delta g_T d_{\partial\Omega_\Gamma}}_{FractureSurfaceFrictionwork\delta W_{fric}} - \underbrace{\sum_{\forall s,m}\int_{\partial\Omega_\Gamma} (q_c^s.\delta T^s + q_c^m.\delta T^m)d_{\partial\Omega_\Gamma}}_{FractureSurfaceThermodynamicwork\delta W_{Fst}}) + \sum_{\forall i|\forall\Omega|\forall\partial\Omega}[$$

$$\underbrace{\{\int_\Omega -R_i\delta T^i d_\Omega + \int_{\partial\Omega} Q_i N_i \delta T^i d_{\partial\Omega}\}}_{Externalwork\delta W_{ext}^{ther}} + \underbrace{\int_\Omega C_i\frac{\partial T}{\partial t}\rho_i\delta T^i d_\Omega}_{Heatinternalwork\delta W_{heat}} + \underbrace{\int_\Omega \kappa_i\nabla T^i.\nabla\delta T^i d_\Omega]}_{Internalwork\delta W_{int}^{ther}}+$$

$$\underbrace{\sum_{\forall\partial\Omega_\Gamma}[\int_{\partial\Omega_\Gamma} TG_c[TG_{Ic}\mid TG_{IIc}\mid TG_{IIIc}][\delta g_N\mid\delta g_T]d_{\partial\Omega_\Gamma}}_{Fracturework\delta W_{frac}} - \underbrace{\sum_{\forall i,j}\int_{\partial\Omega_\Gamma} t_N^i\delta g_N d_{\partial\Omega_\Gamma}]}_{Contactwork\delta W_{contact}} + \underbrace{\sum_{\forall i|\forall\Omega}\int_\Omega \rho_i(\frac{\partial^2 u_i}{\partial t^2})\delta v d_\Omega,}_{Kineticwork\delta W_{\kappa inetic}}$$

$$(5.26)$$

or with the following simple notation

$$\delta W_T(v,T,\delta v,\delta T) = \delta W_{int}^{mech} - \delta W_{ext}^{mech} - \delta W_{trac} + \delta W_{ext}^{ther} + \delta W_{Fst}+$$

$$\delta W_{contact} + \delta W_{fric} + \delta W_{heat} + \delta W_{int}^{ther} + \delta W_{frac} + \delta W_{\kappa inetic}, \qquad (5.27)$$

where $\delta W_{Fst}, \delta W_{fric}, \delta W_{contact}, \delta W_{frac}$ have been described in details in previous chapter [(for more detailed information see appendix C part (5)].

The term δW_{int}^{mech}, the internal mechanical work expression, defined in the reference or current configuration respectively, can also be formulated as

$$\delta W_{int}^{mech} = \sum_{\forall i}\int_\Omega \frac{\partial U_i}{\partial e} : De[\delta v]d_\Omega = \sum_{\forall i}\int_\Omega \sigma_i : [F^{-T}D_{\delta v}E(X,t)F^{-1}]d_\Omega =$$

$$\sum_{\forall i}\int_{\Omega_0} S_i : \{\frac{DE(X,t)}{Dt} = D_{\delta v}E(X,t)\}d_{\Omega_0} = \sum_{\forall i}\int_{\Omega_0} \frac{\partial U_i}{\partial C} : D_{\delta v}C[E(X,t)]d_{\Omega_0} =$$

$$\sum_{\forall i}\int_{\Omega_0} \{P_i = \frac{\partial U_i}{\partial F}\} : D_{\delta v}F d_{\Omega_0} = \sum_{\forall i}\int_{\Omega_0} J\sigma F^{-T} : D_{\delta v}F d_{\Omega_0}, \qquad (5.28)$$

which deserves a little more attention [(for more detailed information see appendix C part (5)]. In the case when all the thermodynamic properties of the system are taken into consideration, the strain energy function $U_i = U_i(F,\theta)$ [generally called Helmholtz free energy function and denoted by $\Psi(F,\theta)$] will be dependent on two independent variables, namely deformation gradient F and temperature θ. Thus, by applying the chain rule, the internal

mechanical work δW_{int}^{mech} can be expressed as

$$\delta W_{int}^{mech} = \sum_{\forall i} \int_{\Omega_0} \{P_i = \frac{\partial U_i}{\partial F}\}_\theta : D_{\delta v} F d_{\Omega_0} + \sum_{\forall i} \int_{\Omega_0} \{\eta_i(X,t) = -\frac{\partial U_i}{\partial \theta}\}_F D_{\delta v} \theta d_{\Omega_0}, \quad (5.29)$$

where $\eta(X,t)$, is the entropy describing thermoelastic materials, and P is the first Piola-Kirchhoff stress.

Note that, the free energy $\Psi(F, \theta(F, \eta))$ can also be expressed as a function of two independent variables, namely deformation gradient F and the entropy η, which is related to the internal energy $e^{int}(F, \eta)$, through the Legendre transformation, by the following expression

$$e^{int}(F, \eta) = \Psi(F, \theta(F, \eta)) + \theta(F, \eta)\eta, \quad (5.30)$$

Where, by using the chain rule again, the time derivative of the equation (5.30) is given by

$$\frac{De^{int}(F,\eta)}{Dt} = \underbrace{P : F^{\cdot} - \eta \theta^{\cdot}}_{\frac{D\Psi(F,\theta(F,\eta))}{Dt}} + \underbrace{\theta^{\cdot}(F,\eta)\eta + \theta(F,\eta)\eta^{\cdot}}_{\frac{D\theta(F,\eta)\eta}{Dt}} = \underbrace{\frac{\partial e^{int}(F,\eta)}{\partial F}}_{P} : F^{\cdot} + \underbrace{\frac{\partial e^{int}(F,\eta)}{\partial \eta}}_{\theta} . \eta^{\cdot},$$

$$(5.31)$$

which leads to the new physical expressions for the first Piola-Kirchhoff stress P and the temperature θ.

Linearisation, Discretization

To process the numerical approximation of the Problem (*MOC*) [- by using a similar strategy when solving the Problem (*NI*)] and in order to develop the discrete equation of motion (and to be able to discuss later the global solution strategy), first, we compute the linearisation[3] of the total work δW_T, in the current description, followed by discretisation.

Detailed linearisation and discretization are contained in Appendix C (part 4), where also solution methods and stability-accuracy analysis are discussed.

5.2.3   Implementation

To simulate the needle insertion and cutting, by using previously described constitutional models, the method (and the implementation) of the modified contact, defined in detail in Chapter 4, has been adapted to the computational models describing the penetration processes, where the independent change between contact with cohesive force and the classical contact makes
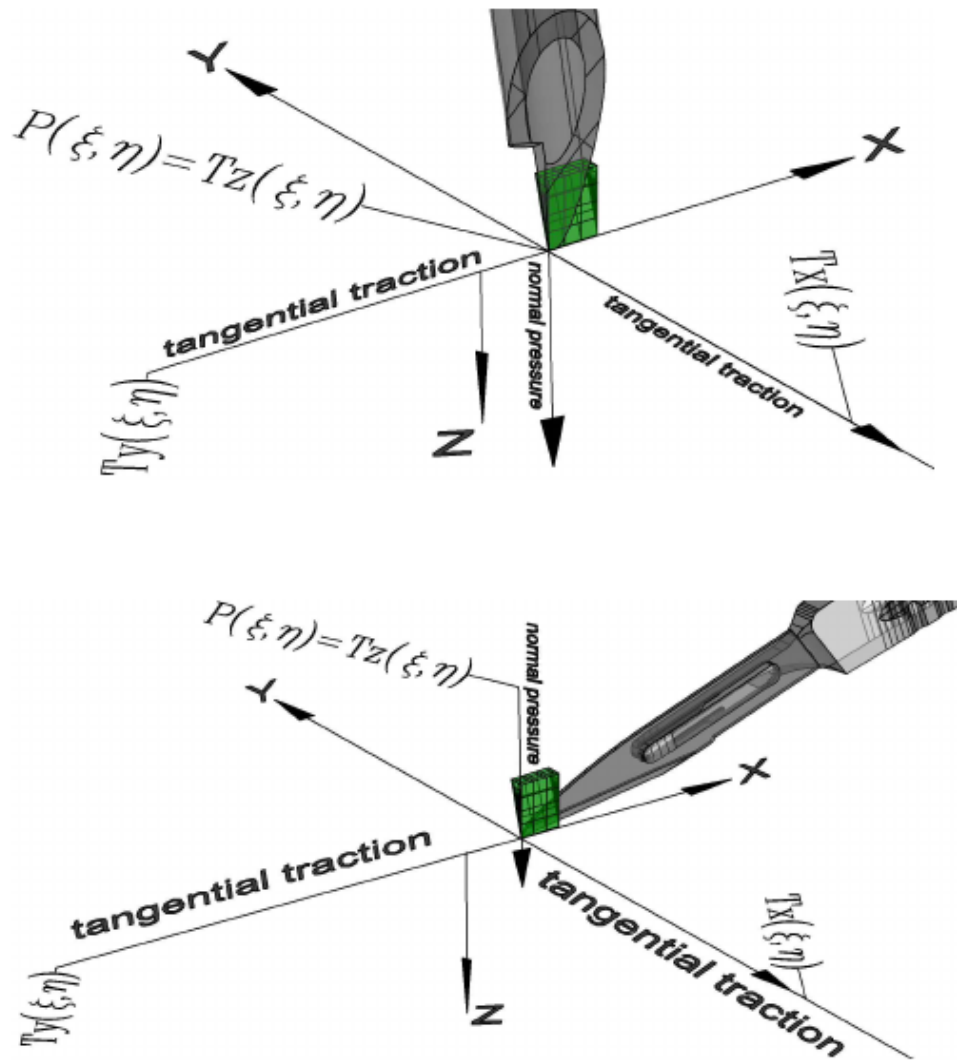
Figure 5.9: Geometrical description of the models

the process of the sharp interaction between the cutting tool and the specimen more accurate and easier to simulate.

The finite element analysis of the needle insertion and cutting, the represented dynamic systems, were carried out by using FEBio package (an implicit non-linear finite element solver) where, beside using the (implemented) existing non-linear constitutive models [compressible, incompressible, nearly incompressible models such as neo- Hookean, Ogden, Mooney-Rivlin, etc. and supported techniques to process different analysis methods (static, quasi static and dynamic) which deal also with a wide range of contact boundary conditions and allow the user to create and analyse complex problem involving complicated mechanical and bio-mechanical behaviour], was making use of the created algorithms based on the specially for-
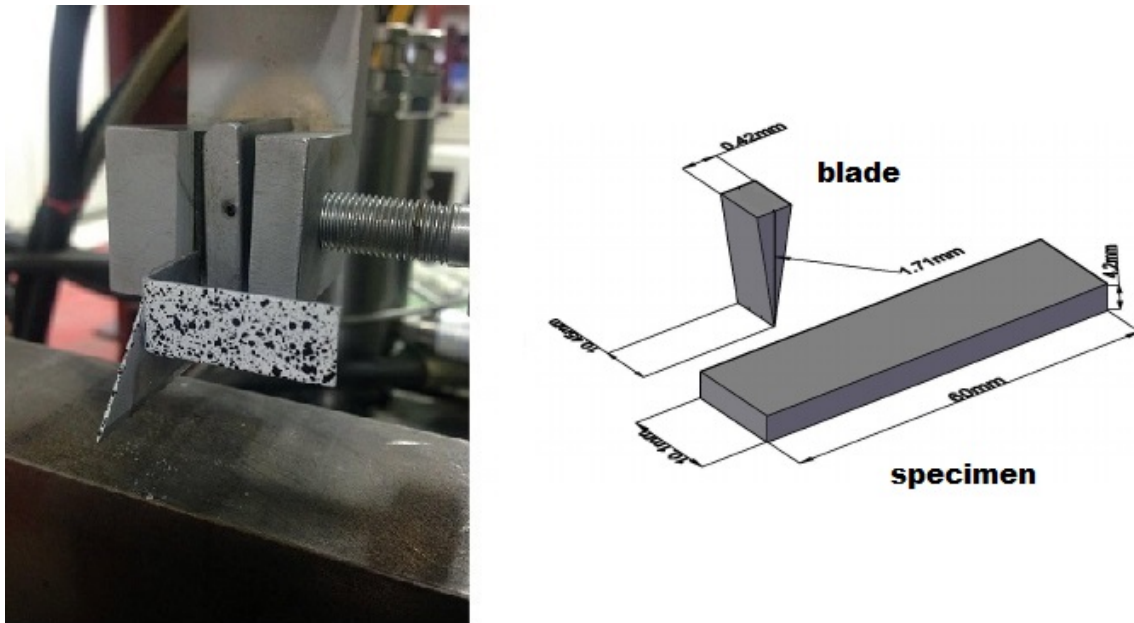
Figure 5.10: Extra body (metal) part attached to the blade for DIC test and the specimen and blade dimensions

mulated non-linear constitutive models [the constitutive model of the cohesive fracture formulation through existing contact mechanics, and additionally the constitutive models of friction and the thermodynamically coupled friction with the associated boundary values that, relevant to a particular field (complicated interactions between the indenter and the specimen during a (full) needle insertion and cutting process), which were implemented and added to the (existing) original FEBio source code, described in the previous Chapter].

5.2.4 Computational and Experimental Models (numerical and experimental approaches)

5.2.4.1 Experimental cutting approaches on silicone rubber

By making use of a tool with sharp prismatic straight cutting edge (Cutting Blade), a series of cutting tests were accomplished with the samples of the different silicone rubber materials (material with different mechanical properties)[with initial width: 10.1 mm, height: 60 mm, depth: 4.2 mm]. Additionally, by using a digital image correlation and tracking technique we were able to collect more accurate 2D and/or 3D measurements of the image sequences during tests which were later used to measure displacement and strain in more accurate ways.

An especially suitable machine which is designed for a wide range of testing situations, the Zwick Roell universal testing machine described in Chapter 3, was used to develop the tests,
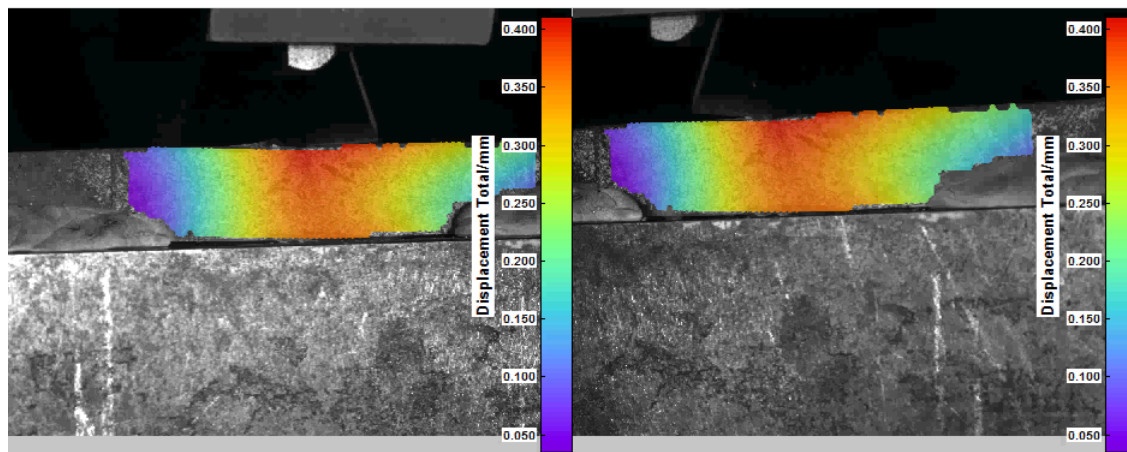
Figure 5.11: The measurements of Digital image correlation (DIC) for full-field image analysis of cutting test on silicone rubber

where the blade was attached to the load cell of the machine [and, as shown in Figure (5.10), an extra metal part was attached to the blade allowing more accurate DIC measurement of the displacement of the cutting tool], which allowed the cutting tool to perform cutting in the direction orthogonal to the surface of the specimen where the samples were supported (freely sliding)by one face to a solid metallic plate (a solid part of the machine).

The machine (arm) was programmed to have constant velocity of $1 - 10\,mm/min$ (to cut at this speed) and maximum load of $9 - 10\,N$, where the resulting forces, for different values of the velocity and load, have been measured by the machine.

The DIC measurements of the entire process of cutting, proceeded first for the displacement field on the surface of the specimen, captured by two cameras on one tripod, where each image, as shown in Figure (5.11), represents capturing the subject from different viewpoints (different angles). The test conditions are given in Table 5.2.

5.2.4.2   Computational model of cutting approaches on silicone rubber

A computational model to simulate the needle insertion and cutting, based on the collected experimental data (experimental model for cutting test on silicon rubber by using the Zwick universal testing machine, described in the previous section), and making use of FEBio package (PreView, PostView, FEBio), has been created and analysed as follows, where the computational model for the simulation of the entire process of the needle insertion and cutting, as shown in Figure (5.10), has been reduced to the simplified model for the sharp interaction.

The steps involved in the construction of a computational model were:

Firstly, the creation of a geometrical model [using PreView-Finite Element (FE) prepro-
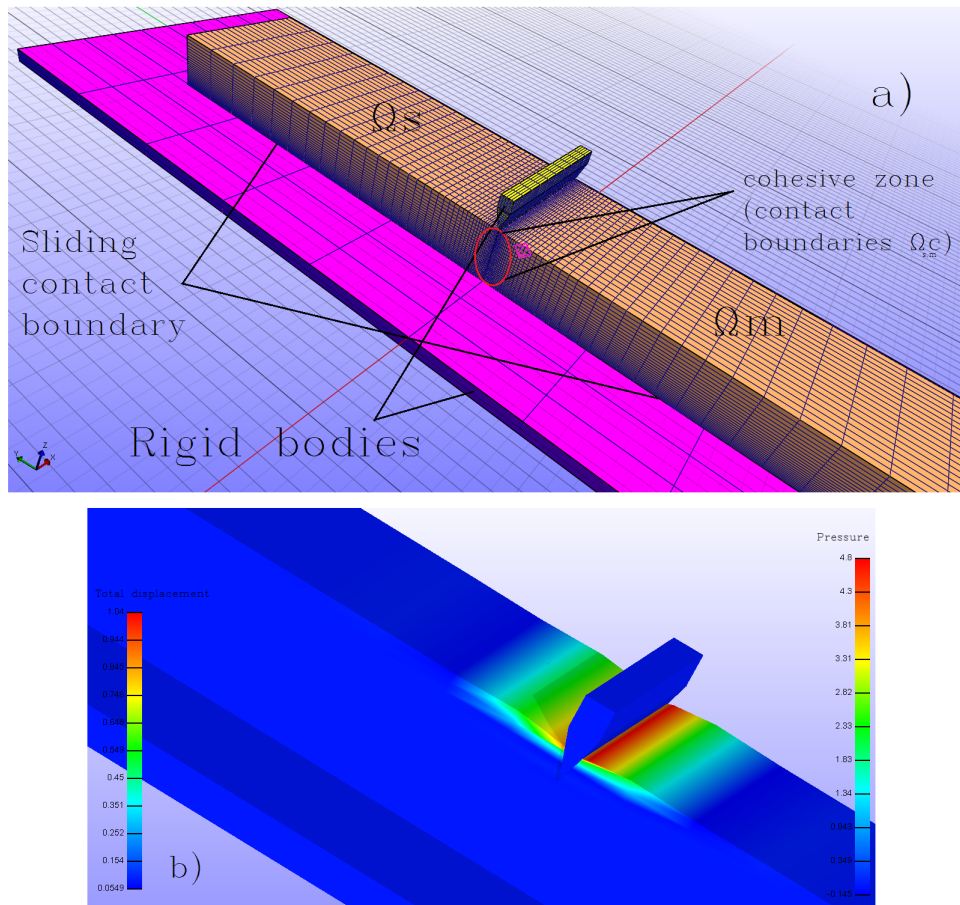
Figure 5.12: a) The Finite Element (FE) Preprossessing model , b) the Finite Element Post-prossessing model of cutting model

Type of material	Young modulus	Poisson's ratio	Interfacial nor./tan.strength
Neo Hookean hyperelastic	$E1 = 0.777\,MPa$	$v1 = 0.48$	$0.61477\,MPa$
Neo Hookean hyperelastic	$E2 = 0.527\,MPa$	$v2 = 0.35$	$0.34235\,MPa$
Neo Hookean hyperelastic	$E3 = 0.813\,MPa$	$v3 = 0.43$	$0.79311\,MPa$
Neo Hookean hyperelastic	$E4 = 0.723\,MPa$	$v4 = 0.41$	$0.59311\,MPa$
Critical strain energy (G_c)	Gap tolerance	Disp. tolerance	Energy tolerance
$277.91\,N/mm$	0	0.001	0.01
Nonlinear solution method	Time steps	Step size	Max retries
$Full-Newton$	1000	0.0001	25
Analysis type	Max step	Min step	Max refs
$Dynamic$	0.01	0.0001	4500
Auto timestep-controller	Penalty	Density	Ch. opening length
$checked$	8190	$1\frac{kg}{m^3}$	$0.0061477\,mm$

Table 5.1: Mechanical properties of the silicone rubber (the specimens) and the cohesive interface and the test conditions (numerical)

Measuring instruments	Zwick universal testing machine
	DIC system
DIC Analysis	software Istra 4D
Calibration plate	size: 105 x 148 mm²
Imaging Speed	500 - 1000 frames/sec
Grip	Circular Bollard Grip
Measuring	Force, displacements and strains

Table 5.2: Test conditions (experimental)

cessor] which was identical in geometry to the experimental model (by making use of the geometrical data of the cutting tool (blade) and the specimen (silicone rubber), collected from experimental tests)[two deformable bodies (width: 10.1 mm, height: 30 mm, depth: 4.2 mm, element type regular linear hexahedral, the parameters of the mesh nx = 20, ny = 10, nz = 26, x-ratio=1, y-ratio=1.1, z-ratio=1.0535) and rigid body (cutting tool, width: 10.45 mm, height: 4.2 mm, depth: 1.71 mm, element type hexahedral, the parameters of the mesh slices=5, loops=10, stacks=10, z-ratio=1 r-ratio=1) and second rigid body (width: 25 mm, height: 80 mm, depth: 1 mm, the parameters of the mesh nx = 10, ny = 10, nz = 10) as shown in Figure (5.12)].

Secondly, a suitable material model was defined that could be effectively used to simulate the cutting process, using a neo Hookean hyperelastic model with the material parameters (based on the previously measured material parameters of the manufactured silicone rubbers) given in Table 5.1.

Due to the cohesive fracture formulation of the problem which was based on the modified contact formulation, the parameters for the pre-defined cracked surface, the normal and the tangential interfacial strengths and characteristic length, as shown in Figure (4.2), were defined. The model consisted of two identical bodies (two deformable bodies as described earlier) connected with each other at the contact surfaces (master and slave surfaces), where the cohesive zone was defined by using the modified contact (the parameters are given in Table 5.1). Also a sliding contact was defined between second rigid body and the two deformable bodies (contact type sliding node-on-facet, penalty=8190, no augmented Lagrangian and enabled auto penalty). To keep the virtual cutting tool at a constant orientation, during the simulation rigid constraints were applied [rigid fixed displacement (applying constraint to x,y,Rx,Ry,Rz degree of freedoms) and rigid prescribed displacement=-215.162] to the rigid body (the cutting tool).

Final step, after setting up the boundary conditions was, setting up the analysis which was Structural Mechanics analysis [and selecting the analysis type dynamic and setting up energy,
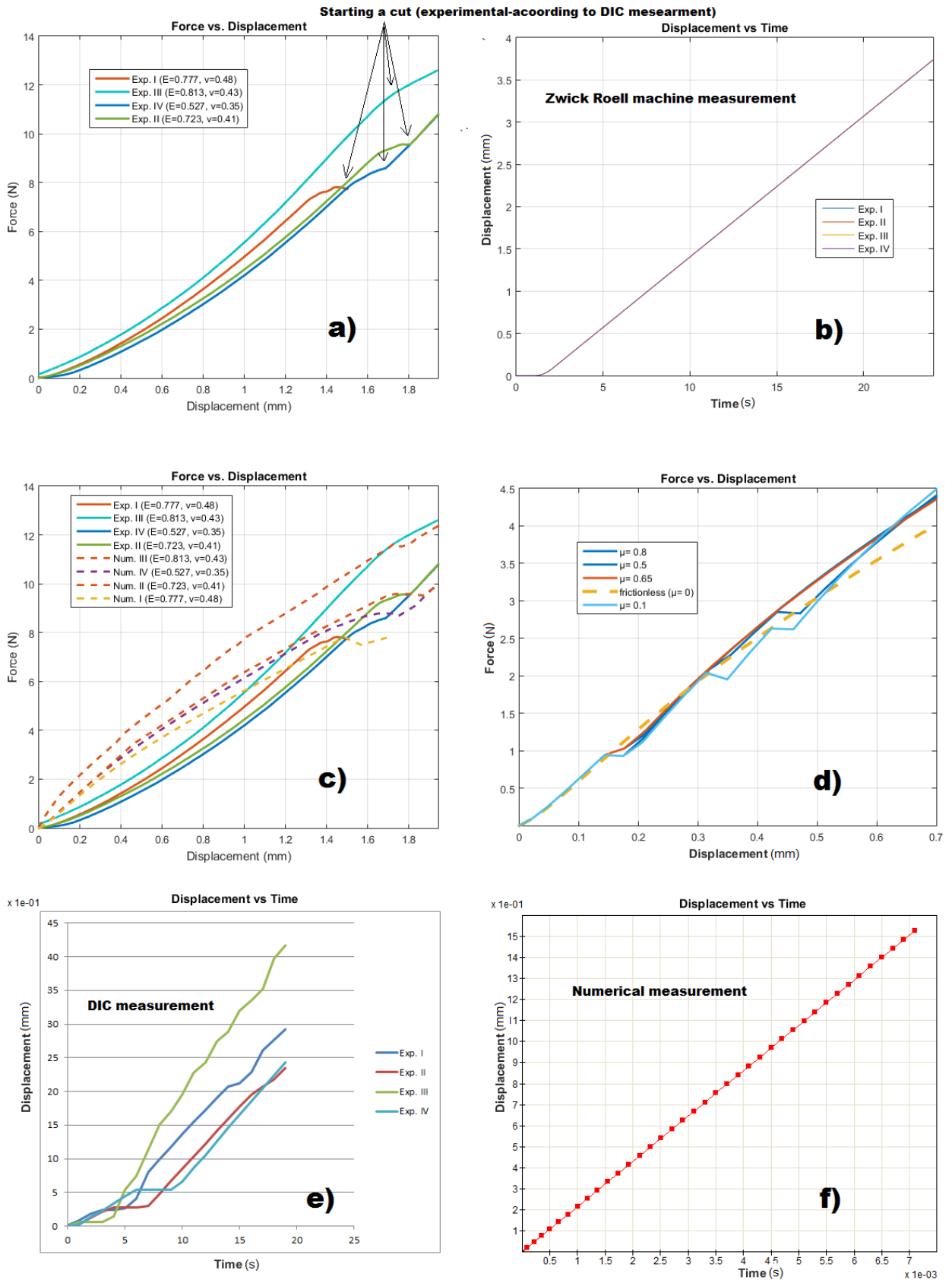
Figure 5.13: a) Experimentally measured force-displacement curves, b) Experimentally measured displacement-time curves, c) Computational vs. Experimental results, d) Numerical measurement of (reaction) forces vs. displacement for the different friction coefficient values $\mu = 0.1 - 0.8$, e) DIC measurements, f) Computational displacement-time curve

displacement and residual tolerances and other parameters such as time step, step size etc. (given in Table 5.1)] and running FEBio.

5.2.4.3   Results

The test results (analysed in Postview-finite element post processor), as shown in Figure (5.13-a, b), are the force-displacement and displacement-time curves created by the Zwick Roell machine, where the cutting tests with the various silicon rubber materials (silicon rubbers with different material properties) have been proceeded.

Further insight can be gained by looking at Figure (5.13-a), which shows some limitations of the experimental data, where without using the DIC measurements, the exact determination of the cutting start point from the data can not be easily done (the limitations can be also effected by the velocity of the cutting tool during the test). More specifically, as can be seen in Figure (5.13-a), this limitation is clearly visible for the silicone rubber specimen with the material property $E3 = 0.813\,(MPa)$ and $v3 = 0.43$. Another detection limit of the experimental apparatus was the limitation to measure the effect of friction, more precisely, the determination of the coefficient of friction for the various models. As a direct consequence of this limitation, can be the limitation of computational approaches (which could correctly predicts/reproduces experimental results) where the sensibility of the algorithm to the effect of friction is high. Although this is a fairly minor point for the proposed cutting problem, nevertheless, consideration of the effect of friction in numerical models could improve the results.

Figure (5.13-d) shows the numerical measurement of the virtual cutting tool (reaction) forces vs. displacement, where the frictional contact problem [the friction force due to the sliding contact between cutting tool and the deformable bodies and due to the friction force between master and slave surfaces (contact-cohesive zone)] was considered by choosing different values for the friction parameters, namely the friction coefficient and the friction penalty value $\mu = 0.1 - 0.8$, $\varepsilon_f = 100$. As can be seen in Figure (5.13-d), the presence of the friction has a appreciable effect on the deformation pattern.

Figure (5.13-e) also shows the DIC measurements obtained in the cutting test of silicon rubber specimens where the measurement of the displacement of the cutting tool from the start of the cutting test to the end point of the test was based on displacement of the extra attached metal part to the blade [see Figure (5.10)].

The variation in (reaction) force in relation to displacement (in z direction-zero reaction forces and displacement in x and y directions) of the virtual cutting tool, the plotted computational simulation result and the experimental cutting test (experimental versus numerical), as shown in Figure (5.13-c), the results obtained for the various models reveals a good agree-

ment between the results obtained with the proposed finite element algorithm for the cutting problem in comparisons with the experimental results. Note that Figure (5.13-c) shows similar variation of reaction forces with respect to vertical displacement, specially where the first cutting occurs along the cutting tool (the specimens start cutting) for both numerical and experimental models.

Summarizing, despite some important local behaviour captured due to the contact cohesive treatment, these numerical experiments suggest that the computational model of cutting is able to describe and simulate experimental cutting process where the above-mentioned also suggest to get more qualitative fit to experimental data (as was mentioned earlier in previous chapter), beside the optimal choice for (contact, friction etc) parameters, the reduction of the non smoothness of the contact interactions with the aim of making the numerical approach more robust (for example smooth surface parametrisation such as bi-Hermitian smoothing procedure), also improving the result in terms of cohesive fracture formulation, and other factors such as adaptive mesh refinement need to be considered.

5.3   Conclusion/Discussion

In this chapter, in terms of the cohesive fracture formulation, described and developed in the previous chapter, the constitutional models of the needle insertion and cutting process were developed, where the introduced constitutional models in this chapter were able to cover the definitions of the local deformation before penetration, the fracture process, the friction and the thermodynamic.

The major purpose of the present chapter was to validate the computational model (computational model using modified contact with experimental validation) where, due to reasons of convenience, the experimental and the computational models of the needle insertion and cutting were defined by simplifying the models as a sharp interaction (cutting and interaction) between a deformable body and a cutting tool [described as a tool with sharp prismatic straight cutting edge (cutting blade)] where silicon rubber type materials as deformable bodies/specimens were chosen for the experimental cutting tests and for the computational cutting tests a Neo Hookean hyperelastic material type was selected.

The computational model, developed in this chapter, was not limited to the uniform vertical motion of the cutting tool, where the efficient models [e.g. the solution was independent of the topology of mesh (confirming or non-confirming mesh] could also be used to simulate a complex cutting process involving horizontal and vertical motion of the cutting tool simultaneously during simulation.

This is aside from issues related to the computational model, listed as follows:

- Dependence of the solution on the normal and tangential interfacial strengths and the characteristic opening lengths.

- In the case of large deformation, the mesh refinement techniques must be considered.

- The crack path is predefined in the finite element mesh.

- Frictional contact, which causes a lack of convergence (convergence is not occurring every time).

An interesting issue which has been examined is the sensitivity of the experimental result to the velocity of the cutting tool during the test which would have a direct effect on the under-resolving of some local details. In addition to this issue which make the determination of the cutting start point (measurement of the amount of force needed when the specimens first start cutting), very difficult task, another issue was the detection limit of the experimental apparatus with regard to measurement of the effect of friction, more specifically, the determination of the coefficient of friction for the various models, where consideration of the effect of friction in numerical models could improve the numerical results and provide more qualitative fit to experimental data. At this point it's important to say that although the results obtained from the application of different values of the friction coefficients to the computational model revealed that setting a best-fit friction coefficient (manually setting for the best empirical match) can improve the overall results, but it increases computational complexity, which for example in the case of implementation of an efficient parallel algorithm (improvement of algorithmic efficiency) could be overcome. However, comparison the proposed finite element algorithm for the cutting problem with experimental data which was made for all experimental results obtained for the various models where a good agreement between numerical and experimental results was to be noted in general, suggest that to achieve more desired results, using the modified contact algorithm in this way, beside applying three dimensional surface smoothing techniques such as bi-Hermitian patches or Gregory patches to three dimensional finite element mesh with the goal to reduce the non smoothness of the contact interactions, applying re-meshing techniques, other factors such as optimum boundary condition, coefficient of friction, material property etc. need to be considered as well.

Chapter 6

Conclusion

The principal aim of this thesis was to develop important knowledge of the mechanical (bio-mechanical) properties of human skin, which is a required step, particularly in the development of physical models of the skin suitable for cutting and needle insertion. Gaining a broad knowledge of human skin, in other words, having a deep understanding of the human skin bio-mechanics made it possible for this thesis developer to better understand and analyse the cutting process and needle insertion, allowing for an effective, repeatable and informative engineering solution to the penetration problem.

To be able to develop a mutually beneficial and deep knowledge of the mechanical properties of human skin, in Chapter 2 the functionality of human skin was discussed. It was followed by the description of the skin layers in terms of the functions of three primary layers of skin, namely the epidermis, the dermis and the hypodermis. Then, a detailed summary of the most recently employed methods within experimental and computational modelling techniques of the skin (the computational models of the skin that have been clinically and experimentally validated) was presented.

Chapter 3 aimed to establish methods which were used to develop a physical model of human skin suitable for cutting test and needle insertion into human skin where the methods allowed accurate measurement of the mechanical properties of the physical model. The tensile tests and indentation measurements were applied to the manufactured silicon rubber in the laboratory by using the Zwick compression-tensile testing machine and Digital Image Correlation (DIC) technique to characterise the mechanical properties of the sample. The measurement of the mechanical properties of the samples (such as shear modulus, Young's modulus etc.) were performed (for each manufactured silicon rubber in the laboratory) using an analytical study on the indentation method, curve fitting technique and DIC measurements, where MATLAB and Microsoft Excel were used for non-linear curve fitting and the goodness of fit, which is typically used to measure the similarity between measured values and

the values of the model in a problem, was examined for input functions (Neo-Hookean material model). Then, the results were compared to the experimentally obtained mechanical properties of human skin in vivo/ ex vivo (from published studies). Based on the results, this study suggests, adding fibres to silicone rubber could improve the tensile strength of silicone properties and provide more quantitative and qualitative fit with experimental data. Applying Digital Image Correlation powerful functions such as strain and displacement mapping to the test analysis methodology has proven the DIC technique to be an accurate method, which made it able to produce the desired outcome for most cases involved in this project. Also it was shown that the full 3D DIC is capable of handling the tensile and indentation tests more accurately than the conventional methods. However, besides experimental conditions and issues, additional work - such as improvement of the DIC data processing software - can be investigated to improve the DIC results. Due to the very complex material behaviour of skin, with its non-homogeneous, anisotropic, non-linear viscoelastic mechanical characteristics, it was noted that the so generated physical model of skin can be used to simulate its general mechanical behaviour, and to provide fully accurate results, high level investigations need to be built. It needs to be said that the variations in the mechanical characteristics of the physical model of the skin in comparison to the real skin model are not just limited to the physical model of the skin. It has also been shown by some researchers that even in vivo and ex vivo measurements of the mechanical properties of the skin vary Groves (2008), Kiss and Brebbia (2013) (An overview of such in vivo and in vitro experiments revealed that in most of these experimentally performed tests, the complexity of the mechanical properties of the skin are reduced and regarded, for example, as a homogeneous non-linear elastic solid where mostly quite simple constitutive equations are used for highlighting the fundamental principles and straightforward nature of the mechanical behaviour of skin).

The main focus of Chapter 4 was on the objective " implementation of the Modified Contact Mechanics using traditional finite element method (FEM)" where the modification of the classical contact to provide a specific implementation of a mesh independence method for straight forward controlling of non-linear fracture mechanical processes using the Mixed Mode Cohesive-Zone method, and the determination of the constitutive relationship which consisted of a combination of both contact mechanics formulations and the Strong Cohesive Law, alongside the thermodynamically coupled friction formulated in one contact structure, was discussed. Then, it was followed by the implementation (modifying FEBio-package), computational models, practical and analytical tests, where the proceeded practical and analytical test methods of classical contact, contact with cohesive forces, the thermodynamically coupled frictional problem, in support of successful algorithms and implementations and their constituents, were presented. The convergence analysis of the numerical methods was also

provided. Using the methods of (the so-called) mortar finite element analysis for contact mechanics, variational inequality and hemivariational inequality, the development of the convergence analysis of the unilateral contact problem, frictional contact problem and frictional-Contact-Cohesive problem, were proceeded. It was shown that, with modified contact definition, the so-called discontinuities can be modelled in different complex geometry and analysed in a sophisticated way. It has also been proved that the redefinition of contact mechanics in this way fulfils the condition of the cohesive zone law and additionally supports the physical ideas and mathematical structures of the classical contact mechanic. Also, this study suggests, making use of the modified contact approach could help to overcome the issue with cohesive surface location and orientation [due the fact that the placement of cohesive zones can presenting a problem, specially, when the choice of cohesive surface location and orientation can be an important fact where the solid is appropriately modelled as homogeneous Needleman (2014), in other words, because the interface elements are aligned with elements boundaries, so the orientation of cracks is restricted and limited which makes the placement of cohesive interfaces between all continuum not completely mesh independent van der Zwaag (2007)].

In Chapter 5, using the constitutional models of the cohesive fracture formulation through the contact mechanics described and developed in Chapter 4, the constitutional models of the needle insertion and cutting process were developed, where the introduced constitutional models in this chapter, the mathematical and physical clarification of the mechanisms of cutting and needle insertion formulated as a general framework for the energy consistent treatment of the total system (the total energy balance of a globally conserved system) under consideration of Griffith's theory and the internal and external mechanical and thermal energies (the work done by external and internal forces), were able to cover the definitions of the local deformation before penetration, the fracture process, the friction and the thermodynamic. For reasons of convenience, the experimental and the computational models of the needle insertion and cutting were defined by simplifying the models as a sharp interaction (cutting) between a deformable body and a cutting tool [described as a tool with sharp prismatic straight cutting edge (Cutting Blade)] where the previously manufactured silicon rubber in the laboratory as deformable bodies/specimens were chosen for the experimental cutting tests (experimental tests using Zwick compression-tensile testing machine and Digital Image Correlation (DIC) technique) and for the computational cutting tests Neo Hookean hyperelastic material type were selected).

The computational model, developed in Chapter 5, was not limited to the uniform vertical motion of the cutting tool, where the efficient models [e.g. the solution was independent of the topology of mesh (confirming or non-confirming mesh] could also be used to simulate

complex cutting process involving horizontal and vertical motion of the cutting tool simultaneously during simulation.

Aside from the issues related to computational model (which were, the solution dependence on the normal and tangential interfacial strengths and the characteristic opening lengths, necessary consideration of the mesh refinement techniques in the case of large deformation and defining fracture model independent of the existence of any predefined crack in the finite element mesh) an interesting observation, beside some experimental apparatus limitations such as accurate measurement of the effect of friction, which was made was the sensitivity of the experimental result to the velocity of the cutting tool during the test, which would have a direct effect on the under-resolving of some local details.

Naturally there were several important issues (detected or undetected) related to modified contact formulation, depending on the different applications which need to be considered. An especially significant issue relating to modified contact was the sensibility of models to geometrical information (e.g. projection to surface and gap function was extremely dependent on correct geometrical information) which had a direct result on the unsuccessful termination of FEBio [the generated geometrical issues were due to some existing software issue in PreView-Finite Element (FE) preprocessor]. Another case of great significance was the right selection of the (material, contact, etc.) parameters, which could also open the possibility of the disadvantageous and divergence from desired results.

Nonetheless, a comparison of the models based on numerical, analytical and experimental examinations revealed good to very good agreement between numerical, analytical and experimental results, where the numerical experiments suggest to get more qualitative results, beside the optimal choice for contact cohesive parameters, the reduction of the non smoothness of the contact interactions (applying smooth surface parametrisation such as bi-Hermitian smoothing procedure), need to be considered.

Despite the success of this study, further investigations, such as additional validation procedures of the computational cutting model, fixing existing issues (e.g. solution difficulty such as "negative Jacobian" , etc.), effective mesh refinement, implementation of an efficient parallel algorithm and accuracy improvement of finite element solutions, need to be done to improve algorithmic efficiency.

Chapter 7

Future work

As mentioned earlier in this study, further investigations need to be done to improve the accuracy, efficiency and robustness of the algorithms. Accordingly, aside from the generation of a more accurate physical model of skin, the future work of this project will be to undertake the following actions using the modified FEBio source code, developed in this study.

It needs to be said that the future work of this study will also be to develop an additional validation method by using experimental data to validate the numerical cutting model. In other words, by using full-field optical strain measurements obtained using digital image correlation and full-field strain measurements obtained from the computational cutting model, and based on the Fourier-Tchebichef decomposition method introduced in the study Sebastian *et al.* (2011), further validation procedures of the computational cutting model will be performed.

7.1 Mesh optimization

It is a known fact that dealing with boundary value problems associated with large deformations using traditional finite element methods is often a difficult task. In most cases, particularly large deformation problems experience mesh distortions, especially in large sliding-deformation contact problems where it is mostly difficult to obtain a convergent solution. Consequently, using the finite element code, a wide variety of research techniques are implemented in mesh optimisation-refinement studies, such as combining an updated Lagrangian method with an efficient adaptive re-meshing algorithm, Arbitrary Lagrangian Eulerian (ALE) and re-meshing algorithm Mengoni *et al.* (2016), h-adaptive mesh refinement algorithm Mohammadi and Taiebat (2015), the Coupled Eulerian-Lagrangian (CEL) approach Ducobu *et al.* (2016).

Generally, the mesh-optimisation-refinement strategy, while avoiding the mesh distortion

problem specially in large deformations, requires prior to FE analysis the determination of the

Jacobian matrix $\begin{pmatrix} J_{11} & J_{12} & J_{13} & ... \\ J_{21} & J_{22} & J_{23} & ... \\ J_{31} & J_{32} & J_{33} & ... \\ ... & ... & ... & ... \end{pmatrix}$ for all mesh elements. The Jacobian value depends

on the configuration of the element nodes and ranges from -1.0 to 1.0, where 1.0 represents a perfectly shaped element. If, for a given node, the Jacobian is negative $J^e_{node} < 0$, the element is invalid and, consequently, an element with the negative Jacobian cannot be solved, meaning the FE analysis cannot be accomplished.

Furthermore, Jacobian Ratio $J^e_{ratio}(at\ a\ node) = \frac{J^e_{node}}{maximum_{node \in e}J^e_{node}}$ which measures the quality of the mesh node (indicating good or poor quality) is used to get overall distortion information.

To process the mesh-optimisation-refinement (relaxation procedure), first the variation of Jacobian $\frac{\partial J^e_{node}}{\partial x^{node}_i}$ or Jacobian Ratio must be calculated, then the optimisation process must be carried out by improving the mesh nodes which Jacobian need to be improved, while to avoid computation complexity, fixing strategy is proceeded only on the repair regions R where all nodes inside the regions are repaired and the configuration of the outside regions stays unchanged. Additionally, the so-called validity energy $E_{valid} = \sum_{J \in R} \overbrace{\varepsilon(J)}^{1-e^{-kJ}}$, using a penalty function $\varepsilon(J)$, is defined and through a maximisation process is used to find a configuration where all the Jacobian values in the repair regions are positive Bucki *et al.* (2011).

Depending on the application of various types of meshing elements (tetrahedral, hexahedral etc.) to different classes of finite element problems, different mesh refinement strategies are proposed by a wide range of studies, such as DelaunayÕs tetrahedral reconstruction method (DelaunayÕs refinement method) Li *et al.* (2013), automatic adaptive mesh refinement based on modified superconvergent patch recovery (MSPR) Khoei *et al.* (2013), mesh refinement algorithm based on a decentralised approach using tetrahedral meshes Olas and Wyrzykowski (2012). The finite element mesh regeneration, which could be applied to FEBio to repair invalid or eventually poor element quality, mostly, could be mesh regeneration algorithms for hexahedral meshes, because (for example) quadrilateral surface elements associated with hexahedral elements, particularly defined on sliding interface where the integration points are located at the nodes, would not imply zero weight at the corner nodes. Also the curvature of the surface at $\psi_m(\bar{Y}(X))$, $\kappa_{\alpha\beta} = v.\psi_m(\bar{Y}(X))_{,\alpha\beta}$, would not be zero (in contrast to triangular surface elements). One such algorithm which could be used to generate high quality hexahedral meshes, applicable for various types of solid models, is introduced by Sun and Zhao (2016).
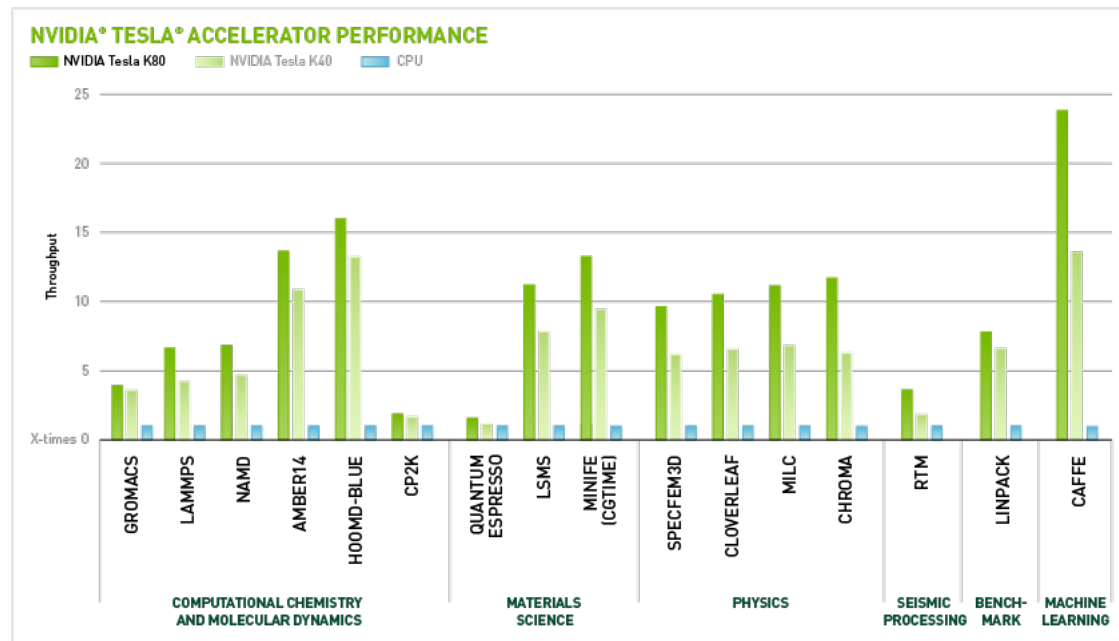
Figure 7.1: CPU versus GPU performance [the possible performance levels of new generation NVIDIA GPU (NVIDIA® Tesla® GPU accelerators)]

7.2 Parallel Computing using CUDA

Nowadays, the finite element method (FEM) has become one of the most accurate and effective methods for finding approximate solutions to (initial) boundary value problems for partial differential equations (PDE). However, the overall computational complexity of the algorithms, Which are used to develop FEM, grow with the precision of the results and becoming increasingly expensive. One way of solving the computational complexity problem would be by defining simpler complexity classes which could be used to solve the same problem. Moreover, an elegant way to control the amount of resources that are needed by the FEM algorithm to solve a problem, would be using a powerful parallel computing platform for scientific applications, generally speaking, by making use of graphics processing units (GPU).

It needs to be said that using the parallel computing platform is not just limited by FEM; for instance, a parallel computing based on the element by element (EBE) method and using unified device architecture (CUDA[1]) reported by Wu *et al.* (2015), a formulation of the finite-difference time-domain (DGF-FDTD) method on a graphics processing unit (GPU) introduced by Dziubak *et al.* (2015) and a discrete element method (DEM) implementation with CUDA demonstrated by Qi *et al.* (2015).

---

[1]The CUDA® parallel computing platform provides a few simple C and C++ extensions that enable the expression of fine-grained and coarse-grained data and task parallelism (NVIDIA)

The implementation and optimisation of the non-linear implicit finite element solver (FE-Bio code) using NVIDIA graphics cards and the CUDA programming environment, while the situation does not change qualitatively for PDEs, can be proceeded by integrating CUDA code into the existing FEBio C++ classes, while because CUDA is written as an extension to the C-Programming Language, we need to put all the CUDA routines into separate (.cu-)files and access them using so called wrapper-functions [e.g. calling the kernel functions (CUDA methods) from the C++ host code]. A framework that can be used for easy CUDA integration in C++ applications is presented by Breitbart (2009).

Very large speed-ups (depending on the generations of GPUs) using CUDA-enabled GPUs will allow us to develop more complex models involving large deformations that are exposed to (extreme) boundary conditions.

7.3   Auto contact mechanics

As noted in Remark 5.1, to define an automated procedure for contact configuration during simulation process, the algorithm of the so-called auto contact mechanic which could be used to define master and slave contact surfaces automatically, could be applied to the modelling problem. Consequently, pre-defined contact interfaces would not be necessary.

Such an approach would limit the computational cost and computational complexity by eliminating (the unnecessary computations for) outside the regions of interest. In particular, once the algorithm of the nearest neighbour has been proceeded, the search algorithm (algorithm for detecting the regions of interest of a surface) of auto contact can be processed to determine and set the temporary master and slave surfaces, while the remainder of the contact algorithm remains unchanged.

Note that the auto contact shall not be exaggerated with the so-called self contact problem, which is a special case of contact problem related to the nearest neighbour search method and can be solved numerically if the master and slave surfaces are defined so that surfaces have coincident.

References

Adra, S., Sun, T., MacNeil, S., Holcombe, M. and Smallwood, R. 2010. Development of a three dimensional multiscale computational model of the human epidermis. *PLoS ONE* 5(1).

Agache, P., Monneur, C., Leveque, J. and De Rigal, J. 1980. Mechanical properties and young's modulus of human skin in vivo. *Archives of Dermatological Research* 269(3), pp. 221–232.

Alfano, M., Furgiuele, F., Leonardi, A., Maletta, C. and Paulino, G. 2007. Cohesive zone modeling of mode i fracture in adhesive bonded joints. *Key Engineering Materials* 348-349, pp. 13–16.

Annaidh, A. N., Destradea, M., Ottenio, M., Bruyere, K. and Gilchrist, D. M. 2014. Strain rate effects on the failure characteristics of excised human skin. *9th International Conference on the Mechanics of Time Dependent Materials* University College Dublin.

Annaidh, A. N., Destradea, M., Ottenio, M., Bruyere, K., Gilchrist, D. M. and OMaanio, S. L. 2012. Characterization of the anisotropic mechanical properties of excised human skin. *Journal of the Mechanical Behavior of Biomedical Materials* 5(1), pp. 139 – 148.

Arruda, E. M. and Boyce, M. C. 1993. A three-dimensional constitutive model for the large stretch behavior of rubber elastic materials. *Journal of the Mechanics and Physics of Solids* 41(2), pp. 389 – 412.

Auricchio, F. 1996. Augmented lagrangian finite-elements for plate contact problems. *International Journal for Numerical Methods in Engineering* 39, pp. 4 141–4158.

Azar, T. and Hayward, V. 2008. Estimation of the fracture toughness of soft tissue from needle insertion. *4th International Symposium* 5104, pp. 166–175.

Bader, D. and Bowker, P. 1983. Mechanical characteristics of skin and underlying tissues in vivo. *Biomaterials* 4.

Bancelin, S., Lynch, B., Bonod-Bidaud, C., Ducourthial, G., Psilodimitrakopoulos, S., Dok-ladal, P., Allain, J.-M., Schanne-Klein, M.-C. and Ruggiero, F. 2015. Ex vivo multiscale quantitation of skin biomechanics in wild-type and genetically-modified mice using multi-photon microscopy .

Barel, A., Courage, W. and Clarys, P. 1995. Suction method for measurement of skin mechanical properties: the cutometer In: Serup, J. and Jemec, G.B.E. (eds.) Handbook of Non-Invasive Methods and the skin. Boca Raton, CRC Press.

Bischoff, J. E., Arruda, E. M. and Grosh, K. 2000. Finite element modeling of human skin using an isotropic, nonlinear elastic constitutive model. *Journal of Biomechanics* 33(6), pp. 645 – 652.

Bodhale, D., Nisar, A. and Afzulpurkar, N. 2010. Structural and microfluidic analysis of hollow side-open polymeric microneedles for transdermal drug delivery applications. *Microfluidics and Nanofluidics* 8(3), pp. 373–392.

Breitbart, J. 2009. *A framework for easy CUDA integration in C++ applications*. Ph.D. thesis, Computer Science and Electrical Engineering, Universitšat Kassel.

Bucki, M., Lobos, C., Payan, Y. and Hitschfeld, N. 2011. Jacobian-based repair method for finite element meshes after registration. *Engineering with Computers* 27(3), pp. 285–297.

Buganza Tepole, A., Gosain, A. and Kuhl, E. 2014. Computational modeling of skin: Using stress profiles as predictor for tissue necrosis in reconstructive surgery. *Computers and Structures* 143, pp. 32–39.

Buitrago, D., Ruiz, L. and Ramos, O. 2015. Stress-strain analysis and simulation for estimation of cutting forces on the skin. *International Review of Mechanical Engineering* 9(6), pp. 583–588.

Conroy, M., Kinloch, A., Williams, J. and Ivankovic, A. 2015. Mixed mode partitioning of beam-like geometries: A damage dependent solution. *Engineering Fracture Mechanics* 149(1), pp. 351–367.

Dabrowska, A. K., Rotaru, G.-M., Derler, S., Spano, F., Camenzind, M., Annaheim, S., Stäm-pfli, R., Schmid, M. and Rossi, R. M. 2016. Materials used to simulate physical properties of human skin. *Skin Research and Technology* 22(1), pp. 3–14.

Dancik, Y. H. 2004. A computational model of transient drug/chemical diffusion through human skin in the vicinity of a hair follicle. *Controlled Release* 98, pp. 367–378. Chemical and Biological Engineering, University at Buffalo.

De Morais, A. 2014. Cohesive zone beam modelling of mixed-mode i-ii delamination. *Composites Part A: Applied Science and Manufacturing* 64, pp. 124–131.

Dijk, B. V. 2007. The nonlinear mechanicalproperties of engineered soft biological tissues determined by finite spherical indentation Eindhoven University of Technology.

Doyen, D., Ern, A. and Piperno, S. 2010. A three-field augmented lagrangian formulation of unilateral contact problems with cohesive forces. *ESAIM: Mathematical Modelling and Numerical Analysis* 44(2), pp. 323–346.

Ducobu, F., Rivière-Lorphèvre, E. and Filippi, E. 2016. Application of the coupled eulerian-lagrangian (cel) method to the modeling of orthogonal cutting. *European Journal of Mechanics, A/Solids* 59, pp. 58–66.

Dziubak, T., Wiktor, M., Orlowski, S. and Stefanski, T. 2015. Acceleration of the dgf-fdtd method on gpu using the cuda technology.

Escoffier, C., Rigal, J. D., Rochefort, A., Vasselet, R., Leveque, J. and Agache, P. 1986. Age related mechanical properties of human skin. *Investigative Dermatology* 93.

Evans, S. and Holt, C. 2009. Measuring the mechanical properties of human skin in vivo using digital image correlation and finite element modelling. *Journal of Strain Analysis for Engineering Design* 44(5), pp. 337–345.

Fakhouri, S., Hutchens, S. and Crosby, A. 2015. Puncture mechanics of soft solids. *Soft Matter* 11(23), pp. 4723–4730.

Fan, H. and Li, S. 2016. A three-dimensional surface stress tensor formulation for simulation of adhesive contact in finite deformation. *International Journal for Numerical Methods in Engineering* 107(3), pp. 252–270.

Galvanetto, U. and Aliabadi, M. 2009. *Multiscale Modeling in Solid Mechanics: Computational Approaches*. Computational and Experimental Methods in Structures.

Gasser, T. C., Holzapfel, G. A. and Ogden, R. W. 2005. Hyperelastic modelling of arterial layers with distributed collagen fibre orientations pp. 15–35. Published online 2005.

Geerligs, M., Gerrit, W., Paul, P., Cees, A., Oomens, W. and Baaijens, F. P. 2008. Linear viscoelastic behavior of subcutaneous adipose tissue Eindhoven University of Technology.

Gladilin, E. 2002. Biomechanical modeling of soft tissue and facial expressions for craniofacial surgery planning pp. 1–145. Universitaet Berlin.

Grebenyuk, L. and Utenkin, A. 1994. Mechanical properties of the human skin Human Physiology.

Groves, R., Coulman, S., Birchall, J. and Evans, S. 2012. Quantifying the mechanical properties of human skin to optimise future microneedle device design. *Computer Methods in Biomechanics and Biomedical Engineering* 15(1), pp. 73–82.

Groves, R. B. 2008. *Quantifying the mechanical properties of skin in vivo and ex vivo to optimise microneedle device design*. Ph.D. thesis, Cardiff University.

Han, W., Migorski, S. and Sofonea, M. 2014. A class of variational-hemivariat ional inequalities with applications to frictional contact problems. *SIAM Journal on Mathematical Analysis* 46(6), pp. 3891–3912.

Harper, P. and Hallett, S. 2008. Cohesive zone length in numerical simulations of composite delamination. *Engineering Fracture Mechanics* 75(16), pp. 4774–4792.

Hayes, W. C., Keer, L. M., Herrmann, G. and Mockros, L. F. 1970. A mathematical analysis for indentation tests of articular cartilage Department of Applied Mechanics. Stanford University, Stanford. California.

Hellan, K. 1984. *Introduction to Fracture Mechanics*. McGraw-Hill Inc.,US. ISBN-13: 978-0070280489.

Hendriks, F. M. 2005. Mechanical behaviour of human epidermal and dermal layers in vivo Technische Universiteit Eindhoven.

Hillerborg, A., Modéer, M. and Petersson, P.-E. 1976. Analysis of crack formation and crack growth in concrete by means of fracture mechanics and finite elements. *Cement and Concrete Research* 6(6), pp. 773–781.

Holzapfel, G. A. 2000a. Biomechanics of soft tissue Graz University of Technology.

Holzapfel, G. A. 2000b. *Nonlinear Solid Mechanics: A Continuum Approach for Enineering: A Continuum Approach for Engineering (Mechanical Engineering)*. Wiley; 1 edition. ISBN-13: 978-0471823193.

Jemec, G., Jemec, B., Jemec, B. and Serup, J. 1990. The effect of superficial hydration on the mechanical properties of human skin in vivo: Implications for plastic surgery. *Plastic and Reconstructive Surgery* 85(1), pp. 100–103.

Kaliske, M., Özenç, K., Fleischhauer, R. and Steinke, C. 2015. Modelling of fracture in elastomers. pp. 13–22.

Khoei, A., Eghbalian, M., Moslemi, H. and Azadi, H. 2013. Crack growth modeling via 3d automatic adaptive mesh refinement based on modified-spr technique. *Applied Mathematical Modelling* 37(1-2), pp. 357–383.

Kim, J. H., Lim, J. H., Lee, J. H. and Im, S. 2008. A new computational approach to contact mechanics using variable-node finite elements. *International Journal for Numerical Methods in Engineering* 73(13), pp. 1966–1988.

Kiss, R. and Brebbia, C. A. 2013. *Modelling in medicine and biology X*. Southampton : WIT Press.

Koppel, D., Chandrasekaran, S. and Wang, Y.-F. 2008. A new framework for behavior modeling of organs and soft tissue using the boundary-element method.

Kravchuk, A. S. and Neittaanmäki, P. J. 2007. *Variational and Quasi-Variational Inequalities in Mechanics*. Springer Netherlands. ISBN 978-1-4020-6377-0.

Kundu, T. 2008. *Fundamentals of Fracture Mechanics*.

Labanda, N., Giusti, S. and Luccioni, B. 2015. Stability and error estimate of a cohesive zone model implemented using the augmented lagrangian method. pp. 314–326.

Lapeer, R. J., Gasson, P. D. and Karri, V. 2011. A hyperelastic finite-element model of human skin for interactive real-time surgical simulation. *IEEE Transactions on Biomedical Engineering* 58(4), pp. 1013–1022.

Laursen, T., Yang, B. and Pusot, M. 2004. Implementation of frictional contact conditions in surface to surface, mortar based computational frameworks.

Laursen, T. A. 2003. *Computational Contact and Impact Mechanics: Fundamentals of Modeling Interfacial Phenomena in Nonlinear Finite Element Analysis*. Springer, ISBN: 9783540429067.

Lebedev, L. P., Vorovich, I. I. and Cloud, M. J. 2012. *Functional Analysis in Mechanics*. Springer Science & Business Media. ISBN: 1461458676, 9781461458678.

Lebedev, L. P., Vorovich, I. I. and Gladwell, G. 2002. *Functional Analysis: Applications in Mechanics and Inverse Problems*. Springer Science & Business Media. ISBN: 1402006675, 9781402006678.

Li, L. and Carmen, S.-L. 2009. Rendering human skin using a multi-layer reflection model. *International Journal of Mathematics and Computers in Simulation* 3(1), pp. 44–53.

Li, Y., Zhang, J. and Wang, H. 2013. Tetrahedron model reconstruction and optimization. pp. 42–47.

Liang, X. and Boppart, S. A. 2010. Biomechanical properties of in vivo human skin from dynamic optical coherence elastography pp. 1–7. University of Illinois.

Liu, P. and Islam, M. 2013. A nonlinear cohesive model for mixed-mode delamination of composite laminates. *Composite Structures* 106, pp. 47–56.

Lopes, P. A. D., Jorge, R. N. and Ferreira, A. 2006. A comparative study of several material models for prediction of hyperelastic properties: Application to silicone-rubber and soft tissues pp. 135–147.

Lorenzis, L. D. and Zavarise, G. 2009. Cohesive zone modeling of interfacial stresses in plated beams Department of Innovation Engineering, Università del Salento, 73100 Lecce, Italy.

Lucchini, R. 2013. *Mechanics of stretchable interconnects for stretchable electronics devices*. Ph.D. thesis. Politecnico di Milano.

Luo, C.-C., Qian, L.-X., Li, G.-Y., Jiang, Y., Liang, S. and Cao, Y. 2015. Determining the in vivo elastic properties of dermis layer of human skin using the supersonic shear imaging technique and inverse analysis. *Medical Physics* 42(7), pp. 4106–4115.

Mahmud, J., Holt, C. A., Evans, S. L. and Manan, N. F. A. 2013. Quantifying skin properties using a novel integration experiment-finite element simulation and skin pre-stretch model. *Computational and Theoretical Nanoscience* .

Mahvash, M. 2010. Mechanics of dynamic needle insertion into a biological material. *Transactions on Biomedical Engineering* 57.

Mahvash, M. and Hayward, V. 2001. Haptic rendering of cutting, a fracture mechanics approach. *Journal of Haptics Research (www.haptics-e.org* 2, p. 2001.

Maiti, R., Gerhardt, L.-C., Lee, Z., Byers, R., Woods, D., Sanz-Herrera, J., Franklin, S., Lewis, R., Matcher, S. and Carré, M. 2016. In vivo measurement of skin surface strain and subsurface layer deformation induced by natural tissue stretching. *Journal of the Mechanical Behavior of Biomedical Materials* 62, pp. 556–569.

Manschot, J. 1985. The mechanical properties of human skin in vivo Ph.D. thesis, Catholic University of Nijmegen.

Meglinsky, I. V. and Matcher, S. J. 2000. Computational model of human skin for reflected spectra simulation. vol. 4001, pp. 327–335.

Mendizabal, A., Aguinaga, I. and Sánchez, E. 2015. Characterisation and modelling of brain tissue for surgical simulation. *Journal of the Mechanical Behavior of Biomedical Materials* 45, pp. 1–10.

Mengoni, M., Ponthot, J.-P. and Boman, R. 2016. Mesh management methods in finite element simulations of orthodontic tooth movement. *Medical Engineering and Physics* 38(2), pp. 140–147.

Meo, M. and Thieulot, E. 2005. Delamination modelling in a double cantilever beam. *Composite Structures* 71(3-4), pp. 429–434.

Mircea, S. and Andaluzia, M. 2009. *Variational Inequalities with Applications, A Study of Antiplane Frictional Contact Problems*. ISBN 978-0-387-87460-9.

Misra, S., Reed, K. B., Douglas, A. S., Ramesh, K. T. and Okamura, A. M. 2008. Needle-tissue interaction forces for bevel-tip steerable needles pp. 224–231.

Mithraratne, K., Lavrijsen, T. and Hunter, P. 2009. A coupled soft tissue continuum-transient blood flow model to investigate the circulation in deep veins of the calf under compression. vol. 23, pp. 1878–1882.

Mohammadi, S. and Taiebat, H. 2015. H-adaptive updated lagrangian approach for large-deformation analysis of slope failure. *International Journal of Geomechanics* 15(6).

Needleman, A. 2014. Some issues in cohesive surface modeling. *Procedia IUTAM* 10, pp. 221 – 246.

Nikooyanz, A. A. and Zadpoor, A. A. 2011. Mass spring damper modelling of the human body to study running and hopping. *Engineering in Medicine* 225, pp. 1–15. Department of Biomechanical Engineering, Delft University of Technology (TU Delft).

Nunez, A. S. 2014. *A Physical Model of Human Skin and Its Application for Search and Rescue*. Ph.D. thesis, AIR FORCE INSTITUTE OF TECHNOLOGY.

Olas, T. and Wyrzykowski, R. 2012. Adaptive fem package with decentralized parallel adaptation of tetrahedral meshes. *Lecture Notes in Computer Science (including subseries Lecture Notes in Artificial Intelligence and Lecture Notes in Bioinformatics)* 7116 LNCS, pp. 622–629.

Oldfield, M., Dini, D., Giordano, G. and y Baena, F. R. 2013. Detailed finite element modelling of deep needle insertions into a soft tissue phantom using a cohesive approach. *Computer Methods in Biomechanics and Biomedical Engineering* 16(5), pp. 530–543. PMID: 22229447.

Parry, G., Mairtin, E., Beltz, G. and McGarry, J. 2014. Potential based and non potential based cohesive zone formulations under mixed mode separation and over closure. *Journal of the Mechanics and Physics of Solids* 63(1).

Qi, J., Li, K.-C., Jiang, H., Zhou, Q. and Yang, L. 2015. Gpu-accelerated dem implementation with cuda. *International Journal of Computational Science and Engineering* 11(3), pp. 330–337.

Rackl, M. 2015. Curve fitting for ogden, yeoh and polynomial models Ostbayerische Technische Hochschule Regensburg Mechanical Engineering Department.

Retel, V., Vescovo, P., Jacquet, E., Trivaudey, F., Varchon, D. and Burtheret, A. 2001. Nonlinear model of skin mechanical behaviour analysis with finite element method .

Rice, J. R. 1968. A path independent integral and the approximate analysis of strain concentration by notches and cracks. *J. Appl. Mech* p. 8. Brown University, Providence, R. I.

Sauer, R. and DeLorenzis, L. 2015. An unbiased computational contact formulation for 3d friction. *International Journal for Numerical Methods in Engineering* 101(4), pp. 251–280.

Sebastian, C., Patterson, E. and Ostberg, D. 2011. Comparison of numerical and experimental strain measurements of a composite panel using image decomposition. *Applied Mechanics and Materials* 70, pp. 63–68.

Selvadurai, A. 2001. On boussinesq's problem. *International Journal of Engineering Science* 39, pp. 317–322. Department of Civil Engineering and Applied Mechanics, McGill University,.

Sengeh, D., Moerman, K., Petron, A. and Herr, H. 2016. Multi-material 3-d viscoelastic model of a transtibial residuum from in-vivo indentation and mri data. *Journal of the Mechanical Behavior of Biomedical Materials* 59, pp. 379–392.

Serpa, A. L. 2000. Contact with friction using the augmented lagrangian method: a conditional constrained minimization problem. *Journal of the Brazilian Society of Mechanical Sciences* 22.

Seshaiyer, P. and Suri, M. 2000. Hp submeshing via non-conforming finite element methods. *Computer Methods in Applied Mechanics and Engineering* 189(3), pp. 1011–1030.

Shergold, O. and Fleck, N. 2004. Mechanisms of deep penetration of soft solids, with application to the injection and wounding of skin. *Proceedings of the Royal Society A: Mathematical, Physical and Engineering Sciences* 460(2050), pp. 3037–3058.

Shergold, O., Fleck, N. and Radford, D. 2006. The uniaxial stress versus strain response of pig skin and silicone rubber at low and high strain rates. *International Journal of Impact Engineering* 32(9), pp. 1384–1402.

Shirado, H., Nonomura, Y. and Maeno, T. 2007. Development of artificial skin having human skin-like texture (realization and evaluation of human skin-like texture by emulating surface shape pattern and elastic structure). *Nihon Kikai Gakkai Ronbunshu, C Hen/Transactions of the Japan Society of Mechanical Engineers, Part C* 73(2), pp. 541–546.

Silver, F., Freeman, J. and Devore, D. 2001. Viscoelastic properties of human skin and processed dermis. *Skin Research and Technology* 7(1), pp. 18–23.

Smolen, J. and Patriciu, A. 2009. Model based stabilization of soft tissue targets in needle insertion procedures. *Conference proceedings : ... Annual International Conference of the IEEE Engineering in Medicine and Biology Society. IEEE Engineering in Medicine and Biology Society. Conference* pp. 5084–5087.

Sneddon, I. N. 1965. The relation between load and penetration in the axisymmetric boussinesq problem for a punch of arbitrary profile. *Int. J. Engng Sci.* 3, pp. 47–57. Department of Mathematics, University of Glasgow, Scotland.

Su, J., Zou, H. and Guo, T. 2009. The study of mechanical properties on soft tissue of human forearm in vivo. *3rd International Conference on Bioinformatics and Biomedical Engineering* .

Sun, L. and Zhao, G. 2016. Adaptive hexahedral mesh generation and quality optimization for solid models with thin features using a grid-based method. *Engineering with Computers* 32(1), pp. 61–84.

Tang, Y. M. 2010. Modeling skin deformation using boundary element method pp. 1–108. Hong Kong Polytechnic University.

Tenga, Z., Yuan, J., Feng, J., Zhang, Y., Brown, A. J., Wang, S., Lu, Q. and Gillard, J. H. 2015. The influence of constitutive law choice used to characterise atherosclerotic tissue material properties on computing stress values in human carotid plaques. *Biomechanics* 48.

Terzini, M., Bignardi, C., Castagnoli, C., Cambieri, I., Zanetti, E. M. and Audenino, A. L. 2016. Ex vivo dermis mechanical behavior in relation to decellularization treatment length pp. 34–42. University of Perugia.

Thalmann, N. M., Kalra, P., Leveque, J., Bazin, R., Batisse, D. and Querleux, B. 2002. A computational skin model: fold and wrinkle formation. *IEEE Transactions on Information Technology in Biomedicine* 6(4), pp. 317–323.

van der Zwaag, S., ed. 2007. *Self Healing Materials, an Alternative Approach to 20 Centuries of Materials Science*. Springer Netherlands, 1 ed.

Van Gele, M., Geusens, B., Brochez, L., Speeckaert, R. and Lambert, J. 2011. Three-dimensional skin models as tools for transdermal drug delivery: Challenges and limitations. *Expert Opinion on Drug Delivery* 8(6), pp. 705–720.

Villaggio, P. 1980. A unilateral contact problem in linear elasticity. *Journal of Elasticity* 10(2), pp. 113–119.

Wang, J. T. 2010. Relating cohesive zone model to linear elastic fracture mechanics NASA/TM-2010-216692, NF1676L-10672, L-19873.

Wang, T., Zhao, F., Li, Z., Wang, Y. and Han, J. 2015. The physical modeling and simulation of soft tissue deformation based on lssvm. vol. 2015-September, pp. 1929–1934.

Wu, D., Yan, X., Tang, R., Xie, D. and Chen, Z. 2015. Gpu acceleration of ebe method for 3-d linear steady eddy current field. pp. 325–328.

Xiao, M.-L., Zhang, Y.-B., Wang, Z.-H., Fu, H.-M. and Yang, X. 2016. Effect analysis of delamination damage on the residual strength of notched composite laminates. *Hangkong Dongli Xuebao/Journal of Aerospace Power* 31(5), pp. 1081–1086.

Xu, Q., Nian, G., Shan, Y., Qu, S. and Peng, H.-X. 2016. Numerical investigation on the loading-delamination-unloading behavior of adhesive joints. *Composites Part A: Applied Science and Manufacturing* 90, pp. 45–50.

Xu, X. and Needleman, A. 1993. Void nucleation by inclusion debonding in a crystal matrix. *Modelling and Simulation in Materials Science and Engineering* 1(2), pp. 111–132.

Xuan, Z., Papadopoulos, P., Li, J. and Zhang, L. 2016. An entropy-based evaluation of contact forces in continuum mechanics of elastic structures. *Finite Elements in Analysis and Design* 114(Supplement C).

Yang, B., Mall, S. and Ravi-Chandar, K. 2001. A cohesive zone model for fatigue crack growth in quasibrittle materials. *International Journal of Solids and Structures* 38(22-23), pp. 3927–3944.

Yao, W., Zhang, P., Gao, H. and Hu, X. 2016. An analytical singular element for the study of cohesive zone model based crack propagation. *International Journal of Fracture* pp. 1–11.

Yevtushenko, A. and Grzes, P. 2016. Mutual influence of the sliding velocity and temperature in frictional heating of the thermally nonlinear disc brake. *International Journal of Thermal Sciences* 102, pp. 254–262.

Yidong, B. and Dongmei, W. 2015. Virtual training system with physical viscoelastic model and blood flow simulation based on a range-based sph method. *Journal of Biomimetics, Biomaterials and Biomedical Engineering* 25, pp. 41–53.

Zhang, S., Gu, L., Huang, P. and Xu, J. 2009. Real-time simulation of deformable soft tissue based on mass-spring and medial representation pp. 1–8. Shanghai Jiaotong University.

Zhou, B., Xu, F., Chen, C. and Lu, T. 2010. Strain rate sensitivity of skin tissue under thermomechanical loading. *Philosophical Transactions of the Royal Society A: Mathematical, Physical and Engineering Sciences* 368(1912), pp. 679–690.

Zhou, F., Molinari, J.-F. and Shioya, T. 2005. A rate-dependent cohesive model for simulating dynamic crack propagation in brittle materials. *Engineering Fracture Mechanics* 72(9), pp. 1383–1410.

Appendix A

Variation of the equation's parameters

...............................(Part 1)...............................

The directional derivative of virtual gap functions

Virtual Normal gap function derivative :

The quantity $\Delta \delta g$ is given by:

$$\Delta \delta g = m^{\gamma \beta} [v. \frac{\partial(\delta \varphi(y^{\|\vdash}))}{\partial \gamma} + v. \frac{\partial^2(\delta \varphi(y^{\|\vdash}))}{\partial \alpha \partial \gamma} \tau^{\alpha} \{\delta \varphi(X) - \delta \varphi(y^{\|\vdash})\}] g_n(x, y^{\|\vdash}).$$

$$[v. \frac{\Delta \partial(\varphi(y^{\|\vdash}))}{\partial \beta} + v. \frac{\partial^2(\delta \varphi(y^{\|\vdash}))}{\partial \alpha \partial \beta} \tau^{\alpha} \{\Delta \varphi(X) - \Delta \varphi(y^{\|\vdash})\}]$$

$$+ \tau^{\beta} \{\delta \varphi(X) - \delta \varphi(y^{\|\vdash})\} v. \frac{\Delta \partial(\varphi(y^{\|\vdash}))}{\partial \beta} + \tau^{\beta} \{\Delta \varphi(X) - \Delta \varphi(y^{\|\vdash})\} v. \frac{\partial(\delta \varphi(y^{\|\vdash}))}{\partial \gamma} +$$

$$v. \frac{\partial^2(\delta \varphi(y^{\|\vdash}))}{\partial \alpha \partial \beta} \tau^{\beta}. \{\delta \varphi(X) - \delta \varphi(y^{\|\vdash})\} \tau^{\alpha} \{\Delta \varphi(X) - \Delta \varphi(y^{\|\vdash})\} \qquad (A.1)$$

Virtual Tangential gap function derivative :

The quantity $\triangle(\delta \xi^{\alpha})$ is given by:

$$[m_{\alpha \beta} + g \kappa_{\alpha \beta}] \triangle(\delta \xi^{\alpha}) = -\tau_{\alpha}. \delta \varphi_t^{(2)}(\bar{Y}(X))_{,\beta} \triangle \xi^{\beta} - \tau_{\alpha}. \triangle \varphi_t^{(2)}(\bar{Y}(X))_{,\beta} \delta \xi^{\beta} -$$

$$[\tau_\alpha.\varphi_t^{(2)}(\bar{Y}(X))_{,\beta\gamma} + gv.\varphi_t^{(2)}(\bar{Y}(X))_{,\alpha\beta\gamma}]\delta\xi^\beta\triangle\xi^\beta - \delta\xi^\beta\tau_\beta.[\triangle\varphi_t^{(2)}(\bar{Y}(X))_{,\alpha}+$$

$$\varphi_t^{(2)}(\bar{Y}(X))_{,\alpha\gamma}\triangle\xi^\gamma] - \triangle\xi^\beta\tau_\beta.[\delta\varphi_t^{(2)}(\bar{Y}(X))_{,\alpha} + \varphi_t^{(2)}(\bar{Y}(X))_{,\alpha\gamma}\delta\xi^\gamma] - gv.[\delta\varphi_t^{(2)}(\bar{Y}(X))_{,\alpha\beta}\triangle\xi^\beta+$$

$$\triangle\varphi_t^{(2)}(\bar{Y}(X))_{,\alpha\beta}\delta\xi^\beta] + [\delta\varphi^{(1)}(X) - \delta\varphi^{(2)}(\bar{Y}(X))].[\triangle\varphi_t^{(2)}(\bar{Y}(X))_{,\alpha} + \varphi_t^{(2)}(\bar{Y}(X))_{,\alpha\gamma}\triangle\xi^\gamma]+$$

$$[\triangle\varphi^{(1)}(X) - \triangle\varphi^{(2)}(\bar{Y}(X))].[\delta\varphi_t^{(2)}(\bar{Y}(X))_{,\alpha} + \varphi_t^{(2)}(\bar{Y}(X))_{,\alpha\gamma}\delta\xi^\gamma] \qquad (A.2)$$

.................................(Part 2).................................

Convergence analysis

A.0.1 Unilateral contact problem

The quasi-static (where the inertial effects are negligible) problem of two initially unconstrained bodies, defined on two bounded domains Ω_1, Ω_2, and subjected to body forces f, the boundaries $\partial\Omega_\Gamma = \Gamma_c, \partial\Omega_u = \Gamma_u, \partial\Omega_\sigma = \Gamma_\sigma$ (discontinuity, Dirichlet and Neumann boundary conditions) and satisfy the following equation (defined for both of the bodies)[relying on ideas originally presented by Laursen (2003) and Mircea and Andaluzia (2009)]

$$\begin{cases} div\sigma(u) + f = 0 & in\,\Omega \\ \sigma(u)n = t & on\,\partial\Omega_\sigma \\ u = \bar{u} & on\,\partial\Omega_u, \\ where\,\sigma_{ij} = c_{ijkl}u_{k,l} & c_{ijkl} - stiffness\,tensor \\ u,\ is\,the\,exact\,solution \end{cases} \qquad (A.3)$$

called the Unilateral Contact Problem if it is additionally subjected to the following contact conditions on the contact boundaries

$$
\begin{cases}
t_n(u) = t_c^1(u)\nu(u) = \nu(u)\sigma^1(u)\eta^1(u) \rightsquigarrow t_n(u) = \\
-\eta^1(u)\sigma^1(u)\eta^1(u) \; if \; \nu(u) \approx -\eta^1(u) \\
\eta^1(u)\sigma^1(u)\eta^1(u) = -\eta^2(u)\sigma^2(u)\eta^2(u) \qquad Newton's\,Third\,Law \\
g(u) = g_0(u) + (u^1 - u^2(y^\perp))\eta^1(u) \qquad gap\,function \\
t_t(u^1) = t_t(u^2) = 0 \qquad\qquad\qquad\quad zero\,friction \\
t_n(u) \geq 0 \,;\, g(u) \leq 0 \,;\, t_n(u)g(u) = 0 \quad Kuhn-Tucker\,conditions,
\end{cases} \tag{A.4}
$$

where $\nu, \sigma, \eta, t, t_n$ are the unit normal to the master surface at contact point $\bar{Y}(X)$, the Cauchy stress, outward normal to the contact surface, the Cauchy traction and the contact pressure.

Keeping the above definitions in mind, we consider the following problem (VF).

The variational formulation of the problem, defined on the vector field of the product space $\forall u, w \in W^i \times W^i \,|_{i=1,2}$, equipped with the broken energy norm,[1] has the form

$$
(\forall w \;\in\; K, find\, u \in K \subset W^1 \times W^2)\, such\,that\, a(u, w-u) - L(w-u) \geq 0 \; (VF), \tag{A.5}
$$

where K is assumed to be a closed and convex subset of the product space $W^1 \times W^2$. Assuming $a(u, w-u)$ is continuous ($\exists C > 0, \forall u, w\, such\,that\, |\,a(u,w-u)\,| \leq C \parallel u \parallel \parallel v \parallel$) and coercive ($\exists C > 0, \forall u\, such\,that\, a(u,u) \geq C \parallel u \parallel^2$), thus, there exists a unique solution $u \in K$ for the variation formulation (VF) [see Stampacchia's Theorem or Mircea and Andaluzia (2009)].

Note that the equality sign by the variation formulation (VF) when the normal gap function is less or equal to zero ($g_N \leq 0$) and inequality when the normal gap function is greater than zero ($g_N > 0$, the enforcement of the classical contact constraints).

Let K^h be the discrete convex subset of the product space $W^{1^h} \times W^{2^h}$ and $u^h \in K^h$ be the discrete solution of (VF). The finite element formulation of the equation (4.86) is given by

$$
(\forall w^h \;\in\; K^h, find\, u^h \in K^h \subset W^{1^h} \times W^{2^h}) \;|\; a(u^h, w^h - u^h) - L(w^h - u^h) \geq 0 \tag{A.6}
$$

---

[1] Assuming the domain Ω is divided into sub-domain Ω_s such that satisfy the following property $\cup_{s=1}^{s} cl(\Omega_s) = cl(\Omega)\,;\,\Omega_s \cap \Omega_k = \varnothing\,;\,with\,cl(Set)\,as\,the\,closure\,of\,a\,set\,(Set)$ $a(u,w) = \sum_{s=1;\Omega_s}^{s} a_s(u,w),$

thus, we can define the broken energy norm expressed as $\parallel v \parallel_a := \{a(v,v)\}^{\frac{1}{2}}$

where using again Stampacchia's Theorem, leads to proving the existence and uniqueness of the solution $u^h \in K^h$.

Next, let u_{exact} be the exact solution of (VF), $u_{discrete} \in U^h$ the discrete one, using the triangle inequality we have: $\forall w^h \in U^h$

$\| u_{exact} - u_{discrete} \|_a = \| u_{exact} + inf_{v \in U^h} \| v - u_{exact} \|_a - inf_{v \in U^h} \| v - u_{exact} \|_a - u_{discrete} \|_a \leq \| u_{exact} - inf_{v \in U^h} \| v - u_{exact} \|_a \|_a + \| inf_{v \in U^h} \| v - u_{exact} \|_a - u_{discrete} \|_a \leq inf \| u_{exact} - w^h \|_a + \| inf_{v \in U^h} \| v - u_{exact} \|_a - u_{discrete} \|_a$

Where $inf_{v \in U^h} \| v - u_{exact} \|_a = U^s$ refers to the member of U^h which is the closest function to u_{exact} in terms of the a norm. Then, using Cauchy-Schwartz inequality we get

$$| a(inf_{v \in U^h} \| v - u_{exact} \|_a - u_{discrete}, w^h) | \leq \| inf_{v \in U^h} \| v - u_{exact} \|_a -$$

$$u_{discrete} \|_a \cdot \| w^h \|_a \Rightarrow \| inf_{v \in U^h} \| v - u_{exact} \|_a - u_{discrete} \|_a =$$

$$sup_{w^h \neq 0} \frac{| a(inf_{v \in U^h} \| v - u_{exact} \|_a - u_{discrete}, w^h) |}{\| w^h \|_a}, \tag{A.7}$$

where

$$a(inf_{v \in U^h} \| v - u_{exact} \|_a - u_{discrete}, w^h) = a(\underbrace{\overbrace{inf_{v \in U^h} \| v - u_{exact} \|_a}^{a(u_{exact}, w^h)}}_{projection\ of\ solution\ into\ the\ function\ space}, w^h) -$$

$$a(u_{discrete}, w^h) = \underbrace{\int_\Omega w^h f_l d\Omega - a(u_{discrete}, w^h)}_{=0} + \int_{\cup \Omega^h_{c1,c2}} (w^h_{c1} - w^h_{c2}) t_l d\Gamma_c, \tag{A.8}$$

where $a(u_{discrete}, w^h) = \int_\Omega w^h f_l d\Omega$ is not always true, because of the discontinuities in w^h which need to be considered.

Thus, $\| u_{exact} - u_{discrete} \|_a$ can be expressed now

$$\| u_{exact} - u_{discrete} \|_a \leq \underbrace{sup_{w^h \neq 0} \frac{\overbrace{| \int_{\cup \Omega_{c1,c2}^h} (w_{c1}^h - w_{c2}^h)\sigma^1(u)\eta^1(u))d\Gamma_c |}^{| \int_{\cup \Omega_{c1,c2}^h} (w_{c1}^h - w_{c2}^h)t_l d\Gamma_c |}}{\| w^h \|_a}}_{consistency\,error}$$

$$+inf \| u_{exact} - w^h \|_a, \tag{A.9}$$

where $inf \| u_{exact} - w^h \|_a$ refers to approximation error.

Prior to the estimation of the errors, first, we need to define the piecewise polynomials $P^k(\Omega_s^e)$ of k order which is applied to elements in each sub-domain of regular families of mesh (for the approximations of u^h, w^h). Following the definition of the weighting space W^i and solution space U^i we define new weighting W_M^h and weighting-solution Υ^h spaces namely

$$WM^h = \left\{ wm^h, wm^h \in L_2(\cup\Gamma_{c1,c2}) \mid \begin{cases} wm^h \in P^k(\Omega_s^e) \mid cl(\Omega_s^e) \cap (\partial\Gamma_c) = \varnothing \\ wm^h \in P^{k-1}(\Omega_s^e) \mid cl(\Omega_s^e) \cap (\partial\Gamma_c) \neq \varnothing \end{cases} \right\} \tag{A.10}$$

$$\Upsilon^h = \left\{ w^h \mid w^h \in L_2(\Omega), \forall wm^h \in WM^h \quad \int_{\cup\Gamma_{c1,c2}} (w_{c1}^h - w_{c2}^h)wm^h d\Gamma_c = 0, orthogonality \right\}, \tag{A.11}$$

where Ω_s^e refers to an element of the non-mortar surface (the slave surface where the Lagrange multipliers will be interpolated and consequently the mortar surface, the master surface), $cl(\Omega_s^e)$ the closure of Ω_s^e, $\partial\Gamma_c$ boundary of the surface. Note that, by the interpolation, WM^h has the same order as the solution u^h on the interior of the surfaces and one order less for the elements on the boundaries of these surfaces.

Thus, we have [Seshaiyer and Suri (2000)]

$$| \int_{\cup\Gamma_{c1,c2}} (w_{c1}^h - w_{c2}^h)t_l d\Gamma_c | = | \int_{\cup\Gamma_{c1,c2}} (w_{c1}^h - w_{c2}^h)(t_l - wm^h)d\Gamma_c | \leq$$

$$\underbrace{inf \| t_l - wm^h \|_{H_{\cup\Gamma_{c1,c2}}^{\frac{1}{2}}}}_{\leq Ch^{k+\frac{1}{2}} \|u\|_{H_i(\Omega)|_{\frac{1}{2}<i<2}}} \cdot \| w^h \|, \tag{A.12}$$

where h is the characteristic parameter size of the mesh (all sub-domain) and due to the fact that all the norms of finite dimensional spaces are equivalent ($c_1 \parallel w^h \parallel_b \leq \parallel w^h \parallel_a \leq c_2 \parallel w^h \parallel_b$), an interpolated norm combined with triangle inequality and trace theorem[2] has been applied to each sub-domain and then summed over individual approximation errors. Where also the orthogonality condition $\int_{\cup \Gamma_{c1,c2}} (w^h_{c1} - w^h_{c2}) wm^h d\Gamma_c = 0$ has been applied. Note that, the consistency error converges at the order of $k + \frac{1}{2}$.

Next, we introduce the projection operator p^{k,c_1} defined on the non-mortar space, given by

$$\forall wm^h \in WM^h, \forall \psi \in L_2(\Gamma_{c1}), \int_{\Gamma_{c1}} (\psi - p^{k,c_1}\psi) wm^h d\Gamma_c = 0, \psi p^{k,c_1} \mid_{\partial \Gamma_c} = 0, \qquad (A.13)$$

where the projection operator p^{k,c_1} is an orthogonal projection which is supposed to be zero at the boundaries of these discretised surfaces.

To evaluate the approximation error of the nodal interpolation, we use the standard estimation of the error of a finite element solution theory Laursen (2003), so we get

$$\sum_{s=1}^{s} \parallel u_{exact} - w^h_n \parallel_{H_1|L_2(\Omega_s)} \leq \sum_{s=1}^{s} Ch^k \parallel u_{exact} \parallel_{H_2(\Omega_s)}, \qquad (A.14)$$

where w^h_n is the nodal interpolate of u_{exact}, and C is a constant.

On the other hand we have

$$\forall wm^h \in WM^h, \underbrace{\int_{\Gamma_{c1}} \overbrace{[(w^h_{n|c_1} - w^h_{n|c_2}) + p^{k,c_i}(w^h_{n|c_1} - w^h_{n|c_2})]}^{[U^s_{c1} - U^s_{c2}]} wm^h d\Gamma_c}_{=0\,by\,(3.94)}, \qquad (A.15)$$

where $w^h_{n|c_1}, w^h_{n|c_2}$ are the nodal interpolate of u_{exact} on the mortar and non-mortar surfaces and $U^s_{c1} = w^h_{n|c_1} + p^{k,c_i}(w^h_{n|c_1} - w^h_{n|c_2})$ are the values of U^s on the non-mortar surface.

Thus,

$$\parallel u_{exact} - w^h \parallel_a \leq \sum_{s=1}^{s} \parallel u_{exact} - w^h_n \parallel_{H_1|L_2(\Omega_s)} + \underbrace{\sum_{s=1}^{s} \parallel p^{k,c_1}(\Omega^{c_1}_s - \Omega^{c_2}_s) \parallel_{L_2(\Omega_s)}}_{\leq h^{\frac{-1}{2}} \parallel u_{exact} - w^h_n \parallel_{H_1|L_2(\Omega_s)}}$$

---

[2] $[\gamma \mid_{\frac{1}{2} < s < \frac{3}{2}, \partial \Omega} : H^s(\Omega) \to H^{s-\frac{1}{2}}(\Omega) \ \gamma \mid_{\partial \Omega} u(x) = u(x) ; \forall x \in \partial \Omega, \sum_{i=1}^{n} \psi_i(x) = 1 \Rightarrow \gamma \mid_{\partial \Omega} u(x) = \sum_{i=1}^{n} (\psi_i u)(x)] \Longrightarrow \parallel \gamma \mid_{\partial \Omega} u \parallel_{H^{s-\frac{1}{2}}(\partial \Omega)} \leq C \parallel u \parallel_{H^s(\partial \Omega)}$

$$\leq Ch^k \parallel u_{exact} \parallel_{H_2(\Omega)} \tag{A.16}$$

The combination of the estimation results of the consistency error and the approximation error leads to

$$\parallel u_{exact} - u_{discrete} \parallel_a \leq Ch^k \parallel u_{exact} \parallel_{H_2(\Omega)}, \tag{A.17}$$

and it shows the order of k convergence (order of the piecewise polynomials) in the associated norm (broken norm).

A.0.2 Frictional Contact problem

With some of the methods described in the previous section in hand, and based on the studies Han *et al.* (2014), Mircea and Andaluzia (2009), Lebedev *et al.* (2012), and making use of the definition of the hemivariational inequality, the general variational framework for the treatment of mortar frictional problem is formulated in the following global form.

Given two linearly elastic bodies (Ω_1, Ω_2), subjected to the boundaries $\partial\Omega_c, \partial\Omega_u, \partial\Omega_\sigma$ (discontinuity, Dirichlet and Neumann boundary conditions) with frictional contact on $\partial\Omega_c$, Ω an open bounded subset with Lipschitz continuous boundary,[3] an operator $a : \Omega \to \Omega^*$, $\Omega \subset H^1(\Omega, R^m)$,[4] body force $f_b \in L^2(\Omega; R^m)$, surface traction $\bar{t} \in L^2(\partial\Omega_u; R^m)$, trace operator $\gamma : \Omega \to L^2(\partial\Omega_c; R^m)$ and a functional $f : \Omega \to R^m$,

and additionally the following conditions

$$\begin{cases} (I)\, t_N = t_n(u) = t_{Nc}^1(u)v(u) = v(u)\sigma_n^1(u)\eta^1(u) \rightsquigarrow t_n(u) = \quad (contact\,normal\,traction) \\ -\eta^1(u)\sigma_n^1(u)\eta^1(u) \; if \; v(u) \approx -\eta^1(u) \\ (II)\, \eta^1(u)\sigma_n^1(u)\eta^1(u) = -\eta^2(u)\sigma_n^2(u)\eta^2(u) \\ (III)\, t_F = t_T(u) = -\sigma_n(u)v(u) + (\eta^1(u)\sigma_n^1(u)\eta^1(u))v(u) = \quad (friction\,traction) \\ (IV)\, g_t(u) = (u^1 - u^2(y^\perp)) + ((u^1 - u^2(y^\perp)).\eta^1(u))\eta^1(u) = \\ \begin{cases} \kappa t_n(u) & \kappa = 0; \parallel t_T(u) \parallel < \mu t_n(u) \\ \kappa t_n(u) & \kappa \geq 0; \parallel t_T(u) \parallel = \mu t_n(u) \end{cases} \quad (tangential\,gap\,function\,and\,Coulomb's\,law) \end{cases}$$

and

---

[3] $\forall \chi \in \partial\Omega, \exists r \in R > 0 \; and \; \exists \mu : \{x \in R^d \;|\parallel x - \chi \parallel < r\} \longmapsto Q \;\mid \mu \; and \; \mu^{-1} \, lipschitz\,continuous \; \mu(\{x \in R^d \;|\parallel x - \chi \parallel < r\} \cap \Omega) = Q^+ \; \& \; \mu(\{x \in R^d \;|\parallel x - \chi \parallel < r\} \cap \partial\Omega) = Q^0$

[4] $(\Omega^*, topological\,dual\,of\,\Omega)$

$$\begin{cases} (V)\, g_t(u) \neq 0 \Longrightarrow t_T(u) = \mu t_n(u) \frac{g_t(u)}{\|g_t(u)\|} \ (slip) \\ \mu,\ (friction\,coefficient) \\ (VI)\, g_n(u) = g_0(u) + (u^1 - u^2(y^\perp))\eta^1(u) \ (normal\,gap\,function) \\ (VII)\, t_n(u) \geq 0\,;\ g_n(u) \leq 0\,;\ t_n(u)g_n(u) = 0 \quad (Kuhn-Tucker\,conditions), \end{cases} \tag{A.18}$$

$\forall w \in \Omega$ find an element $u \in \Omega$ such that

$$\underbrace{\int_\Omega [(\sigma(u) = C^l \varepsilon(u))\varepsilon(w-u) + \{\rho(w-u)\frac{\partial^2 u}{\partial t^2} = 0\}]d\Omega}_{<au,w-u>|_{\Omega^* \times \Omega}} + \int_{\partial\Omega_c} \underbrace{\delta g_n.t_N}_{t_n(u)\eta(u)(\varphi(w_n)-\varphi(u_n))} d\partial\Omega_c$$

$$+ \int_{\partial\Omega_c} \underbrace{\delta g_t t_F}_{t_F(u)\tau(u)(w_t-u_t)} d\partial\Omega_c \geq \underbrace{\int_{\partial\Omega_\sigma} (w-u)\bar{t}d\partial\Omega_\sigma + \int_\Omega (w-u)f_b d\Omega}_{<f,w-u>|_{\Omega^* \times \Omega}}, \qquad (HVF)$$

$$\tag{A.19}$$

where $\forall w_n, u_n \in \partial\Omega_c, \exists C > 0\,such\,that\ |\varphi(w_n) - \varphi(u_n)| \leq C \| w_n - u_n \|_{\partial\Omega_c}$ (closest point projection)

In the case of dealing with the numerical approximation of the problem (HVF) , we have: $\forall w^h \in \Omega^h \subset \Omega$ (Ω^h, finite dimensional subspace-finite element space), find an element $u^h \in \Omega^h$ (u^h, approximation of u; $h > 0$ spatial discretisation parameter) such that satisfies the Hemivariational Formulation (HVF).

In order to perform the analysis of the fully discrete approximation scheme for solving the (HVF), first some definitions will be introduced which will be used later [recall the following definitions from Lebedev *et al.* (2002), Han *et al.* (2014), Mircea and Andaluzia (2009).

Recall the classical directional derivative definition and let Ω be a Banach space (complete $[\forall x^n \in \Omega, \exists x \in \Omega \mid lim_{n\to\infty} \| x^n - x \|_\Omega = 0]$ normed vector space), the directional derivative of a function $F : \Omega \to R$ at $x \in \Omega$ in the direction $u \in \Omega$ is given by

$$\nabla F(x;u) = lim_{\varepsilon \to 0} \frac{F(x+\varepsilon u) - F(x)}{\varepsilon}, \tag{A.20}$$

and under the assumption of locally Lipschitz function $F : \Omega \to R$ at $x \in \Omega$ in the direction $u \in \Omega$, the Clarke generalised definition of directional derivative is given by

$$\nabla^o F(x;u) = lim_{\begin{cases} \varepsilon \to 0 \\ y \to x \end{cases}} sup \frac{F(y+\varepsilon u) - F(y)}{\varepsilon}, \tag{A.21}$$

where in the case of regularity we have:

$\exists \nabla F(x;u) \, of \, a \, function \, F : \Omega \to R$ at $x \in \Omega$(in the direction $\forall u \in \Omega$) $such \, that \, \nabla F(x;u) = \nabla^o F(x;u)$

Following, we recall the general definition of sub-differential. Let the function $F : \Omega \to R$ be convex ($\forall x, y \in \Omega, \forall t \in [0,1] \implies F[tx + (1-t)y] \leq tF[x] + (1-t)F[y]$), lower semi-continuous ($\forall x^n, x \in \Omega, x^n \to x \Rightarrow F(x) \leq lim \, inf \, F(x^n)$) and proper ($\forall x \in \Omega, F(x) \neq +\infty$), the sub-differential of F at $x \in \Omega$ defined by the mapping $\partial F(x) : \Omega \to 2^{\Omega^*}$) $[2^{\Omega^*}$,the set of all subsets of $\Omega^*]$ is given by

$$\partial F(x) = \{z(subgradient) \in \Omega^* : \forall v \in \Omega, \underbrace{<z, v-x>|_{\Omega^* \times \Omega}}_{duality\,pairing} \leq F(v) - F(x)\}, \quad \text{(A.22)}$$

and the Clarke sub-differential of $F : \Omega \to R$ at $x \in \Omega$ is a subset of Ω^* defined by

$$\partial F(x) = \{z \in \Omega^* : \forall u \in \Omega, <z, u>|_{\Omega^* \times \Omega} \leq \nabla^o F(x;u)\} \quad \text{(A.23)}$$

Let $\Lambda : R^m \to R$, for a given friction coefficient μ, and using the Clarke sub-differential, the friction condition $t_T(u) = \mu t_n(u) \frac{g_t(u)}{\|g_t(u)\|}$ can be expressed as $t_T \in \partial \Lambda(g_t(u))$ Han *et al.* (2014) where

$$\forall \alpha \in R^m, \Lambda(\alpha) = \int_0^{\|\alpha\|} \mu t_n(u) dU \quad \text{(A.24)}$$

.

Using the property of the non negative contact normal traction (contact pressure) $[t_n = \lambda + \varepsilon g]; t_n : [0, \infty) \to R$ which also satisfies the following conditions

$$\begin{cases} \exists \varepsilon > 0 \mid t_n(g_2) - t_n(g_1) \leq \varepsilon(g_2 - g_1), \forall g_2 > g_1 > 0 \\ \exists \varepsilon > 0 \mid \forall g_2, g_1, \| t_{Nc}(g_2) - t_{Nc}(g_1) \|_{L^2(\partial \Omega_c)} \leq \varepsilon \| g_2 - g_1 \|_\Omega, \, t_{Nc}(g) = t_n(g)v(g) \\ t_n, continuous \\ \exists C > 0 \forall g \in R \, such \, as \, \| t_n \| = \| \lambda + \varepsilon g \| \leq \| \lambda \| + \| \varepsilon g \| \leq C + C \| g \|, \end{cases} \quad \text{(A.25)}$$

we will get:

$$\forall \alpha \in R^m, \beta \in \partial \Lambda(\alpha) \implies \| \beta \| \leq \mu(C + C \| \alpha \|) \quad (S1) \quad \text{(A.26)}$$

Next, let $K : \Omega \to \Omega^*$, $M : R^m \to R$, recall the definitions of strong-monotony, pseudo-monotony, maximal-monotony and relaxed monotonicity given by [Han *et al.* (2014)]

$$
\begin{cases}
\exists C > 0 \mid \forall u \in K, \; <Ku,u>|_{\Omega^* \times \Omega} \geq C \parallel u \parallel_{\Omega}^2 & pseudo-monotony \\
\exists C_s > 0 \mid \forall u,w \in K, \; <Ku - Kw, u - w>|_{\Omega^* \times \Omega} \geq C_s \parallel u - w \parallel_{\Omega}^2 & strong-monotony \\
\forall u \in K, <Ku - w, u - w>|_{\Omega^* \times \Omega} \geq 0 \implies Ku = w & maximal-monotony \\
\exists C_r > 0 \mid \forall x_1, x_2 \in R^m, y_1, y_2 \in \partial M(x_1 \mid x_2), \; (x_1 - x_2)(y_1 - y_2) \leq C_r \parallel x_1 - x_2 \parallel_{R^m}^2 \\
relaxed-monotonicity,
\end{cases}
$$
$$(A.27)$$

next, we prove the existence and the uniqueness of the solution $u^h \in \Omega^h$ to the problem (HVF) as follows:

Since $t_n(u) \geq 0$ (due to Kuhn-Tucker conditions), using the definition of the trace operator γ, the fact $\mid \varphi(\gamma w^h) - \varphi(\gamma u^h) \mid \leq C \parallel \gamma w^h - \gamma u^h \parallel_{\partial \Omega_c}$ and the general definition of sub-differential, this implies that $\partial(\int_{\partial \Omega_c} \underbrace{\delta g_n . t_N}_{t_n(u^h)\eta(u^h)(\varphi(\gamma u^h))} d\partial \Omega_c)$ is maximal-monotone.

Using the Clarke generalised directional derivative definition, the mapping Λ and again the definition of the trace operator γ, the friction integral can be shown as

$$
\int_{\partial \Omega_c} \underbrace{\delta g_t t_F}_{t_F(u)\tau(u)(w_t^h - u_t^h)} d\partial \Omega_c = \int_{\partial \Omega_c} \nabla^o F(\gamma u^h; \gamma w^h - \gamma u^h) d\partial \Omega_c \tag{A.28}
$$

For $w^h \in \Omega^h$, let $Dw^h = aw^h + \underbrace{\partial(\int_{\partial \Omega_c} \nabla F(\gamma u^h; \gamma w^h) d\partial \Omega_c)}_{b(w^h)}$, next we claim $a + b$ is coercive, pseudo-monotone and bounded if the operator a is coercive, pseudo-monotone and bounded.

According to the statement $S1$ (equation (4.107)) we have:

$\forall w^h, u^h, \exists C, B > 0, \parallel \partial \gamma \parallel \parallel (\partial \int_{\partial \Omega_c} \nabla F(\gamma u^h; \gamma w^h) d\Omega_c) \parallel \leq (C \parallel \gamma \parallel + B \parallel \gamma \parallel \parallel \gamma w^h \parallel) \leq (C \parallel \gamma \parallel + B \parallel \gamma \parallel \parallel \gamma \parallel \parallel w^h \parallel)$ which is poof of boundedness of the operator b [Han *et al.* (2014)].

To prove the pseudo-monotony of the operator b, let first $w \in \Omega^h \to v \in \Omega^h$ weakly in Ω^h, due to boundedness of b and closeness and boundedness of the trace operator γ, it implies $\alpha \in b(w) \to \beta \in b(v)$ and $< \partial(\int_{\partial \Omega_c} \nabla F(\gamma u^h; \gamma w^h) d\Omega_c), w > \to < \partial(\int_{\partial \Omega_c} \nabla F(\gamma u^h; \gamma w^h) d\Omega_c), v >$ which is proof of the pseudo-monotony of the operator b.

Due to the known fact that the set of multivalued pseudo-monotone operators is closed under the addition of mappings, this implies $a + b$ is also pseudo-monotone.

The coercivity of b simply follows from boundedness of b namely;

$\forall w \in \Omega^h, < \partial(\int_{\partial\Omega_c} \nabla F(\gamma u^h; \gamma w^h)d\partial\Omega_c), w >> \geq - \| w \| (C \| \gamma \| + B \| \gamma \| \| \gamma \| \| w \|)$ with constants C, B, thus, $a + b$ is also coercive [Han *et al.* (2014)].

Using the following theorem,

Theorem 4.1: Let X be a Reflexive Banach Space, $A : X \to 2^{X^*}$ (X^* is dual vector space of X) a pseudo monotone operator and $B : X \to 2^{X^*}$ a maximal monotone operator, where suppose $\exists u' \in D(B) \mid A(u')$ and/or $B(u')$ bounded. Assuming also there exists a function $C : \mathbb{R}^+ \to \mathbb{R}, C(t) \to +\infty\, as\, t \to +\infty \mid \forall(u, u^*) \in Gr(A), < u^*, u - u' >_{X^* \times X} \geq C(\| u \|_X) \| u \|_X$, then $A + B$ is surjective($R(A + B) = X^*$).

---

and applying the definition of sub-differential to $\partial(\int_{\partial\Omega_c} \underbrace{\delta g_n.t_N}_{t_n(w^h)\eta(w^h)(\varphi(\gamma w^h))} d\partial\Omega_c)$, we will

have [5] (*with $w^h \in \Omega^h$ as a solution*)

$$aw^h + \underbrace{\partial(\int_{\partial\Omega_c} \nabla F(\gamma u^h; \gamma w^h)d\partial\Omega_c)}_{b(w^h)} + \partial(\int_{\partial\Omega_c} \underbrace{\delta g_n.t_N}_{t_n(w^h)\eta(w^h)(\varphi(\gamma w^h))} d\partial\Omega_c) \ni f \qquad (A.29)$$

On the other hand, we have (due to the general definition of sub-differential and Clarke sub-differential)

$$\forall w \in \partial\Omega_c^h, < \partial(\int_{\partial\Omega_c} \nabla F(\gamma u^h; \gamma w^h)d\partial\Omega_c), w > \leq \nabla^o F(\gamma u^h; w) \leq \int_{\partial\Omega_c} \nabla^o F(\gamma u^h; w)d\partial\Omega_c,$$
$$(A.30)$$

and

$$\forall v \in \Omega^h, < \partial(\int_{\partial\Omega_c} \underbrace{\delta g_n.t_N}_{t_n(w^h)\eta(w^h)(\varphi(\gamma w^h))} d\partial\Omega_c), v - w^h > \leq \int_{\partial\Omega_c} \underbrace{\delta g_n.t_N}_{t_n(w^h)\eta(w^h)(\varphi(\gamma v))} d\partial\Omega_c -$$

$$\int_{\partial\Omega_c} \underbrace{\delta g_n.t_N}_{t_n(w^h)\eta(w^h)(\varphi(\gamma w^h))} d\partial\Omega_c, \qquad (A.31)$$

which together implies that $w^h \in \Omega^h$ is a solution of the following inequality

---

[5] $\Longleftrightarrow aw^h + \xi + \varsigma = f, - \quad ; \xi \in \underbrace{\partial(\int_{\partial\Omega_c} \nabla F(\gamma u^h; \gamma w^h)d\Omega_c)}_{b(w^h)}, \varsigma \in \partial(\int_{\partial\Omega_c} \underbrace{\delta g_n.t_N}_{t_n(w^h)\eta(w^h)(\varphi(\gamma w^h))} d\Omega_c)$

$$< aw^h, v - w^h >_{|\Omega^* \times \Omega} + \int_{\partial \Omega_c} \nabla^o F(\gamma w^h; \gamma v - \gamma w^h) d\partial \Omega_c +$$

$$\int_{\partial \Omega_c} \underbrace{\delta g_n.t_N}_{t_n(w^h)\eta(w^h)(\varphi(\gamma v) - \varphi(\gamma w^h))} d\partial \Omega_c) \geq < f, v - w^h >_{|\Omega^* \times \Omega} \qquad , Problem(hv) \qquad (A.32)$$

To prove the uniqueness of the solution, we assume two solutions (u_1, u_2) to the problem(hv).

Setting for $w^h = u_1 \mid u_2$ and $v = u_2 \mid u_1$, we will get

$$< au_1, u_2 - u_1 >_{|\Omega^* \times \Omega} + \int_{\partial \Omega_c} \nabla^o F(\gamma u_1; \gamma u_2 - \gamma u_1) d\partial \Omega_c +$$

$$\int_{\partial \Omega_c} \underbrace{\delta g_n.t_N}_{t_n(u_1)\eta(u_1)(\varphi(\gamma u_2) - \varphi(\gamma u_1))} d\partial \Omega_c) \geq < f, u_2 - u_1 >_{|\Omega^* \times \Omega} \qquad (A.33)$$

$$< au_2, u_1 - u_2 >_{|\Omega^* \times \Omega} + \int_{\partial \Omega_c} \nabla^o F(\gamma u_2; \gamma u_1 - \gamma u_2) d\partial \Omega_c +$$

$$\int_{\partial \Omega_c} \underbrace{\delta g_n.t_N}_{t_n(u_2)\eta(u_2)(\varphi(\gamma u_1) - \varphi(\gamma u_2))} d\partial \Omega_c) \geq < f, u_1 - u_2 >_{|\Omega^* \times \Omega} \qquad (A.34)$$

Adding together the inequalities and using strong-monotony of the operator a and applying relaxed monotonicity to $\int_{\partial \Omega_c} \nabla^o F(\gamma u_1; \gamma u_2 - \gamma u_1) d\Omega_c$, more specifically $[\exists C_r \geq 0, \forall \alpha, \beta \in \Omega, x \in \partial \Omega_c C_r \in [0, C_s) \mid \nabla^o F(x, \alpha; \beta - \alpha) + \nabla^o F(x, \beta; \alpha - \beta) \leq C_r \parallel \alpha - \beta \parallel_\Omega^2]$, we will have:

$$-C_s \parallel u_1 - u_2 \parallel_\Omega^2 + C_r \parallel \gamma \parallel \parallel \gamma \parallel \parallel u_1 - u_2 \parallel_\Omega^2 \geq 0 \qquad (A.35)$$

.

Applying smallness condition[6] to the trace operator γ, after substitution, the inequality (A.35) leads to the proof of the uniqueness of the solution to the problem(hv). Note that, first we allowed the t_N to be not explicitly dependent on the solution, then using Banach fixed point theorem and applying to the Problem(hv) where assuming first

$$t_N : \Omega \to \Omega, \quad \forall \eta \in \Omega, t_N(\eta) = u_\eta, \qquad (A.36)$$

then formulating the problem(hv) by letting for $u = u_\eta$ and $\eta = \eta_1$[with $w = u_2$] and

---

[6]assuming $\exists \alpha, \beta, C > 0$ *such that* $\alpha \parallel \gamma \parallel + \beta \parallel \gamma \parallel^2 < C$ [Han *et al.* (2014)]

$\eta = \eta_2$[with $w = u_1$], and adding resulting inequalities we will get

$$\| t_N(\eta_1) - t_N(\eta_2) \|_\Omega \leq M \| \eta_1 - \eta_2 \|_{\Omega, \, M>0 \, and \, M<1,} \tag{A.37}$$

which shows that the operator t_N given by the above equation is a contraction on the space Ω and due to the fact that the Banach fixed point theorem has a unique fixed point $\eta^{unique} \in \Omega$. It follows that the problem(hv) has a solution $u_{\eta^{unique}}$, where by using the uniqueness of the fixed point of the operator t_N concludes the proof of the uniqueness of the solution.

Next, the centre of interest is the analysis of the approximation error of the problem(hv). Due to the strong-monotony condition of operator a we have

$$C_s \| u - u^h \|_\Omega^2 \leq < au - au^h, u - u^h >|_{\Omega^* \times \Omega} \leq < au, u - u^h >|_{\Omega^* \times \Omega}$$

$$- < au^h, u - u^h >|_{\Omega^* \times \Omega} \leq < au, u - u^h >|_{\Omega^* \times \Omega} + < au^h, u^h - u >|_{\Omega^* \times \Omega}, \tag{A.38}$$

where (setting $w^h = u$ and $v = u^h$ in the problem(hv))

$$< au, u - u^h >|_{\Omega^* \times \Omega} \leq \int_{\partial\Omega_c} \nabla^o F(\gamma u; \gamma u^h - \gamma u) d\partial\Omega_c +$$

$$\int_{\partial\Omega_c} \underbrace{\delta g_n . t_N}_{t_n(u)\eta(u)(\varphi(\gamma u^h) - \varphi(\gamma u))} d\partial\Omega_c) - < f, u^h - u >|_{\Omega^* \times \Omega}, \tag{A.39}$$

and (setting $w^h = u^h$ and $v = u$ in problem(hv))

$$< au^h, u^h - u >|_{\Omega^* \times \Omega} \leq \int_{\partial\Omega_c} \nabla^o F(\gamma u^h; \gamma u - \gamma u^h) d\partial\Omega_c +$$

$$\int_{\partial\Omega_c} \underbrace{\delta g_n . t_N}_{t_n(u^h)\eta(u^h)(\varphi(\gamma u) - \varphi(\gamma u^h))} d\partial\Omega_c) - < f, u - u^h >|_{\Omega^* \times \Omega}, \tag{A.40}$$

so after substitution we will get

$$C_s \| u - u^h \|_\Omega^2 \leq \int_{\partial\Omega_c} \left(\nabla^o F(\gamma u^h; \gamma u - \gamma u^h) + \nabla^o F(\gamma u; \gamma u^h - \gamma u) \right) d\partial\Omega_c$$

$$- < f, u - u^h >_{|\Omega^* \times \Omega} - < f, u^h - u >_{|\Omega^* \times \Omega} + \int_{\partial \Omega_c} \underbrace{\delta g_n.t_N}_{[t_n(u^h)\eta(u^h)-t_n(u)\eta(u)](\varphi(\gamma u)-\varphi(\gamma u^h))} d\partial \Omega_c,$$

(A.41)

where, by using some of the above definitions and properties, each term in the right hand side of the inequality (A.41) can be bounded as follows:

First we have

$$\int_{\partial \Omega_c} \underbrace{\delta g_n.t_N}_{[t_n(u^h)\eta(u^h)-t_n(u)\eta(u)](\varphi(\gamma u)-\varphi(\gamma u^h))} d\partial \Omega_c) \le \underbrace{\| \left[t_n(u^h)\eta(u^h) - t_n(u)\eta(u) \right] \|}_{\|[t_n(u^h)\eta(u^h)-t_n(u)\eta(u)]\|_{L^2(\partial \Omega_c;R^m)} \le C_a \|u-u^h\|_\Omega} \quad .$$

$$\underbrace{\| (\varphi(\gamma u) - \varphi(\gamma u^h)) \|}_{\|(\varphi(\gamma u)-\varphi(\gamma u^h))\|_{L^2(\partial \Omega_c;R^m)} \le \|\gamma\|\|C_b\|u-u^h\|_\Omega} \le C_a C_b \| \gamma \| \| u - u^h \|^2_\Omega,$$

(A.42)

additionally, using relaxed monotonicity we will get

$$\int_{\partial \Omega_c} \underbrace{\left(\nabla^o F(\gamma u^h; \gamma u - \gamma u^h) + \nabla^o F(\gamma u; \gamma u^h - \gamma u) \right)}_{\left(\nabla^o F(\gamma u^h; \gamma u-\gamma u^h)+\nabla^o F(\gamma u;\gamma u^h-\gamma u) \right) \le C_r \|\gamma u-\gamma u^h\|^2_{L^2(\partial \Omega_c;R^m)}} d\partial \Omega_c \le C_r \| \gamma u - \gamma u^h \|^2_{L^2(\partial \Omega_c;R^m)}$$

(A.43)

Now, the inequality(A.41) can be expressed in the following form (with constants C_a, C_b, C_r)

$$C_s \| u - u^h \|^2_\Omega \le C_a C_b \| \gamma \| \| u - u^h \|^2_\Omega + C_r \| \gamma u - \gamma u^h \|^2_{L^2(\partial \Omega_c;R^m)}$$

(A.44)

Using the smallness condition again and after some simple algebra, finally, we will have the optimal error bound as the following (with new constants A, B, c and $diam(e)$ diameter of an element e, regular triangle meshes)

$$\| u - u^h \|_\Omega \le B \underbrace{\| \gamma u - \gamma u^h \|_{L^2(\partial \Omega_c;R^m)}}_{\forall (\gamma u)_e \in L^2(\partial \Omega_c(e);R^m), \|\gamma u-\gamma u^h\|_{L^2(\partial \Omega_c;R^m)} \le A \underbrace{diam(e)}_{diam(e) \simeq h_e}} \le (AB)h \le ch$$

(A.45)

A.0.3 Frictional-Contact-Cohesive problem

In this section, based on the definitions and results from the previous section, the convergence analysis of the frictional contact problem with cohesive force will be provided, where some theorems on the solvability, existence and uniqueness of the associated hemivariational inequality, to provide the convergence results, will be presented.

The Hemivariational inequality of Frictional-Contact-Cohesive problem is formulated as follows:

Given two linearly elastic bodies (Ω_1, Ω_2), subjected to boundaries $\partial\Omega_c, \partial\Omega_u, \partial\Omega_\sigma$ (discontinuity, Dirichlet and Neumann boundary conditions) with frictional contact on $\partial\Omega_c$, normal cohesive traction $T_n^c \in L^2(\partial\Omega_c; R^m)$ and tangential cohesive traction $T_t^c \in L^2(\partial\Omega_c; R^m)$ on $\partial\Omega_c$, Ω an open bounded subset with Lipschitz continuous boundary, an operator $a : \Omega \to \Omega^*$, $\Omega \subset H^1(\Omega, R^m)$, body force $f_b \in L^2(\Omega; R^m)$, surface traction $\bar{t} \in L^2(\partial\Omega_u; R^m)$, trace operator $\gamma : \Omega \to L^2(\partial\Omega_c; R^m)$, a functional $f : \Omega \to R^m$, and additionally, to the conditions $(I) - (VII)$ from previous section [equation (A.18)], the following conditions

$$
\begin{cases}
T_n^c = T_n^c(u) = t_n^c(u)v^c(u) = v^c(u)\sigma_n^c(u)\eta_n^c(u) = \sigma_{nc}(u) = K_n(u)g_n(u) \,, v^c(u) \approx \eta_n^c(u) \\
T_t^c = T_t^c(u) = t_t^c(u)\tau^c(u) = \tau^c(u)\sigma_t^c(u)\eta_t^c(u) = \sigma_{tc}(u) = K_t(u)g_t(u) \,, \tau^c(u) \approx \eta_t^c(u),
\end{cases}
$$
(A.46)

$\forall w^h \in \Omega^h$ find an element $u^h \in \Omega^h$ such that $(\Omega^h \subset \Omega)$

$$
\underbrace{\int_\Omega [(\sigma(u^h) = C^l\varepsilon(u^h))\varepsilon(w^h - u^h) + \{\rho(w^h - u^h)\frac{\partial^2 u^h}{\partial t^2} = 0\}]d\Omega}_{<au^h, w^h - u^h>|_{\Omega^* \times \Omega}} +
$$

$$
\int_{\partial\Omega_c} \underbrace{\delta g_n . t_N}_{t_n(u^h)\eta(u^h)(\varphi(w_n^h) - \varphi(u_n^h))} d\partial\Omega_c + \int_{\partial\Omega_c} \underbrace{\delta g_n . t_n^c}_{t_n^c(u^h)\eta(u^h)(\varphi(w_n^h) - \varphi(u_n^h))} d\partial\Omega_c +
$$

$$
\int_{\partial\Omega_c} \underbrace{\delta g_t t_t^c}_{t_t^c(u^h)\tau(u^h)(\psi(w_t^h) - \psi(u_t^h))} d\Omega_c + \int_{\partial\Omega_c} \underbrace{\delta g_t t_F}_{t_F(u^h)\tau(u^h)(w_t^h - u_t^h)} d\partial\Omega_c
$$

$$
\geq \underbrace{\int_{\partial\Omega_\sigma} (w^h - u^h)\bar{t} d\partial\Omega_\sigma + \int_\Omega (w^h - u^h)f_b d\Omega}_{<f, w^h - u^h>|_{\Omega^* \times \Omega}} \quad (HVC),
$$
(A.47)

where t_N is the contact normal pressure, $K_n(u), K_t(u)$ are the normal and tangential interfacial stiffness and

$$
\begin{cases}
t_n^c = t_n^{max} \cdot \left(\frac{g_n(X,\bar{Y}(X))}{\varepsilon_n}\right) \cdot e^{\left(1-\left(\frac{g_n(X,\bar{Y}(X))}{\varepsilon_n}\right)\right)} e^{-\left(\frac{g_t(X,\bar{Y}(X))^2}{\varepsilon_t^2}\right)} & (normal\ cohesive\ traction) \\[2mm]
t_t^c = 2t_t^{max} \cdot \sqrt{\frac{1}{2}e}\left(\frac{g_t(X,\bar{Y}(X))}{\varepsilon_t}\right) \cdot \left(1 + \frac{g_n(X,\bar{Y}(X))}{\varepsilon_n}\right) \cdot \\[2mm]
e^{-\left(\frac{g_n(X,\bar{Y}(X))}{\varepsilon_n} + \frac{g_t(X,\bar{Y}(X))^2}{\varepsilon_t^2}\right)} & (tangential\ cohesive\ traction),
\end{cases}
\tag{A.48}
$$

where $g_n(X,\bar{Y}(X)), g_t(X,\bar{Y}(X))$ are the normal and tangential openings, $\varepsilon_n, \varepsilon_t$ are the normal and tangential characteristic opening length and t_n^{max}, t_t^{max} are the maximum normal opening traction and the maximum tangential opening traction.

Note that, due to the modified contact formulation defined in previous sections, in the case of the perfect impenetrability, the contact integral is given by

$$
\int_{\partial \Omega_c} \underbrace{\delta g_n \cdot t_N}_{t_n(u^h)\eta(u^h)(\varphi(w_n^h)-\varphi(u_n^h))} d\Omega_c = 0
\tag{A.49}
$$

Using the definition of exponential function $e^x = \sum_{i=0}^{\infty} \frac{x^i}{i!}$ and the fact that

$$
\forall 0 \leq x < 1,\ e^x \leq \frac{1}{1-x},
\tag{A.50}
$$

the bound of non negative normal cohesive traction and tangential cohesive traction are given by:

$\exists C, B, c > 0$ such that

$$
\begin{cases}
0 \leq \| t_n^c \| \leq C \| g_n \| \| e^{-g_n} \| \| e^{-g_t^2} \| \leq C \| g_n \| \| \frac{1}{1-(\alpha-g_n)} \| \| \frac{1}{1-(\beta-g_t^2)} \| & (1) \\[2mm]
0 \leq \| t_t^c \| \leq B \| c + g_n \| \| g_t \| \| e^{-g_n} \| \| e^{-g_t^2} \| \leq B \| c + g_n \| \| g_t \| \| \frac{1}{1-(\alpha-g_n)} \| \| \frac{1}{1-(\beta-g_t^2)} \| & (2)
\end{cases}
\tag{A.51}
$$

Assuming the g_n, g_t are bounded (it is fact that the upper and lower limit of the normal and tangential openings g_n, g_t, from the numerical point of view, has been given prior to the analysis), and the sub-assumption

$$
\exists \alpha, \beta > 0\ such\ that,\ 0 \leq \alpha - g_n < 1,\ 0 \leq \beta - g_t^2 < 1,
$$

which implies the inequalities (1),(2) [equation (A.51)] are bounded too.

Since $t_n^c(u) \geq 0, t_t^c(u) \geq 0$ [due to the inequalities(1),(2)], using the definition of the trace operator γ, the fact $\exists C, B, | \varphi(\gamma w^h) - \varphi(\gamma u^h) | \leq C \| \gamma w^h - \gamma u^h \|_{\partial \Omega_c}, | \psi(\gamma w^h) - \psi(\gamma u^h) | \leq B \|$

$\gamma w^h - \gamma u^h \parallel_{\partial \Omega_c}$ and using the general definition of sub-differential, it also implies that,

$\partial(\int_{\partial \Omega_c} \underbrace{\delta g_n . t_n^c}_{t_n^c(u^h)\eta(u^h)(\varphi(\gamma u^h))} d\partial \Omega_c)$ and $\partial(\int_{\partial \Omega_c} \underbrace{\delta g_t t_t^c}_{t_t^c(u^h)\tau(u^h)(\psi(\gamma u^h))} d\partial \Omega_c)$ are maximal-monotone.

Again, for $w^h \in \Omega^h$ let $Dw^h = aw^h + \underbrace{\partial(\int_{\partial \Omega_c} \nabla F(\gamma u^h; \gamma w^h) d\partial \Omega_c)}_{b(w^h)}$ (see previous section).

From the previous section we know that $a + b$ is coercive, pseudo-monotone and bounded if the operator a is coercive, pseudo-monotone and bounded. With this in mind, using Theorem 4.1 and after applying the definition of sub-differential to

$$\partial(\int_{\partial \Omega_c} \underbrace{\delta g_n . t_n^c}_{t_n^c(u^h)\eta(u^h)(\varphi(\gamma u^h))} d\partial \Omega_c), \partial(\int_{\partial \Omega_c} \underbrace{\delta g_t t_t^c}_{t_t^c(u^h)\tau(u^h)(\psi(\gamma u^h))} d\partial \Omega_c), \quad (A.52)$$

we will have (*with $w^h \in \Omega^h$ as a solution*)

$$aw^h + \underbrace{\partial(\int_{\partial \Omega_c} \nabla F(\gamma u^h; \gamma w^h) d\partial \Omega_c)}_{b(w^h)} + \partial(\int_{\partial \Omega_c} \underbrace{\delta g_n . t_n^c}_{t_n^c(w^h)\eta(w^h)(\varphi(\gamma w^h))} d\partial \Omega_c) +$$

$$\partial(\int_{\partial \Omega_c} \underbrace{\delta g_t t_t^c}_{t_t^c(w^h)\tau(w^h)(\psi(\gamma w^h))} d\partial \Omega_c) + \partial(\int_{\partial \Omega_c} \underbrace{\delta g_n . t_N}_{t_n(w^h)\eta(w^h)(\varphi(\gamma w^h))} d\partial \Omega_c) \ni f \quad (A.53)$$

We also know $\forall v \in \Omega^h, \forall w \in \partial \Omega_c^h$(see previous section)

$I :\, < \partial(\int_{\partial \Omega_c} \underbrace{\delta g_n . t_N}_{t_n(w^h)\eta(w^h)(\varphi(\gamma w^h))} d\partial \Omega_c), v - w^h > \leq \int_{\partial \Omega_c} \underbrace{\delta g_n . t_N}_{t_n(w^h)\eta(w^h)(\varphi(\gamma v))} d\partial \Omega_c -$

$$\int_{\partial \Omega_c} \underbrace{\delta g_n . t_N}_{t_n(w^h)\eta(w^h)(\varphi(\gamma w^h))} d\partial \Omega_c$$

$II :\, < \partial(\int_{\partial \Omega_c} \underbrace{\delta g_n . t_n^c}_{t_n^c(w^h)\eta(w^h)(\varphi(\gamma w^h))} d\partial \Omega_c), v - w^h > \leq \int_{\partial \Omega_c} \underbrace{\delta g_n . t_N}_{t_n^c(w^h)\eta(w^h)(\varphi(\gamma v))} d\partial \Omega_c -$

$$\int_{\partial \Omega_c} \underbrace{\delta g_n . t_N}_{t_n^c(w^h)\eta(w^h)(\varphi(\gamma w^h))} d\partial \Omega_c$$

$III :\, < \partial(\int_{\partial \Omega_c} \underbrace{\delta g_t t_t^c}_{t_t^c(w^h)\tau(w^h)(\psi(\gamma w^h))} d\partial \Omega_c), v - w^h > \leq \int_{\partial \Omega_c} \underbrace{\delta g_t t_t^c}_{t_t^c(w^h)\tau(w^h)(\psi(\gamma v))} d\partial \Omega_c -$

$$\int_{\partial \Omega_c} \underbrace{\delta g_t t_t^c}_{t_t^c(w^h)\tau(w^h)(\psi(\gamma w^h))} d\partial \Omega_c$$

$$IV :< \partial(\int_{\partial\Omega_c} \nabla F(\gamma u^h; \gamma w^h) d\partial\Omega_c), w >\leq \int_{\partial\Omega_c} \nabla^o F(\gamma u^h; w) d\partial\Omega_c, \qquad (A.54)$$

which implies that $w^h \in \Omega^h$ is a solution of the following inequality

$$< aw^h, v-w^h >_{|\Omega^* \times \Omega} + \int_{\partial\Omega_c} \nabla^o F(\gamma w^h; \gamma v - \gamma w^h) d\partial\Omega_c + \int_{\partial\Omega_c} \underbrace{\delta g_n.t_N}_{t_n(w^h)\eta(w^h)(\varphi(\gamma v)-\varphi(\gamma w^h))} d\partial\Omega_c)+$$

$$\int_{\partial\Omega_c} \underbrace{\delta g_t t_t^c}_{t_t^c(w^h)\tau(w^h)(\psi(\gamma v)-\psi(\gamma w^h))} d\partial\Omega_c + \int_{\partial\Omega_c} \underbrace{\delta g_n.t_N}_{t_n^c(w^h)\eta(w^h)(\varphi(\gamma v)-\varphi(\gamma w^h))} d\partial\Omega_c \geq < f, v-w^h >_{|\Omega^* \times \Omega} \quad (hvc)$$

$$(A.55)$$

The proof of the uniqueness of the solution follows the same methods As the previous section, which are:

Setting for $w^h = u_1 \mid u_2$ and $v = u_2 \mid u_1$ in inequality (hvc) adding together the resultant inequalities and using $\exists C_1, C_2, \parallel t_t^c(w) - t_t^c(v) \parallel \leq C_1 \parallel w - v \parallel_{\partial\Omega_c}, \parallel t_n^c(w) - t_n^c(v) \parallel \leq C_2 \parallel w - v \parallel_{\partial\Omega_c}$, strong-monotony, relaxed monotonicity and smallness condition, which will conclude the proof of uniqueness of the solution.

Next, we provide the results of the analysis of the approximation error of the problem (HVC).

For an arbitrary function $l^h \in \Omega^h$ we have

$< au - au^h, u - l^h + l^h - u^h >_{|\Omega^* \times \Omega} = < au - au^h, u - l^h >_{|\Omega^* \times \Omega} + < au - au^h, l^h - u^h >_{|\Omega^* \times \Omega} = < au - au^h, u - l^h >_{|\Omega^* \times \Omega} + < au, l^h - u^h >_{|\Omega^* \times \Omega} - < au^h, l^h - u^h >_{|\Omega^* \times \Omega} = < au - au^h, u - l^h >_{|\Omega^* \times \Omega} + < au, l^h - u + u - u^h >_{|\Omega^* \times \Omega} - < au^h, l^h - u^h >_{|\Omega^* \times \Omega} = < au - au^h, u - l^h >_{|\Omega^* \times \Omega} + < au, l^h - u >_{|\Omega^* \times \Omega} + < au, u - u^h >_{|\Omega^* \times \Omega} + < au^h, u^h - l^h >_{|\Omega^* \times \Omega}$

Due to the strong-monotony condition of the operator a we also have (see previous section)

$$C_s \parallel u - u^h \parallel_\Omega^2 \leq < au - au^h, u - u^h >_{|\Omega^* \times \Omega} \leq \underbrace{< au - au^h, u - l^h >_{|\Omega^* \times \Omega}}_{(1)} + \underbrace{< au, l^h - u >_{|\Omega^* \times \Omega}}_{(2)} +$$

$$\underbrace{< au, u - u^h >_{|\Omega^* \times \Omega}}_{(3)} + \underbrace{< au^h, u^h - l^h >_{|\Omega^* \times \Omega}}_{(4)} \qquad (A.56)$$

By Lipschitz Continuity $(f : X \to Y, \forall x_1, x_2 \in X, \exists C_l > 0 \mid \mid f(x_2) - f(x_1) \mid \leq C_l \mid x_2 -$

x_1 |) of the operator a we have

$$\underbrace{< au - au^h, u - l^h >|_{\Omega^* \times \Omega}}_{(1)} \leq \| au - au^h \|_{\Omega^*} \| u - l^h \|_{\Omega} \leq C_l \| u - u^h \|_{\Omega} \| u - l^h \|_{\Omega} \quad (A.57)$$

By replacing for $w^h = u$ and $v = 2u - l^h$ in (hvc) we get

$$\underbrace{< au, l^h - u >|_{\Omega^* \times \Omega}}_{(2)} = - < au, u - l^h >|_{\Omega^* \times \Omega} \leq \int_{\partial \Omega_c} \nabla^o F(\gamma u; ((2\gamma u - \gamma l^h) - \gamma u) d\partial \Omega_c +$$

$$\int_{\partial \Omega_c} \underbrace{\delta g_n . t_N}_{t_n(u)\eta(u)(\varphi(2\gamma u - \gamma l^h) - \varphi(\gamma u))} d\partial \Omega_c + \int_{\partial \Omega_c} \underbrace{\delta g_t t_t^c}_{t_t^c(u)\tau(u)(\psi(2\gamma u - \gamma l^h) - \psi(\gamma u))} d\partial \Omega_c +$$

$$\int_{\partial \Omega_c} \underbrace{\delta g_n . t_N}_{t_n^c(u)\eta(u)(\varphi(2\gamma u - \gamma l^h) - \varphi(\gamma u))} d\partial \Omega_c - < f, u - l^h >|_{\Omega^* \times \Omega}, \quad (A.58)$$

setting for $w^h = u$ and $v = u^h$ in (hvc) we get

$$\underbrace{< au, u - u^h >|_{\Omega^* \times \Omega}}_{(3)} = - < au, u^h - u >|_{\Omega^* \times \Omega} \leq \int_{\partial \Omega_c} \nabla^o F(\gamma u; \gamma u^h - \gamma u) d\partial \Omega_c +$$

$$\int_{\partial \Omega_c} \underbrace{\delta g_n . t_N}_{t_n(u)\eta(u)(\varphi(\gamma u^h) - \varphi(\gamma u))} d\partial \Omega_c + \int_{\partial \Omega_c} \underbrace{\delta g_t t_t^c}_{t_t^c(u)\tau(u)(\psi(\gamma u^h) - \psi(\gamma u))} d\partial \Omega_c +$$

$$\int_{\partial \Omega_c} \underbrace{\delta g_n . t_N}_{t_n^c(u)\eta(u)(\varphi(\gamma u^h) - \varphi(\gamma u))} d\partial \Omega_c - < f, u^h - u >|_{\Omega^* \times \Omega}, \quad (A.59)$$

and setting for $w^h = l^h$ in (HVC) we get

$$\underbrace{< au^h, u^h - l^h >|_{\Omega^* \times \Omega}}_{(4)} = - < au^h, l^h - u^h >|_{\Omega^* \times \Omega} \leq \int_{\partial \Omega_c} \nabla^o F(\gamma u^h; \gamma l^h - \gamma u^h) d\partial \Omega_c +$$

$$\int_{\partial \Omega_c} \underbrace{\delta g_n . t_N}_{t_n(u^h)\eta(u^h)(\varphi(\gamma l^h) - \varphi(\gamma u^h))} d\partial \Omega_c + \int_{\partial \Omega_c} \underbrace{\delta g_t t_t^c}_{t_t^c(u^h)\tau(u^h)(\psi(\gamma l^h) - \psi(\gamma u^h))} d\partial \Omega_c +$$

$$\int_{\partial \Omega_c} \underbrace{\delta g_n . t_N}_{t_n^c(u^h)\eta(u^h)(\varphi(\gamma l^h) - \varphi(\gamma u^h))} d\partial \Omega_c - < f, l^h - u^h >|_{\Omega^* \times \Omega}, \quad (A.60)$$

after substitution and some algebra we get:

(with $C_n, C_r, C_j, C_k, C_m, C_j^n, C_m^n, C_k^n, C_j^t, C_m^t, C_k^n$ as constants)

(Friction integral)

$$\int_{\partial \Omega_c} [\underbrace{\nabla^o F(\gamma u; \gamma u^h - \gamma u)}_{\nabla^o F(\gamma u; \gamma u^h - \gamma u) \leq C_r \| \gamma u - \gamma u^h \|^2_{L^2(\partial \Omega_c; R^m)} - \nabla^o F(\gamma u; \gamma u - \gamma u^h)} + \underbrace{\nabla^o F(\gamma u; (\gamma u - \gamma l^h)}_{\leq C_n \| \gamma u - \gamma l^h \|_{R^m}} +$$

$$\underbrace{\nabla^o F(\gamma u^h; \gamma l^h - \gamma u^h)}_{\nabla^o F(\gamma u^h; \gamma l^h - \gamma u^h) \leq \nabla^o F(\gamma u; \gamma u - \gamma u^h) + \nabla^o F(\gamma u; (\gamma u - \gamma l^h)}] d\partial \Omega_c \leq$$

$$C_r \parallel \gamma u - \gamma u^h \parallel_{L^2(\partial \Omega_c; R^m)}^2 + 2C_n \parallel \gamma u - \gamma l^h \parallel_{L^2(\partial \Omega_c; R^m)}, \tag{A.61}$$

and the following inequalities,

(Contact integral)

$$\int_{\partial \Omega_c} \{ \underbrace{t_n(u)\eta(u)}_{\leq \|t_n(u)\|_{L^2(\partial\Omega_c;R^m)}} \underbrace{[\varphi(\gamma u^h) - \varphi(\gamma u) + \varphi(2\gamma u - \gamma l^h) - \varphi(\gamma u)]}_{\leq C_j(\|\gamma u - \gamma l^h\|_{L^2(\partial\Omega_c;R^m)} + \|\gamma u - \gamma l^h\|_{L^2(\partial\Omega_c;R^m)})} +$$

$$\underbrace{[t_n(u)\eta(u) - t_n(u^h)\eta(u^h)]}_{\leq C_m\|u-u^h\|_\Omega} \underbrace{(-\varphi(\gamma l^h) + \varphi(\gamma u^h))}_{\leq C_k\|\gamma u^h - \gamma l^h\|_{L^2(\partial\Omega_c;R^m)}} \} d\partial \Omega_c \leq$$

$$2C_j \parallel t_n(u) \parallel_{L^2(\partial\Omega_c;R^m)} \parallel \gamma u - \gamma l^h \parallel_{L^2(\partial\Omega_c;R^m)} + C_m C_k \parallel u - u^h \parallel_\Omega \underbrace{\parallel \gamma u^h - \gamma l^h \parallel_{L^2(\partial\Omega_c;R^m)}}_{\leq \|\gamma\|(\|u-u^h\|_\Omega + \|u-l^h\|_\Omega)},$$
$$\tag{A.62}$$

(Mixed mode Fracture integral mode I)

$$\int_{\partial \Omega_c} \{ \underbrace{t_n^c(u)\eta(u)}_{\leq \|t_n^c(u)\|_{L^2(\partial\Omega_c;R^m)}} \underbrace{[\varphi(\gamma u^h) - \varphi(\gamma u) + \varphi(2\gamma u - \gamma l^h) - \varphi(\gamma u)]}_{\leq C_j^n(\|\gamma u - \gamma l^h\|_{L^2(\partial\Omega_c;R^m)} + \|\gamma u - \gamma l^h\|_{L^2(\partial\Omega_c;R^m)})} +$$

$$\underbrace{[t_n^c(u)\eta(u) - t_n^c(u^h)\eta(u^h)]}_{\leq C_m^n\|u-u^h\|_\Omega} \underbrace{(-\varphi(\gamma l^h) + \varphi(\gamma u^h))}_{\leq C_k^n\|\gamma u^h - \gamma l^h\|_{L^2(\partial\Omega_c;R^m)}} \} d\partial \Omega_c \leq$$

$$2C_j^n \parallel t_n^c(u) \parallel_{L^2(\partial\Omega_c;R^m)} \parallel \gamma u - \gamma l^h \parallel_{L^2(\partial\Omega_c;R^m)} + C_m^n C_k^n \parallel u - u^h \parallel_\Omega \underbrace{\parallel \gamma u^h - \gamma l^h \parallel_{L^2(\partial\Omega_c;R^m)}}_{\leq \|\gamma\|(\|u-u^h\|_\Omega + \|u-l^h\|_\Omega)},$$
$$\tag{A.63}$$

(Mixed mode Fracture integral mode II)

$$\int_{\partial \Omega_c} \{ \underbrace{t_t^c(u)\tau(u)}_{\leq \|t_t^c(u)\|_{L^2(\partial\Omega_c;R^m)}} \underbrace{[\psi(\gamma u^h) - \psi(\gamma u) + \psi(2\gamma u - \gamma l^h) - \psi(\gamma u)]}_{\leq C_j^t(\|\gamma u - \gamma l^h\|_{L^2(\partial\Omega_c;R^m)} + \|\gamma u - \gamma l^h\|_{L^2(\partial\Omega_c;R^m)})} +$$

$$\underbrace{[t_t^c(u)\tau(u) - t_t^c(u^h)\tau(u^h)]}_{\leq C_m^t\|u-u^h\|_\Omega} \underbrace{(-\psi(\gamma l^h) + \psi(\gamma u^h))}_{\leq C_k^t\|\gamma u^h - \gamma l^h\|_{L^2(\partial\Omega_c;R^m)}} \} d\partial \Omega_c \leq$$

$$2C_j^t \parallel t_t^c(u) \parallel_{L^2(\partial\Omega_c;R^m)} \parallel \gamma u - \gamma l^h \parallel_{L^2(\partial\Omega_c;R^m)} + C_m^t C_k^t \parallel u - u^h \parallel_\Omega \underbrace{\parallel \gamma u^h - \gamma l^h \parallel_{L^2(\partial\Omega_c;R^m)}}_{\leq \|\gamma\|(\|u-u^h\|_\Omega + \|u-l^h\|_\Omega)}$$
$$\tag{A.64}$$

Now, the strong-monotony condition of operator a [inequality (A.56)] can be expressed as

$$C_s \parallel u - u^h \parallel_{\Omega}^2 \leq C_r \parallel \gamma u - \gamma u^h \parallel_{L^2(\partial \Omega_c; R^m)}^2 + 2C_n \parallel \gamma u - \gamma l^h \parallel_{L^2(\partial \Omega_c; R^m)} + 2C_j \parallel t_n(u) \parallel_{L^2(\partial \Omega_c; R^m)}$$

$$\parallel \gamma u - \gamma l^h \parallel_{L^2(\partial \Omega_c; R^m)} + C_m C_k \parallel u - u^h \parallel_{\Omega} \underbrace{\parallel \gamma u^h - \gamma l^h \parallel_{L^2(\partial \Omega_c; R^m)}}_{\leq \parallel \gamma \parallel (\parallel u - u^h \parallel_{\Omega} + \parallel u - l^h \parallel_{\Omega})} + 2C_j^n \parallel t_n^c(u) \parallel_{L^2(\partial \Omega_c; R^m)}$$

$$\parallel \gamma u - \gamma l^h \parallel_{L^2(\partial \Omega_c; R^m)} + C_m^n C_k^n \parallel u - u^h \parallel_{\Omega} \underbrace{\parallel \gamma u^h - \gamma l^h \parallel_{L^2(\partial \Omega_c; R^m)}}_{\leq \parallel \gamma \parallel (\parallel u - u^h \parallel_{\Omega} + \parallel u - l^h \parallel_{\Omega})} + 2C_j^t \parallel t_t^c(u) \parallel_{L^2(\partial \Omega_c; R^m)}$$

$$\parallel \gamma u - \gamma l^h \parallel_{L^2(\partial \Omega_c; R^m)} + C_m^t C_k^t \parallel u - u^h \parallel_{\Omega} \underbrace{\parallel \gamma u^h - \gamma l^h \parallel_{L^2(\partial \Omega_c; R^m)}}_{\leq \parallel \gamma \parallel (\parallel u - u^h \parallel_{\Omega} + \parallel u - l^h \parallel_{\Omega})} + C_l \parallel u - u^h \parallel_{\Omega} \parallel u - l^h \parallel_{\Omega}$$

$$\tag{A.65}$$

Considering the fact $2 \parallel u - u^h \parallel_{\Omega} \parallel u - l^h \parallel_{\Omega} \leq \parallel u - u^h \parallel_{\Omega}^2 + \parallel u - l^h \parallel_{\Omega}^2$, thus, the complicated expression (A.65) can be simplified to

$$C_s \parallel u - u^h \parallel_{\Omega}^2 \leq 2 \parallel \gamma \parallel \parallel u - l^h \parallel_{\Omega} (C_j \parallel t_n(u) \parallel_{L^2(\partial \Omega_c; R^m)} + C_j^n \parallel t_n^c(u) \parallel_{L^2(\partial \Omega_c; R^m)} +$$

$$C_j^t \parallel t_t^c(u) \parallel_{L^2(\partial \Omega_c; R^m)}) + C_r \parallel \gamma \parallel^2 \parallel u - u^h \parallel_{\Omega}^2 + (C_m C_k + C_m^n C_k^n + C_m^t C_k^t) \parallel \gamma \parallel (\frac{3}{2} \parallel u - u^h \parallel_{\Omega}^2 +$$

$$\frac{1}{2} \parallel u - l^h \parallel_{\Omega}^2) + C_l(\frac{1}{2} \parallel u - u^h \parallel_{\Omega}^2 + \frac{1}{2} \parallel u - l^h \parallel_{\Omega}^2) \tag{A.66}$$

Due to the inequalities (1),(2) [equation (A.51)] and the boundedness of the g_n, g_t and additionally smallness condition, the above relation [expression (A.66)] reduced to

$$\parallel u - u^h \parallel_{\Omega}^2 \leq C_1 \parallel u - l^h \parallel_{\Omega}^2 + C_2 \parallel \gamma \parallel \parallel u - l^h \parallel_{\Omega} \Longrightarrow$$

$$\parallel u - u^h \parallel_{\Omega} \leq C \inf_{l^h \in \Omega^h} (\underbrace{\parallel u - l^h \parallel_{\Omega}}_{\leq O(h)} + \underbrace{\parallel u - l^h \parallel_{\Omega}^{\frac{1}{2}}}_{\leq O(h^{\frac{1}{2}})}), \tag{A.67}$$

where C_1, C_2, C represent positive constants. Since $l^h \in \Omega^h$ is an arbitrary function, we conclude the error bound.

Using additionally the standard finite element interpolation error estimate, finally, we get the optimal error bound shown as (assuming regular triangle meshes)[7]

$$\| u - u^h \|_\Omega \leq c(h + h^{\frac{1}{2}}) \tag{A.68}$$

---

[7]Using solution regularity conditions ($u \in H^2(\Omega; R^m)$, $\gamma u \in H^2(\partial\Omega_c; R^m)$), one can also show $\| u - u^h \|_\Omega \leq c(h)$

Appendix B

The vectors

Modified contact vectors

$$k_N^{coh^c} = H(g_N)(t_{N,N}^{coh/})\mathbf{NN^T} + (t_{N,T_\alpha}^{coh/})(m_{\alpha\beta}\mathbf{N}D_\beta^T + \mathbf{N}G_\alpha^T) + (t_{N,T_\beta}^{coh/})(m_{\beta\alpha}\mathbf{N}D_\alpha^T + \mathbf{N}G_\beta^T) +$$

$$t_N^{coh}\{g_N[m^{11}\mathbf{\bar{N}_1}\mathbf{\bar{N}_1^T} + m^{12}(\mathbf{\bar{N}_1}\mathbf{\bar{N}_2^T} + \mathbf{\bar{N}_2}\mathbf{\bar{N}_1^T}) + m^{22}\mathbf{\bar{N}_2}\mathbf{\bar{N}_2^T}] -$$

$$D_1\mathbf{N_1^T} - D_2\mathbf{N_2^T} - \mathbf{N_1}D_1^T - \mathbf{N_2}D_2^T + \kappa_{12}(D_1D_2^T + D_2D_1^T)\}, \tag{B.1}$$

where $t_{N,N}^{coh/} = \frac{\partial t_N^{coh}}{\partial g_N}$, $t_{N,T_\alpha}^{coh/} = \frac{\partial t_N^{coh}}{\partial g_T^\alpha}$, $t_{N,T_\beta}^{coh/} = \frac{\partial t_N^{coh}}{\partial g_T^\beta}$ and

$$G_\alpha = \{-\mathbf{T}_{\alpha\beta} - \mathbf{T}_{\beta\alpha} + [\varphi_t^{(2)}(\bar{Y}(X))_{,\beta\gamma}.\tau_\alpha + \varphi_t^{(2)}(\bar{Y}(X))_{,\alpha\gamma}.\tau_\beta]D_\gamma\}g_T^\beta \tag{B.2}$$

The quantity $k_{T_\alpha}^{coh^c}$ is given by

$$k_{T_\alpha}^{coh^c} = \mathbf{T}_{\alpha\beta}D_\beta^T + D_\beta\mathbf{T}_{\alpha\beta}^T - (\varphi_t^{(2)}(\bar{Y}(X))_{,\beta\gamma}.\tau_\alpha)D_\beta D_\gamma^T + \bar{T}_{\beta\alpha}D_\beta^T + D_\beta\bar{T}_{\beta\alpha}^T +$$

$$g_N(\mathbf{N}_{\alpha\beta}D_\beta^T + D_\beta\mathbf{N}_{\alpha\beta}^T) - \mathbf{N}\bar{N}_\alpha^T - \mathbf{T}_\beta m^{\beta\gamma}\bar{T}_{\gamma\alpha}^T - \bar{N}_\alpha\mathbf{N}^T - \bar{T}_{\gamma\alpha}m^{\beta\gamma}\mathbf{T}_\beta^T \tag{B.3}$$

and the quantity $k_T^{coh^c}$ is given by

$$k_T^{coh^c} = (t_{T,N}^{coh/})D_\alpha\mathbf{N^T} + H(g_N)(t_{T,N}^{coh/})D_\beta\mathbf{N^T} + (t_{T,T_\alpha}^{coh/})(m_{\alpha\beta}D_\alpha D_\beta^T + D_\alpha G_\alpha^T) +$$

$$(t_{T,T_\beta}^{coh/})(m_{\beta\alpha}D_\beta D_\alpha^T + D_\beta G_\beta^T), \tag{B.4}$$

where $t_{T,N}^{coh/} = \frac{\partial t_T^{coh}}{\partial g_N}$, $t_{T,T_\alpha}^{coh/} = \frac{\partial t_T^{coh}}{\partial g_T^\alpha}$, $t_{T,T_\beta}^{coh/} = \frac{\partial t_T^{coh}}{\partial g_T^\beta}$ and $\mathbf{T}_\alpha, \mathbf{N}_\alpha, \mathbf{N}, D_1, D_2, \bar{\mathbf{N}}_1, \bar{\mathbf{N}}_2$ vectors have been defined by equations (6.56) and (6.57) and $\mathbf{N}_{\alpha\beta}, \mathbf{T}_{\alpha\beta}, \mathbf{P}_\alpha$ are defined as follows

$$\mathbf{T}_{\alpha\beta} = \begin{bmatrix} 0 \\ -N_{1,\beta}(\bar{Y}(X))\tau_\alpha \\ . \\ . \\ -N_{4,\beta}(\bar{Y}(X))\tau_\alpha \end{bmatrix}, \mathbf{N}_{\alpha\beta} = \begin{bmatrix} 0 \\ -N_{1,\alpha\beta}(\bar{Y}(X))v \\ . \\ . \\ -N_{4,\alpha\beta}(\bar{Y}(X))v \end{bmatrix}, \mathbf{P}_\alpha = \begin{bmatrix} 0 \\ -N_{1,\alpha}(\bar{Y}(X))p_T \\ . \\ . \\ -N_{4,\alpha}(\bar{Y}(X))p_T \end{bmatrix}$$

(B.5)

and

$$\begin{cases} \bar{T}_{\alpha 1} = \mathbf{T}_{\alpha 1} - (\varphi_t^{(2)}(\bar{Y}(X))_{,12}.\tau_\alpha)D_2 \\ \bar{T}_{\alpha 2} = \mathbf{T}_{\alpha 2} - (\varphi_t^{(2)}(\bar{Y}(X))_{,12}.\tau_\alpha)D_1 \\ \bar{P}_1 = \mathbf{P}_1 - (\varphi_t^{(2)}(\bar{Y}(X))_{,12}.p_T)D_2 \\ \bar{P}_2 = \mathbf{P}_2 - (\varphi_t^{(2)}(\bar{Y}(X))_{,12}.p_T)D_1 \end{cases}$$

(B.6)

Friction vectors

$$k_{direct}^c = \begin{cases} \varepsilon_T[m_{\alpha\beta}D_\alpha D_\beta^T + D_\alpha G_\alpha^T] \ (stick) \\ -\mu p_{T_\alpha}\varepsilon_N H(g)D_\alpha \mathbf{N}^T + \frac{\mu\varepsilon_T t_N}{\|T_T^{n+1}\|}[\delta_\alpha^\beta - p_T^\beta p_{T_\alpha}][m_{\beta\gamma}D_\alpha D_\gamma^T + D_\alpha G_\beta^T] - \\ \mu t_N p_T^\alpha p_{T_\beta}D_\beta \bar{P}_\alpha^T \quad (slip), \end{cases}$$

(B.7)

where

$$G_\alpha = \{-\mathbf{T}_{\alpha\beta} - \mathbf{T}_{\beta\alpha} + [\varphi_t^{(2)}(\bar{Y}(X))_{,\beta\gamma}.\tau_\alpha + \varphi_t^{(2)}(\bar{Y}(X))_{,\alpha\gamma}.\tau_\beta]D_\gamma\}g_t^\beta$$

(B.8)

The quantity $k_{T_\alpha}^c$ is given by

$$k_{T_\alpha}^c = \mathbf{T}_{\alpha\beta}D_\beta^T + D_\beta \mathbf{T}_{\alpha\beta}^T - (\varphi_t^{(2)}(\bar{Y}(X))_{,\beta\gamma}.\tau_\alpha)D_\beta D_\gamma^T + \bar{T}_{\beta\alpha}D_\beta^T + D_\beta \bar{T}_{\beta\alpha}^T +$$

$$g(\mathbf{N}_{\alpha\beta}D_\beta^T + D_\beta \mathbf{N}_{\alpha\beta}^T) - \mathbf{N}\bar{\mathbf{N}}_\alpha^T - \mathbf{T}_\beta m^{\beta\gamma}\bar{T}_{\gamma\alpha}^T - \bar{\mathbf{N}}_\alpha \mathbf{N}^T - \bar{T}_{\gamma\alpha}m^{\beta\gamma}\mathbf{T}_\beta^T,$$

(B.9)

where $\mathbf{N}_{\alpha\beta}, \mathbf{T}_{\alpha\beta}, \mathbf{P}_{\alpha}$ are defined as follows

$$\mathbf{T}_{\alpha\beta} = \begin{bmatrix} 0 \\ -N_{1,\beta}(\bar{Y}(X))\tau_{\alpha} \\ . \\ . \\ -N_{4,\beta}(\bar{Y}(X))\tau_{\alpha} \end{bmatrix}, \mathbf{N}_{\alpha\beta} = \begin{bmatrix} 0 \\ -N_{1,\alpha\beta}(\bar{Y}(X))v \\ . \\ . \\ -N_{4,\alpha\beta}(\bar{Y}(X))v \end{bmatrix}, \mathbf{P}_{\alpha} = \begin{bmatrix} 0 \\ -N_{1,\alpha}(\bar{Y}(X))p_T \\ . \\ . \\ -N_{4,\alpha}(\bar{Y}(X))p_T \end{bmatrix}$$

(B.10)

and

$$\begin{cases} \bar{T}_{\alpha 1} = \mathbf{T}_{\alpha 1} - (\varphi_t^{(2)}(\bar{Y}(X)),_{12}.\tau_{\alpha})D_2 \\ \bar{T}_{\alpha 2} = \mathbf{T}_{\alpha 2} - (\varphi_t^{(2)}(\bar{Y}(X)),_{12}.\tau_{\alpha})D_1 \\ \bar{P}_1 = \mathbf{P}_1 - (\varphi_t^{(2)}(\bar{Y}(X)),_{12}.p_T)D_2 \\ \bar{P}_2 = \mathbf{P}_2 - (\varphi_t^{(2)}(\bar{Y}(X)),_{12}.p_T)D_1 \end{cases}$$

(B.11)

The temperature vectors

$$\mathbf{a} = \begin{bmatrix} 0 \\ 0 \\ 1 \\ --- \\ 0 \\ 0 \\ -N_1(\bar{\xi}) \\ . \\ . \\ 0 \\ 0 \\ -N_{mnode}(\bar{\xi}) \end{bmatrix}, \mathbf{b} = \begin{bmatrix} 0 \\ 0 \\ R1 \\ --- \\ 0 \\ 0 \\ R2N_1(\bar{\xi}) \\ . \\ . \\ 0 \\ 0 \\ R2N_{mnode}(\bar{\xi}) \end{bmatrix}, \mathbf{c} = \begin{bmatrix} 0 \\ 0 \\ T^s \\ --- \\ 0 \\ 0 \\ T_1^m \\ . \\ . \\ 0 \\ 0 \\ T_{mnode}^m \end{bmatrix}$$

(B.12)

and the vectors

$$
\mathbf{d} = \begin{bmatrix} 0 \\ 0 \\ 0 \\ --- \\ 0 \\ 0 \\ N_{1,1}(\bar{\xi}) \\ . \\ . \\ . \\ 0 \\ 0 \\ -N_{mnode}(\bar{\xi}) \end{bmatrix}, \ \mathbf{e} = \begin{bmatrix} 0 \\ 0 \\ 1 \\ --- \\ 0 \\ 0 \\ 0 \\ . \\ . \\ . \\ 0 \\ 0 \\ 0 \end{bmatrix}, \ \mathbf{f} = \begin{bmatrix} 0 \\ 0 \\ 0 \\ --- \\ 0 \\ 0 \\ N_{1}(\bar{\xi}) \\ . \\ . \\ . \\ 0 \\ 0 \\ N_{mnode}(\bar{\xi}) \end{bmatrix} \tag{B.13}
$$

Additionally, we need to (re)define the following vectors [defined in the equation (6.56)]

$$
\mathbf{N} = \begin{bmatrix} v \\ 0 \\ --- \\ -N_{1}(\bar{\xi})v \\ 0 \\ . \\ . \\ -N_{mnode}(\bar{\xi})v \\ 0 \end{bmatrix}, \ \mathbf{T}_{\alpha} = \begin{bmatrix} \tau_{\alpha} \\ 0 \\ --- \\ -N_{1}(\bar{\xi})\tau_{\alpha} \\ 0 \\ . \\ . \\ -N_{mnode}(\bar{\xi})\tau_{\alpha} \\ 0 \end{bmatrix}, \ \mathbf{N}_{\alpha} = \begin{bmatrix} 0 \\ 0 \\ 0 \\ --- \\ -N_{1,\alpha}(\bar{\xi})v \\ 0 \\ . \\ . \\ -N_{mnode,\alpha}(\bar{\xi})v \\ 0 \end{bmatrix}
$$

and the following vectors

$$\mathbf{T}_{\alpha\beta} = \begin{bmatrix} 0 \\ 0 \\ 0 \\ --- \\ -N_{1,\beta}(\bar{Y}(X))\tau_\alpha \\ 0 \\ . \\ . \\ -N_{mnode,\beta}(\bar{Y}(X))\tau_\alpha \\ 0 \end{bmatrix}, \mathbf{N}_{\alpha\beta} = \begin{bmatrix} 0 \\ 0 \\ 0 \\ --- \\ -N_{1,\alpha\beta}(\bar{Y}(X))v \\ 0 \\ . \\ . \\ -N_{4,\alpha\beta}(\bar{Y}(X))v \\ 0 \end{bmatrix} \tag{B.14}$$

contact stiffness is defined as the following expressions

$$k^c_{conduction} = Rt_N(\mathbf{a}.\mathbf{c})\mathbf{d}D_1^T - RH(g)\varepsilon_N(\mathbf{a}.\mathbf{c})\mathbf{a}\mathbf{N}^T + Rt_N\mathbf{a}\mathbf{a}^T - Rt_N(\mathbf{d}.\mathbf{c})\mathbf{a}D_1^T \tag{B.15}$$

$$k^c_{dissipation} = R2 \mid t_{T_1} \mid \mid \frac{(\xi^1_{n+1} - \xi^1_n)}{\Delta t} \mid \mathbf{d}D_1^T + \frac{\mid t_{T_1} \mid}{\Delta t}\mathbf{b}D_1^T \tag{B.16}$$

$$k^c_{heatsinks} = H(g)\varepsilon_N(-R3(\mathbf{c}.\mathbf{e}) + R4)\mathbf{e}\mathbf{N}^T + H(g)\varepsilon_N(-R5(\mathbf{c}.\mathbf{f}) + R6)\mathbf{f}\mathbf{N}^T$$

$$+R3t_N\mathbf{e}\mathbf{e}^T + R5t_N\mathbf{f}\mathbf{f}^T + (R5(\mathbf{c}.\mathbf{f}) - R6)t_N\mathbf{d}D_1^T \tag{B.17}$$

$$k^c_{direct} = R^1_{extra}D_1\mathbf{e}^T \quad (slip), \tag{B.18}$$

where D_1, D_2 vectors have been defined by equations (6.57) and k^c_{direct} denotes the linearisation of the term $\triangle t_{T_\alpha}\frac{\partial(\xi^\alpha)}{\partial t}$ with respect to temperature degree of freedom(in the case of slip) and

$$R^\alpha_{extra} = W_\alpha \frac{1}{1 + \frac{\varepsilon_T \Delta t}{t_N \eta}}t_N[K(\alpha + T_m) + \mu(T_m)], \tag{B.19}$$

where η is a fluidity parameter (associated with viscoplastic shearing effects), T_m is the maximum absolute temperature on the two contact surfaces, $K(\alpha + T_m)$ is a user defined con-

trol function of the evaluation of the frictional stress under steady state conditions and

$$W_\alpha = \frac{\varepsilon_T \Delta t}{t_N \eta} \frac{T_{T_\alpha}^{n+1}}{\parallel T_T^{n+1} \parallel} \tag{B.20}$$

$$\mu(T_m) = \mu_0 \frac{(T_d - T_0)^2}{(T_m - T_d)^2}, \tag{B.21}$$

where T_d, T_0 are the damage temperatures on the two contact surfaces and the reference temperature and μ_0 the static coefficient of friction at reference temperature.

Note that, in the case of stick, due to the fact that the frictional stress is not dependent on interface temperature, therefore, the linearisation of the term $\triangle t_{T_\alpha} \frac{\partial(\xi^\alpha)}{\partial t}$ with respect to temperature degree of freedom will tend to be zero.

Appendix C

The related equations

...................................**part(1)**..............................

The displacement equations

$$r = (x^2 + y^2 + z^2)^{\frac{1}{2}}$$

$$u_x = \frac{1+v}{2\pi E}\left(\frac{xz}{r^3} - \frac{(1-2v)x}{r(r+z)}\right)F_z,$$

$$u_y = \frac{1+v}{2\pi E}\left(\frac{yz}{r^3} - \frac{(1-2v)y}{r(r+z)}\right)F_z,$$

$$u_z = \frac{1+v}{2\pi E}\left(\frac{z^2}{r^3} + \frac{(2-2v)}{r}\right)F_z,$$

and the stresses equations

$$\sigma_{xx} = \frac{1}{2\pi}\left(-3\frac{x^2z}{r^5} - (1-2v)\left(\frac{x^2(2r+z)}{r^3(r+z)^2} - \frac{r^2-rz-z^2}{r^3(r+z)}\right)\right)F,$$

$$\sigma_{yy} = \frac{1}{2\pi}\left(-3\frac{y^2z}{r^5} - (1-2v)\left(\frac{y^2(2r+z)}{r^3(r+z)^2} - \frac{r^2-rz-z^2}{r^3(r+z)}\right)\right)F,$$

$$\sigma_{zz} = \frac{3z^3}{2\pi r^5}F,$$

$$\tau_{xy} = \frac{1}{2\pi}\left(-3\frac{xyz}{r^5} + (1-2v)\left(\frac{xy(2r+z)}{r^3(r+z)^2}\right)\right)F,$$

$$\tau_{yz} = \frac{3yz^2}{2\pi r^5}F,$$

$$\tau_{xz} = \frac{3xz^2}{2\pi r^5}F.$$

Also, since $-\partial U = -F\partial\delta$ (U the stored potential mechanical energy due to the elastic deformation), so we will have the following express ion for the potential energy

$$U = \int F\partial\delta = \int \frac{4}{3}E^*\delta^{\frac{3}{2}}R^{\frac{1}{2}}\partial\delta = \frac{8}{15}E^*\delta^{\frac{5}{2}}R^{\frac{1}{2}} \tag{C.1}$$

...............................**part(2)**..............................

The first derivative of stress $\sigma_T(\delta_n, \delta_t)\{\sigma_T = \sigma_t + \sigma_f\}$ with respect to x (opening direction- see Figure 3.16 c)) is given by

$$\frac{\sigma_T(\delta_n,\delta_t)}{\partial x} = \left[\frac{K_t(\delta_n,\delta_t)}{\partial x} = \frac{\partial^2 \sigma_t(\delta_n,\delta_t)}{\partial x^2}\right][U_H^2(x) - U_H^1(x)] + K_t(\delta_n,\delta_t)\left[\frac{\partial U_H^2(x)}{\partial x} - \frac{\partial U_H^1(x)}{\partial x}\right] +$$

$$\mu_f.\left\{K_n(\delta_n,\delta_t)\left[\frac{\partial U_v^2(x)}{\partial x} - \frac{\partial U_v^1(x)}{\partial x}\right] = \frac{\partial \sigma_n(\delta_n,\delta_t)}{\partial x}\right\} \tag{C.2}$$

Using Hooke's law again for isotropic materials we will get($\varepsilon_{ij} = \frac{1}{2}(\frac{\partial u_i}{\partial x_j} + \frac{\partial u_j}{\partial x_i})$)

$$\varepsilon_{11} = \varepsilon_2^H(x) = \frac{\partial U_H^2(x)}{\partial x} = \frac{1}{E_2}\left[\sigma_{11} - \nu_2(\sigma_{22} + \sigma_{33})\right] = \frac{1}{E_2}\left[\sigma_t(\delta_n,\delta_t) - \nu_2(\sigma_{22} + \sigma_{33})\right]$$

$$\varepsilon_{11} = \varepsilon_1^H(x) = \frac{\partial U_H^1(x)}{\partial x} = \frac{1}{E_1}\left[-\sigma_{11} - \nu_1(\sigma_{22} + \sigma_{33})\right] = \frac{1}{E_1}\left[-\sigma_t(\delta_n,\delta_t) - \nu_1(\sigma_{22} + \sigma_{33})\right]$$

$$\varepsilon_{31} + \varepsilon_{13} = \varepsilon_2^v(x) = \frac{\partial U_v^2(x)}{\partial x} = \frac{2(1+\nu_2)\sigma_{31}}{E_2} - \frac{\partial U_H^2(x)}{\partial z}$$

$$\varepsilon_{31} + \varepsilon_{13} = \varepsilon_1^v(x) = \frac{\partial U_v^1(x)}{\partial x} = \frac{2(1+\nu_1)\sigma_{31}}{E_1} - \frac{\partial U_H^2(x)}{\partial z}$$

..............................part(3)..............................

Mathematical description of Digital Image Correlation (DIC):

$$u_p = u + \frac{\partial u}{\partial r}.(r_p - r_c) + \frac{\partial u}{\partial s}.(s_p - s_c) \tag{C.3}$$

$$v_p = v + \frac{\partial v}{\partial r}.(r_p - r_c) + \frac{\partial v}{\partial s}.(s_p - s_c) \tag{C.4}$$

$$C_{cor}(u,v) = \sum_i \sum_j G_{ini}(r_i,s_j)G_{def}(r_i+u_p,s_j+v_p) \tag{C.5}$$

$$C_{cor}^{norm}(u,v) = \frac{\sum_i \sum_j G_{ini}(r_i,s_j)G_{def}(r_i+u_p,s_j+v_p)}{\sqrt{\sum_i \sum_j G_{ini}^2(r_i,s_j)\sum_i \sum_j G_{def}^2(r_i+u_p,s_j+v_p)}}, \tag{C.6}$$

where, u,v are the in-plane displacements of the subset $(2n \times 2n)$ centre point (r_c,s_c), u_p,v_p are the displacements of the subset arbitrary point (r_p,s_p), G_{ini},G_{def} are the grey values (the intensity) of a pixel with the coordinates $(r_i,s_j)/(r_i+u_p,s_j+v_p)$ inside the subset or facet in the reference and the deformed images, $C_{cor}(u,v),C_{cor}^{norm}(u,v)$ are the correlation coefficient and the normalised correlation coefficient (with the maximum value at one), where the computed maximum value for the equation (C.5), based on the reference and the deformed images, indicates the maximum similarity of the pattern matching.

In order to calculate the in-plane deformation in the x and y directions, we need to solve the above equations for the variables u and v.

..............................part(4)..............................

Linearisation, Discretization:

To begin, we recall the non-linear equation (5.26) of the total work δW_T (in the case of the directional derivative of E_{total} in the direction of the incremental virtual velocity, we will get the total virtual work δW_T), and for reasons of convenience and to reduce the use of notations,

instate the equation (5.26) we process the linearisation of the equation (5.27) as follows:

$$D_{\Delta v, \triangle T} \delta W_T(v_i, T_i, \delta v, \delta T) = D_{\Delta v, \triangle T} \{ \delta W_{int}^{mech} - \delta W_{ext}^{mech} - \delta W_{trac} + \delta W_{ext}^{ther} +$$

$$\delta W_{Fst} + \delta W_{contact} + \delta W_{fric} + \delta W_{heat} + \delta W_{int}^{ther} + \delta W_{frac} + \delta W_{\kappa inetic} \} =$$

$$\frac{d}{d\varepsilon, \omega} \delta W_T(v_i + \varepsilon \Delta v, T_i + \omega \triangle T; \delta v, \delta T) \mid_{\varepsilon, \omega = 0} = \frac{d}{d\varepsilon, \omega} \{ \delta W_{int}^{mech} - \delta W_{ext}^{mech} -$$

$$\delta W_{trac} + \delta W_{ext}^{ther} + \delta W_{Fst} + \delta W_{contact} + \delta W_{fric} + \delta W_{heat} + \delta W_{int}^{ther} +$$

$$\delta W_{frac} + \delta W_{\kappa inetic} \} (u_i + \varepsilon \Delta v, T_i + \omega \triangle T; \delta v, \delta T) \mid_{\varepsilon, \omega = 0}, \tag{C.7}$$

where

$$D_{\Delta v} \delta W_{int}^{mech}(v_i, \delta v) \quad = \frac{d}{d\varepsilon} \delta W_{int}^{mech}(v_i + \varepsilon \Delta v) \mid_{\varepsilon = 0} = \sum_{\forall i | \forall \Omega} \int_{\Omega} \{ D_{\Delta v}(\frac{\partial U_i}{\partial e}) : De[\delta v] +$$

$$\frac{\partial U_i}{\partial e} : D_{\Delta v}(De[\delta v]) \} d_{\Omega} = \sum_{\forall i | \forall \Omega} \int_{\Omega} \{ \nabla \delta v : \nabla \Delta v \sigma + \nabla \delta v : \underbrace{c}_{elasticity tensor} : \nabla \Delta v \} d_{\Omega} \tag{C.8}$$

$$D_{\Delta v} \delta W_{ext}^{mech}(v_i, \delta v) \quad = 0 \tag{C.9}$$

$$D_{\Delta v} \delta W_{frac}(v_i^c, \delta v \mid \delta g) \quad = \sum_{\forall \partial \Omega_{\Gamma}} \int_{\partial \Omega_{\Gamma}} \{ D_{\Delta v} T G_c [T G_{Ic} \mid T G_{IIc} \mid T G_{IIIc}][\delta g_N \mid \delta g_T] +$$

$$T G_c [T G_{Ic} \mid T G_{IIc} \mid T G_{IIIc}] D_{\Delta v} [\delta g_N \mid \delta g_T] \} d_{\partial \Omega_{\Gamma}} \tag{C.10}$$

$$if\ static(\frac{\partial^2 u_i}{\partial t^2} = 0) \rightarrow D_{\Delta v}\delta W_{\kappa inetic}(v_i, \delta v) = 0 \quad ; if\ dynamic \rightarrow D_{\Delta v}\delta W_{\kappa inetic}(v_i, \delta v) =$$

$$\sum_{\forall i|\forall\Omega}\int_{\Omega}\rho_i\{D_{\Delta v}(\frac{\partial^2 u_i}{\partial t^2})\delta v + \frac{\partial^2 u_i}{\partial t^2}D_{\Delta v}\delta v\}d_\Omega \tag{C.11}$$

$$D_{\Delta v}\delta W_{trac}(v_i^c, \delta v \mid \delta g) \quad = \sum_{\forall\partial\Omega_\Gamma}\{\int_{\partial\Omega_\Gamma}[D_{\Delta v}T_x\delta g_N + T_xD_{\Delta v}\delta g_N]d_{\partial\Omega_\Gamma}+$$

$$\int_{\partial\Omega_\Gamma}[D_{\Delta v}T_y\delta g_T + T_yD_{\Delta v}\delta g_T]d_{\partial\Omega_\Gamma} + \int_{\partial\Omega_\Gamma}\{D_{\Delta v}[P = T_z]\delta g_T + [P = T_z]D_{\Delta v}\delta g_T\}d_{\partial\Omega_\Gamma}\} \tag{C.12}$$

$$D_{\triangle T}\delta W_{heat}(T_i, \delta T) \quad = \sum_{\forall i|\forall\Omega}\int_{\Omega}C_i\rho_i[D_{\triangle T}\frac{\partial T}{\partial t}\delta T^i + \frac{\partial T}{\partial t}D_{\triangle T}\delta T^i]d_\Omega \tag{C.13}$$

$$D_{\triangle T}\delta W_{int}^{ther}(T_i, \delta T) \quad = \sum_{\forall i|\forall\Omega}\int_{\Omega}\kappa_i\{D_{\triangle T}\nabla T^i.\nabla\delta T^i + \nabla T^i.D_{\triangle T}\nabla\delta T^i\}d_\Omega \tag{C.14}$$

$$D_{\triangle T}\delta W_{ext}^{ther}(T_i, \delta T) = \sum_{\forall i|\forall\Omega|\forall\partial\Omega}\{\int_{\Omega}-D_{\triangle T}[R_i\delta T^i]d_\Omega + \int_{\partial\Omega}D_{\triangle T}[Q_iN_i\delta T^i]d_{\partial\Omega}\} \tag{C.15}$$

$$D_{\triangle T}\delta W_{Fst}(v_i^c, T_i, \delta T) \quad = \sum_{\forall\partial\Omega_\Gamma|\forall s,m}\int_{\partial\Omega_\Gamma}\{(D_{\triangle T}q_c^s.\delta T^s + q_c^s.D_{\triangle T}\delta T^s+$$

$$D_{\triangle T}q_c^m.\delta T^m + q_c^m.D_{\triangle T}\delta T^m)d_{\partial\Omega_\Gamma} \tag{C.16}$$

$$D_{\Delta v}\delta W_{fric}(v_i^c, \delta v \mid \delta g) \quad = \sum_{\forall\partial\Omega_\Gamma|\forall i,j,\beta}\int_{\partial\Omega_\Gamma}\{D_{\Delta v}t_f^i.\delta g_T + t_f^i.D_{\Delta v}\delta g_T\}d_{\partial\Omega_\Gamma} \tag{C.17}$$

$$D_{\Delta v}\delta W_{contact}(v_i^c,\delta v \mid \delta g) = \sum_{\forall \partial \Omega_\Gamma \mid \forall i,j} \int_{\partial \Omega_\Gamma} \{D_{\Delta v}t_N^i \delta g_N + t_N^i D_{\Delta v} \delta g_N\} d_{\partial \Omega_\Gamma}, \qquad (C.18)$$

where the computation of the derivative of the quantities $t_N, \delta g_N, t_f, \delta g_T, \delta T, TG_{Ic} \mid TG_{IIc} \mid TG_{IIIc}$ have been given in detail in the previous chapter.

Next, we process the discretisation of the weak or the variational form of the Problem (*MOC*) [the non-linear equation (5.26)], where it follows the general Galerkin approximation solution method with member approximation of the solution spaces (finite dimensional solution spaces V_t^h, T_t^h) and the weighting spaces (finite dimensional weighting spaces W^h, T_w^h) expressed as

$$V_t^h := \{v_t^h = \sum_{\forall nodal\,points(p)} N_p \dot{d}_p^t \mid N_p : \bar{\Omega} \to R^d; v_t^h(X) \approx \bar{v}_t(X), X \in \Gamma_u\} \qquad (C.19)$$

$$W^h := \{w^h = \sum_{\forall nodal\,points(p)} N_p c_p \mid N_p : \bar{\Omega} \to R^d; w^h(X) = 0, X \in \Gamma_u\} \qquad (C.20)$$

$$T_t^h := \{T_t^h = \sum_{\forall nodal\,points(p)} N_p T_p^t \mid T_t^h : \bar{\Omega} \to R, T_t^h > 0; T_t^h(X) \approx \bar{T}_t(X), X \in \Gamma_T\} \quad (C.21)$$

$$T_w^h := \{T_w^h = \sum_{\forall nodal\,points(p)} N_p c_p^T \mid T_w^h : \bar{\Omega} \to R, T_w^h(X) = 0, X \in \Gamma_T\}, \qquad (C.22)$$

where N_p is the shape function associated with node P, T_p^t is the time dependent temperature of node point p, d_p^t is a d-dimensional vector containing the time dependent coordinate of node point p where the velocity field is denoted by $v = \dot{d}$.

After substitution of the finite dimensional counterpart of the solutions and variations, the equations (C.19), (C.20), (C.21) and (C.22) into the work expression $\delta W_T(v_i, T_i, \delta v, \delta T)$, equation (5.26), we will have

$$\underbrace{\sum_{\forall i|\forall \Omega}\int_{\Omega}\rho_i(\frac{\partial^2 u_i}{\partial t^2})\delta v d_\Omega}_{Kinetic\,virtual\,work\,\delta W_{Kinetic}} \approx \underbrace{\sum_{\forall i|\forall \Omega^h}\int_{\Omega^h}\rho_i(\sum_{\forall nodal\,points(p)}N_p\ddot{d}_p^t)\sum_{\forall nodal\,points(q)}N_q c_q d_\Omega}_{Discretized\,Kinetic\,virtual\,work\,\delta W_{Kinetic}} =$$

$$\sum_{\forall i|\forall \Omega^h}\underbrace{\sum_{\forall nodal\,points(p)}\sum_{\forall dimension(\alpha)}}_{\sum_{\forall degree\,of\,freedom}}\underbrace{\sum_{\forall nodal\,points(q)}\sum_{\forall dimension(\beta)}}_{\sum_{\forall degree\,of\,freedom}}\int_{\Omega^h}\rho_i\delta_{\alpha\beta}(N_p\ddot{d}_p^t(\alpha))N_q c_q(\beta)d_\Omega =$$

$$\sum_{\forall i|\forall \Omega^h}\sum_{\forall degree\,of\,freedom(dq)}c_{dq}\underbrace{\{\underbrace{\sum_{\forall degree\,of\,freedom(pq)}\int_{\Omega^h}\rho_i\delta_{\alpha\beta}(N_p)N_q d_\Omega}_{element\,of\,mass\,matrix(M)}\,\ddot{d}_{pq}^t\}}_{Mass\,matrix(M)} \qquad (C.23)$$

$$\underbrace{\sum_{\forall i|\forall \Omega|\forall \partial\Omega_\sigma}\{\int_{\Omega}b_i.\delta v d_\Omega + \int_{\partial\Omega_\sigma}t_\sigma^i.\delta v d_{\partial\Omega_\sigma}\}}_{External\,virtual\,work\,\delta W_{ext}^{mech}} \approx \sum_{\forall i|\forall\Omega^h|\forall\partial\Omega_\sigma^h}\sum_{\forall dof(dq)}c_{dq}\underbrace{\{\int_{\Omega^h}b_i.N_q d_\Omega + \int_{\partial\Omega_\sigma^h}t_\sigma^i.N_q d_{\partial\Omega_\sigma}\}}_{External\,force\,vector[F_{ext}^{mech}(t)]}$$
$$(C.24)$$

$$\underbrace{\sum_{\forall i|\forall \Omega}\int_{\Omega}\frac{\partial U_i}{\partial e}:De[\delta v]d_\Omega}_{Internal\,virtual\,work\,\delta W_{int}^{mech}} \approx \underbrace{\sum_{\forall i|\forall \Omega^h}\int_{\Omega^h}\sigma^h:\nabla[\sum_{\forall nodal\,points(q)}N_q c_q]d_\Omega}_{Discretized\,Internal\,virtual\,work\,\delta W_{int}^{mech}} =$$

$$\sum_{\forall i|\forall \Omega^h}\int_{\Omega^h}\sigma^h:[\sum_{\forall nodal\,points(q)}\nabla N_q \otimes c_q]d_\Omega = \sum_{\forall i|\forall \Omega^h}\int_{\Omega^h}[\sum_{\forall nodal\,points(q)}\sum_{\forall dimension(\alpha)}$$

$$\sum_{\forall dimension(\beta)}\frac{\partial N_q}{\partial \beta}c_q(\alpha)\sigma_{\alpha\beta}^h]d_\Omega = \sum_{\forall i|\forall \Omega^h}\sum_{\forall degree\,of\,freedom(dq)}c_{dq}\underbrace{\int_{\Omega^h}[\sum_{\forall dimension(\beta)}\frac{\partial N_q}{\partial \beta}\sigma_{\alpha\beta}^h]d_\Omega}_{Internal\,force\,vector[F_{int}^{mech}(d)]}$$
$$(C.25)$$

$$\underbrace{\sum_{\forall \partial\Omega_\Gamma}(\int_{\partial\Omega_\Gamma}T_x\delta g_N d_{\partial\Omega_\Gamma} + \int_{\partial\Omega_\Gamma}T_y\delta g_T d_{\partial\Omega_\Gamma} + \int_{\partial\Omega_\Gamma}[P=T_z]\delta g_T d_{\partial\Omega_\Gamma})}_{D_{\delta v}(\iint_s Tx(\xi,\eta)\phi d\xi d\eta + \iint_s Ty(\xi,\eta)\phi d\xi d\eta + \iint_s[P(\xi,\eta)=Tz(\xi,\eta)]\phi d\xi d\eta)=\delta W_{trac}} \approx$$

$$\underbrace{\sum_{\forall \partial \Omega_\Gamma^h} \Big(\int_{\partial \Omega_\Gamma^h} \{T_x.(-v) + (T_y + T_z)(\tau^\alpha)\} \Big(\sum_{\forall nodal points(p)} c_p - \sum_{\forall nodal points(p^\mp)} N_{p^\mp} c_{p^\mp} \Big) d_{\partial \Omega_\Gamma}}_{Discretized \delta W_{trac}}$$

$$\sum_{\forall \partial \Omega_\Gamma^h} \sum_{\forall degree of freedom(dq)} c_{dq} \underbrace{\Big(\int_{\partial \Omega_\Gamma^h} [T_x.(v) + (T_y + T_z)(\tau^\alpha)](1, -N_{p^\mp} \mid_{\forall nodal points(p^\mp)}) d_{\partial \Omega_\Gamma} \Big)}_{Force vector[F_{trac}(d)]} \qquad (C.26)$$

$$\underbrace{\sum_{\forall \partial \Omega_\Gamma} \int_{\partial \Omega_\Gamma} TG_c[TG_{Ic} \mid TG_{IIc} \mid TG_{IIIc}][\delta g_N \mid \delta g_T] d_{\partial \Omega_\Gamma}}_{Fracture virtual work \delta W_{frac}} \approx$$

$$\underbrace{\sum_{\forall \partial \Omega_\Gamma^h} \int_{\partial \Omega_\Gamma^h} TG_c(-v \mid \tau^\alpha) \Big(\sum_{\forall nodal points(p)} c_p - \sum_{\forall nodal points(p^\mp)} N_{p^\mp} c_{p^\mp} \Big) d_{\partial \Omega_\Gamma}}_{Discretized Fracture virtual work \delta W_{frac}} =$$

$$\sum_{\forall \partial \Omega_\Gamma^h} \sum_{\forall degree of freedom(dq)} c_{dq} \underbrace{\int_{\partial \Omega_\Gamma^h} TG_c(v \mid \tau^\alpha)(1, -N_{p^\mp} \mid_{\forall nodal points(p^\mp)}) d_{\partial \Omega_\Gamma}}_{Fracture force vector[F_{frac}(d)]} \qquad (C.27)$$

$$\underbrace{\sum_{\forall \partial \Omega_\Gamma \mid \forall i,j} \int_{\partial \Omega_\Gamma} t_N^i \delta g_N d_{\partial \Omega_\Gamma}}_{Contact V work \delta W_{contact}} \approx$$

$$\underbrace{\sum_{\forall \partial \Omega_\Gamma^h \mid \forall i,j} \int_{\partial \Omega_\Gamma^h} t_N^i(-v) \Big(\sum_{\forall nodal points(p)} c_p - \sum_{\forall nodal points(p^\mp)} N_{p^\mp} c_{p^\mp} \Big) d_{\partial \Omega_\Gamma}}_{Discretized Contact V work \delta W_{contact}} =$$

$$\sum_{\forall \partial \Omega_\Gamma^h \mid \forall i,j} \sum_{\forall degree of freedom(dq)} c_{dq} \underbrace{\int_{\partial \Omega_\Gamma^h} t_N^i(v)(1, -N_{p^\mp} \mid_{\forall nodal points(p^\mp)}) d_{\partial \Omega_\Gamma}}_{Contact force vector[F_{con}(d)]} \qquad (C.28)$$

$$\underbrace{\sum_{\forall \partial \Omega_\Gamma \mid \forall i,j,\beta} \int_{\partial \Omega_\Gamma} t_f^i . \delta g_T d_{\partial \Omega_\Gamma}}_{Fracture Surface Friction virtual work \delta W_{fric}} \quad \approx$$

$$\underbrace{\sum_{\forall \partial \Omega_\Gamma^h | \forall i,j,\beta} \int_{\partial \Omega_\Gamma^h} t_f^i(\beta).(\tau^\beta)(\sum_{\forall nodal points(p)} c_p - \sum_{\forall nodal points(p^\mp)} N_{p^\mp} c_{p^\mp}) d_{\partial \Omega_\Gamma} =}_{Discretized Fracture Surface Friction virtual work \delta W_{fric}}$$

$$\sum_{\forall \partial \Omega_\Gamma^h | \forall i,j,\beta} \sum_{\forall degree of freedom(dq)} c_{dq} \underbrace{\int_{\partial \Omega_\Gamma^h} t_f^i(\beta).(\tau^\beta)(1, -N_{p^\mp} \mid_{\forall nodal points(p^\mp)}) d_{\partial \Omega_\Gamma}}_{Friction force vector [F_{fric}(d)]} \qquad (C.29)$$

$$\underbrace{\sum_{\forall \partial \Omega_\Gamma | \forall s,m} \int_{\partial \Omega_\Gamma} (q_c^s.\delta T^s + q_c^m.\delta T^m) d_{\partial \Omega_\Gamma}}_{Fracture Surface Thermodynamic virtual work \delta W_{Fst}} \approx$$

$$\underbrace{\sum_{\forall \partial \Omega_\Gamma^h | \forall s,m} \int_{\partial \Omega_\Gamma^h} (q_c^s. \sum_{\forall nodal points(ps)} N_{ps} c_{ps}^T + q_c^m. \sum_{\forall nodal points(pm)} N_{pm} c_{pm}^T) d_{\partial \Omega_\Gamma} =}_{Discretized Fracture Surface Thermodynamic virtual work \delta W_{Fst}}$$

$$\sum_{\forall \partial \Omega_\Gamma^h | \forall s,m} \sum_{\forall degree of freedom(dq)} c_{dq} \underbrace{\int_{\partial \Omega_\Gamma^h} [(q_c^s.N_{ps}) + (q_c^m.N_{pm})] d_{\partial \Omega_\Gamma}}_{Fracture Surface Thermodynamic force vector [F_{Fst}(d,T)]} \qquad (C.30)$$

$$\underbrace{\sum_{\forall i | \forall \Omega | \forall \partial \Omega} \{\int_\Omega -R_i \delta T^i d_\Omega + \int_{\partial \Omega} Q_i N_i \delta T^i d_{\partial \Omega}\}}_{External virtual work \delta W_{ext}^{ther}} \approx$$

$$\underbrace{\sum_{\forall i | \forall \Omega^h | \forall \partial \Omega^h} \{\int_{\Omega^h} -R_i \sum_{\forall nodal points(p)} N_p c_p^T d_\Omega + \int_{\partial \Omega^h} Q_i N_i \sum_{\forall nodal points(p)} N_p c_p^T d_{\partial \Omega}\} =}_{Discretized External virtual work \delta W_{ext}^{ther}}$$

$$\sum_{\forall i | \forall \Omega^h | \forall \partial \Omega^h} \sum_{\forall degree of freedom(dq)} c_{dq} \underbrace{\{\int_{\Omega^h} -R_i N_p d_\Omega + \int_{\partial \Omega^h} Q_i N_i N_p d_{\partial \Omega}\}}_{External force vector [F_{ext}^{ther}(t)]} \qquad (C.31)$$

$$\underbrace{\sum_{\forall i|\forall\Omega}\int_{\Omega}\kappa_i\nabla T^i.\nabla\delta T^i d_\Omega}_{Internal\,virtual\,work\,\delta W_{int}^{ther}}\approx\underbrace{\sum_{\forall i|\forall\Omega^h}\int_{\Omega^h}\kappa_i\nabla(\sum_{\forall nodal\,points(p)}N_pT_p^t).\nabla(\sum_{\forall nodal\,points(p)}N_pc_p^T)d_\Omega=}_{Discretized\,Internal\,virtual\,work\,\delta W_{int}^{ther}}$$

$$\sum_{\forall i|\forall\Omega^h}\sum_{\forall degree\,of\,freedom(dq)}c_{dq}\int_{\Omega^h}\kappa_i\sum_{\forall nodal\,points(p)}\nabla(N_pT_p^t).\underbrace{\sum_{\forall dimension(\beta)}\frac{\partial N_q}{\partial\beta}d_\Omega}_{Internal\,force\,vector[F_{int}^{ther}(T)]}\qquad(C.32)$$

$$\underbrace{\sum_{\forall i|\forall\Omega}\int_{\Omega}C_i\frac{\partial T}{\partial t}\rho_i\delta T^i d_\Omega}_{Heat\,internal\,virtual\,work\,\delta W_{heat}}\approx\underbrace{\sum_{\forall i|\forall\Omega^h}\int_{\Omega^h}C_i\frac{\partial(\sum_{\forall nodal\,points(q)}N_qT_q^t)}{\partial t}\rho_i(\sum_{\forall nodal\,points(p)}N_pc_p^T)d_\Omega=}_{Discretized\,Heat\,internal\,virtual\,work\,\delta W_{heat}}$$

$$\sum_{\forall i|\forall\Omega^h}\int_{\Omega^h}C_i\frac{\partial(\sum_{\forall nodal\,points(q)}N_qT_q^t)}{\partial t}\rho_i(\sum_{\forall nodal\,points(p)}N_pc_p^T)d_\Omega=$$

$$\sum_{\forall i|\forall\Omega^h}\sum_{\forall degree\,of\,freedom(dq)}c_{dq}\sum_{\forall nodal\,points(q)}\underbrace{\int_{\Omega^h}C_i(N_q\mid N_p^T)\rho_i(N_p)d_\Omega}_{Heat\,Capacitance\,matrix(C)}\frac{\partial(T_q^t)}{\partial t}\qquad(C.33)$$

Assuming $d=(d,T)$, where the vector d contains nodal value for motion and temperature, the generic form of the global variation equation (5.26), summarised, takes the form of a non-linear ordinary differential equation, the discrete equation of motion, expressed as

(which holds $\forall degree\,of\,freedom(dq),c_{dq}$ with appropriated boundary conditions)

$$M\ddot{d}(t)+C\dot{d}(t)+F_{int}^{ther}[d(t)]+F_{Fst}[d(t)]+F_{fric}[d(t)]+F_{frac}[d(t)]+F_{con}[d(t)]+$$

$$F_{trac}[d(t)]+F_{int}^{mech}[d(t)]=F_{ext}^{mech}(t)+F_{ext}^{ther}(t)\quad Discrete\,Momentum\,Balance(DMB)\,\,(C.34)$$

Note that,

$$F_{fric}[d(t)]+F_{con}[d(t)]+F_{frac}[d(t)]+F_{trac}[d(t)]+F_{Fst}[d(t)]=F_{contact}[d(t)],\qquad(C.35)$$

which has been formulated in the modified contact mechanic as a generalised contact force vector $F_{contact}[d(t)]$ where, in this case, the term $F_{con}[d(t)]$ can be eliminated in equation (C.35) because it is automatically part of the contact formulation.

Solution methods:

The solution strategy or procedure generally is subdivided into two different problem

classes of finite differencing procedure (in most cases applied to the time interval of interest), quasi-static and dynamic.

In the case of quasi-static, due to the assumption that the inertial load/term can be disregarded (too unimportant to be worth consideration in comparison to internal forces and applied loads), the Discrete Momentum Balance (*DMB*) equation takes a new form, which can be expressed by using the residual vector concept, as in the following equation (where C is the heat capacitance matrix)

$$R(d_{n+1}) = F_{ext}^{mech}(t_{n+1}) + F_{ext}^{ther}(t_{n+1}) - \{C\dot{d}_{n+1} + F_{int}^{mech}[d_{n+1}] + F_{int}^{ther}[d_{n+1}] +$$

$$\underbrace{F_{Fst}[d_{n+1}] + F_{fric}[d_{n+1}] + F_{con}[d_{n+1}] + F_{frac}[d_{n+1}] + F_{trac}[d_{n+1}]}_{F_{contact}[d_{n+1}]}\}, \tag{C.36}$$

where beginning with an (initial) equilibrium state $R(d_n) = 0$, calculate

$$\triangle d = d_{n+1} - d_n \quad (displacement\, increnent) \tag{C.37}$$

$$\triangle F_{ext} = F_{ext}(t_{n+1}) - F_{ext}(t_n) \quad (load\, increnent), \tag{C.38}$$

and determine d_{n+1} such that $R(d_{n+1}) = 0$.

In contrast to the case of quasi-static analysis, in the case of dynamic analysis we will have other formulations where, due to the Non-negligible inertial load/term, additionally, the concepts of accuracy and stability come into question.

The problem can be appropriately formulated as:

Given $[\ddot{d}_n \mid a_n], d_n, v_n$

find $[\ddot{d}_{n+1} \mid a_{n+1}], d_{n+1}, v_{n+1}$ such that

$$d_{n+\alpha} = \alpha d_{n+1} + (1-\alpha)d_n, \tag{C.39}$$

and additionally

$I:\ M[\ddot{d}_{n+\alpha} \mid a_{n+\alpha}] + C\dot{d}_{n+\alpha} + F_{int}^{mech}[d_{n+\alpha}] + F_{int}^{ther}[d_{n+\alpha}] +$

$\underbrace{F_{Fst}[d_{n+\alpha}] + F_{fric}[d_{n+\alpha}] + F_{con}[d_{n+\alpha}] + F_{frac}[d_{n+\alpha}] + F_{trac}[d_{n+\alpha}]}_{F_{contact}[d_{n+\alpha}]} = F_{ext}^{mech}(t_{n+\alpha}) + F_{ext}^{ther}(t_{n+\alpha})$

$II:\ d_{n+1} = d_n + v_n(t_{n+1} - t_n) + \frac{1}{2}[2\beta a_{n+1} + (1-2\beta)a_n](t_{n+1} - t_n)^2$

$III:\ v_{n+1} = v_n + [\gamma a_{n+1} + (1-\gamma)a_n](t_{n+1} - t_n)$

$IV:\ T_{n+1} = \frac{[D_{mechanical dissipation}^{n+1} + R_{d_{n+1}} - DIV(Q_{d_{n+1}})]}{[\eta_{n+1} - \eta_n]}(t_{n+1} - t_n)$

$V:\ T_{n+1}^{contact}(T_{n+1}^{contact} - T_n^{contact}) = \frac{T_0[\xi\|t_f^{n+1}\| + t_N^{n+1}h_c^m\theta_m^{n+1} + t_N^{n+1}h_c^s\theta_s^{n+1}]}{C_{contact}^{heatsink}},$

where the formulation of the equation V, is based on the combination of the equations (4.63), (4.64), (4.65) and (4.66), α, β, γ are the stability and the accuracy parameters, η is the portion of the entropy formulated by the gradient of the free energy of the solid[2], $[\ddot{d}_n \mid a_n], d_n, v_n$ are the acceleration, the solution vector and the velocity at time t_n and to calculate ξ the relation $\frac{dg_T}{dt} = \xi \frac{T_T}{\|T_T\|}$ has been taken into account.

Note that the algorithm is divided into two phases given by:

I : *With fixed temperature, calculate* d_{n+1}.

II : *With fixed* d_{n+1}, *calculate temperature at* t_{n+1}.

Stability-accuracy analysis:

Prior to the development of a full thermo-mechanical contact-cohesive formulation (a functional that describes the dynamic system) and doing a stability-accuracy (analysis) estimation of the total system, we briefly survey the theory of some of the common existing algorithms/methods used in describing the stability and the accuracy of the system and solving techniques.

Setting different values for α, β, γ (the stability and the accuracy parameters) and substituting into $I - III$, one can obtain different cases for the stability and the accuracy of the method. Two commonly used values for these parameters are described in the following Laursen (2003)

$$
\begin{cases}
Trapezoidal\ rule\ [\alpha = 1, \beta = \frac{1}{4}, \gamma = \frac{1}{2}] \\
(unconditionally\ stable\ and\ second\ order\ accuracy) \\
Central\ differences\ [\alpha = 1, \beta = 0, \gamma = \frac{1}{2}] \\
(conditionally\ stable\ and\ second\ order\ accuracy),
\end{cases}
$$

where the algorithms corresponding to the above choices of the parameters can be used by different solving techniques for the determination of the unknown{commonly $Gi\check{v}en\ [\ddot{d}_n \mid a_n], d_n, v_n\ \overrightarrow{Find}\ [\ddot{d}_{n+1} \mid a_{n+1}], d_{n+1}, v_{n+1}$}.

Two common solving techniques, known as implicit and explicit finite element methods, in combination with the Trapezoidal and the Central differences algorithms, are widely implemented. In the following, using the equations $I - III$, the fundamental ideas behind the implicit finite element method (in more detailed description based on FEBio implementation) will be provided.

Implicit-Trapezoidal method:

Setting $[\alpha = 1, \beta = \frac{1}{4}, \gamma = \frac{1}{2}]$ and substituting into equations $I - III$ we get

I : $\underbrace{F_{Fst}[d_{n+1}] + F_{fric}[d_{n+1}] + F_{con}[d_{n+1}] + F_{frac}[d_{n+1}] + F_{trac}[d_{n+1}]}_{F_{contact}[d_{n+1}]} + M[a_{n+1}] + C\dot{d}_{n+1} +$

$$F_{int}^{mech}[d_{n+1}] + F_{int}^{ther}[d_{n+1}] + = F_{ext}^{mech}(t_{n+1}) + F_{ext}^{ther}(t_{n+1})$$

$II: d_{n+1} = d_n + v_n(t_{n+1}-t_n) + \frac{1}{4}[a_{n+1}+a_n](t_{n+1}-t_n)^2 \iff (II): a_{n+1} = \frac{4d_{n+1}}{(t_{n+1}-t_n)^2} - (a_n + \frac{4d_n}{(t_{n+1}-t_n)^2} + \frac{4v_n}{(t_{n+1}-t_n)})$

$III: v_{n+1} = v_n + [a_{n+1}+a_n]\frac{(t_{n+1}-t_n)}{2},$

where the first equation I can be expressed in a coupled form by using the residual vector $R(d_{n+1})$, expressed as the following equation

$$R(d_{n+1}) \overset{(II)}{=} F_{ext}^{mech}(t_{n+1}) + F_{ext}^{ther}(t_{n+1}) - M[\frac{4d_{n+1}}{(t_{n+1}-t_n)^2}] + M(a_n + \frac{4d_n}{(t_{n+1}-t_n)^2} + \frac{4v_n}{(t_{n+1}-t_n)}) -$$

$$\underbrace{\{F_{Fst}[d_{n+1}] + +F_{con}[d_{n+1}] + F_{fric}[d_{n+1}] + F_{frac}[d_{n+1}] + F_{trac}[d_{n+1}]}_{F_{contact}[d_{n+1}]} + C\dot{d}_{n+1} +$$

$$F_{int}^{mech}[d_{n+1}] + F_{int}^{ther}[d_{n+1}]\} = 0 \tag{C.40}$$

After taking the derivative of the equation (C.40), the residual vector $R(d_{n+1})$ with respect to d we get

$$\frac{\partial R}{\partial d}\mid_{d_{n+1}} = -M[\frac{4}{(t_{n+1}-t_n)^2}] - \{\frac{C\partial \dot{d}}{\partial d} + [K^{mech}(d_{n+1}) = \frac{\partial F_{int}^{mech}}{\partial d}] + [K^{ther}(d_{n+1}) = \frac{\partial F_{int}^{ther}}{\partial d}] +$$

$$\underbrace{[K^{Fst}(d_{n+1}) = \frac{\partial F_{Fst}}{\partial d}] + [K^{fric}(d_{n+1}) = \frac{\partial F_{fric}}{\partial d}] + [K^{con}(d_{n+1}) = \frac{\partial F_{con}}{\partial d}]}_{[K^{contact}(d_{n+1}) = \frac{\partial F_{contact}}{\partial d}]partI} +$$

$$\underbrace{[K^{frac}(d_{n+1}) = \frac{\partial F_{frac}}{\partial d}] + [K^{trac}(d_{n+1}) = \frac{\partial F_{trac}}{\partial d}]\}}_{[K^{contact}(d_{n+1}) = \frac{\partial F_{contact}}{\partial d}]partII} \tag{C.41}$$

where $K^{mech}, K^{ther}, K^{Fst}, K^{fric}, K^{frac}, K^{trac}, K^{con}, K^{contact}$ are the stiffness matrices respectively.

Finally, substituting the equations (C.40) and (C.41) into the equation (based on the Newton-Raphson technique)

$$R + \frac{\partial R}{\partial d}\triangle d = 0, \tag{C.42}$$

we get an equation that can be solved (by a non-linear solution strategy); for example, by Newton-Raphson iterative solution method[1].

---

[1]The Newton-Raphson iterative solution strategy:

$R(d_{n+1}^{iter}) + (\triangle d = d_{n+1}^{iter+1} - d_{n+1}^{iter})[\frac{\partial R}{\partial d}]_{d_{n+1}^{iter}} = 0$

with $\| \triangle d \| < Tolerance\ or/and\ \| R(d_{n+1}^{iter}) \| < Tolerance\ or/and\ small\ value\ for\ energy\ norm\ \triangle d.R(d_{n+1}^{iter})$

Stability estimate for the dynamic problem:

To prove the stability (the stability of an equilibrium point) of the (autonomous $x^{\cdot} = f(x); f(locally Lipschitz) : L \subseteq R^n \to R^n$) non-linear system [energy functional ($Problem(MOC)$)], we use Lyapunov's direct (or indirect) methods known as the first (or second) method (Note that, in this study we just use Lyapunov's direct method). To make it possible, and to get the fundamental idea of the method, first, we need to introduce some definition and theorem as follows:

<u>**Definition(5.1):**</u>

The equilibrium point $\bar{x}$ (or by changing the variable $\hat{x} = x - \bar{x}$, the new equilibrium point $\hat{x} = 0$ of $x^{\cdot} = f(x)$) is

$(I)\, Stable$: if $\forall \delta > 0, \exists \varepsilon > 0, such that, \forall t > t_0, \| x(t_0) \| < \varepsilon \Longrightarrow \| x(t) \| < \delta$

$(II)\, Asymptotically stable$ if $\forall \varepsilon > 0, \exists \delta > 0, such that, \| x(t_0) \| < \varepsilon \Longrightarrow lim_{t \to \infty} \| x(t) \| = 0$

Theorem 5.1: The equilibrium point $\hat{x} = 0 \in L \subset R^n$ of $\frac{dx}{dt} = x^{\cdot} = f(x)$ is a stable point if: For a continuously differentiable function $V : L \to R$ (called Lyapunov's function) we have

$$V(0) = 0 \, and \, \forall x \in L \smallsetminus \{0\}, V(x) > 0$$

$$\forall x \in L, \frac{dV(x)}{dt} = \dot{V}(x) = \frac{\partial V(x)}{\partial x}\frac{dx}{dt} = \frac{\partial V(x)}{\partial x}f(x) \leq 0$$

Furthermore, it is asymptotically stable if:

$$\forall x \in L \smallsetminus \{0\}, \dot{V}(x) < 0$$

[The proof of the theorem (1) can be found in any related textbook]

To begin, we introduce a functional $V(F, \psi_c^t, \eta, T^t)[E_{total}]$,. It will be proven in the following that it is not increasing during the time evaluation of the problem (MOC).

By using the equations (5.23), and

$$\underbrace{\overbrace{\frac{D\Pi_{ext}(t)}{Dt}}^{-P_{ext}(t)} + \overbrace{\frac{D\Pi_{int}(t)}{Dt}}^{P_{int}(t)} + \overbrace{\frac{D\kappa(t)}{Dt}}^{\frac{D\frac{1}{2}\int_\Omega \rho v^2 dV}{Dt}}}_{E_{int,ext}} = 0, \tag{C.43}$$

and (5.30) [2]

$$\frac{D\{e^{int}(F,\eta)-\theta(F,\eta)\eta\}}{Dt} = \frac{De^{int}}{Dt} - \underbrace{\frac{D\theta(F,\eta)\eta}{Dt}}_{T_0\dot{\eta}} = \frac{D\Psi(F,\theta(F,\eta))}{Dt}, \tag{C.44}$$

where

$$\frac{De^{int}}{Dt} = P:\dot{F} + \underbrace{\frac{D\left(\int_\Omega \eta(x,t)\theta(x,t)d\Omega\right)}{Dt}}_{T\dot{\eta}} - D_{mtaldissipation}, \tag{C.45}$$

and $(T = \theta)$

$$D_{mtaldissipation} = D_{mech} + D_{thermal}, \tag{C.46}$$

$$D_{totaldissipation} = D_{mtaldissipation} \underbrace{-\frac{1}{\theta}QGrad(\theta)}_{\geq 0(D_{conductiondissipation})}, \tag{C.47}$$

$$T\dot{\eta} = D_{mtaldissipation} + R - DIVQ, \tag{C.48}$$

where also in the case of having an alternative formulation for the entropy, namely $\eta = \eta^{elastic} + \eta^{plastic}$, and additionally by applying the divergence theorem, the equation (C.48) can be re-expressed as [Laursen (2003)]

$$T(\eta^{\dot{e}lastic} + \eta^{\dot{p}lastic}) = D_{mech} + \underbrace{T\eta^{\dot{p}lastic}}_{D_{thermal}} + D_{conductiondissipation} + R - DIVQ, \tag{C.49}$$

so we can determine the time derivative of the functional $V(F,\psi_c^t,g_N,g_T,\eta,T^t)$ (for the sake of convenience defined over Ω_s,Ω_m), by assuming $(T = T_0)$ on all boundaries outside the contact zone, $R = 0$ (zero heat source) and no supplied heat fluxes on the surfaces of the bodies, in the following simplified form

$(\Psi^{con}(g_N,g_T^{elastic},T_c) = \Psi^{con}(\chi))$

---

[2] $e^{int}(F,\eta), \theta(F,\eta)\eta, \Psi(F,\theta(F,\eta))$ are defined for both, the contact and the thermodynamic regime outside the contact

$$\dot{V}(F,\psi_c^t,g_N,g_T,\eta,T^t) = \frac{DV(F,\psi_c^t,g_N,g_T,\eta,T^t)}{Dt} = \sum_{i=1}^{2}\int_{\Omega_i}\{T\dot{\eta} - (D_{mtaldissipation} + T_0\eta^{e\dot{l}astic})\}d\Omega +$$

$$\int_{\partial\Omega_s}\underbrace{\{\frac{\partial\Psi^{con}(\chi)}{\partial g_N}\frac{Dg_N}{Dt} + \frac{\partial\Psi^{con}(\chi)}{\partial g_T}\frac{Dg_T}{Dt} + \frac{\partial\Psi^{con}(\chi)}{\partial T_c}\frac{DT_c}{Dt} + T_0\eta^{\dot{c}on}\}d_{\partial\Omega_\Gamma}}_{\frac{D\Psi^{con}(g_N,g_T^{elastic},T_c)}{Dt}} +$$

$$\underbrace{\int_{\partial\Omega_s}t_f^\alpha.(\frac{Dg_T}{Dt})_\alpha d_{\partial\Omega_\Gamma}}_{frictionwork} + \underbrace{\int_{\partial\Omega_s}TG_c[TG_{Ic}\mid TG_{IIc}\mid TG_{IIIc}][\frac{Dg_N}{Dt}\mid\frac{Dg_T}{Dt}]d_{\partial\Omega_\Gamma}}_{fracturework} - \underbrace{\int_{\partial\Omega_s}(q_c^s + q_c^m)d_{\partial\Omega_\Gamma}}_{thermodynamicwork} -$$

$$\underbrace{\int_{\partial\Omega_s}T_x\frac{Dg_N}{Dt}d_{\partial\Omega_\Gamma} + \int_{\partial\Omega_s}T_y\frac{Dg_T}{Dt}d_{\partial\Omega_\Gamma} + \int_{\partial\Omega_s}[P=T_z]\frac{Dg_T}{Dt}d_{\partial\Omega_\Gamma})}_{tractionswork} - \underbrace{\int_{\partial\Omega_s}T_N\frac{Dg_N}{Dt}d_{\partial\Omega_\Gamma}}_{contactwork}, \quad \text{(C.50)}$$

where
$$A = -\underbrace{\int_{\partial\Omega_s}T_x\frac{Dg_N}{Dt}d_{\partial\Omega_\Gamma} + \int_{\partial\Omega_s}T_y\frac{Dg_T}{Dt}d_{\partial\Omega_\Gamma} + \int_{\partial\Omega_s}[P=T_z]\frac{Dg_T}{Dt}d_{\partial\Omega_\Gamma})}_{tractionswork} +$$

$$\underbrace{\int_{\partial\Omega_s}TG_c[TG_{Ic}\mid TG_{IIc}\mid TG_{IIIc}][\frac{Dg_N}{Dt}\mid\frac{Dg_T}{Dt}]d_{\partial\Omega_\Gamma} \le 0,}_{fracturework} \quad \text{(C.51)}$$

because the (total) work done by advancing the cutting tool, in the case of the cutting, should always be equal to or greater than the (total) irreversible work done by the fracture formulation.

On the other hand, by making use of the equations (4.60), (4.62), (4.63), (4.64), (C.44) and (C.49) we get

$$\dot{V}(F,\psi_c^t,g_N,g_T,\eta,T^t) = -\sum_{i=1}^{2}\int_{\Omega_i}\frac{T_0}{T}\underbrace{\{D_{mech} + D_{conductiondissipation}\}}_{\ge 0}d\Omega + A -$$

$$\int_{\partial\Omega_s} \frac{T_0}{T_c} \underbrace{\left\{ \frac{q_c^s(T^s - T_c)}{T^s} + \frac{q_c^m(T^m - T_c)}{T^m} + t_f^\alpha.\left(\frac{Dg_T}{Dt}\right)_\alpha \right\}}_{\geq 0(D_{contactdissipation})} d_{\partial\Omega_\Gamma} \tag{C.52}$$

where $D_{contactdissipation}$, as shown by the equation (C.52), refers to the sum of the contact mechanical dissipation and the contact thermal dissipation (due to the conduction of heat across the master and slave surfaces), which is supposed to be positive at all times.

Thus,

$$\dot{V}(F, \psi_c^t, g_N, g_T, \eta, T^t) \leq 0, \tag{C.53}$$

which indicates that, for all possible evaluations of the dynamic system, the functional $\dot{V}(F, \psi_c^t, g_N, g_T, \eta, T^t)$ is non-increasing. In other words, it determines the stability of the full thermo-mechanical system (thermodynamically coupled frictional contact-cohesive problem) and provides a suitable stability estimate for the dynamic problem.

.................................part(5)..............................

Mechanics of cutting:

Due to the balance of mechanical energy (conservation of energy during a dynamic process) and the balance of thermal energy we have:

$\frac{D\Pi_{ext}(t)}{Dt} = -P_{ext}(t) = -(\int_{\Omega_0} B.vdV + \int_{\partial\Omega_0} T.vdS) \qquad external\ stress\ power$

$\frac{D\Pi_{int}(t)}{Dt} = P_{int}(t) = \int_{\Omega_0} P : \frac{DF}{Dt}dV \qquad internal\ stress\ power$

$P_{int}(t) = \frac{DE_{int}(t)}{Dt} - (\underbrace{\int_{\Omega_0} RdV + \int_{\partial\Omega_0} Q_NdS}_{Q(t)}) \qquad Q(t), thermal\ power\,; \frac{DE_{int}(t)}{Dt}, the\ rate\ of\ internal\ energy$

$\underbrace{\Pi_{int}(t) + \Pi_{ext}(t) + \frac{1}{2}\int_{\Omega_0} \rho v^2 dV = constant}_{E_{total}} \implies \frac{DE_{total}}{Dt} = 0$

(with ε, ω as scalars, T temperature field , δT temperature (incremental) variation)

$\delta W_T(v_i, T_i, \delta v, \delta T) = D_{\delta u, \delta T}\frac{DE_{total}(u_i, T_i)}{Dt} = \frac{d}{d\varepsilon, \omega}\frac{DE_{total}(u_i + \varepsilon\delta u, T_i + \omega\delta T)}{Dt}|_{\varepsilon, \omega = 0}$

Note that, in the case of consideration of entropy production (by conduction of heat), and due to the second law of thermodynamics ($\frac{D\left(\int_{\Omega_0} \eta(x,t)dV\right)}{Dt} - \int_{\Omega_0}[R^\eta = \frac{R}{\theta(x,t)}]dV + \int_{\partial\Omega_0}[Q^\eta = \frac{Q}{\theta(x,t)}]NdS \geq 0$ - entropy inequality principle) and Clausius-Plank inequality, the local balance of energy with respect to production of entropy is given by

$$P_{int}(t) = \frac{DE_{int}(t)}{Dt} + \underbrace{\frac{D\left(\int_{\Omega_0} \eta(x,t)\theta(x,t)dV\right)}{Dt}}_{\Xi} - D_{mechanical dissipation} - \underbrace{\left(\int_{\Omega_0} RdV + \int_{\partial\Omega_0} Q_N dS\right)}_{Q(t)}$$

So, $\delta W_{int}^{ther} = \sum_{\forall i}\int_\Omega \kappa_i \nabla T^i . \nabla \delta T^i d\Omega + \sum_{\forall i}\int_\Omega (-D_{i,mechanical dissipation}^{current} + \Xi_i^{current})\delta T^i d\Omega$

$\eta(x,t)$ entropy per unit reference volume , $\theta(x,t)$ absolute temperature field, R^η, Q^η entropy sources and Cauchy entropy flux

—————————————————————————

By using the following relations

$D_{\delta v}F(X,t) = \frac{d\nabla(x+\varepsilon\delta v)}{d\varepsilon}|_{\varepsilon=0} = \frac{\partial\delta v}{\partial X} = \frac{\partial}{\partial t}(\frac{\partial\chi(X,t)}{\partial X}) = \frac{DF(X,t)}{Dt}$

$D_{\delta v}E(X,t) = \frac{DE(X,t)}{Dt} = \frac{1}{2}(\frac{\partial F^T}{\partial t}.F + F^T\frac{\partial F}{\partial t}), \frac{\partial C}{\partial t} = 2\frac{\partial E}{\partial t}$

$De[\delta v] = \frac{1}{2}([\frac{\partial\delta v}{\partial X}]^T + \frac{\partial\delta v}{\partial X}), e = \frac{1}{2}([\frac{\partial u}{\partial x}]^T + \frac{\partial u}{\partial x}) - \frac{1}{2}[\frac{\partial u}{\partial x}]^T\frac{\partial u}{\partial x}, E = \frac{1}{2}([\frac{\partial U}{\partial X}]^T + \frac{\partial U}{\partial X}) + \frac{1}{2}[\frac{\partial U}{\partial X}]^T\frac{\partial U}{\partial X}$

$De[\delta v] = D_{\delta v}[F^{-T}F^T eFF^{-1}] = F^{-T}D_{\delta v}(F^T eF)F^{-1} = F^{-T}D_{\delta v}E(X,t)F^{-1}$

$P = FS, \sigma = J^{-1}FSF^T$

and $\int_{\partial\Omega} t_\sigma(x,t,n)ds = \int_{\partial\Omega}\sigma(x,t)nds = \int_\Omega div\sigma(x,t)dV$

————————————————-

Linearisation:

Based on the first order Taylor's expansion of a smooth non-linear function $F = F(v)$ we have

$$F(v,\triangle v) = F(v) + \underbrace{\overbrace{\triangle F(v,\triangle v)}^{Linearization}}_{\Delta := D_{\triangle v}F(v) = \frac{d}{d\varepsilon}F(v+\varepsilon\triangle v)|_{\varepsilon=0}} + \underbrace{o(\triangle v)}_{smaller\,rortends\,to\,zero\,faster\,than\,\triangle v \to 0}$$

Appendix D

Pseudocode (modified and classical contact algorithms):

Algorithm D.1 (part 1)

1: **Begin Thread**
2: (initialize counters, rigid bodies, nonlinear constraints, material point data, the stresses)
3: **(initialize contact)**

Require: (nr of surface pair interactions) > 0 and (Γ_m,Γ_s master and slave interfaces)
Ensure: $\varepsilon_N, \lambda_N, t_N^{max}, t_T^{max}, \varepsilon_n^{coh}, \varepsilon_t^{coh}, \varepsilon_T, \mu$, and nr of steps=Stn, max nr of reformations=Mmn and newton iterations=Nitn

4: $n \leftarrow 0$
5: $m \leftarrow 0$
6: $l \leftarrow 0$
7: $d \leftarrow (d, T)$
8: Set Newmark parameters:
9: $\alpha \leftarrow 1$
10: $\beta \leftarrow \frac{1}{4}$
11: $\gamma \leftarrow \frac{1}{2}$
12: **while** $Stn \geqq n$ **do**
13:     [**Compute force vectors**]
14:     **foreach** slave element nodes **do**
15:     **if** $\exists elem \in \Gamma_m \mid projection(elem \in \Gamma_m, nod \in \Gamma_s) \leftarrow true$ **then**
16:         $A_{\alpha\beta}^{n+1} \delta \xi^{\alpha(n+1)} \leftarrow [\delta \psi_s(X) - \delta \psi_m(\bar{Y}(X))]^{n+1} . \tau_\alpha^{n+1} - \{gv\}^{n+1} . [\frac{\partial \delta \psi_m^{n+1}(\bar{Y}(X))}{\partial \alpha}]$
17:         $g_N^{(n+1)}(X, \bar{Y}(X)) \leftarrow -v^{(n+1)} . \{\psi_s^{(n+1)}(X) - \psi_m^{(n+1)}(\bar{Y}(X))\}$
18:         $g_T^{(n+1)}(X, \bar{Y}(X)) \leftarrow \varepsilon_T m_{\alpha\beta}^{(n+1)} (\xi_{n+1}^\beta - \xi_n^\beta)$
19:         **if** $g_N^{(n+1)}(X, \bar{Y}(X)) > 0$ **then**
20:             $t_N^{(n+1)} \leftarrow \lambda_N^{(n+1)} + \varepsilon_N g_N^{(n+1)}$
21:             **if** $\mu . \varepsilon_T > 0$ **then**
22:                 $T_{T_\alpha}^{n+1} \leftarrow T_{T_\alpha}^n + \varepsilon_T m_{\alpha\beta} (\xi_n^\beta - \xi_{n-1}^\beta)$
23:                 **if** $\| T_T^{n+1} \| - \mu t_N^{n+1} > 0\, (slip)$ **then**
24:                     $T_{T_\alpha}^{n+1} \leftarrow \mu t_N^{n+1} \frac{T_{T_\alpha}^{n+1}}{\|T_T^{n+1}\|},$
25:                 **end if**
26:                 $D_{mech}^{(n+1)} \leftarrow \mid T_{T_\alpha}^{(n+1)} . \frac{(\xi_{n+1}^\alpha - \xi_n^\alpha)}{\Delta t} \mid$
27:                 $q_c^{s(n+1)} \leftarrow t_N^{(n+1)}[R(T_{(n+1)}^s - T_{(n+1)}^m) + (R3)T_{(n+1)}^s - (R4)] + (R1)D_{mech}^{(n+1)}$
28:                 $q_c^{m(n+1)} \leftarrow t_N^{(n+1)}[R(T_{(n+1)}^s - T_{(n+1)}^m) + (R5)T_{(n+1)}^m - (R6)] + (R2)D_{mech}^{(n+1)}$
29:             **end if**
30:         **end if**
31:         **if** $g_N^{(n+1)}(X, \bar{Y}(X)) \leqq 0$ **then**
32:             $t_N^{(n+1)coh} \leftarrow t_N^{max} . (\frac{g_N^{(n+1)}(X)}{\varepsilon_n^{coh}}) . e^{(1 - (\frac{g_N^{(n+1)}(X)}{\varepsilon_n^{coh}}))} e^{-(\frac{(g_T^{(n+1)}(X))^2}{(\varepsilon_t^{coh})^2})}$
33:             $t_T^{(n+1)coh} \leftarrow 2\sqrt{\frac{1}{2}e} . t_T^{max} . (\frac{g_T^{(n+1)}(X)}{\varepsilon_t^{coh}}) . (1 + \frac{g_N^{(n+1)}(X)}{\varepsilon_n^{coh}}) . e^{-(\frac{g_N^{(n+1)}(X)}{\varepsilon_n^{coh}} + \frac{(g_T^{(n+1)}(X))^2}{(\varepsilon_t^{coh})^2})}$
34:             **if** $\mu . \varepsilon_T > 0$ **then**
35:                 **Case:** $g_N^{(n+1)}(X, \bar{Y}(X)) \leqq \varepsilon_n^{coh}$
36:                 $T_{T_\alpha}^{n+1} \leftarrow t_{T_\alpha}^n + \varepsilon_T m_{\alpha\beta} (\xi_{n+1}^\beta - \xi_n^\beta)$
37:                 **if** $\| T_T^{n+1} \| - \mu t_N^{(n+1)coh} > 0\, (slip)$ **then**
38:   ▷ Next page

Algorithm D.2 (part 2)

39: $$T_{T_\alpha}^{n+1} \leftarrow \mu t_N^{(n+1)} coh \frac{T_{T_\alpha}^{n+1}}{\|T_T^{n+1}\|},$$

40: **end if**

41: $$D_{mech}^{(n+1)} \leftarrow |\, T_{T_\alpha}^{(n+1)}.\frac{(\xi_{n+1}^\alpha - \xi_n^\alpha)}{\Delta t}\,|$$

42: $$q_c^{s(n+1)} \leftarrow t_N^{(n+1)} coh [R(T_{(n+1)}^s - T_{(n+1)}^m) + (R3)T_{(n+1)}^s - (R4)] + (R1)D_{mech}^{(n+1)}$$

43: $$q_c^{m(n+1)} \leftarrow t_N^{(n+1)} coh [R(T_{(n+1)}^s - T_{(n+1)}^m) + (R5)T_{(n+1)}^m - (R6)] + (R2)D_{mech}^{(n+1)}$$

44: **Case:** $g_N^{(n+1)}(X,\bar{Y}(X)) > \varepsilon_n^{coh}$

45: $$T_{T_\alpha}^{n+1} \leftarrow \mu t_N^{(n+1)} coh \frac{T_{T_\alpha}^{n+1}}{\|T_T^{n+1}\|},$$

46: $$D_{mech}^{(n+1)} \leftarrow |\, T_{T_\alpha}^{(n+1)}.\frac{(\xi_{n+1}^\alpha - \xi_n^\alpha)}{\Delta t}\,|$$

47: $$q_c^{s(n+1)} \leftarrow t_N^{(n+1)} coh [R(T_{(n+1)}^s - T_{(n+1)}^m) + (R3)T_{(n+1)}^s - (R4)] + (R1)D_{mech}^{(n+1)}$$

48: $$q_c^{m(n+1)} \leftarrow t_N^{(n+1)} coh [R(T_{(n+1)}^s - T_{(n+1)}^m) + (R5)T_{(n+1)}^m - (R6)] + (R2)D_{mech}^{(n+1)}$$

49: **end if**

50: **end if**

51: $$f_{nod}^{total(n+1)} \leftarrow f_{nod}^{con(n+1)} + f_{nod}^{coh(n+1)} + f_{nod}^{fric(n+1)} + f_{nod}^{therm(n+1)}$$

52: **end if**

53: $$F_{force}^{global} \leftarrow A_{ssemble}^{\forall elem \in \Gamma_s, k=(1,|IntP \in elem|)} W_k j(\eta_k) f_k^{total(n+1)}$$

54: (calculate the internal (stress) forces, the body forces, the inertial forces for dynamic problems, the forces due to surface loads, the nonlinear constraint forces, the nodal fluxes, the heat surface fluxes, the heat generation from heat sources)

55: [**Compute Stiffness**]

56: **foreach** slave element nodes **do**

57: **if** $\exists elem \in \Gamma_m \mid projection(elem \in \Gamma_m, nod \in \Gamma_s) \leftarrow true$ **then**

58: $$A_{\alpha\beta}^{n+1} \delta\xi^{\alpha(n+1)} \leftarrow [\delta\psi_s(X) - \delta\psi_m(\bar{Y}(X))]^{n+1}.\tau_\alpha^{n+1} - \{gv\}^{n+1}.[\frac{\partial\delta\psi_m^{n+1}(\bar{Y}(X))}{\partial\alpha}]$$

59: $$g_N^{(n+1)}(X,\bar{Y}(X)) \leftarrow -\nu^{(n+1)}.\{\psi_s^{(n+1)}(X) - \psi_m^{(n+1)}(\bar{Y}(X))\}$$

60: $$\triangle g_N^{(n+1)}(X,\bar{Y}(X)) \leftarrow \triangle[-\nu^{(n+1)}.\{\psi_s^{(n+1)}(X) - \psi_m^{(n+1)}(\bar{Y}(X))\}]$$

61: $$\triangle g_T^{(n+1)}(X,\bar{Y}(X)) \leftarrow \triangle\{\varepsilon_T m_{\alpha\beta}^{(n+1)}(\xi_{n+1}^\beta - \xi_n^\beta)\}$$

62: **if** $g_N^{(n+1)}(X,\bar{Y}(X)) > 0$ **then**

63: $$k_{(n+1)}^{con} \leftarrow Heaviside(g^{(n+1)})\varepsilon_N \triangle g^{(n+1)} \delta g^{(n+1)} + t_N^{(n+1)} \triangle\delta g^{(n+1)}$$

64: **if** $\mu.\varepsilon_T > 0$ **then**

65: $$k_{(n+1)}^{con,fric} \leftarrow \triangle T_{T_\alpha}^{(n+1)} \delta\xi^{\alpha(n+1)} + T_{T_\alpha}^{(n+1)} \triangle(\delta\xi^{\alpha(n+1)})$$

66: **if** $\| T_T^{n+1} \| - \mu t_N^{n+1} \leq 0\,(stick)$ **then**

67: $$\triangle T_{T_\alpha}^{(n+1)} \leftarrow \triangle T_{T_\alpha}^n + \triangle\{\varepsilon_T m_{\alpha\beta}^{(n+1)}(\xi_{n+1}^\beta - \xi_n^\beta)\}$$

68: **end if**

69: **if** $\| T_T^{n+1} \| - \mu t_N^{n+1} > 0\,(slip)$ **then**

70: $$\triangle T_{T_\alpha}^{(n+1)} \leftarrow \triangle\{\mu t_N^{n+1} \frac{T_{T_\alpha}^{n+1}}{\|T_T^{n+1}\|}\},$$

71: **end if**

72: $$\triangle D_{mech}^{(n+1)} \leftarrow \triangle \mid T_{T_\alpha}^{(n+1)}.\frac{(\xi_{n+1}^\alpha - \xi_n^\alpha)}{\Delta t} \mid$$

73: $$k_{(n+1)}^{c,qs} \leftarrow \triangle\{t_N^{(n+1)}[R(T_{(n+1)}^s - T_{(n+1)}^m) + (R3)T_{(n+1)}^s - (R4)] + (R1)D_{mech}^{(n+1)}\}$$

74: $$k_{(n+1)}^{c,qm} \leftarrow \triangle\{t_N^{(n+1)}[R(T_{(n+1)}^s - T_{(n+1)}^m) + (R5)T_{(n+1)}^m - (R6)] + (R2)D_{mech}^{(n+1)}\}$$

75: ▷ Next page

Algorithm D.3 (part 3)

76:	**end if**
77:	**end if**
78:	**if** $g_N^{(n+1)}(X, \bar{Y}(X)) \leqq 0$ **then**
79:	$k_{(n+1)}^{coh,norm} \leftarrow \dfrac{\partial t_N^{(n+1)coh}}{\partial g_N^{(n+1)}} . \triangle g_N^{(n+1)} + \dfrac{\partial t_N^{(n+1)coh}}{\partial g_T^{(n+1)}} . \triangle g_T^{(n+1)}$
80:	$k_{(n+1)}^{coh,tang} \leftarrow \dfrac{\partial t_T^{(n+1)coh}}{\partial g_N^{(n+1)}} . \triangle g_N^{(n+1)} + \dfrac{\partial t_T^{(n+1)coh}}{\partial g_T^{(n+1)}} . \triangle g_T^{(n+1)}$
81:	**if** $\mu.\varepsilon_T > 0$ **then**
82:	**Case:** $g_N^{(n+1)}(X, \bar{Y}(X)) \leqq \varepsilon_n^{coh}$
83:	**if** $\| T_T^{n+1} \| - \mu t_N^{(n+1)coh} \leqq 0 \, (stick)$ **then**
84:	$\triangle T_{T_\alpha}^{(n+1)} \leftarrow \triangle T_{T_\alpha}^n + \triangle\{\varepsilon_T m_{\alpha\beta}^{(n+1)}(\xi_{n+1}^\beta - \xi_n^\beta)\}$
85:	**end if**
86:	**if** $\| T_T^{n+1} \| - \mu t_N^{(n+1)coh} > 0 \, (slip)$ **then**
87:	$\triangle T_{T_\alpha}^{(n+1)} \leftarrow \triangle\{\mu t_N^{(n+1)coh} \dfrac{T_{T_\alpha}^{n+1}}{\|T_T^{n+1}\|}\},$
88:	**end if**
89:	$\triangle D_{mech}^{(n+1)} \leftarrow \triangle \mid T_{T_\alpha}^{(n+1)} . \dfrac{(\xi_{n+1}^\alpha - \xi_n^\alpha)}{\triangle t} \mid$
90:	$k_{(n+1)}^{ch,qs} \leftarrow \triangle\{t_N^{(n+1)c}[R(T_{(n+1)}^s - T_{(n+1)}^m) + (R3)T_{(n+1)}^s - (R4)] + (R1)D_{mech}^{(n+1)}\}$
91:	$k_{(n+1)}^{ch,qm} \leftarrow \triangle\{t_N^{(n+1)c}[R(T_{(n+1)}^s - T_{(n+1)}^m) + (R5)T_{(n+1)}^m - (R6)] + (R2)D_{mech}^{(n+1)}\}$
92:	**Case:** $g_N^{(n+1)}(X, \bar{Y}(X)) > \varepsilon_n^{coh}$
93:	$\triangle T_{T_\alpha}^{(n+1)} \leftarrow \triangle\{\mu t_N^{(n+1)coh} \dfrac{T_{T_\alpha}^{n+1}}{\|T_T^{n+1}\|}\},$
94:	$\triangle D_{mech}^{(n+1)} \leftarrow \triangle \mid T_{T_\alpha}^{(n+1)} . \dfrac{(\xi_{n+1}^\alpha - \xi_n^\alpha)}{\triangle t} \mid$
95:	$k_{(n+1)}^{ch,qs} \leftarrow \triangle\{t_N^{(n+1)c}[R(T_{(n+1)}^s - T_{(n+1)}^m) + (R3)T_{(n+1)}^s - (R4)] + (R1)D_{mech}^{(n+1)}\}$
96:	$k_{(n+1)}^{ch,qm} \leftarrow \triangle\{t_N^{(n+1)c}[R(T_{(n+1)}^s - T_{(n+1)}^m) + (R5)T_{(n+1)}^m - (R6)] + (R2)D_{mech}^{(n+1)}\}$
97:	**end if**
98:	**end if**
99:	$k_{nod}^{total(n+1)} \leftarrow k_{nod}^{con(n+1)} + k_{nod}^{ch(n+1)} + k_{nod}^{fric(n+1)} + k_{nod}^{therm(n+1)}$
100:	**end if**
101:	$K_{stiffness}^{global} \leftarrow A_{ssemble}^{\forall elem \in \Gamma_s, m=(1,|IntP \in elem|)} W_m j(\eta_m) k_m^{total(n+1)}$
102:	(calculate the internal stiffness, the body force stiffness, the mass matrix for dynamic problems, the stiffness for surface loads, the nonlinear constraint stiffness, the capacitance matrix, the conduction stiffness, the convective heat flux stiffness)
103:	**while** not converged **do**
104:	**if** $Mmn < m \vee Nitn < l$ **then** goto End
105:	**end if**
106:	$S^{converge} \leftarrow true$
107:	Solve the equations for $d_{n+\alpha}^l, T_{n+\alpha}^l$:
108:	$I : R^{global}[d_{n+\alpha}^l] = F_{ext}^{mech}(t_{n+\alpha}) + F_{ext}^{ther}(t_{n+\alpha}) - M[\ddot{d}_{n+\alpha}^l \mid a_{n+\alpha}^l] - C\dot{d}_{n+\alpha}^l - F_{int}^{mech}[d_{n+\alpha}^l] - F_{int}^{ther}[d_{n+\alpha}^l] - F^C[d_{n+\alpha}^l]$
109:	$II : d_{n+\alpha}^l = d_n + v_n(t_{n+\alpha} - t_n) + \frac{1}{2}[2\beta a_{n+\alpha}^l + (1 - 2\beta)a_n](t_{n+\alpha} - t_n)^2$
110:	$III : v_{n+\alpha}^l = v_n + [\gamma a_{n+\alpha}^l + (1 - \gamma)a_n](t_{n+\alpha} - t_n)$
111:	

Algorithm D.4 (part 4)

112:      $IV: T^l_{n+\alpha} = \dfrac{[D^{(n+\alpha)^l}_{mechanical\,dissipation} + R_{d^l_{n+\alpha}} - DIV(Q_{d^l_{n+\alpha}})]}{[\eta^l_{n+\alpha} - \eta_n]}(t_{n+\alpha} - t_n)$

113:      $V: T^{contact^l}_{n+\alpha}(T^{contact^l}_{n+\alpha} - T^{contact}_n) = \dfrac{T_0[\xi\|t^{(n+\alpha)^l}_f\| + t^{(n+\alpha)^l}_N h^m_c \theta^{(n+\alpha)^l}_m + t^{(n+\alpha)^l}_N h^s_c \theta^{(n+\alpha)^l}_s]}{C^{heat\,sink}_{contact}}$

114:      $L(s) \leftarrow d^T_{n+1}R(d^l_{n+1} + s\triangle d)$ [perform a linesearch]

115:      **if** $\mid L(s) \mid \geq Tol \mid L(0) \mid \vee L(0)L(1) < 0$ **then**

116:          Iterate $for\, s \in (0,1), such\,that \mid L(s) \mid \leq Tol \mid L(0) \mid$

117:      **else**

118:          $s \leftarrow 1$ [Update(geometry), Update(residual)]

119:      **end if**

120:      **if** $\dfrac{R^{global}(d^l_{n+1} + s\triangle d) * R^{global}(d^l_{n+1} + s\triangle d)}{R^{global}(d^l_{n+1}) * R^{global}(d^l_{n+1})} > R^{tol} \wedge R^{tol} > 0$ **then**

121:          $S^{converge} \leftarrow false$

122:      **end if**

123:      **if** $\dfrac{(s\triangle d) * (s\triangle d)}{(d^l_{n+1} + s\triangle d) * (d^l_{n+1} + s\triangle d)} > d^{tol} * d^{tol} \wedge d^{tol} > 0$ **then**

124:          $S^{converge} \leftarrow false$

125:      **end if**

126:      **if** $\dfrac{s * \mid \triangle d * R^{global}(d^l_{n+1} + s\triangle d) \mid}{\mid \triangle d * R^{global}(d^l_{n+1}) \mid} > E^{tol} \wedge E^{tol} > 0$ **then**

127:          $S^{converge} \leftarrow false$

128:      **end if**

129:      **if** $s < LineS^{stp}_{min} \wedge LineS^{tol} > 0$ **then**

130:          $S^{converge} \leftarrow false$

131:      **end if**

132:      **if** $s * \mid \triangle d * R^{global}(d^l_{n+1} + s\triangle d) \mid > \mid \triangle d * R^{global}(d^l_{n+1}) \mid$ **then**

133:          $S^{converge} \leftarrow false$

134:      **end if**

135:      **if** $S^{converge} \leftarrow false$ **then**

136:          **do**

137:          $m \leftarrow m + 1$ [ReformStiffness()]

138:          **if** $Mmn < m$ **then**

139:              **break**

140:          **end if**

141:      **end if**

142:      **else if** $augmentations \leftarrow true$

143:      Augment()

144:      **if** $maximum\,augmentations \leftarrow true$ **then**

145:          **break**

146:      **end if**

147:      $l \leftarrow l + 1$

148:      **end while**

149:      **if** converged **then**

150:          update the total displacements, the kinematics (the velocity and the accelerations, the rigid bodies data), the temperatures, the element stresses, the body loads, the nonlinear constraints, the contact interfaces

151:          $n \leftarrow n + 1$

152:      **end if**

153: **end while**

154: **End Thread**